

Active matter: from collective self-propelled rods to cell-like particles

Inaugural-Dissertation

zur

Erlangung des Doktorgrads

der Mathematisch-Naturwissenschaftlichen Fakultät

der Universität zu Köln

vorgelegt von

Clara Abaurrea Velasco

aus Zaragoza, Spanien

Jülich 2018

Berichterstatter: Prof. Dr. Gerhard Gompper

Prof. Dr. Matthias Sperl

Prof. Dr. Ulrich Schwarz

Tag der mündlichen Prüfung: 07. Mai 2018

*A mis padres,
Jesús y Curra.*

*"Sometimes I sits and thinks,
and sometimes I just sits."*

-A.A. Milne, Winnie-the-Pooh

Zusammenfassung

Aktive Materie umfasst Systeme, deren Komponenten kontinuierlich Energie aufnehmen und dissipieren. Aktive Systeme mit vielen Agenten zeigen ein sehr reiches und komplexes kollektives Verhalten auf vielen verschiedenen Größenordnungen: Zytoskelettfilamente, bewegliche Zellen, phoretische Mikroschwimmer, Fischschwärme und Vogelschwärme. Kleine Änderungen auf der Ebene des Einzelagenten können sich rasch ausbreiten und auf lange Sicht entstehende Strukturen und Ordnung erzeugen. Zellskelett-Filamente und Motorproteine beispielweise bilden aktive viskoelastische Netzwerke und Bündel, welche die Form und Bewegung von Zellen bestimmen. Bakterien, die mit niedriger Reynolds-Zahl schwimmen, bilden aktive Kolonien, in denen turbulente Dynamik beobachtet wird. Wir untersuchen das kollektive Verhalten und die Dynamik von Bakterien und aktiven Filamenten mit Hilfe von Computersimulationen von selbstangetriebenen Stäben sowohl in Systemen mit periodischen Randbedingungen, als auch in Systemen mit räumlicher Einschränkung.

Phoretische Mikroschwimmer und genetisch veränderte *E. coli* Bakterien zeigen einen dichteabhängig-reduzierten Antrieb. Wir untersuchen das kollektive Verhalten und die Dynamik von selbstangetriebenen Stäben (SPRs) mit dichteabhängiger Antriebskraft. Während SPRs mit dichteunabhängigem Antrieb Streifen und gigantisch-wurmähnliche Cluster bilden, bilden SPRs mit dichteabhängig reduziertem Vortrieb Asten und polare Bänder. Die dichteabhängige Verlangsamung verstärkt die polare Ordnung und Clusterbildung der Stäbe und induziert eine lotrechte Anordnung an den Clustergrenzen. Daher sind Regionen mit geringer Dichte in Clusterphasen nahezu leer von Stäben. Dieses Phänomen wird in Clusterphasen klassischer SPRs nicht beobachtet.

Wir untersuchen auch SPRs innerhalb von mobilen, starren, kreisförmigen Begrenzungen, welche somit komplexe, selbstangetriebene, starre Ringe bilden. Die Stäbe sind am Ring verankert, können jedoch entlang der Kontur des Rings gleiten. Dies erlaubt uns, Systeme mit Schub-, Zug- und Mischstäben zu studieren. Die Stabdynamik und die emergenten Strukturen bestimmen die Ringdynamik und Bewegung. Zudem vermittelt die Ringmotilität SPR-Clusterbildung. Aktive Brownsche Teilchen weisen für kurze Beobachtungszeiten ein thermisches Diffusionsregime, für mittlere Zeiten ein ballistisches Regime und für lange Zeiten ein aktives Diffusionsregime auf. Die zusätzlichen internen Freiheitsgrade im komplexen, selbstangetriebenen Ring führen zu einer Gesamttringdynamik, die nicht durch das aktive Brownsche Teilchenmodell erfasst werden kann. Die Stab-Selbstorganisation führt zu komplexen Motilitätsmustern, wie Run-and-Tumble und Run-and-Circle Bewegungen. Diese Motilitätsmuster, werden auch bei beweglichen Zellen beobachtet.

In einem weiteren Schritt hin zur Modellierung der Zellmotilität untersuchen wir SPRs in mobilen, deformierbaren Ringen. Neben der Ringmotilität spielt die Deformierbarkeit eine entscheidende Rolle für die SPR-Ausrichtung und Clusterbildung. In Abhängigkeit von der Aktivität der Stäbchen und der Reibung zwischen dem Ring und dem Substrat finden wir drei verschiedene Klassen von Ringformen: fluktuierend, keratozytenähnlich und neutrophilartig. Hier sind Zugkräfte an der Rückseite der Ringe von entscheidender Bedeutung für die Erlangung von zellähnlichen Formen und

Bewegungsmustern. Die Streuung keratozytenähnlicher Ringe an Wänden zeigt, dass der Austrittswinkel unabhängig vom Eintrittswinkel ist, was mit experimentellen Beobachtungen von Keratozyten an Grenzflächen zwischen glatten und mikro-strukturierten Oberflächen übereinstimmt. Darüber hinaus haben experimentelle Studien gezeigt, dass Substrateigenschaften, wie die Haftfestigkeit, die Form und Bewegung der Zelle stark beeinflussen. In Übereinstimmung mit Experimenten zeigen Simulationen verformbarer Ringe an Reibungsgrenzflächen Formänderungen und Ablenkungen der Bewegungsrichtung der Ringe.

Unsere Simulationen beschreiben aktive Systeme mit stabförmigen Komponenten, deren Antrieb sich an die Umgebung anpasst. Während SPRs mit dichteabhängiger Verlangsamung teilweise das beobachtete Verhalten von Bakterien mit dichteabhängig-reduziertem Antrieb erfassen, können SPRs in einer ringähnlichen Begrenzung als minimales, Weiche-Materie-Modell für Zellmotilität angesehen werden. Mit unseren Simulationen können wir systematisch den Einfluss verschiedener Parameter wie Zellantrieb und Substrateigenschaften auf die Zellmotilität charakterisieren. Obwohl unsere Modelle biochemische Aspekte biologischer Systeme nicht berücksichtigen, ermöglichen sie uns, entscheidende mechanische Aspekte zu identifizieren. Sie erlauben uns verschiedene zugrunde liegende Mechanismen zu testen, um mikroskopische Beobachtungen zu interpretieren.

Abstract

Active matter comprises systems with sustained energy uptake and dissipation of its constituents. This applies to systems across many scales: cytoskeletal filaments, motile cells, phoretic microswimmers, fish schools, and bird flocks. Active systems with many agents show very rich and complex collective behavior. Small changes on the single-agent level can quickly propagate and generate emergent order and structures on the large scale. Cytoskeletal filaments and motor proteins form active viscoelastic networks and bundles which dictate the cell shape and motion. Bacteria, which are organisms that swim at low Reynolds number, form active colonies where turbulent-like dynamics is observed.

We study ensembles of self-propelled rods (SPRs) in periodic boundaries and in confinement to mimic the collective behavior and dynamics of bacteria, and active filaments. All our simulations are performed using Brownian dynamics, where friction and noise are chosen to fulfill the fluctuation dissipation theorem. Our models describe active systems that allow the propulsion to adapt to its environment. While SPRs with density-dependent slowing down partially capture the behavior observed for bacteria, SPRs in ring-like confinements can be considered as a minimal, soft matter model for cell motility.

Phoretic microswimmers and genetically modified *E. coli* show density-dependent reduced propulsion. This motivates the investigation of the collective behavior and dynamics of SPRs with density-dependent propulsion force. While SPRs with density-independent propulsion form lanes and giant worm-like clusters, SPRs with density-dependent reduced propulsion form asters and polar bands. The density-dependent slowing down enhances polar ordering and cluster formation, and induces rod perpendicularity at cluster borders. Therefore, low-density regions in clustered phases are nearly empty of rods. This phenomenon is not observed in clustered phases of classical SPRs.

As a model of cellular motility due to cytoskeletal activity, SPRs inside mobile, rigid circular confinement are considered, which build complex self-propelled rings. The rods are anchored to the ring, but they can still slide along the ring. This allows us to study systems with pushing, pulling and mixed rods. The rod dynamics and emergent structures dictate the ring dynamics and motion, and the ring motility enhances SPR cluster formation. Active Brownian particles show a thermal diffusive regime at short times, a ballistic regime at intermediate times, and an active diffusive regime at long times. The additional internal degrees of freedom in a complex self-propelled ring lead to overall ring dynamics that cannot be captured by the active Brownian particle model. The rod self-organization gives rise to complex motility patterns, such as run-and-tumble and run-and-circle motion. Motility patterns observed for self-propelled rigid rings are also observed for motile cells.

Taking a further step towards a more realistic modeling of cell motility, we study SPRs inside mobile, deformable rings. In addition to ring motility, also ring deformability plays a crucial role in SPR alignment and cluster formation. Depending on rod activity and friction between the ring and substrate, we find three different classes of

ring shapes: fluctuating, keratocyte-like, and neutrophil-like. Here, pulling forces at the back of the rings are crucial to recovering cell-like shapes and motion. Scattering of keratocyte-like rings at walls shows that the angle of exit is independent of the initial angle, which agrees with experimental findings for keratocytes at interfaces between smooth and microgrooved surfaces. Furthermore, experimental studies have proven that substrate properties, such as adhesion strength, profoundly affect the cell shape and motion. In agreement with the experiments, simulations for deformable rings at friction interfaces show shape changes, and deflection of the ring trajectory.

Our simulations allow the systematic characterization of the effect of different parameters, such as cell propulsion and substrate properties, on cell motility. While our models do not take into account biochemical aspects of biological systems, they allow the identification of crucial mechanical aspects, and help to test different underlying mechanisms to interpret microscopic observations.

Contents

| | | |
|----------|---|-----------|
| 1 | Introduction | 1 |
| 1.1 | Active matter | 1 |
| 1.2 | Cytoskeleton | 3 |
| 1.2.1 | Cytoskeletal filaments | 3 |
| 1.2.2 | Molecular motors | 9 |
| 1.2.3 | Motility assays | 9 |
| 1.3 | Lipid bilayers and plasma membranes | 11 |
| 1.4 | Cell motility | 16 |
| 1.5 | Outline of the thesis | 17 |
| 2 | Theoretical background, model and simulation techniques | 21 |
| 2.1 | Swimming at low Reynolds number | 22 |
| 2.2 | Langevin equation | 23 |
| 2.3 | Anisotropic rod friction | 24 |
| 2.4 | Active Brownian particle model | 26 |
| 2.5 | Penetrable self-propelled rods | 27 |
| 2.6 | Semiflexible polymer ring | 30 |
| 2.7 | Rod-ring interaction | 33 |
| 2.8 | Brownian dynamics simulations | 35 |
| 3 | Collective behavior of density-dependent self-propelled rods | 39 |
| 3.1 | Density-independent propulsion force | 40 |
| 3.2 | Density-dependent propulsion force: phase diagrams | 43 |
| 3.3 | Density-dependent slowing-down enhances polarity | 47 |
| 3.4 | Density-dependent propulsion enhances clustering | 50 |
| 3.5 | Density-dependent propulsion induces perpendicularity | 52 |
| 3.6 | Rod dynamics | 54 |
| 4 | Self-propelled rigid rings | 57 |
| 4.1 | Internal structure and rod dynamics of stationary rings | 58 |
| 4.2 | Internal structure of mobile rings | 67 |
| 4.3 | Active Brownian motion | 72 |
| 4.4 | Beyond the active Brownian particle description | 76 |

CONTENTS

| | | |
|----------|--|------------|
| 5 | Self-propelled deformable rings | 79 |
| 5.1 | Deformable rings: phase diagrams and motility | 80 |
| 5.1.1 | Shape analysis | 82 |
| 5.1.2 | Motility analysis | 87 |
| 5.1.3 | Mixed systems | 90 |
| 5.2 | Deformable rings at walls | 91 |
| 5.2.1 | Trajectory and shape analysis for rings close to walls | 94 |
| 5.2.2 | Bending rigidity dependence of rings interacting with walls | 99 |
| 5.2.3 | Interaction of mixed systems with walls | 101 |
| 5.3 | Deformable rings at friction interfaces | 105 |
| 6 | Conclusions and Outlook | 113 |
| 6.1 | Collective behavior of self-propelled rods with density-dependent reduced propulsion | 113 |
| 6.2 | Self-propelled rods in rigid rings: cell-like motility patterns | 115 |
| 6.3 | Self-propelled rods in deformable rings as model cells | 116 |
| 6.4 | Cell scattering at walls and interfaces | 117 |
| 6.5 | Outlook | 118 |
| A | Density-dependent rods: Systems with $n_r = 18$ and $Pe = 100$ and tables for polar and nematic order parameter | 121 |
| B | Self-propelled rods inside a channel | 125 |
| C | Moments of a distribution | 127 |

Chapter 1

Introduction

1.1 Active matter

Active matter comprises systems where activity, produced at the single agent level, is converted into collective motion, stress or growth at larger scales, i.e., out-of-equilibrium systems. [1–3]. This applies to systems across many scales: cytoskeletal motility assays and active gels [4–9], motile cells and tissues [10–15], phoretic microswimmers [16–19], fish schools and bird flocks [20–26].

From a physics point of view, active matter systems are fascinating. Because the systems are out-of-equilibrium, the development of new tools in the field of non-equilibrium-physics has been necessary [30–33]. However, in many cases it is possible to make analogies between active systems and equilibrium statistical mechanics. For example, active nematics and bacterial colonies can be studied using liquid crystal theory [31, 34]. Magnetic colloids in external magnetic fields show active turbulent behavior for small Reynolds number, which has similar characteristics to classical turbulence [35]. Active particles show phase segregation [36–38]. Tissue shows a glass transition due to jamming and caging between cells [39–41].

Most systems found in biology are active matter systems that show collective behavior. A group of fish that stay together is called a shoal of fish; if the group swims collectively, it is called a school of fish, see Fig. 1.1a. There are many benefits which derive from shoaling behavior: defense against predators (better predator detection and reducing the probability of individual capture) [42, 43], enhanced foraging [44], higher chances of finding a mate [45] and hydrodynamic efficiency [23, 24]. Collective cell migration is essential for wound healing [15], where the primary goal for epithelial cells is to restore the epithelial barrier, see Fig. 1.1b. Recent studies have found that cells respond differently to the same directional cues when they are isolated than when they form part of a cohesive group. Swarming is a rapid and collective way for bacteria to move. In vitro, swarming depends strongly on nutrient concentration and viscosity of the culture medium. Swarming bacteria that swim away from their original location tend to form dendritic fractal-like patterns, see Fig. 1.1c. The speeds and orientations of swarming cells are correlated over short distances. For swarming *E. coli*, swirling and small vortex-like structures are observed, and the typical run-and-tumble behav-

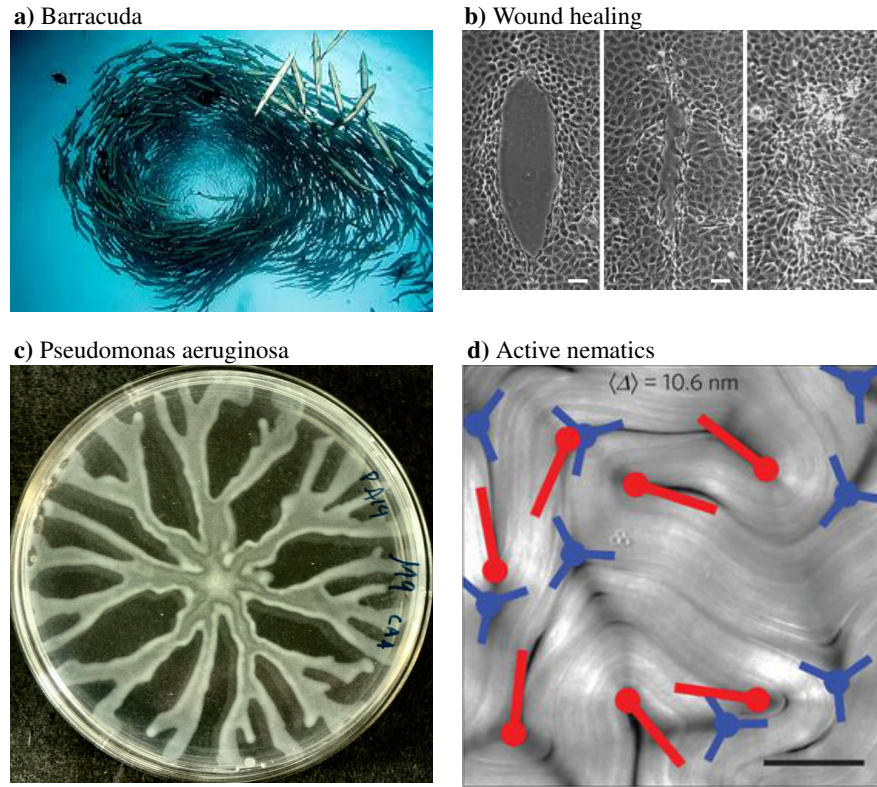


Figure 1.1: Active biological matter. **a)** Barracuda swimming collectively. Figure reproduced from Ref. [27] ©2007 Robin Hughes. **b)** Wound closure in Madin–Darby canine kidney (MDCK) epithelial cell monolayers. Cells are shown immediately after wounding and microinjection, after 6 h, and after 18 h. Figure reproduced from Ref. [28] with permission from Cell Press. **c)** Swarming colony of the bacterium *Pseudomonas aeruginosa*. Figure reproduced from Ref. [29] ©2012 Jacopo Werther. **d)** Active droplet filled with microtubules and kinesin motor mixtures. Red and blue markers indicate locations and orientations of $+1/2$ and $-1/2$ defects, respectively. Figure reproduced from Ref. [8] with permission from the Nature Publishing Group.

ior observed for single cells is suppressed. Active nematics are a new class of liquid crystals, where the systems are driven away from equilibrium by the movement of their rod-like particles [7, 46]. This internally generated activity powers the continuous creation and annihilation of topological defects, which leads to complex streaming flows whose chaotic dynamics seem to destroy long-range order [8, 34, 47]. Topological defects in an active nematics system made of microtubules and kinesins are highlighted by red arrows in Fig. 1.1d. Topological defects are regions where the nematic director field is discontinuous [48].

1.2 Cytoskeleton

The cytoskeleton helps cells maintain their shape and internal organization. Its role is to provide mechanical support for cells to move and divide. The cytoskeleton of eukaryotic cells is made of filamentous proteins, molecular motors, and crosslinkers.

1.2.1 Cytoskeletal filaments

Eukaryotic cells contain three kinds of cytoskeletal filaments: actin, microtubules and intermediate filaments [51–53]. All filaments are formed by polymerization of distinct types of protein subunits, monomers, and each type has its own characteristic shape and mechanical properties. Actin filaments are closely related to crawling cell motility. Actin polymerization and filopodia formation at the front of cells [54–57], and stress fiber formation at the back [58, 59] drive cell shape changes and cell motility. Microtubules are necessary for the active transport of molecules inside cells and play a crucial role in cell division [60, 61], and in neuronal axon growth [62, 63]. Intermediate filaments are one of the main components of desmosomes [64–66], cellular structures in charge of cell-to-cell adhesion. We focus here on actin, the filament that is most closely related to crawling cell motility.

G-actin is a globular protein with a centrally located ATP binding site [67]. If ATP occupies the binding site, multimerization of G-actin monomers occurs, and a helix-shaped polar filamentous polymer called F-actin is formed, see Fig. 1.2a. G-actin attaches to the ATP-binding cleft of another G-actin. Actin filament polymerization occurs over three phases [68]: a nucleation phase, an elongation phase, and a steady-state phase. If the G-actin concentration is larger than the critical nucleation concentration, actin nuclei form. In vivo actin nucleation is regulated by proteins [69, 70], which leads to actin nucleation even if the G-actin concentration in the cell is smaller than the critical nucleation concentration. In the elongation phase, free G-actin molecules in the cell attach to actin, generating growing actin filaments. Finally, in the steady-state phase, the actin filament length reaches a constant value. The rate at which the filament polymerizes is equal to the rate of depolymerization.

Actin filaments are polar filaments; actin monomers do not attach or detach from both ends of the filament at random. G-actin molecules with ATP preferably attach to the growing end of the filament, the + end. As the filament grows, the ATP starts to hydrolyze to ADP and inorganic orthophosphate, P_i . Due to this process, in the middle of the filament, we find many monomers with ADP- P_i . After a while, the P_i

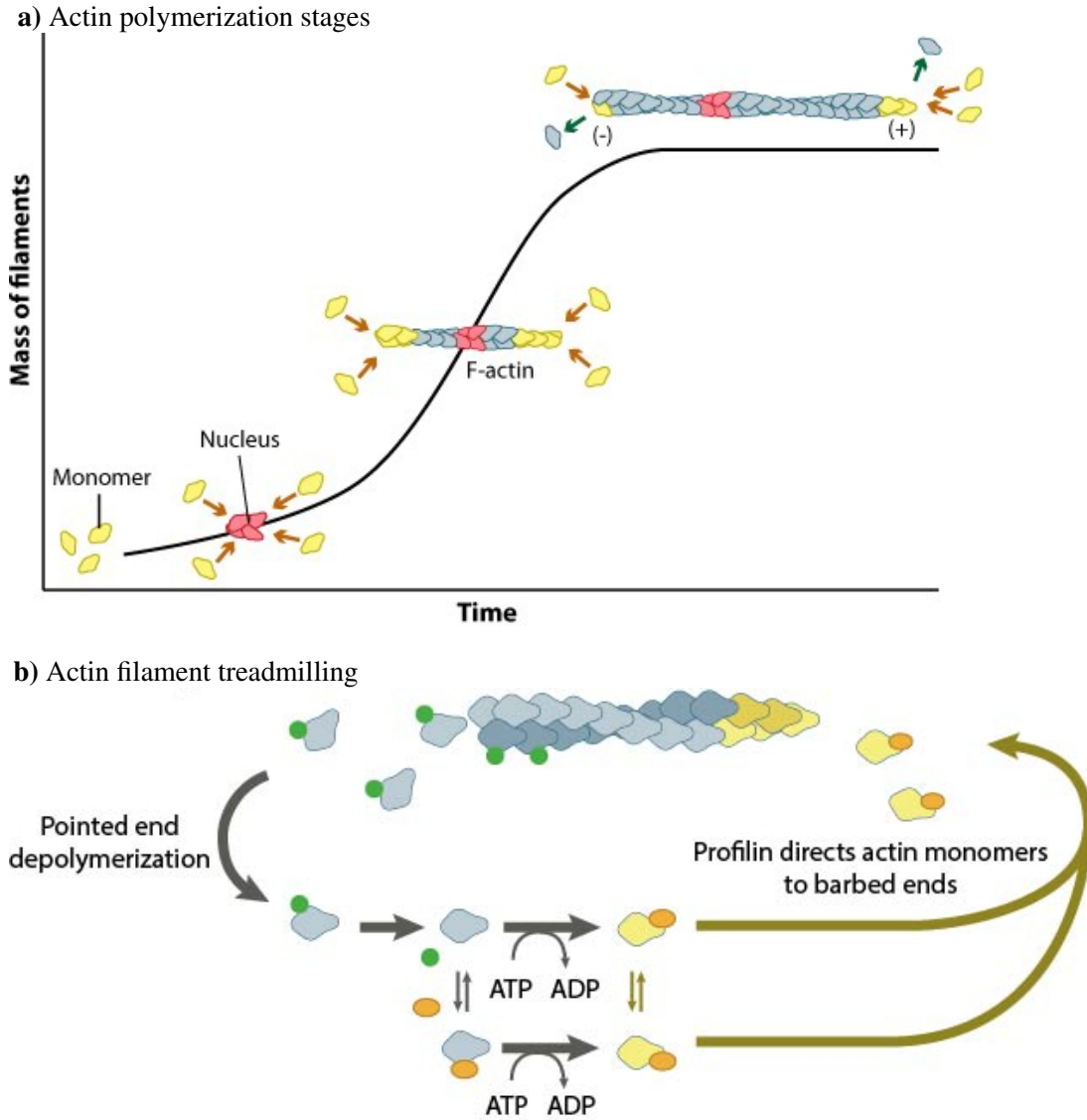


Figure 1.2: Actin polymerization. **a)** Nucleation phase, elongation phase and steady-state phase. Figure reproduced from Ref. [49] with permission from MBInfo ©2018 National University of Singapore. **b)** Actin treadmilling. Monomers bound to ATP attach to the + end of the filament. Monomers bound to ADP detach from the - end of the filament. During this process, the filament length is conserved. Figure reproduced from Ref. [50] with permission from MBInfo ©2018 National University of Singapore.

1.2 Cytoskeleton

| Filament | Persistence length | Filament length | Flexibility |
|--------------|--------------------|---------------------------|--------------|
| Actin | 15 μm | 10 μm | Semiflexible |
| Keratin | 1 μm | 2 μm | Semiflexible |
| Microtubules | 6 mm | 200 nm - 25 μm | Rigid |

Table 1.1: Comparison of persistence length and flexibility between the three main types of cytoskeletal filaments of eukaryotic cells. Keratin is a type of intermediate filament. The values in this table are reproduced from the following Refs. [51–53, 84–86].

dissociates from the G-actin molecules. Actin monomers with ADP preferably detach from the shrinking end, the - end. This process leads to constant actin filament length and is known as actin treadmilling [71, 72], see Fig. 1.2b. Under the microscope, a treadmilling actin filament looks like a polymer of constant length, which is being propelled tangentially.

The actin cytoskeleton is essential for mesenchymal motility. At the front of mesenchymal cells, we find pushing forces due to actin treadmilling. At the cell rear, we find retraction forces caused by actomyosin fibers or myosin-driven actin flow. Here, we focus on the actin polymerization and actin structures at the front of the cell. Actin structures at the rear of the cell are explained in Sec. 1.4.

At the front of crawling cells, we typically find two types of actin structures: branched actin in the lamellipodium, and actin bundles or cables in filopodia, see Fig. 1.3. The most important regulators of the actin assembly machinery in mesenchymal cells are the Arp2/3 complex and formins. Actin in the lamellipodium is nucleated by the combined actions of Arp2/3 and its cofactors [74, 75]. In actin bundles actin polymerization is regulated by formins [76].

Actin filaments are formed by polymerizing actin monomers at the barbed end, the + end. Capping proteins can bind to barbed ends, which inhibits further growth and terminates elongation. When an external stimulus triggers a signaling cascade in the cell, the Arp2/3 complex is activated [77, 78]. This protein can initiate new filament branches on preexisting filaments with a characteristic relative angle difference of $\sim 70^\circ$ between both. Another protein that regulates actin dynamics and polymerization in the lamellipodium is cofilin. Cofilin actively severs actin filaments into actin monomers [79]. Formin is a protein which regulates and promotes actin polymerization [80]. Filopodia are tubule-like protrusions at the front of cells, which are made by several actin filaments bundled together. At the tip of filopodia, the concentration of G-actin monomers tends to be lower than in the lamellipodium, and formin is needed to regulate actin polymerization at the tip of filopodia [81, 82]. The depolymerization of actin bundles in the filopodia is also regulated by cofilin. One of the crosslinkers for actin filaments inside bundles is fimbrin.

In cellular processes, the mechanical properties of cytoskeletal filaments are of course important, in particular, their rigidity, see Fig. 1.4 and Tab 1.1. Filaments with lengths similar to, or larger than the persistence length, such as actin and intermediate filaments, behave as semiflexible polymers. Filaments with lengths much smaller than the persistence length, such as microtubules, behave as rigid rods.

Introduction

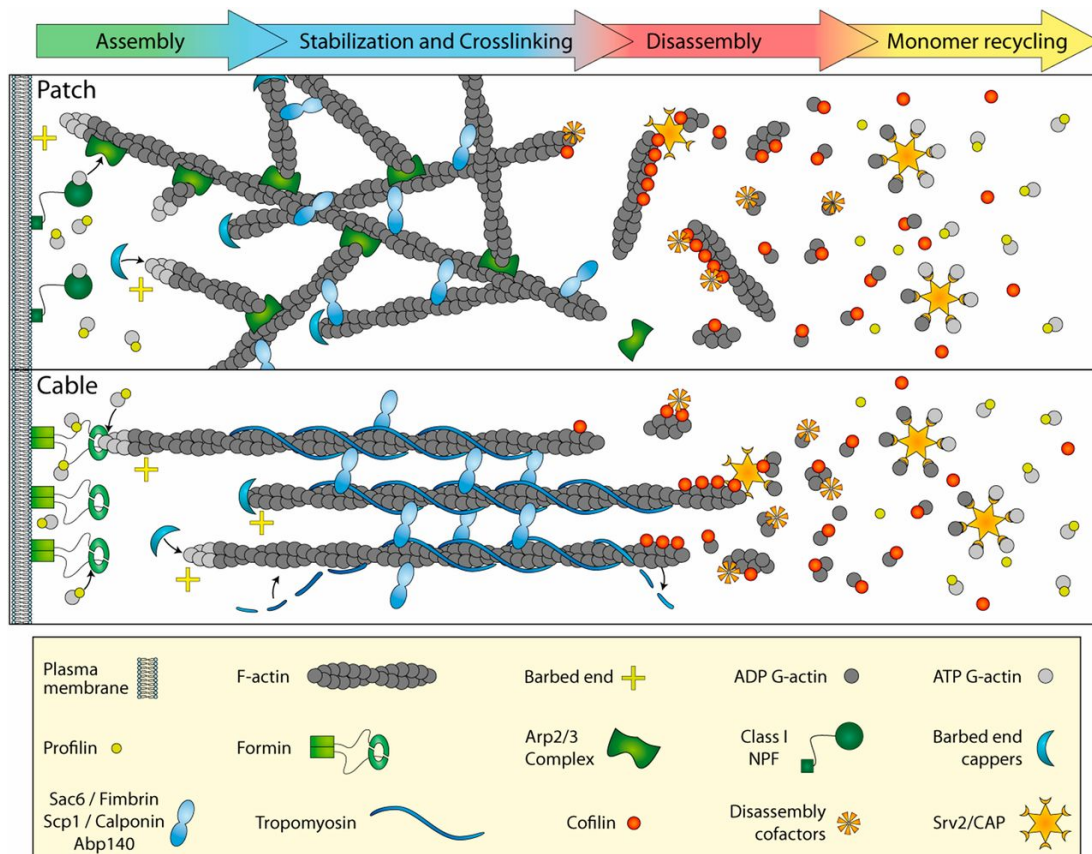


Figure 1.3: Actin structures in vivo at the front of mesenchymal cells. Top row: branched actin structure found in the lamellipodium. Bottom row: actin bundles found in filopodia. The left side of the figure represent the cell lipid bilayer, and the right side of the figure indicates the cell inside. Legend with some of the molecules involved in actin polymerization, depolymerization, crosslinking, and capping is shown at the bottom of the figure. Figure reproduced from Ref. [73] with permission from MBInfo ©2018 National University of Singapore.

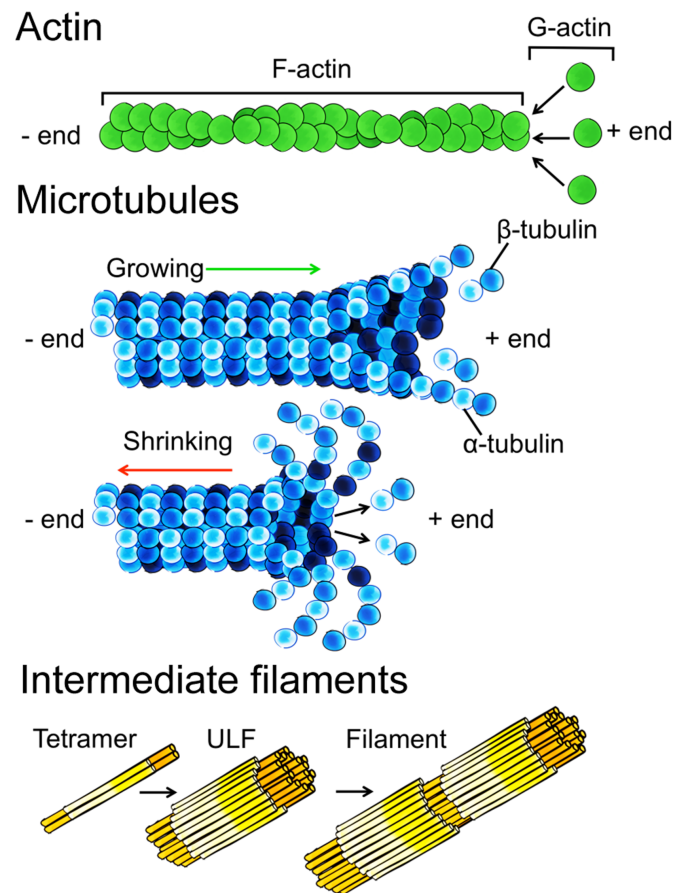


Figure 1.4: Comparison between the shape and dimensions of the three cytoskeletal filaments: actin, microtubules, and intermediate filaments. Figure reproduced from Ref. [83] with permission from the Public Library of Science ©2014 Serge Mostowy.

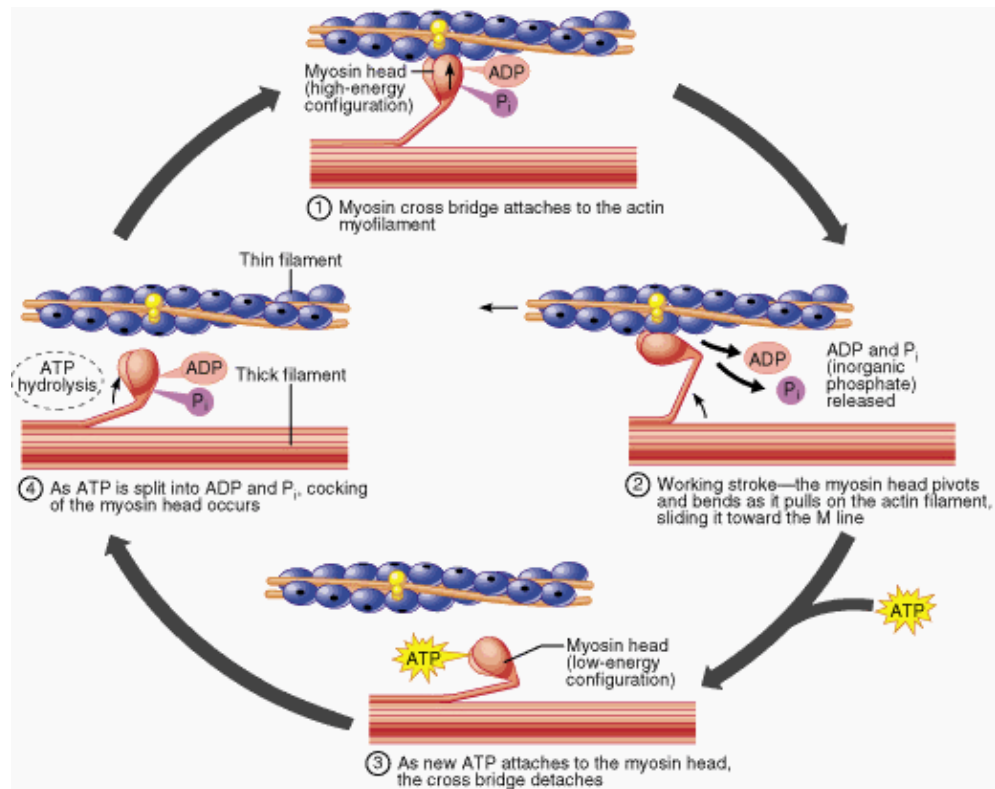


Figure 1.5: Myosin motor reaction cycle. In step 1 the myosin head domain attaches to the actin filament in a perpendicular orientation. In step 2 the ADP and P_i are released, and the myosin head changes configuration pulling on the actin. This step is known as the power stroke. In step 3 ATP binds to the myosin head and the head of the motor detaches from the filament. In step 4 the ATP hydrolyzation occurs and the myosin head recovers the perpendicular orientation with respect to the actin filament. Figure reproduced from Ref. [87] photo credit: Amazonaws.com.

1.2.2 Molecular motors

Actin polymerization and nucleation is an ATP-driven process. However, there is also another component of the cytoskeleton that drives the system out-of-equilibrium. Cytoskeletal motor proteins are a class of molecular motors, composed of a head, a neck, and a tail domain [88], that can move along cytoskeletal filaments [89]. They convert chemical energy into mechanical work by the hydrolysis of ATP. Myosins are associated with actin filaments [88], kinesins [90,91] and dyneins [92,93] with microtubules. The interaction between myosin motors and actin filaments are discussed here since these complexes are prevalent in crawling cells.

Myosins are a superfamily of molecular motors that comprises several types of myosin motors with different functions. Their heads bind filamentous actin and use ATP hydrolysis to generate force and to "walk" along the filaments. Their necks act as linkers and as lever arms that translate the forces generated by the motor domains. Their tails contain the binding sites that determine the specific functions of a particular myosin. The tails of myosins I and V bind to the plasma membrane, that is why these two motors have membrane-related functions [88]. A myosin motor is able to propel actin filaments performing a "walking cycle" [68,94]:

- The myosin head domain forms a new bridge to the adjacent actin molecule. A bound ATP molecule hydrolyzes into ADP+Pi, see step 1 of Fig. 1.5.
- The bound actin causes the release of the ADP and Pi molecules, which leads to a conformational change of the myosin head. This acts as a power stroke, see step 2 of Fig. 1.5.
- A new ATP molecule binds to the myosin head which causes the bridge between the actin filament and the myosin head to break, see step 3 of Fig. 1.5.
- Once the ATP molecule hydrolyzes, and the myosin head is in position to bind to the adjacent actin monomer the cycle starts again, see step 4 of Fig. 1.5.

Through this reaction cycle, myosins can take discrete steps along the actin filament. In *in vitro* assays, the forces and step size per power stroke of skeletal muscle heavy meromyosin (HMM) are $\sim 4\text{pN}$ and $\sim 11\text{nm}$, respectively [95]. The most ubiquitous types of myosin are myosin I, II and V. Myosin I is related to vesicle transport [96]. Myosin I has a single head domain and its step size is $\sim 10\text{ nm}$. Most myosins belong to class II, and they can be found in muscular and non-muscular cells [97]. They consist of two heads, and two tail domains and their step sizes range from ~ 5 to 15 nm . Non-muscular myosin II has a fundamental role in processes such as cell adhesion, cell migration, and cell division. Myosin V is a very processive motor. The motor steps follow one another successively since the motor does not often detach [98,99]. This allows single motors to support the movement of an organelle along its track. Myosin V can move in large steps of $\sim 36\text{nm}$ [100].

1.2.3 Motility assays

Cytoskeletal motility assays are *in vitro* systems, which were first created to better understand the interaction between cytoskeletal filaments and molecular motors [101].

Introduction

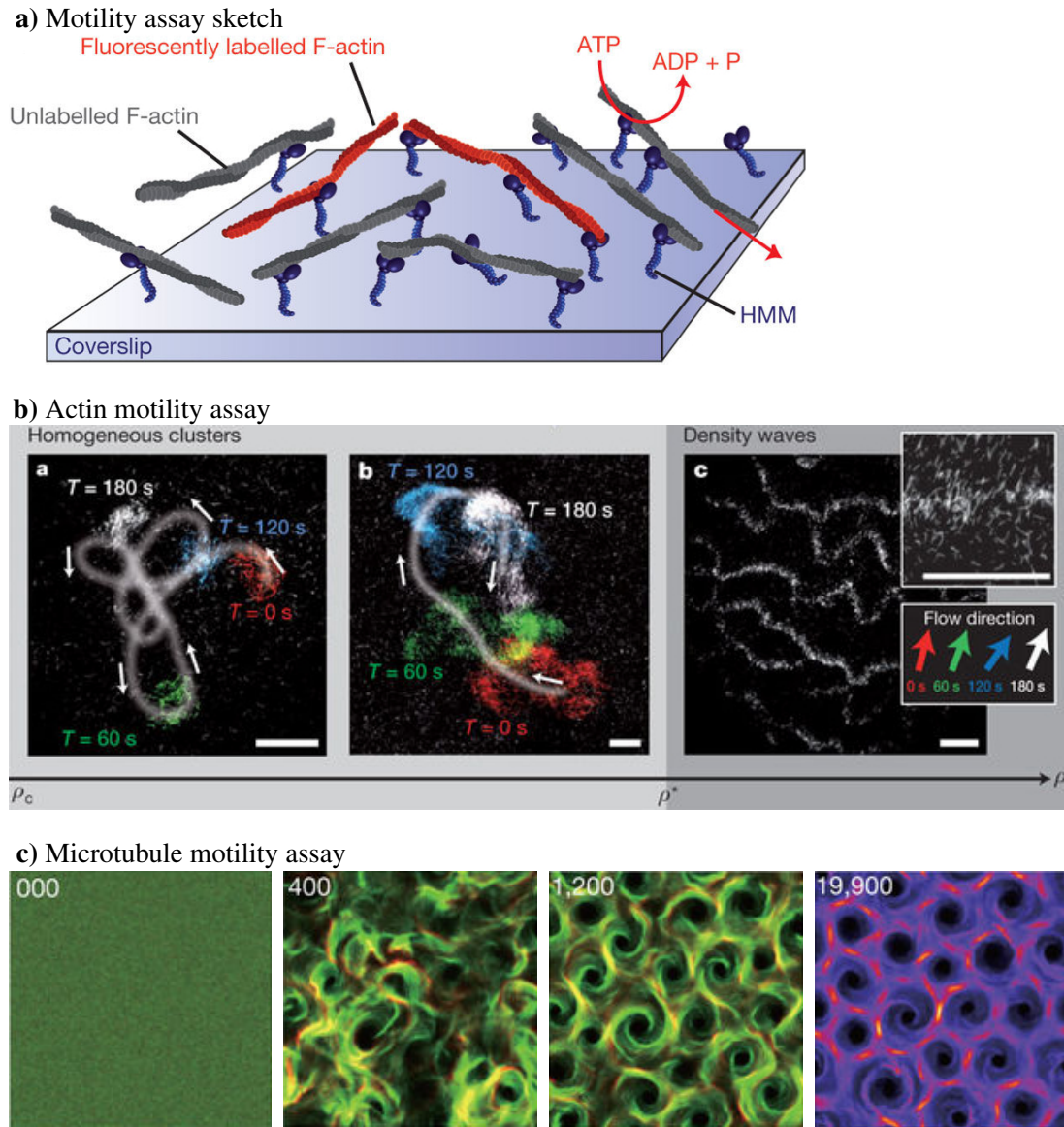


Figure 1.6: Cytoskeletal motility assays. **a)** Molecular motors, HMM, are bound to a coverslip. After addition of ATP free cytoskeletal filaments, actin, are propelled by the molecular motors. Figure reproduced from Ref. [4] with permission from the Nature Publishing Group. **b)** Actin motility assay with HMM as molecular motors. Snapshots show the filaments collective behavior as the filament density increases. Figure reproduced from Ref. [4] with permission from the Nature Publishing Group. **c)** Microtubule motility assay with dynein as molecular motors. The figure shows snapshots of the same system as time evolves, time is given in seconds at the top left corner. At the beginning of the experiment, the microtubules are organized randomly, and at the end of the experiment, the microtubules are organized in hexagonal-like vortices. Figure reproduced from Ref. [5] with permission from the Nature Publishing Group.

1.3 Lipid bilayers and plasma membranes

In a motility assay, molecular motors are bound to a functionalized glass surface. After addition of ATP, free cytoskeletal filaments are moved by the molecular motors over the surface, see Fig. 1.6a. Although apparently a simple system, motility assays give rise to fascinating and complex collective behavior of the cytoskeletal filaments. Nowadays, motility assays are often studied as model systems for active matter. It is experimentally possible to control the filament and motor concentration, such that motility assays have become an ideal system to develop continuum theories for active matter systems [33, 102, 103].

In actin motility assays with myosin II proteins as molecular motors [4], several phase transitions have been found depending on the filament density, see Fig. 1.6b. At small actin filament densities, the filaments organize isotropically. As the density increases, the filaments start to show collective behavior. For densities $\rho > \rho_c$, the filaments organize into motile homogeneous clusters. For densities $\rho > \rho^* > \rho_c$, actin waves have been observed. In microtubule assays with dynein [5], collective behavior is also observed at large enough densities, see Fig 1.6c. For large densities, the alignment between microtubules leads to self-organization of the microtubules into hexagonal-like vortices. Inside the vortices, the microtubules circulate both clockwise and counter-clockwise. In this experiment, single microtubules are on average $\sim 16 \pm 7 \mu\text{m}$ long, whereas the diameters of the vortices are $\sim 400 \mu\text{m}$. Therefore, the structures observed happen on very large scales and can only be explained by the collective behavior of microtubule bundles.

1.3 Lipid bilayers and plasma membranes

Lipids are amphiphilic molecules that consist of a polar head group and non-polar hydrocarbon tails. The head is hydrophilic, whereas the hydrocarbon tails are hydrophobic. Because of their amphiphilic nature, lipids adsorb, for instance, at oil-water interfaces. Here, the head group resides in the water, and the hydrocarbon chains point to the oil. Thus, lipids decrease the interfacial tension [104].

Depending on the lipid concentration, several types of self-organized structures in an aqueous solvent can be observed: bilayer, micelle, and liposomes, see Fig. 1.7a. For small lipid concentrations, the entropy dominates over the energy arising from the repulsion between the hydrophobic tails and the water. As the lipid concentration increases, the minimization of the unfavorable contact between the hydrophobic chains and the water compensates the loss of entropy by micelle formation. The lipid concentration at which micelles are formed is known as critical micelle concentration (CMC) [107]. For even larger lipid concentrations, bilayers and liposomes can be observed.

In monolayers, the lipid type determines the spontaneous curvature. Lipids with large heads, conical lipids, lead to spontaneous positive curvature. Lipids with large tails, inverted-conical lipids, lead to spontaneous negative curvature. Cylindrical lipids lead to planar configurations, see Fig. 1.7b. For lipid bilayers made of one type of lipids, it is the asymmetry between lipid concentrations in both monolayers that leads to spontaneous curvature [108]. In cell membranes, the spontaneous curvature is also related to the asymmetry in the composition between the two monolayers. However, not only lipids but also proteins can give rise to spontaneous curvature [109].

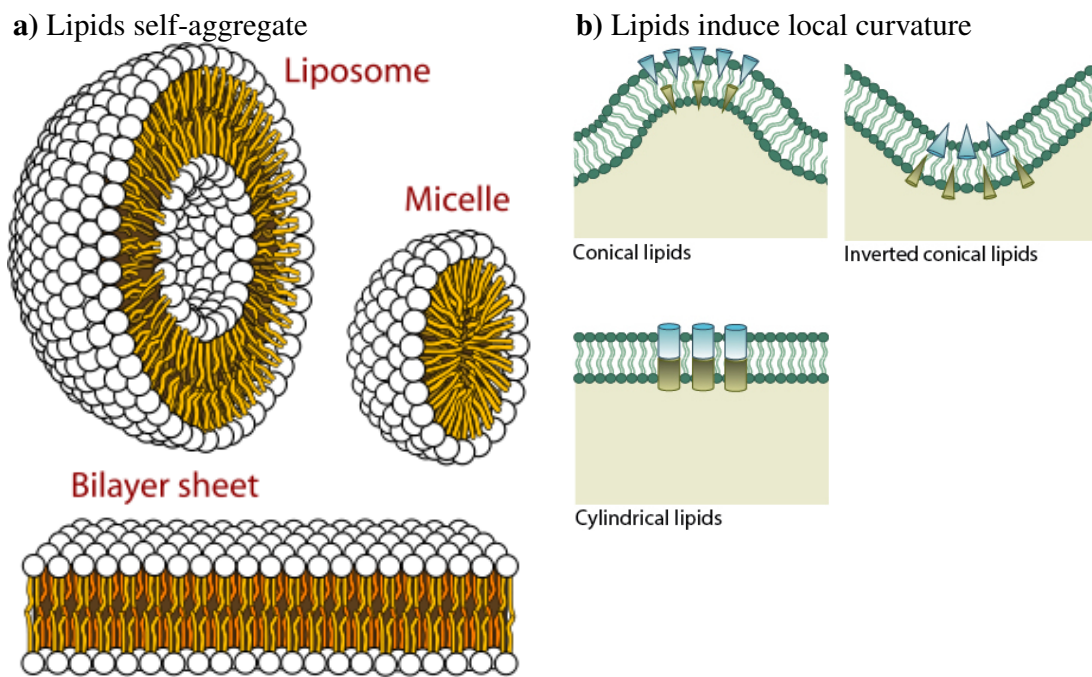


Figure 1.7: Lipid bilayers. **a)** For large enough lipid concentrations lipids aggregate in micelles, liposomes and bilayers. Figure reproduced from Ref. [105]. **b)** Lipids can induce local curvature. Conical lipids induce positive curvature. Inverted-conical lipids induce negative curvature. Cylindrical lipids do not induce spontaneous curvature. Figure reproduced from Ref. [106] with permission from MBInfo ©2018 National University of Singapore.

1.3 Lipid bilayers and plasma membranes

All cells, prokaryotic or eukaryotic, are surrounded by a plasma membrane. This thin and flexible structure acts as the boundary between the interior of the cell and the environment. The plasma membrane is primarily composed of proteins and lipids [110]: lipids give membranes their flexibility, and proteins assist in the transfer of molecules across the membrane, see Fig. 1.8a.

The three main types of lipids that are found in biological membranes are phospholipids, cholesterol, and glycolipids [111]. Phospholipids make up the bulk of the lipids in the cell bilayer. Cholesterols are dispersed between phospholipids, and their role is to modulate plasma membrane permeability, mechanical strength, and biochemical interactions. Glycolipids help the cell to recognize other cells [88].

The cell membrane contains two types of proteins: integral membrane proteins are always inserted into the membrane, whereas peripheral membrane proteins temporarily adhere to the membrane [88, 112]. Membrane proteins fulfill three main functions: structural proteins are related to cell support and shape, receptor proteins help cells communicate with their environment using signaling molecules, transport proteins and channels are in charge of transporting ions and molecules across the cell membrane.

The plasma membrane is a very complex and heterogeneous system. However, compared to the size of an entire cell, the membrane thickness is negligible. Therefore, on the cell scale, the mechanical properties of the plasma membrane can be modeled using a two-dimensional mathematical surface with curvature-elastic constants, see Fig. 1.8b. For such a continuous description, understanding the concept of curvature is necessary. The curvature of a line is calculated as the inverse of the radius of the circular arc that best approximates the curve at a point, R_c , see Fig. 1.8c. To describe a two-dimensional surface, two curvatures at each point are needed. The two principal curvatures, c_1 , and c_2 , at a given point of a surface, are the eigenvalues of the curvature tensor at the point.

In 1973, Helfrich proposed a continuum expression for the membrane bending energy [116],

$$\mathcal{H} = \frac{1}{2} \int_A dS [\kappa(2H + c_0)^2 + \kappa_G K]. \quad (1.1)$$

Here, the integral extends over the entire membrane area, κ is the membrane bending rigidity, κ_G is the Gaussian splay modulus, $H = \frac{1}{2}(c_1 + c_2)$ is the mean curvature, which is calculated as the average of the principal curvatures, c_0 is the spontaneous curvature, and $K = c_1 c_2$ is the Gaussian curvature, which is calculated as the product of the principal curvatures. If $c_0 \neq 0$, there is an asymmetry, such as different lipid and protein concentrations or compositions, between the two monolayers. In such systems, the membrane has a preferred curvature. For simplicity, we only consider cases with $c_0 = 0$. The integral of K over a closed surface is associated with the surface topology. For systems where there are no changes in the global topology, the integral over the Gaussian curvature is constant, as shown by the Gauss-Bonnet theorem. As such, the only remaining term relevant for shape changes of the Helfrich bending energy is the mean curvature H . For coarse-grained simulations of membranes a discretized version of this model using triangulated surfaces is often employed.

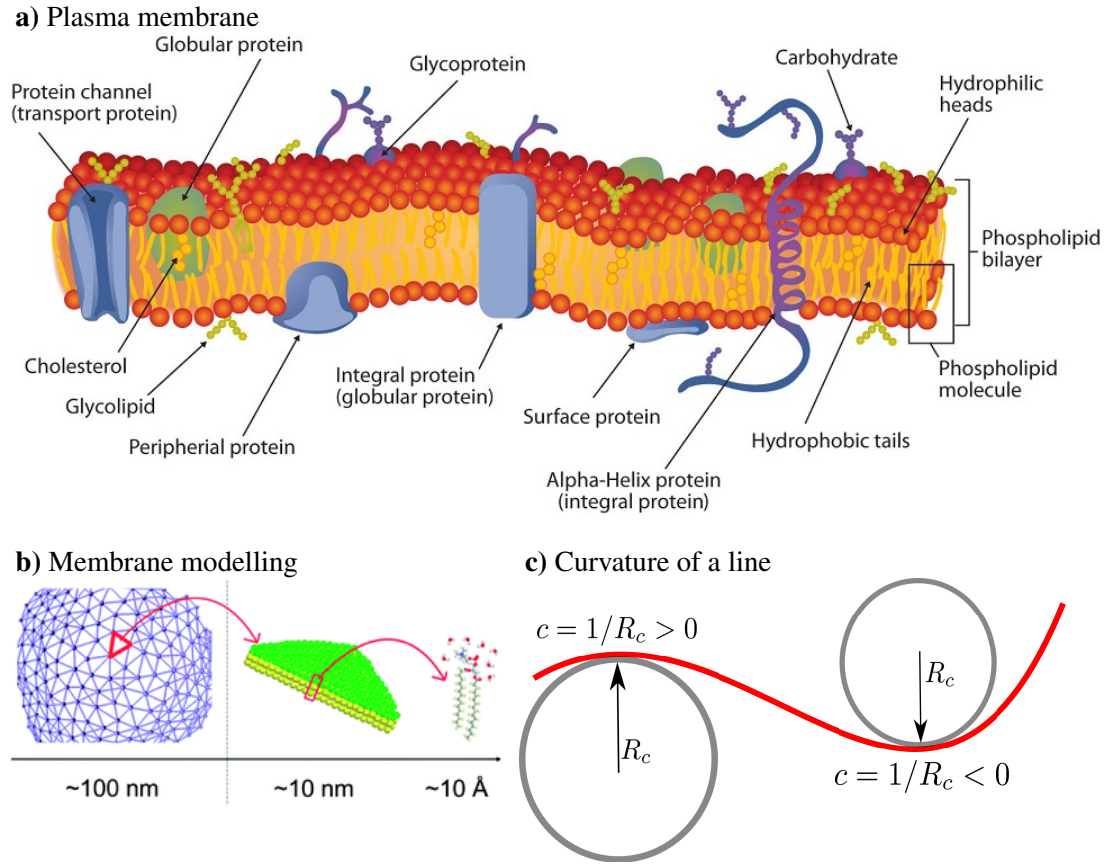


Figure 1.8: Modelling the plasma membrane. **a)** The plasma membrane of eukaryotic cells is primarily composed of lipids and proteins. The types of lipids found in the plasma membrane are phospholipids, cholesterol, and glycolipids. According to their structure, the types of proteins found in the surface are integral proteins and peripheral membrane proteins. According to their function, proteins are divided into structural proteins, receptor proteins, and transport proteins. Figure reproduced from Ref [113]. **b)** On small scales ~ 10 Å, the membrane needs to be modeled in a very detailed manner using an atomistic approach. On larger scales ~ 10 nm, the membrane can be modeled using a coarse-grained approach, e.g., using Martini model [114]. On the cell scale ~ 100 nm, the membrane can be considered as a mathematical surface, which from a computational point of view is often discretized as a triangulated surface. Figure reproduced from Ref. [115] with permission from the Royal Society of Chemistry. **c)** The curvature of a line is at any point calculated as the inverse of the radius of a circle with radius R_c , which best approximates the curve at that point.

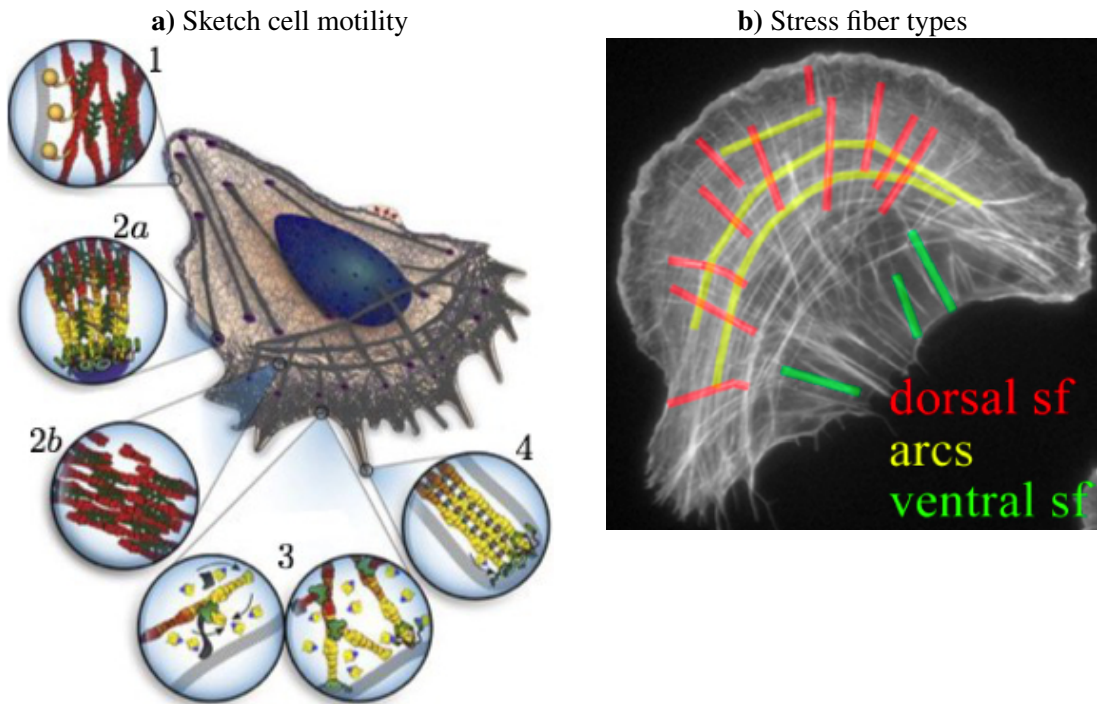


Figure 1.9: Actin and actomyosin structures in mesenchymal cells. **a)** Sketch of actin-based cell motility. **1)** The cortical cytoskeleton is the portion of the cytoskeleton that lies just beneath the plasma membrane. **2)** Focal adhesions are macromolecular assemblies that transmit the forces generated by stress fibers to the substrate. **2b)** Transverse arcs are a particular type of stress fibers found at the lamellipodium. **3)** The lamellipodium hosts rapid and localized polymerization of branched actin networks. Initiation of this network occurs via the activity of the Arp2/3 complex. VASP and FMNL2 favor filament elongation, whereas capping proteins block it. **4)** Filopodia are filled with parallel actin bundles elongated by VASP and formins and held together by fascin and fimbrin. Figure reproduced from Ref. [117] with permission from the American Physiological Society. **b)** Stress fibers are contractile actin bundles found in non-muscle cells. They are made of actin and non-muscle myosin II. Ventral stress fibers are connected by two focal adhesions to the substrate, and they are found at the rear of the cell. Dorsal stress fibers are connected to the substrate by one focal adhesion, and the other end is connected to transverse arcs. They are found at the front of the cell, and they are oriented radially. Transverse arcs are connected to dorsal stress fibers on both ends. They are found in the lamellipodium, and they are oriented transversally. Figure reproduced from Ref. [118] with permission from Rockefeller University Press.

1.4 Cell motility

Cell motility is indispensable for tissue formation during embryogenesis, wound healing and immune response. It is also essential in cancer metastasis, where cancer cells migrate from the original tumor towards new locations where metastases are formed [119]. Mesenchymal cell migration is a motility mode based on adhesion. The cells polarize and form a leading edge that extends actin-rich protrusions, leading to adhesive interactions with the substrate. Retraction of the contractile cell rear leads to cellular movement. There are two different types of structures in mesenchymal cells: viscoelastic actin structures, and elastic, contractile actomyosin structures [117, 120]. Actin structures: lamellipodium, and filopodia exert pushing forces; while actomyosin structures: stress fibers, and myosin-driven actin flow, exert pulling forces. At the front of mesenchymal cells we find the lamellipodium and filopodia, see Fig. 1.9 structures 3 and 4. At the back of the cell, we find myosin-driven actin flow and stress fibers, structures 2a and b. Actin polymerization at the front of the cell both in the lamellipodium and in filopodia is discussed in Sec. 1.2.1.

Stress fibers are contractile actomyosin bundles that have a central role in cell adhesion and morphogenesis. They are composed of bundles of 10 – 30 actin filaments, which are crosslinked together by α -actinin [58]. These actomyosin bundles are typically anchored to focal adhesions, which anchor the actin cytoskeleton to the substrate. Stress fibers can be divided into three categories:

- Dorsal stress fibers are anchored to focal adhesions at their distal ends. These actin filament bundles do not typically contain myosin II [121]. Although they typically do not exert contractile forces, dorsal stress fibers serve as a platform for the assembly of other types of stress fibers and transmit stresses generated by transverse arcs [118, 121].
- Transverse arcs are curved actomyosin filament bundles. They do not directly attach to focal adhesions but are connected to dorsal stress fibers. An important feature of transverse arcs in migrating cells is their ability to flow from the leading cell edge towards the cell center [118, 122]. This process is thought to be driven by the continuous contraction of arcs [123].
- Ventral stress fibers, located at the rear of the cell, are contractile actomyosin bundles that are attached to focal adhesions at both ends. They represent one of the major contractile structures in most mesenchymal cells [122].

Keratocytes, keratinocytes, and neutrophils are motile mesenchymal cells. Keratocytes are highly specialized corneal stroma cells. The stroma is the part of a tissue or organ with a structural or connective role [124]. The cornea is the outermost layer of the eye. It is the transparent, dome-shaped surface that covers the front of the eye and acts as a lens for the eye. Keratocytes play a crucial role in maintaining the structure and transparency of the cornea. They also play essential roles in corneal wound healing and tissue repair. Keratocytes tend to have fan-like shapes and are widely used to study mesenchymal cell motility, see Fig. 1.9a. Fast-moving keratocytes with speeds of $\sim 40 \mu\text{m/s}$ are a classical system to study cell motility. Keratocyte locomotion can also

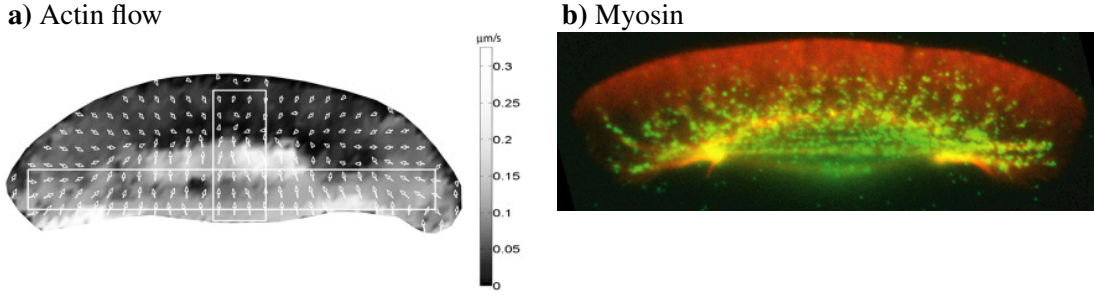


Figure 1.10: Contractile forces in cell motility. **a)** Actin flow in a moving keratocyte. The myosin-driven actin retrograde flow is strongest at the back of the keratocyte. Figure reproduced from Ref. [129] with permission from Cell Press. **b)** Moving keratocyte. Actin is stained in red and myosin is stained in green. The myosin is mainly located at the back of the keratocyte. Figure reproduced from Ref. [12].

proceed in the absence of front protrusion [125], indicating the existence of an active mechanism independent of actin polymerization. Myosin is found at the rear of keratocytes [12, 126], where it contracts the actin network generating a rapid centripetal flow that pulls the rear forward, see Fig. 1.10.

Keratinocytes are the predominant cells in the epidermis [127]. Their primary function is the formation of a barrier against environmental damage by pathogenic bacteria, fungi, parasites, viruses, heat, UV radiation and water loss. Keratinocyte migration plays a crucial role in wound healing. They show elongated half-circular shapes, see Fig. 1.9b. Keratinocytes have a complex network of stress fibers. The flat back of the cells is caused by ventral stress fibers, while the transversal arcs in the lamellipodium help stabilize the half-circular shape.

Neutrophils are the main pathogen-fighting immune cells. Their primary functions are their ability to be recruited to sites of infection, to recognize and phagocytose microbes, and to kill pathogens through a combination of cytotoxic mechanisms. Neutrophils in bulk adopt spherical shapes, neutrophils on surfaces tend to adopt elongated shapes with a roundish front and a pointed rear, see Fig. 1.9c. Neutrophils perform random motion when there are no external stimuli [128]. However, they show much more directed motion when performing chemotaxis, e.g., chasing bacteria.

1.5 Outline of the thesis

We study the collective behavior of self-propelled rods and present a physical model for cell motility with the use of computational tools and coarse-grained models.

In chapter 2, we present the theoretical background and the model used in our simulations. A short introduction to the theory and concepts used subsequently is given. From a simulations point of view, we focus in particular on the model for the self-propelled rods, the deformable rings, and the rod-ring interactions. In chapter 3, we describe and analyze the collective behavior and dynamics of density-dependent

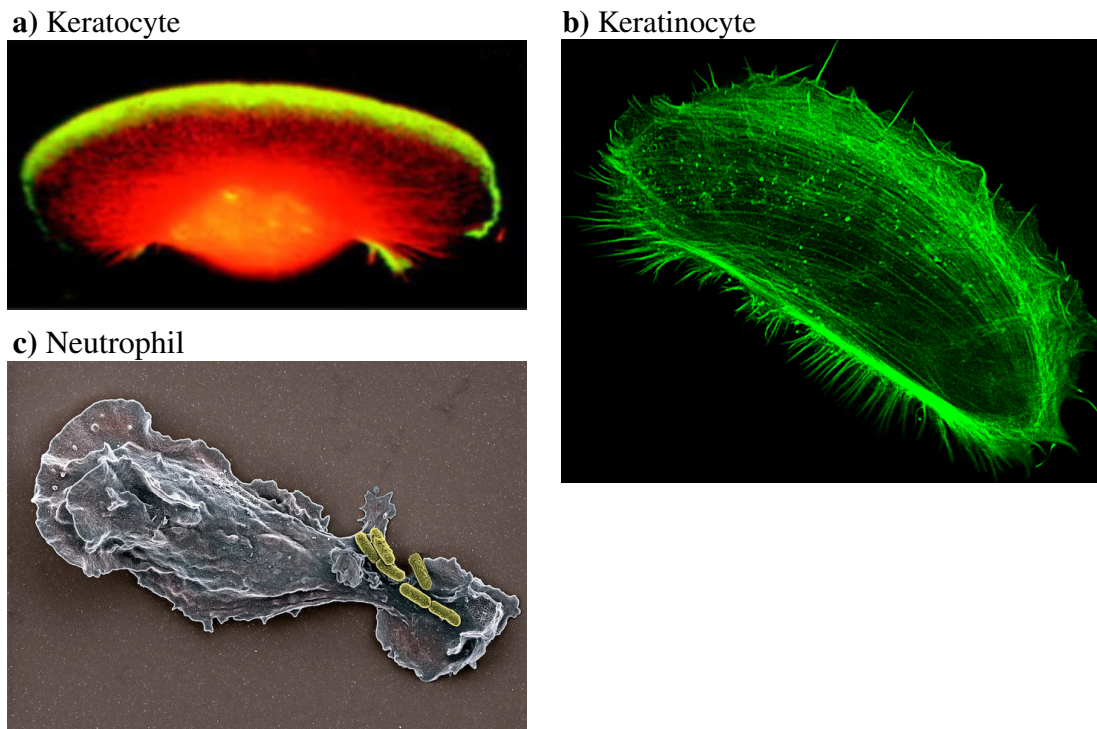


Figure 1.11: Mesenchymal motile cells. **a)** Movin keratocyte. Arp2/3 is stained in green and phalloidin is stained in red. Figure reproduced from Ref. [130] with permission from Rockefeller University Press. Keratocytes typically have fan-like shapes. **b)** Moving keratinocyte. Actin is stained in green. Figure courtesy of Galiya Sakaeva, Dr. Bernd Hoffman, and Prof. Rudolf Merkel. Keratinocytes show elongated half-circular shapes. **c)** Neutrophil, in grey, and bacteria, in yellow. Colored scanning electron micrograph. Neutrophils adhered to surfaces show elongated shapes with a roundish front and pointed rear. Figure reproduced from Ref. [131] with permission from Science Photo Library.

self-propelled rods. The density-dependent mechanism helps the clustering process and introduces perpendicularity between the rods, which leads to aster formation. In chapter 4, we describe the different motility patterns showed by complex-self propelled rings. We model polymerization forces of cytoskeletal filaments by self-propelled rod-like filaments with constant length pushing against a ring-like confinement. Retraction forces are modeled by self-propelled rod-like filaments pulling on the confinement. We correlate the rod dynamics and collective behavior inside the ring with the motion of the ring. Although the model presented is fairly simple, it still manages to reproduce cell-like motility patterns. In chapter 5, we extend the complex-ring model by adding ring deformability. Rod dynamics and alignment now lead to motion and to shape changes of the rings. We systematically characterize the different shapes obtained by this model and correlate ring shape and motion. We also study the behavior of deformable self-propelled rings on walls and at friction interfaces. In chapter 6, we summarize the results obtained in this thesis, explain the limitations of the models and give an outlook for future studies.

Chapter 2

Theoretical background, model and simulation techniques

In this section, we briefly present the theoretical background on which our model is based, and the model and simulation techniques used for our systems. Active matter systems, such as motility assays and cells, tend to be surrounded by water. Basic knowledge of fluid dynamics at low Reynolds number is, therefore, necessary to understand how such systems move and propel themselves. All the systems studied here are soft matter systems. Soft matter is a subfield of condensed matter, in which systems are deformed or structurally altered by thermal or mechanical stresses of the magnitude of thermal fluctuations. Brownian motion plays a crucial role in the dynamics of the systems studied here.

We focus on two-dimensional simulations because the phenomena we are interested in are mainly two-dimensional. Cytoskeletal motility assays are quasi-two-dimensional systems. The cytoskeletal filaments only escape to the third dimension during crossing events [5]. We simulate cytoskeletal motility assays, gliding bacteria, and self-propelled phoretic particles using self-propelled rods, see chapter 3. Cytoskeletal filaments are linear polymers. Their rigidity is given by the ratio of their contour length l and their persistence length l_p . Polymers with $l \gtrsim l_p$ are semiflexible and polymers with $l \ll l_p$ are rigid. In cells, actin filaments behave as semiflexible polymers, whereas microtubules behave as rigid polymers [4, 5]. Values for the persistence lengths and typical lengths of cytoskeletal filaments can be found in Sec. 1.2.1. In our simulations, we consider stiff cytoskeletal filament bundles that we model as rods. The activity in our systems is given by the self-propulsion, this is a good approximation for modeling gliding bacteria and motility assays.

The most interesting aspects of mesenchymal cell motility are two-dimensional. The important effects are the interaction of the cytoskeleton and the lipid bilayer with the substrate: lamellipodium formation [55], filopodia protrusion [56, 57], and stress fibers formation [58, 59]. We use quasi-two-dimensional self-propelled rods inside rings to model cell-like systems, see chapters 4 and 5. In experiments, this would be equivalent to viewing the section of the cell in contact with the substrate. In our simulations, the rings act as the cell lipid bilayer. When considering cell motility, the lipid bilayer can be modeled as a mathematical surface, see Sec. 1.3. Because we only focus on two-

dimensional phenomena for cells attached to planar substrates, we use a semiflexible polymer, instead of the Helfrich Hamiltonian, to model the membrane where it detaches from the substrate.

In the density-dependent rod simulations, rods are initialized inside the simulation box at random positions with random orientations. For the rod-ring simulations, rods are initialized inside the ring with the condition that they cannot cross the ring. This condition holds both for attached and non-attached rods. All rod-rod and rod-ring interactions are calculated using cell lists to minimize computational costs. Also, our code is parallelized using OpenMP.

2.1 Swimming at low Reynolds number

The Navier-Stokes equations were derived by Claude-Louis Navier and George Gabriel Stokes in 1822 [132]. They follow from the conservation and continuity equations, when these are applied to a fluid. For an incompressible fluid, $\nabla \cdot \mathbf{v} = 0$, the Navier-Stokes equations become [133]

$$\rho \left(\frac{\partial \mathbf{v}}{\partial t} + (\mathbf{v} \cdot \nabla) \mathbf{v} \right) = \eta \nabla^2 \mathbf{v} - \nabla p + \mathbf{f}. \quad (2.1)$$

Here, $\mathbf{v} = \mathbf{v}(\mathbf{r}, t)$ is the velocity of a volume element and $\partial \mathbf{v} / \partial t$ is the acceleration. $(\mathbf{v} \cdot \nabla) \mathbf{v}$ is the convective, inertial, or non-linear term and is responsible for the transfer of kinetic energy in the fluid. $\eta \nabla^2 \mathbf{v}$ is the dissipative or viscous term, where η is the fluid viscosity. $\mathbf{f} = \mathbf{f}(\mathbf{r}, t)$ is the external force acting on the volume element. It is possible to make Eq. 2.1 dimensionless by using a characteristic length L and velocity v_0

$$\frac{L \rho v_0}{\eta} \left(\frac{\partial \mathbf{v}'}{\partial t'} + (\mathbf{v}' \cdot \nabla) \mathbf{v}' \right) = \nabla^2 \mathbf{v}' - \nabla p' + \mathbf{f}'. \quad (2.2)$$

Here, the Reynolds number $\mathcal{R} = L \rho v_0 / \eta$ is a dimensionless quantity that represents the ratio of inertial forces to viscous forces. The fluid behaves very differently at low and at large Reynolds number:

- At low Reynolds number there is no transport of momentum and the fluid response to forces is instantaneous. The viscous forces are dominant, the flow is laminar, and is characterized by smooth, constant fluid motion.
- At high Reynolds number the motion of a body transfers momentum to the surrounding fluid, which is convected and slowly dissipated. The inertial forces are dominant, the flow is turbulent and is characterized by vortices and other flow instabilities.

For microscopic swimmers, such as E.coli and other cells, $\mathcal{R} \approx 10^{-4} \ll 1$ [134]. This means that microscopic organisms swim at low Reynolds number and inertial forces are negligible for microswimmers [135]. For small Reynolds numbers $\mathcal{R} \ll 1$, the Navier-Stokes equation becomes the Stokes or creeping-flow equation

$$\mathbf{f} = \nabla p - \eta \nabla^2 \mathbf{v}. \quad (2.3)$$

Compared with Eq. 2.1, Eq. 2.3 is linear and time-independent. Swimming at low Reynolds number has some unexpected consequences:

- All forces are instantaneously balanced: when a microswimmer propulsion force stops, the swimmer immediately stops. All the momentum transferred to the fluid is instantaneously dissipated.
- Eq. 2.3 is time-independent: the swimmer dynamics must fulfill $\mathbf{f}(t) = \mathbf{f}(-t)$. For one-dimensional microswimmers, cyclic motion patterns do not lead to net movement. The forces generated in the first half of the cycle balance the forces in the second half, this is known as the “scallop theorem” [135].
- Microswimmers must have time-irreversible propulsion and a swimming mechanism with more than one degree of freedom. In nature, microswimmers developed complicated swimming mechanisms. There are two main swimming mechanisms for microswimmers: waves and reciprocal forces combined with flexibility [136].

2.2 Langevin equation

When studying the dynamics of a particle in a solvent, if the hydrodynamic interactions are screened or can be considered negligible, the surrounding of the particle and its interaction with the solvent can be described in a stochastic manner. An example of this is the Langevin equation

$$\dot{\mathbf{v}} + \gamma \mathbf{v} = \frac{\mathbf{f}}{m} + \mathbf{\Gamma}. \quad (2.4)$$

Here, \mathbf{v} is the particle velocity, \mathbf{f} is the external force acting on the particle, and $\mathbf{\Gamma}$ is the stochastic force. The interaction between the solvent and the particle is given by $\gamma \mathbf{v}$ and $\mathbf{\Gamma}$, which are the dissipative and stochastic forces, respectively. Typically, the stochastic process is considered Gaussian and Markovian

$$\langle \mathbf{\Gamma}(t) \rangle = 0 \quad (2.5)$$

$$\langle \mathbf{\Gamma}(t) \mathbf{\Gamma}(t') \rangle = a \delta(t - t'), \quad (2.6)$$

where a is a measure for the strength of the noise. If we consider a one-dimensional system with $m = 1$ and no external force, $\mathbf{f} = 0$, the solution of the Langevin equation is

$$v(t) = v_0 e^{-\gamma t} + \int_0^t dt' e^{-\gamma(t-t')} \Gamma(t') \quad (2.7)$$

$$x(t) = x_0 + \frac{v_0}{\gamma} (1 - e^{-\gamma t}) + \frac{1}{\gamma} \int_0^t dt' (1 - e^{-\gamma(t-t')}) \Gamma(t'). \quad (2.8)$$

The velocity autocorrelation function then yields

$$\langle v(t)v(t) \rangle = v_0^2 e^{-2\gamma t} + \frac{a}{2\gamma} (1 - e^{-2\gamma t}) \xrightarrow{t \rightarrow \infty} \frac{a}{2\gamma}. \quad (2.9)$$

If we plug the result of the velocity autocorrelation, for $t \rightarrow \infty$, into the equipartition theorem, we obtain the value of the noise autocorrelation function

$$\langle E \rangle = \frac{k_B T}{2} = \frac{m \langle v^2 \rangle}{2} = \frac{a}{2\gamma}. \quad (2.10)$$

Here, k_B is the Boltzmann constant and T is the temperature. With this last result and the noise autocorrelation function we obtain the fluctuation-dissipation theorem [137]

$$\langle \Gamma(t) \Gamma(t') \rangle = \frac{2\gamma k_B T}{m} \delta(t - t'). \quad (2.11)$$

The fluctuation-dissipation theorem states: when there is a process that dissipates energy, γv , there is a reverse process related to thermal fluctuations, Γ . The fluctuation-dissipation model holds for all systems which fulfill detailed balance.

The mean squared displacement of the particle in the solvent is given by

$$\langle (x(t) - x(0))^2 \rangle = \frac{2\gamma k_B T}{m} \left(\frac{t}{\gamma^2} - \frac{1 - e^{-\gamma t}}{\gamma^3} \right). \quad (2.12)$$

This last equation has two asymptotic behaviors:

- At short times the mean-squared displacement is ballistic

$$\langle (x(t) - x(0))^2 \rangle = \langle v_0^2 \rangle t^2. \quad (2.13)$$

- At long times the mean-squared displacement is diffusive

$$\langle (x(t) - x(0))^2 \rangle = 2Dt. \quad (2.14)$$

Here, D is the diffusion coefficient. The diffusion coefficient can be defined using the mean-squared displacement using the Einstein relation, or from the velocity autocorrelation function using the Green-Kubo relation [137]. Expanding Eq. 2.14 to more dimensions, we obtain

$$\langle |\mathbf{r}(t) - \mathbf{r}(0)|^2 \rangle = 2dDt, \quad (2.15)$$

where d is the number of dimensions.

2.3 Anisotropic rod friction

We consider a rod of length L made up of N beads in a fluid [138]. We assume a thin rod that feels a torque \mathbf{M} and rotates with angular velocity $\boldsymbol{\omega}$. In the overdamped regime,

$$\boldsymbol{\omega} = \frac{\mathbf{M}}{\gamma_r}, \quad (2.16)$$

where γ_r is the rod rotational friction. To calculate γ_r , we can estimate the torque created by the friction forces $\mathbf{M}_{\text{friction}}$ upon rod rotation. Since there are no external forces or torques $\mathbf{M} = \boldsymbol{\omega} \gamma_r = -\mathbf{M}_{\text{friction}}$. For bead i , the linear velocity \mathbf{v}_i is

$$\mathbf{v}_i = \mathbf{M} \times i d\mathbf{l}, \quad (2.17)$$

2.3 Anisotropic rod friction

where d is the bead diameter and \mathbf{l} indicates the direction along the rod axis. The friction force acting on bead i is $\gamma_{\text{hydro}} \mathbf{v}_i$, where γ_{hydro} is the friction obtained from Stoke's law. A spherical particle of diameter d in a fluid feels a friction $\gamma_{\text{hydro}} = 3\pi\eta d$, where η is the fluid viscosity. The friction torque felt by bead i is thus

$$\mathbf{M}_{\text{friction}} = \sum_{i=-N/2}^{N/2} i d \mathbf{l} \times \gamma_{\text{hydro}} \mathbf{v}_i = -\gamma_{\text{hydro}} \sum_{i=-N/2}^{N/2} i^2 d^2 \boldsymbol{\omega} = -\frac{\pi L^3 \eta}{4} \boldsymbol{\omega} \quad (2.18)$$

The rotational friction obtained from this calculation is

$$\gamma_r = \frac{\pi L^3 \eta}{4} \quad (2.19)$$

A more precise hydrodynamic calculation, which consists on the derivation of the Smoluchowski equation by the Kirkwood theory for a cylinder gives a correction term α [138]

$$\gamma_r = \frac{\pi L^3 \eta}{3(\log(L/d) - \alpha)} \quad (2.20)$$

Using the Einstein relation, we obtain the rod rotational diffusion coefficient

$$D_r = \frac{k_B T}{\gamma_r} = \frac{3k_B T (\log(L/d) - \alpha)}{\pi L^3 \eta}. \quad (2.21)$$

We now focus on the rod translation. The translational velocity \mathbf{v} of the rod can be decomposed in its components, $\mathbf{v} = \mathbf{v}_{\parallel} + \mathbf{v}_{\perp}$, parallel and perpendicular to the long axis of the rod, such that the rod force can be written as

$$\mathbf{F} = \gamma_{\parallel} \mathbf{v}_{\parallel} + \gamma_{\perp} \mathbf{v}_{\perp}, \quad (2.22)$$

where γ_{\parallel} is the friction coefficient in the parallel direction and γ_{\perp} is the friction coefficient in the perpendicular direction.

For a system with "dry" friction, where no hydrodynamic interactions are considered, the parallel and perpendicular frictions are equal, $\gamma_{\parallel} = \gamma_{\perp}$. Here, each rod bead is considered as a single particle with isotropic friction. Thus, the total rod friction is also isotropic. For a system where there are hydrodynamic interactions, for a rod in a fluid, the rod frictions are anisotropic $\gamma_{\parallel} \neq \gamma_{\perp}$. We can discretize the rod in Stokeslets, which is the primary Green's function of the Stokes equation, and integrate the flow that each Stokeslet creates over the rod length. The linearity of the Stokes equation for an incompressible fluid, see Eq. 2.3, means that a Green's function \mathbb{G} exists. The Green's function is found by solving the Stokes equations with the force term being replaced by a point force acting at the origin and is known as Oseen Tensor

$$\mathbb{G}_{ij}(\mathbf{r}) = \frac{1}{8\pi\eta r} \left(\delta_{ij} + \frac{r_i r_j}{r^2} \right). \quad (2.23)$$

Here, the second term of Eq. 2.23 gives rise to the anisotropy in the rod friction. In our model, we consider a rod embedded in a fluid. This means that although we perform Brownian dynamics simulations, the rods' friction coefficients come from hydrodynamics.

For a rod with a large aspect ratio in a fluid, the parallel and perpendicular friction coefficients, are [133, 138]

$$\gamma_{\parallel} = \frac{2\pi\eta L}{\log(L/d)} \quad (2.24)$$

$$\gamma_{\perp} = 2\gamma_{\parallel}. \quad (2.25)$$

To obtain the parallel and perpendicular diffusion coefficients we apply the Einstein relations

$$D_{\parallel} = \frac{k_B T}{\gamma_{\parallel}} = \frac{k_B T \log(L/d)}{2\pi\eta L} \quad (2.26)$$

$$D_{\perp} = \frac{k_B T}{\gamma_{\perp}} = \frac{k_B T \log(L/d)}{4\pi\eta L}. \quad (2.27)$$

This means that the diffusion in the parallel direction of the rod is two times higher than the diffusion in the perpendicular direction.

2.4 Active Brownian particle model

A spherical active Brownian particle, ABP, is the simplest possible model for a self-propelled particle. An ABP consists of a bead with self-propulsion velocity v_0 and rotational diffusion D_r . The equations of motion of an ABP are

$$\dot{\mathbf{r}}(t) = v_0 \mathbf{e}(t) + \frac{1}{\gamma_t} (\mathbf{f}(t) + \mathbf{\Gamma}(t)) \quad (2.28)$$

$$\dot{\mathbf{e}}(t) = \mathbf{e}(t) \times \boldsymbol{\xi}(t). \quad (2.29)$$

Here, \mathbf{e} is the orientation vector of the propulsion force, v_0 is the propulsion velocity, γ_t is the translational friction, \mathbf{f} is an external force applied on the particle, $\mathbf{\Gamma}$ is thermal noise associated with the translational motion $\langle \Gamma_i(t) \Gamma_j(t') \rangle = 2k_B T \gamma_t \delta_{ij} \delta(t - t')$, and $\boldsymbol{\xi}$ is the noise associated with the rotational motion $\langle \xi_i(t) \xi_j(t') \rangle = 2D_r \delta_{ij} \delta(t - t')$.

The mean-squared displacement of an ABP is given by [18, 139]

$$\langle (\mathbf{r}(t) - \mathbf{r}(0))^2 \rangle = 4D_t t + \frac{v_0^2 \tau_r^2}{2} \left(\frac{2t}{\tau_r} + \exp(-2t/\tau_r) - 1 \right). \quad (2.30)$$

Here, \mathbf{r} is the ABP position, v_0 is the ABP self-propulsion velocity, D_t is the thermal translation diffusion coefficient for a passive bead, and $\tau_r = 1/D_r$ is the rotational diffusion time of the ABP. Equation 2.30 has three different regimes:

- At short times, $t < 4D_t/v^2$, the motion is diffusive, with the thermal translational diffusion coefficient D_t

$$\langle (\mathbf{r}(t) - \mathbf{r}(0))^2 \rangle = 4D_t t. \quad (2.31)$$

- At intermediate times, $4D_t/v^2 \leq t \leq \tau_r$, the motion is ballistic

$$\langle (\mathbf{r}(t) - \mathbf{r}(0))^2 \rangle = 4D_t t + v^2 t^2. \quad (2.32)$$

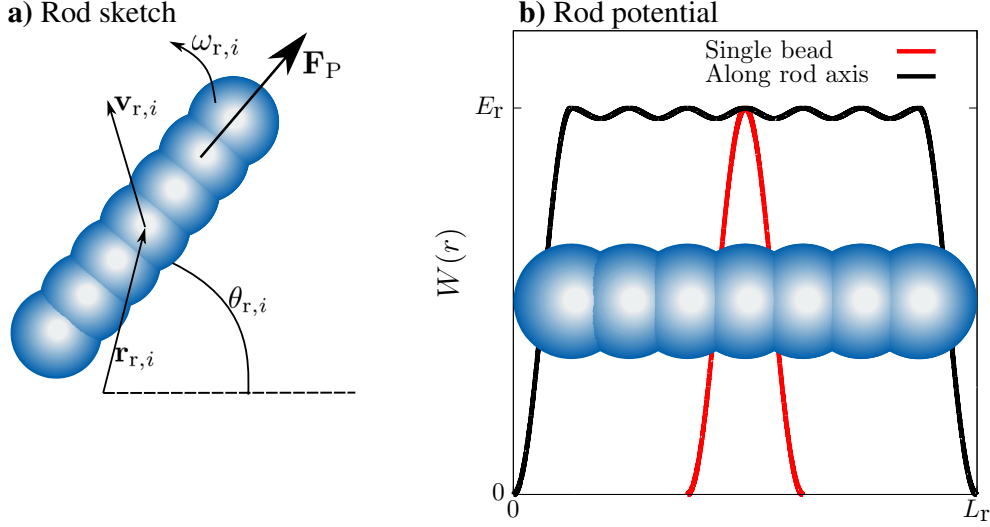


Figure 2.1: Rod-rod interaction. **a)** Sketch of a self-propelled rod. Each rod is discretized into n_r beads, \mathbf{F}_P is the rod propulsion force, $\mathbf{v}_{r,i}$ is the center-of-mass velocity of rod i , $\omega_{r,i}$ is the angular velocity of rod i , $\mathbf{r}_{r,i}$ is the position of the center of mass of rod i , and $\theta_{r,i}$ is the angle that rod i forms with the x-axis. **b)** Potential profile $W(r)$ along the rod axis, E_r is the rod energy barrier. The black curve is the summation of the contributions for all beads of the rod. The rod beads overlap half a bead.

- At long times times, $t > \tau_r$, the motion is diffusive with an effective diffusion coefficient D_{eff}

$$\langle (\mathbf{r}(t) - \mathbf{r}(0))^2 \rangle = (4D_t + v^2 \tau_r) t \equiv 4D_{\text{eff}} t. \quad (2.33)$$

The diffusion coefficient at large times is always larger than the thermal diffusion coefficient, $D_{\text{eff}} > D_t$.

The results shown here for the three different regimes apply to an ABP in two dimensions.

2.5 Penetrable self-propelled rods

It has been experimentally observed that filaments in motility assays have a finite probability to cross each other [5]. To model such systems in two dimensions, we use an interaction potential that allows crossing events to occur. This means that the potential is finite when two rods overlap.

In our simulations each rod has length L_r and is modeled using n_r beads to calculate rod-rod interactions. Rods are characterized by their center-of-mass positions $\mathbf{r}_{r,i}$, their orientation angles $\theta_{r,i}$ with respect to the x axis, their center of mass velocities $\mathbf{v}_{r,i}$, and their angular velocities $\omega_{r,i}$ [140], see Fig. 2.1a. The rod beads partially overlap, such that the effective friction for rod-rod interaction is small and no interlocking

occurs [141]. Beads of neighboring rods therefore interact via a separation-shifted Lennard-Jones potential (SSLJ) [140, 142]

$$W(r) = \begin{cases} 4\epsilon \left[\left(\frac{\sigma^2}{\alpha^2 + r^2} \right)^6 - \left(\frac{\sigma^2}{\alpha^2 + r^2} \right)^3 \right] + W_0 & r \leq r_{\text{cut}} \\ 0 & r > r_{\text{cut}} \end{cases}, \quad (2.34)$$

where r is the distance between two beads, α characterizes the capping of the potential, and W_0 shifts the potential to avoid a discontinuity at $r = r_{\text{cut}}$. The length $\alpha = \sqrt{2^{1/3}\sigma^2 - r_{\text{cut}}^2}$ is calculated by requiring the potential to vanish at the minimum of the SSLJ potential, $\sigma/r_{\text{cut}} = 2.5$, hence the potential is purely repulsive. $E_r = \phi(0) - \phi(r_{\text{cut}})$ is the potential energy barrier. Once E_r has been set to a certain value, we obtain $\epsilon = \alpha^{12}E_r/(\alpha^{12} - 4\alpha^6\sigma^6 + 4\sigma^{12})$. With an effective bead radius is $r_{\text{bead}} = r_{\text{cut}}/2$, and an effective rod thickness r_{cut} , the rod aspect ratio is $a = L/r_{\text{cut}}$. The bead-bead distance within a rod is r_{cut} , see Fig. 2.1b.

A system with penetrable self-propelled rods has three energy scales; the thermal energy $k_B T$, the propulsion strength $|\mathbf{F}_P|L_r$, and the rod energy barrier E_r . Two independent dimensionless ratios can be used to characterize the system: the Péclet number [140]¹

$$\text{Pe} = \frac{\text{Propulsion energy}}{\text{Thermal energy}} = \frac{|\mathbf{F}_P|L_r}{k_B T} = \frac{L_r v_0}{D_{\parallel}}, \quad (2.36)$$

and the penetrability coefficient [140]

$$Q = \frac{\text{Propulsion energy}}{\text{Energy barrier}} = \frac{|\mathbf{F}_P|L_r}{E_r}. \quad (2.37)$$

The Péclet number characterizes the rod activity. If Pe is large, the rod propulsion is high and the effects of the noise are negligible. If Pe is small, the rod propulsion is low compared with the noise. A large Q value indicates that a rod is very penetrable, in such cases crossing events occur often. A small Q value indicates that a rod is impenetrable, in such cases crossing events rarely occur.

The effect of penetrability for self-propelled rods in two dimensions and cytoskeletal filaments next to surfaces has previously been studied both in simulations and experiments [5, 140], see Fig. 2.2. The rod crossing probability $P(\phi)$ can be measured in experiments as a function of the angle between two cytoskeletal filaments ϕ , see Fig. 2.2b. Because it can also be calculated in simulations initializing two rods close to each other, with well-defined mutual orientations, it allows to connect the parameters in simulations with the experimental data. The simulations performed had different orientation, Péclet number, energy barrier, and penetrability coefficient, see Fig. 2.2c.²

¹In our simulations, we define the Péclet number using the translational diffusion coefficient. It is also possible to define the Péclet number using the rotational diffusion coefficient

$$\text{Pe}_{\text{rot}} = \frac{v_0}{D_{\theta} L_r} \quad \text{with} \quad \text{Pe} = 6\text{Pe}_{\text{rot}} \quad (2.35)$$

²In the simulations, a crossing event is counted when two rods intersect significantly, i.e., such that the intersection point is at least $0.2L$ rod away from the ends of each rod. Thus, events where one rod only “touches” the other rod are not counted.

2.5 Penetrable self-propelled rods

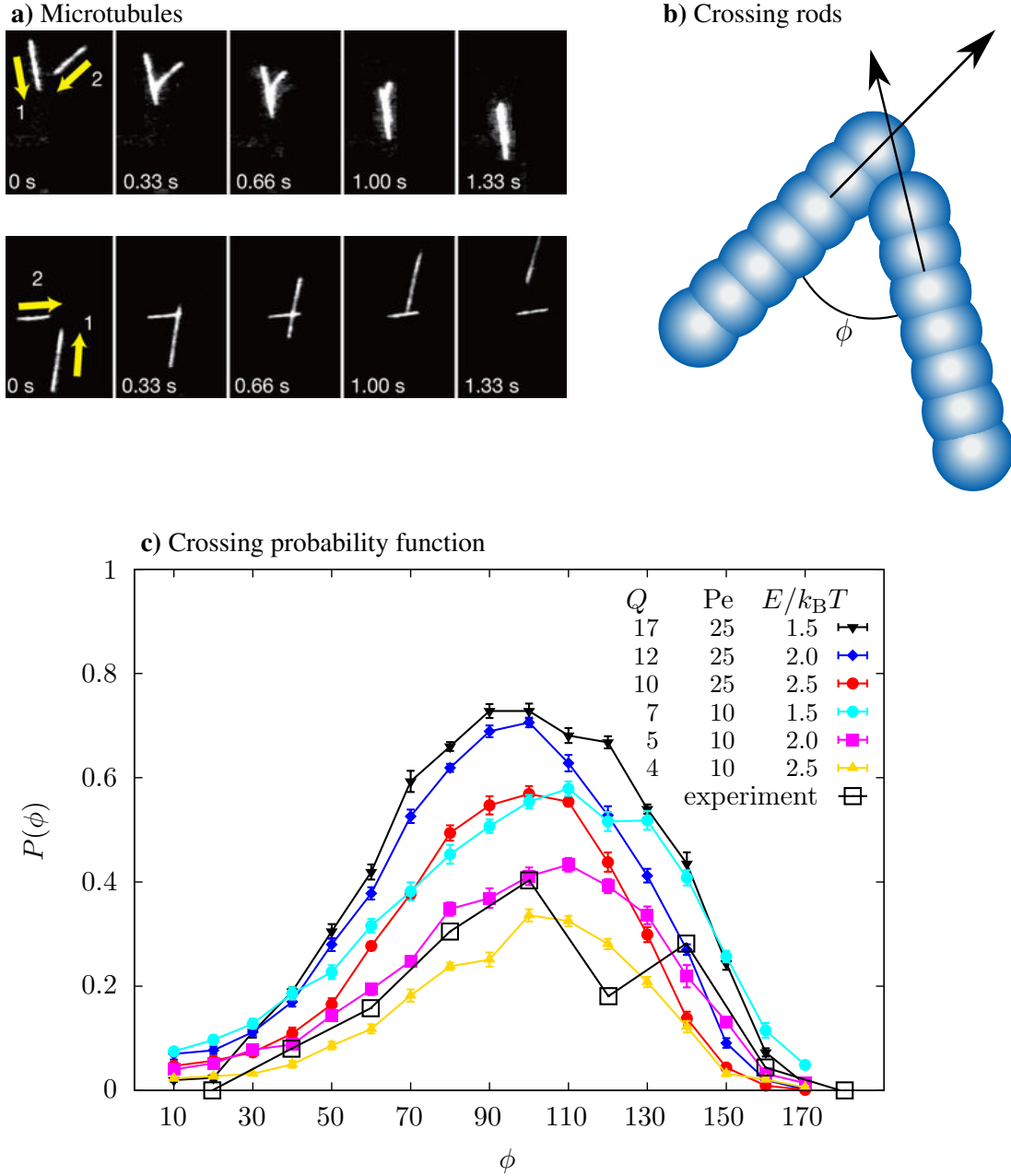


Figure 2.2: Filaments crossing. **a)** Motility assay with microtubules. The top row shows an event where two microtubules cannot cross each other and thus, they align. The bottom row shows a crossing event, thus the original orientations of the microtubules remain unchanged after crossing. Figure reproduced from Ref. [5] with permission from the Nature Publishing Group. **b)** Schematic of two rods crossing. ϕ represents the angle between the rods. **c)** Crossing probability of two rods for various values of Q , Pe and E_r [5, 140]. In the original paper the authors use E instead of E_r to represent the rod energy barrier. Figure reproduced from Ref. [140] with permission from the American Physical Society ©2013 American Physical Society.

2.6 Semiflexible polymer ring

When considering entire cells, the cell membrane can be modeled as a mathematical surface, where the curvature-elastic properties are characterized by a Helfrich Hamiltonian. For crawling cells, we only simulate the area of the cell that is in contact with the substrate. Therefore, the contact line where the membrane detaches from the substrate can be represented by a semiflexible polymer ring. The semiflexible polymer rings, in our simulations, are characterized by their equilibrium radius R_m and are composed of n_b beads. They are discretized into beads that are separated from each other by a distance ζr_{cut} , where $\zeta = L_m/(r_{\text{cut}} n_b)$ is the inverse overlap, and L_m is the perimeter of the ring. For $\zeta = 0$ the beads fall on top of each other, while for $\zeta = 1$ the center-of-mass of the beads are separated by $2r_{\text{cut}}$. To calculate the ring energy, we take into account three contributions:

- Stretching energy,

$$E_S = \frac{k_S}{2} \sum_{i=0}^{n_b-1} (|\mathbf{R}_i| - l_S)^2. \quad (2.38)$$

The ring beads are connected by harmonic bonds. Here, k_s is the spring constant of a bond between two beads and it is given in units of $k_B T / R_m^2$, $l_S = 2R_m \sin(\pi/n_b)$ is the equilibrium bond length, \mathbf{r}_i represents the vector from the center of the polymer ring to monomer i , and $\mathbf{R}_i = \mathbf{r}_{i+1} - \mathbf{r}_i$ is the bond vector from monomer i to monomer $i+1$. The stretching energy controls the length of the polymer both locally and globally. In our model, the springs represent the cortical cytoskeleton. The stretching force exerted on bead i is

$$\mathbf{F}_{S_i} = -k_S \left(\mathbf{R}_{i-1} \frac{|\mathbf{R}_{i-1}| - l_S}{|\mathbf{R}_{i-1}|} - \mathbf{R}_i \frac{|\mathbf{R}_i| - l_S}{|\mathbf{R}_i|} \right). \quad (2.39)$$

- Bending energy,

$$E_B = -\frac{\kappa}{l_S} \sum_{i=0}^{n_b-1} (1 - \cos \theta_i(\mathbf{R}_i, \mathbf{R}_{i+1})). \quad (2.40)$$

Tilting of neighboring bonds is characterized by the bending energy. Here, κ is bending rigidity given in units of $k_B T R_m$, l_S is the bond equilibrium length and $\theta(i)$ is the angle between \mathbf{R}_i and \mathbf{R}_{i+1} . The bending energy is minimized when the polymer is in a straight configuration. The bending force applied to bead i is

$$\begin{aligned} \mathbf{F}_{B_i} = & -\kappa \frac{\frac{\mathbf{R}_{i-1} \cdot \mathbf{R}_{i-2}}{\mathbf{R}_{i-1} \cdot \mathbf{R}_{i-1}}}{\mathbf{R}_{i-1} \cdot \mathbf{R}_{i-1} \mathbf{R}_{i-2} \cdot \mathbf{R}_{i-2}} \\ & + \kappa \frac{\frac{\mathbf{R}_i \cdot \mathbf{R}_{i-1}}{\mathbf{R}_i \cdot \mathbf{R}_i} \mathbf{R}_i - \frac{\mathbf{R}_i \cdot \mathbf{R}_{i-1}}{\mathbf{R}_{i-1} \cdot \mathbf{R}_{i-1}} \mathbf{R}_{i-1} + \mathbf{R}_i - \mathbf{R}_{i-1}}{\mathbf{R}_i \cdot \mathbf{R}_i \mathbf{R}_{i-1} \cdot \mathbf{R}_{i-1}} \\ & + \kappa \frac{\frac{\mathbf{R}_{i+1} \cdot \mathbf{R}_i}{\mathbf{R}_{i+1} \cdot \mathbf{R}_{i+1}} \mathbf{R}_i - \mathbf{R}_{i+1}}{\mathbf{R}_{i+1} \cdot \mathbf{R}_{i+1} \mathbf{R}_i \cdot \mathbf{R}_i} \end{aligned} \quad (2.41)$$

- Area constraint energy,

$$E_A = -\frac{k_A}{2} \left(\sum_{i=0}^{n_b-1} A_i - A_0 \right)^2. \quad (2.42)$$

Here, k_A is the bulk modulus given in units of $k_B T / R_m^4$. The area A_i of the triangle is defined by the vectors \mathbf{r}_i and \mathbf{r}_{i+1} .

$$A_i = \frac{\text{sign}_i}{2} |\mathbf{r}_i \times (\mathbf{r}_{i+1} - \mathbf{r}_i)| = \frac{\text{sign}_i}{2} |\mathbf{r}_i \times \mathbf{r}_{i+1}|, \quad (2.43)$$

with

$$\text{sign} \begin{cases} 1 & \text{if } \mathbf{r}_i \times (\mathbf{R}_i) > 0 \\ -1 & \text{if } \mathbf{r}_i \times (\mathbf{R}_i) < 0 \end{cases}. \quad (2.44)$$

The volume of a cell is controlled by the osmotic pressure. The cortical cytoskeleton combined with the osmotic pressure induce a membrane tension, which favors a spherical cell shape. However, the adhesion strength between the cell and the substrate favors an increased area adhered to the substrate. Both contributions determine the adhered cell area, which we simulate using an area constraint. The area force applied to bead i is

$$\mathbf{F}_{A_i} = -\frac{k_A}{2} \left(\sum_{i=0}^{n_b-1} A_i - A_0 \right) \mathbf{u}_i, \quad (2.45)$$

where \mathbf{u}_i is the ring normal vector at bead i .

We use a very large value for k_S , such that the springs are very stiff and the ring perimeter is roughly kept constant. If we want to study which energy contribution is dominant for the parameters used in our simulations, we only have to consider the area constraint energy E_A and the bending energy E_B . We are particularly interested in studying the bending and area-constraint energy contributions in the keratocyte-like shape, see chapter 5.

For an analytical estimation, we calculate the change in E_A and E_B for a ring that is deformed from a circle to an ellipse. In our calculations, we use dimensionless bending rigidity $\bar{\kappa}$, which is defined as $\bar{\kappa} = \kappa / (k_B T R_m)$, compression modulus \bar{k}_A , which is defined as $\bar{k}_A = k_A R_m^4 / k_B T$, bending energy \bar{E}_B , which is defined as $\bar{E}_B = E_B / k_B T$, and area constraint energy \bar{E}_A , which is defined as $\bar{E}_A = E_A / k_B T$. The bending and area constraint energy for a circle are

$$\bar{E}_B \text{ circle} = \frac{\pi \bar{\kappa}}{R} \quad (2.46)$$

and

$$\bar{E}_A \text{ circle} = \frac{\pi \bar{k}_A R^2}{2}, \quad (2.47)$$

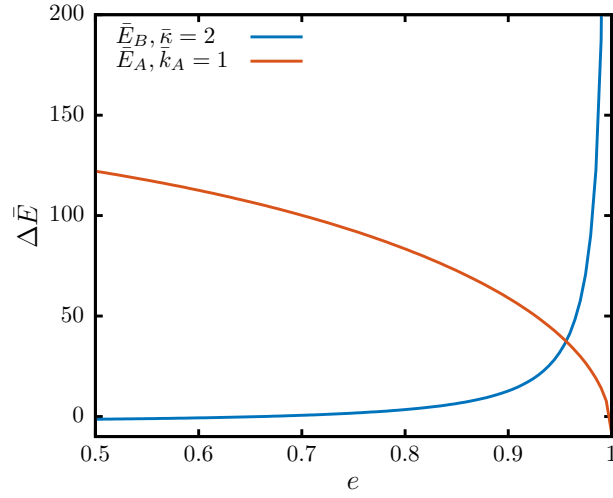


Figure 2.3: Bending and area constraint energy change $\Delta\bar{E}_B$ and $\Delta\bar{E}_A$, respectively versus eccentricity e . Calculations performed with $a = 10$, $\bar{\kappa} = 2$ and $\bar{k}_A = 1$. Here, $\bar{\kappa}$ and \bar{k}_A are the dimensionless bending rigidity and dimensionless compression modulus, respectively.

respectively. The bending and area constraint energy for an ellipse are

$$\bar{E}_B \text{ ellipse} = \frac{2\pi^2\bar{\kappa}}{a(1 - (1 - b^2/a^2))} \quad (2.48)$$

and

$$\bar{E}_A \text{ ellipse} = \frac{\pi\bar{k}_A ab}{2}, \quad (2.49)$$

respectively. Here, a is the semi major axis of the ellipse, and b is the semi minor axis of the ellipse. Defining the eccentricity e in terms of the ellipse semi axes and using the condition that the perimeters of the circle and the ellipse must be equal,

$$e = \sqrt{1 - \frac{b^2}{a^2}} \Rightarrow b^2 = a^2(1 - e^2) \quad (2.50)$$

and

$$2\pi R = \sqrt{2(a^2 + b^2)} \Rightarrow R^2 = \frac{a^2(2 - e^2)}{2\pi^2}. \quad (2.51)$$

The changes in energy for a deformation from a circle to an ellipse are

$$\Delta\bar{E}_B = \frac{\bar{\kappa}\pi^2}{a} \left(\frac{2}{1 - e^2} - \frac{\pi\sqrt{2}}{\sqrt{2 - e^2}} \right) \quad (2.52)$$

and

$$\Delta\bar{E}_A = \frac{\bar{k}_A\pi a^2}{2} \left(\sqrt{1 - e^2} - \frac{2 - e^2}{2\pi^2} \right). \quad (2.53)$$

In our calculations, $a \approx 10$, $\bar{\kappa} = 2$ and $\bar{k}_A = 1$. Figure 2.3 shows the change in bending and area constraint energy as function of the eccentricity. The maximum eccentricity achieved by the keratocyte-like rings is $e \approx 0.88$. In the regime $e \leq 0.88$, the area constraint energy dominates over the bending energy. This indicates that in our simulations the area constraint energy will determine both shape and stiffness of our rings.

2.7 Rod-ring interaction

To study the collective behavior of rods enclosed in rings, the rods and the ring must interact sterically. To model this repulsive interaction, we use an SSLJ potential with a large energy barrier $E_{\text{rm}} = 250k_{\text{B}}T$, such that the rods cannot exit the ring. The SSLJ potential between the rods and the rings is calculated on a bead level. Previous studies [143, 144] show that self-propelled particles collect at the boundaries. If we had passive particles, the density of particles inside the ring would be uniform and equal to the global density $\rho(r) = \rho_0 = N_{\text{r}}/A_{\text{ring}}$. Once the activity is turned on, the system is out-of-equilibrium, and the local density is no longer homogeneous. The larger the activity, the more the particles concentrate at the borders, see App. B. Thus, non-attached self-propelled rods inside rings collect at the ring border and exert pushing forces, see Sec. 4.1. Previous studies have found that the self-propelled particles aggregate in regions where the confinement is highly curved $\rho(s) \propto 1/R(s)$, where $\rho(s)$ is the local particle density, and $R(s)$ is the local radius of curvature [145].

To mimic the retraction forces found at the rear of crawling cells [12, 146], we need to model rods that exert pulling forces on the ring. Therefore, an attachment between the rods and the ring is needed. This attachment, can be mediated by a FENE spring

$$W_{\text{att}}(r) = \begin{cases} -\frac{1}{2}k_{\text{F}}b_{\text{F}}^2 \ln \left[1 - \left(\frac{r}{b_{\text{F}}} \right)^2 \right], & r \leq r_{\text{cut}} \\ \infty, & r > r_{\text{cut}} \end{cases}. \quad (2.54)$$

Here, k_{F} is the FENE spring stiffness and b_{F} is the length of the FENE spring. This attachment controls the radial distance between the rod and the ring, while still allowing the rods to slide along the ring. By adding the attachment between rods and rings, we not only have the possibility to transmit pulling forces to the ring, but also the rod motion becomes quasi-one-dimensional.

The direction of the propulsion force with respect to the attachment defines whether an attached rod pushes or pulls. For attached-pushing rods, the propulsion force points towards the ring, see Fig. 2.4a. For attached-pulling rods, the propulsion force points away from the ring, see Fig. 2.4b. Although most of the work presented in this thesis has been done with attached rods, the systems with both non-attached and attached rods are discussed in chapter 4.

Due to the ring being discretized into beads, rods feel an effective friction μ when they slide along the ring. This effective friction can be used to mimic the friction that a cytoskeletal filament experiences because of the viscosity of the cell membrane [147]. The ring beads are separated from each other by a distance ζr_{cut} , where $\zeta =$

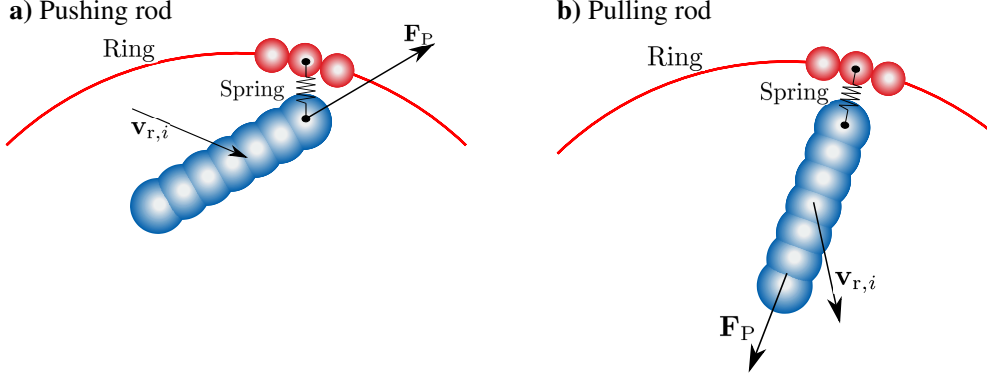


Figure 2.4: Rod-ring interaction schematics. Ring beads are colored in red, rod beads are colored in blue and a spring links the first bead of the rod with a ring bead. \mathbf{F}_P represents the rod-propulsion force and $\mathbf{v}_{r,i}$ represents the velocity of rod i . **a)** Interaction between an attached-pushing rod and a ring. For attached-pushing rods the propulsion force is oriented towards the ring. **b)** Interaction between an attached-pulling rod and a ring. For attached-pulling rods the propulsion force is oriented away from the ring.

$L_m/(r_{\text{cut}}n_b)$ is the inverse overlap, and L_m is the perimeter of the ring. For $\zeta = 0$ the beads fall on top of each other, while for $\zeta = 1$ the beads are separated by r_{cut} .

The effective friction that rods feel as they slide along the ring is

$$\mu = \left\langle \frac{\mathbf{F}_P \cdot \mathbf{e}_t}{\mathbf{v}_r \cdot \mathbf{e}_t} \right\rangle_{N_r, t}, \quad (2.55)$$

where \mathbf{e}_t is the unit vector along the tangential direction of the ring, \mathbf{F}_P the rod propulsion force, and \mathbf{v}_r the rod velocity measured in the simulations. Figure 2.5 shows the normalized friction coefficient, $(\mu - \mu_0)/\mu_0$, versus the inverse overlap, ζ , for $N_r = 1$ and 6 and $E_r/k_B T = 10$, where μ_0 is the effective friction for rods sliding along a continuous ring. The normalized effective friction coefficient $(\mu - \mu_0)/\mu_0$ versus ζ can be fitted using

$$\frac{\mu - \mu_0}{\mu_0} = a\zeta^b, \quad (2.56)$$

where a and b are fit parameters, see Tab. 2.1.

For the studied systems, the only parameters that play a role in the effective friction are N_r and ζ , see Fig. 2.5. For small rod densities, where the rods do not cluster, the friction between the ring and rods only depends on ζ . The values for a and b increase as N_r increases, both for attached and non-attached rods.

For deformable rings, the attachment between the rods and the ring is modeled using a harmonic spring

$$\phi_{\text{att}}(r) = \begin{cases} \frac{1}{2}k_H (r - b_H)^2, & r \leq r_{\text{cut}} \\ \infty, & r > r_{\text{cut}} \end{cases}, \quad (2.57)$$

where k_H is the harmonic spring stiffness and b_H is the equilibrium length of the harmonic spring.

2.8 Brownian dynamics simulations

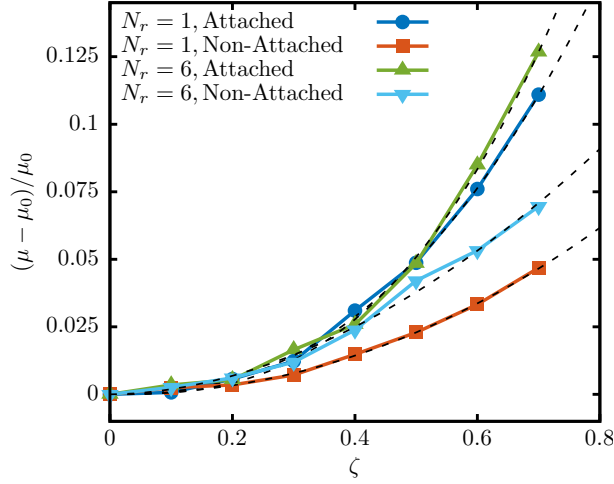


Figure 2.5: Normalized effective friction coefficient $(\mu - \mu_0)/\mu_0$ versus inverse overlap ζ , for attached and non-attached rods for various values of N_r . The dashed lines are fits using Eq. 2.56. Figure reproduced from publication (A) Ref. [141] with permission from the Royal Society of Chemistry.

| Types of rods | N_r | a | b |
|---------------|-------|-----|-----|
| Attached | 1 | 0.3 | 2.4 |
| | 6 | 0.3 | 2.7 |
| Non-Attached | 1 | 0.1 | 2.1 |
| | 6 | 0.2 | 2.1 |

Table 2.1: Fit parameters for the normalized friction coefficient $(\mu - \mu_0)/\mu_0 = a\zeta^b$. The values shown in the table were extracted from the simulation data corresponding to the systems shown in Fig. 2.5. Table reproduced from publication (A) Ref. [141] with permission from the Royal Society of Chemistry.

2.8 Brownian dynamics simulations

In the systems studied here, the motion of the particles is always affected by the interaction with their surrounding medium. The random motion of the passive particles, called Brownian motion, is caused by collisions between the particles and solvent molecules [133].

Brownian dynamics (BD) simulations are a mesoscopic approach to modeling particles that are coupled to an implicit solvent. In BD, the solvent is modeled by friction and stochastic forces that are applied to the particles, such that the fluctuation-dissipation theorem is fulfilled, see Eq. 2.11. This approach is only valid if the characteristic time scale for the motion of the particles of interest is much larger than that for the motion of the solvent molecules and if hydrodynamic interactions are negligible. In solutions of colloids, polymers, and in biological systems in the micro and mesoscale, the characteristic time scale of the particles is always much larger than that of motion of the

solvent molecules [148–150].

Brownian dynamics is overdamped Langevin dynamics

$$\dot{\mathbf{x}} = \frac{1}{\gamma} (\mathbf{f} + \mathbf{\Gamma}), \quad (2.58)$$

where \mathbf{x} is the particle position, \mathbf{f} is the force acting on the particle, and $\mathbf{\Gamma}$ is the stochastic force. For the fluctuation-dissipation theorem to be fulfilled, $\langle \mathbf{\Gamma}(t) \mathbf{\Gamma}(t') \rangle = 2\gamma k_B T \delta(t - t')$. The stochastic force must be drawn from a Gaussian distribution with $\sigma^2 = 2\gamma k_B T$.

The equations used to calculate the dynamics of rods inside rings are

$$\mathbf{v}_{r_i \parallel} = \frac{1}{\gamma_{r \parallel}} \left(\sum_{j \neq i}^{N_r} \mathbf{F}_{r_{i,j} \parallel} + \mathbf{F}_{rm_i \parallel} + \mathbf{F}_{att_i \parallel} + \xi_{r \parallel} \mathbf{e}_{\parallel} + \mathbf{F}_p \right) \quad (2.59)$$

$$\mathbf{v}_{r_i \perp} = \frac{1}{\gamma_{r \perp}} \left(\sum_{j \neq i}^{N_r} \mathbf{F}_{r_{i,j} \perp} + \mathbf{F}_{rm_i \perp} + \mathbf{F}_{att_i \perp} + \xi_{r \perp} \mathbf{e}_{\perp} \right) \quad (2.60)$$

$$\omega_{r_i} = \frac{1}{\gamma_{r \theta}} \left(\sum_{j \neq i}^{N_r} \mathbf{M}_{r_{i,j}} + \mathbf{M}_{m_i} + \mathbf{M}_{att_i} + \xi_{r \theta} \mathbf{e}_{\theta} \right). \quad (2.61)$$

Here, \mathbf{e}_{\parallel} and \mathbf{e}_{\perp} are unit vectors parallel and perpendicular to the rod axis, respectively, and \mathbf{e}_{θ} is oriented normal to the plane of rod motion. \mathbf{F}_p is the propulsion force for each rod. $\mathbf{F}_{r_{i,j}}$ and $\mathbf{M}_{r_{i,j}}$ are the steric force and the torque from rod j to rod i , and \mathbf{F}_{rm_i} and \mathbf{M}_{rm_i} are the steric force and the torque from rod i to the ring, respectively. All steric forces and torques due to bead-bead interactions are calculated using Eq. 2.34. Finally, \mathbf{F}_{att_i} and \mathbf{M}_{att_i} are the attachment force and torque from rod i to the ring, which is calculated using Eq. 2.54. For non-attached rods, $\mathbf{F}_{att} = \mathbf{M}_{att} = 0$. The rod friction coefficients are $\gamma_{r \parallel} = \gamma_0 L_r$, $\gamma_{r \perp} = 2\gamma_{\parallel}$ and $\gamma_{r \theta} = \gamma_{\parallel} L_r^2/6$, which are obtained from hydrodynamics for the rod slim-body approximation, see Sec. 2.3 [138]. $\xi_{r \parallel}$, $\xi_{r \perp}$, and $\xi_{r \theta}$ are the corresponding rod parallel, perpendicular and rotational noise, respectively.

The equations used to calculate the dynamics of rigid rings are

$$\mathbf{v}_{m,x} = \frac{1}{\gamma_{mt}} \left(\sum_{j=1}^{N_r} \mathbf{F}_{m_j x} + \sum_{j=1}^{N_r} \mathbf{F}_{att_j x} + \xi_{mt} \mathbf{e}_x \right) \quad (2.62)$$

$$\mathbf{v}_{m,y} = \frac{1}{\gamma_{mt}} \left(\sum_{j=1}^{N_r} \mathbf{F}_{m_j y} + \sum_{j=1}^{N_r} \mathbf{F}_{att_j y} + \xi_{mt} \mathbf{e}_y \right) \quad (2.63)$$

$$\omega_m = \frac{1}{\gamma_{m \theta}} \left(\sum_{i=j}^{N_r} \mathbf{M}_{m_j \theta} + \sum_{j=1}^{N_r} \mathbf{M}_{att_j \theta} + \xi_{m \theta} \mathbf{e}_{\theta} \right). \quad (2.64)$$

The ring translational and rotational friction coefficients $\gamma_{mt} = 6\pi\eta R_m$ and $\gamma_{m \theta} = 8\pi\eta R_m^3$, respectively. They correspond to the three-dimensional friction of a spherical particle of radius R_m in a fluid with viscosity η . ξ_{mt} and $\xi_{m \theta}$ are the corresponding ring

2.8 Brownian dynamics simulations

translational and rotational noise, respectively. Please note that subscript m refers to the entire ring.

The equations used to calculate the dynamics of deformable rings are

$$\mathbf{v}_{b_i x} = \frac{1}{\gamma_b} \left(\sum_{j=1}^{N_r} \mathbf{F}_{rb_j x} + \sum_{j=1}^{N_r} \mathbf{F}_{att_j x} + \sum_{j=-2}^2 \mathbf{F}_{bb_{i,i-j} x} + \xi_b \mathbf{e}_x \right) \quad (2.65)$$

$$\mathbf{v}_{b_i y} = \frac{1}{\gamma_b} \left(\sum_{j=1}^{N_r} \mathbf{F}_{rb_j y} + \sum_{j=1}^{N_r} \mathbf{F}_{att_j y} + \sum_{j=-2}^2 \mathbf{F}_{bb_{i,i-j} y} + \xi_b \mathbf{e}_y \right), \quad (2.66)$$

where γ_b is the ring bead friction, motivated by solid-solid friction between the deformable ring beads and the substrate. \mathbf{F}_{rb_i} is the steric force from rod j to ring bead i , and $\mathbf{F}_{bb_{i,i-j}}$ represents the force that ring bead $i-j$ exerts on ring bead i . $\mathbf{F}_{bb_{i,i-j}}$ consists of stretching, bending, and area-constraint forces, for more details see Sec. 2.6. For deformable rings, \mathbf{F}_{att} is calculated using Eq. 2.57. The noises $\xi_{r\parallel}$, $\xi_{r\perp}$, $\xi_{r\theta}$, ξ_{mt} , $\xi_{m\theta}$, and ξ_b are drawn from Gaussian distributions with variances $\sigma^2 = 2k_B T \gamma / t$, such that the fluctuation-dissipation theorem is fulfilled, at equilibrium. Please note that subscript b refers to a certain ring bead.

Chapter 3

Collective behavior of self-propelled rods with density-dependent slowing down

The results of this chapter have been published in (B) (see list of publications on page 143), the text is reproduced with permission from the American Physical Society ©2018 American Physical Society. All verbatim quotes within this chapter are quotations of (B) and are indicated as “ ... ”. Such verbatim quotes can extend over several pages.

“Many active systems in nature show collective behavior, ranging from bird flocks, fish schools, and ant colonies [151, 152] to sperm and bacteria [153, 154]. All these systems share a common characteristic: local alignment or jamming of neighboring agents gives rise to collective behavior. This alignment can result from steric interaction between self-propelled elongated particles [102, 140, 155], but it can also emerge from other mechanisms, such as motility-induced clustering [141, 156, 157] and long-ranged, vision-like interactions [158, 159]. In systems with steric interactions, the shape of the particles strongly influences the collective behavior. Disks and spheres, for instance, tend to form round clusters [156, 160, 161], while elongated objects, such as worm-like and rod-like particles, form elongated clusters and are often found in swarming phases [140, 162–164]. Motility assays with cytoskeletal filaments, such as actin filaments and microtubules, show clustering, swirling and wave-like patterns [4, 5]. Self-propelled particles can also be used to construct composite “complex objects” [141, 165], where the structure and dynamics of the internal self-propelled agents induce the motility of the composite particle.”

Self-propelled particles tend to accumulate where they move more slowly. Vice versa, they may also slow down at high density, due to steric repulsion, biochemical signaling, or changes in the chemical environment. The positive feedback between accumulation-induced reduced propulsion and reduced propulsion-induced accumulation leads to motility-induced phase separation (MIPS) between dense and dilute fluid phases [37]. MIPS has been observed experimentally in genetically modified *E. coli* [166, 167]. Previous studies have used systems with density-dependent diffusion to

model pattern formation in bacterial colonies [168].

Several systems display a modified propulsion force at high densities. For example, a decreased propulsion force at high densities has been experimentally observed for phoretic self-propelled particles [169–171]. Phoretic propulsion mechanisms have been reported for particles in externally-imposed gradients of solute concentration, electric potential, or temperature [172]. “When phoretic self-propelled particles are close to each other, the gradients around the particles decrease, and the particle propulsion force decreases [16, 172–174].” In nature, *Bacillus subtilis* increase their swimming velocity with density [175], this increase of the swimming velocity has been observed to lead to band formation [176, 177]. “Genetically modified *E. coli* reduce their propulsion velocity as the bacterial density increases [166, 167]. This reduction of the swimming velocity helps biofilm formation.” In theoretical studies for density-dependent reduced propulsion, bands, moving clumps, asters, and lanes have been found [178].

In this chapter, we quantify the effect that a rod propulsion force that decreases with increasing number of neighboring rods has on the collective behavior of self-propelled rods (SPRs) in two dimensions. “The rods interact via a capped-repulsive potential that allows for crossing events, such that we effectively model a thin film with the computational costs for two-dimensional simulations [140]. The density-dependent propulsion force gives rise to a qualitatively new alignment mechanism compared with the constant-propulsion force case. This leads to new phases that are not observed for SPRs with density-independent propulsion: polar hedgehog clusters, stripes, bands, and asters.” Furthermore, density-dependent slowing down increases the polarity of the systems.

“In the simulations we employ the following units and parameters. Lengths are measured in units of rod length L_r , energies in units of $k_B T$, and times in units of $\tau_0 = 1/D_{r0}$, where D_{r0} is the rod rotational diffusion coefficient. The systems size is $L_x = L_y = 16L_r$.” Rod positions and orientations are initialized randomly. “The systems studied have rods which consist of $n_r = 9$ and 18 beads. The global rod density is $\rho_0 = N/(L_x \times L_y)$, where N is the rod number. We use $\rho_0 L_r^2 = 6.4$ and 12.8 for systems with $n_r = 9$ and 18, respectively. We study systems with Péclet numbers $25 \leq \text{Pe} \leq 400$, rod energy barriers $1.5 \leq E/k_B T \leq 10$, base propulsion weights $0 \leq v_1 \leq 0.5$, and deceleration ratios $0.1 \leq \lambda \leq 5$.”

3.1 Density-independent propulsion force

This chapter aims to study the effect of density-dependent propulsion force on the collective behavior of SPRs. “Before analyzing the changes that the density-dependent propulsion force induces, we need to know how constant-propulsion SPRs behave. Here, we show phase diagrams and snapshots for constant-propulsion SPRs with 9 and 18 beads, see Figs. 3.1 and 3.2.”

For rods with $n_r = 9$, the dynamic phase diagram is shown in Fig. 3.1. “We observe four different phases. For systems with small E_r , we find an isotropic phase (I). For intermediate E_r , we find a clustered nematic phase (CN). For intermediate E_r and small Pe , the rods form polar clusters (PC). Finally, for large energy barrier, we observe a polar domains phase (PD).”

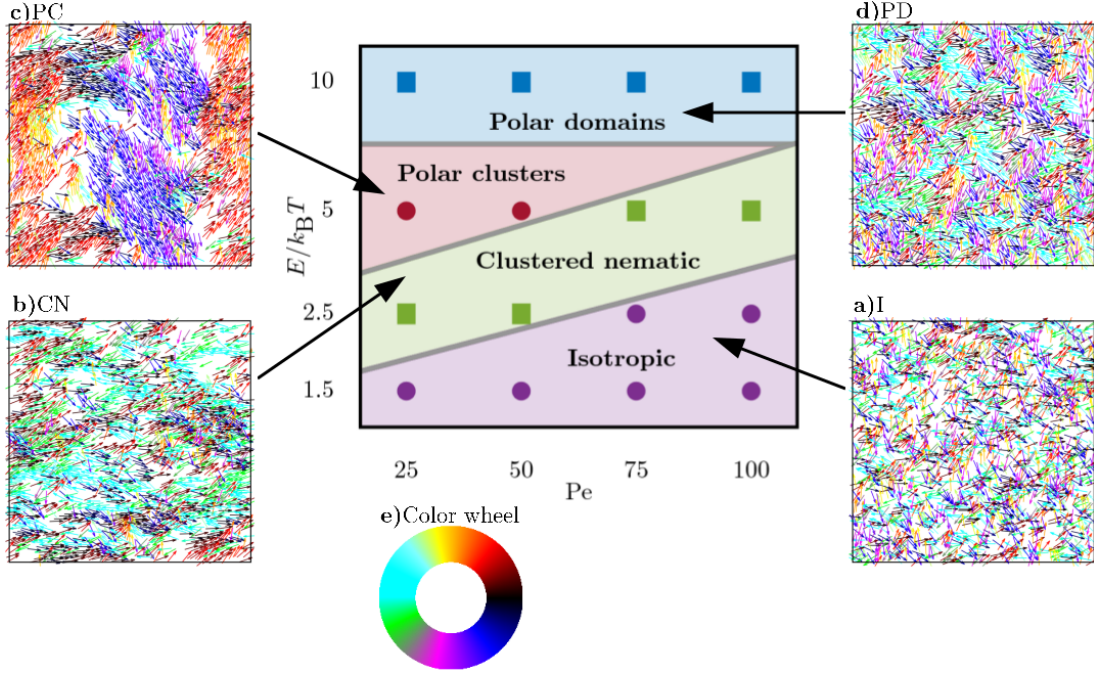


Figure 3.1: Snapshots and phase diagram of self-propelled rod systems with $n_r = 9$ beads, $\rho_0 L_r^2 = 6.4$, and density-independent propulsion ($\lambda = 0$), where λ is the deceleration ratio. **a)** Isotropic phase (I), system with $E_r/k_B T = 1.5$, and $Pe = 100$. **b)** Clustered nematic phase (CN), system with $E_r/k_B T = 5$, and $Pe = 100$. **c)** Polar clusters phase (PC), system with $E_r/k_B T = 5$, and $Pe = 50$. **d)** Polar domains phase (PD), system with $E_r/k_B T = 10$, and $Pe = 25$. **e)** Color wheel that indicates rod orientation. Figure reproduced from publication (B) Ref. [179] with permission from the American Physical Society ©2018 American Physical Society.

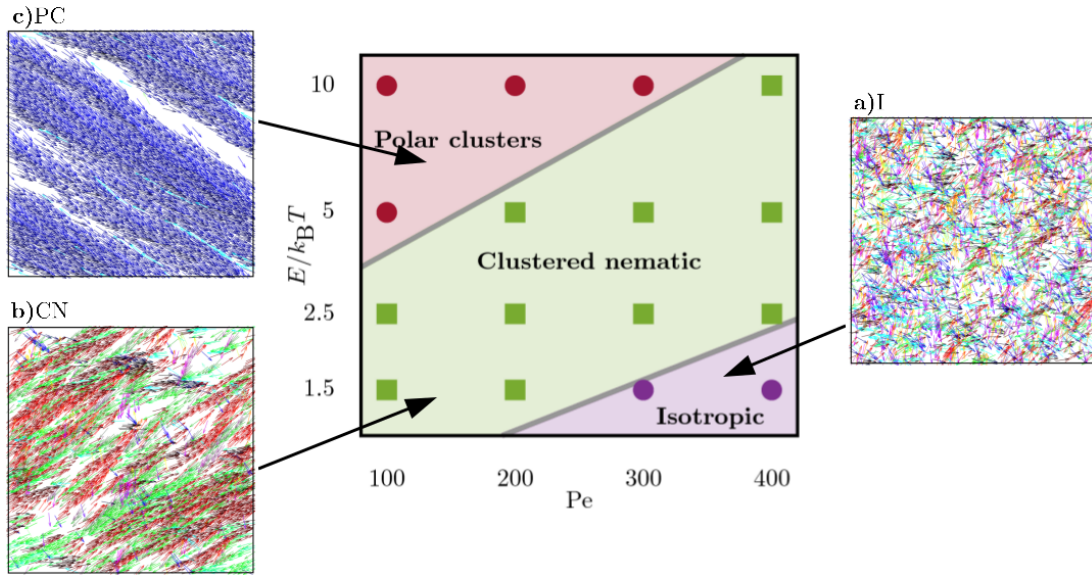


Figure 3.2: Snapshots and phase diagram of self-propelled rod systems with $n_r = 18$ beads, $\rho_0 L_r^2 = 12.8$, and density-independent propulsion ($\lambda = 0$), where λ is the deceleration ratio. **a)** Isotropic phase (I), system with $E_r/k_B T = 1.5$, and $Pe = 400$. **b)** Clustered nematic phase (CN), system with $E_r/k_B T = 5$, and $Pe = 400$. **c)** Polar clusters phase (PC), system with $E_r/k_B T = 5$, and $Pe = 100$. Figure reproduced from publication (B) Ref. [179] with permission from the American Physical Society ©2018 American Physical Society.

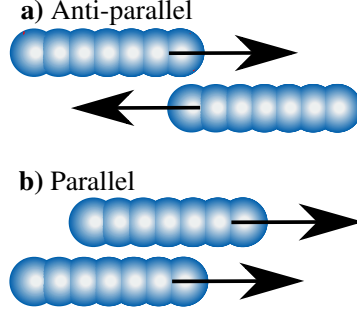


Figure 3.3: Schematic representation of rod interaction and propulsion. **a)** Anti-parallel orientation between two rods, the angle between the rods is π . **b)** Parallel orientation between two rods, the angle between the rods is 0. Figure reproduced from publication (B) Ref. [179] with permission from the American Physical Society ©2018 American Physical Society.

“Let us take a closer look at the structure of the phases as shown by the snapshots of rod configurations in Fig. 3.1. Rods with small energy barrier cross each other easily, as such the classical SPR alignment mechanism plays a small role and the rods form an isotropic phase (I). In the clustered nematic phase (CN), there are fewer crossing events. This leads to rod alignment and rod clustering. In the polar cluster phase (PC), the increase in energy barrier and decrease of Pe hinders anti-parallel rod orientation. Thus, leading to global polar ordering. In the polar domain phase (PD), the energy barrier is so large that no crossing events occur. In our systems as the energy barrier increases the rods become thicker. These two effects lead to “frozen” systems with small polar domains.”

“For rods with $n_r = 18$, the dynamic phase diagram is shown in Fig. 3.2. We observe three different phases. For systems with small E_r , we find an isotropic phase (I). For intermediate E_r , we find a clustered nematic phase (CN). For large E_r , the rods form polar clusters (PC).”

“The mechanism of alignment of rods with 9 and 8 beads are the same. The increase in aspect ratio enhances cluster formation and alignment. As such, the region of the clustered nematic phase is larger for rods with $n_r = 18$ than for rods with $n_r = 9$. We observe no polar domains phase for rods with $n_r = 18$.” The increase in aspect ratio prevents this phase from occurring.

3.2 Density-dependent propulsion force: phase diagrams

For our density-dependent systems, the propulsion force is [178]

$$\mathbf{F}_p = \mathbf{F}_0 \left(v_0 e^{-\lambda m} + v_1 \right), \quad (3.1)$$

where m is the number of neighboring beads surrounding the rod, λ is the deceleration ratio, v_0 is the weight of the density-dependent propulsion force, v_1 is the weight of the

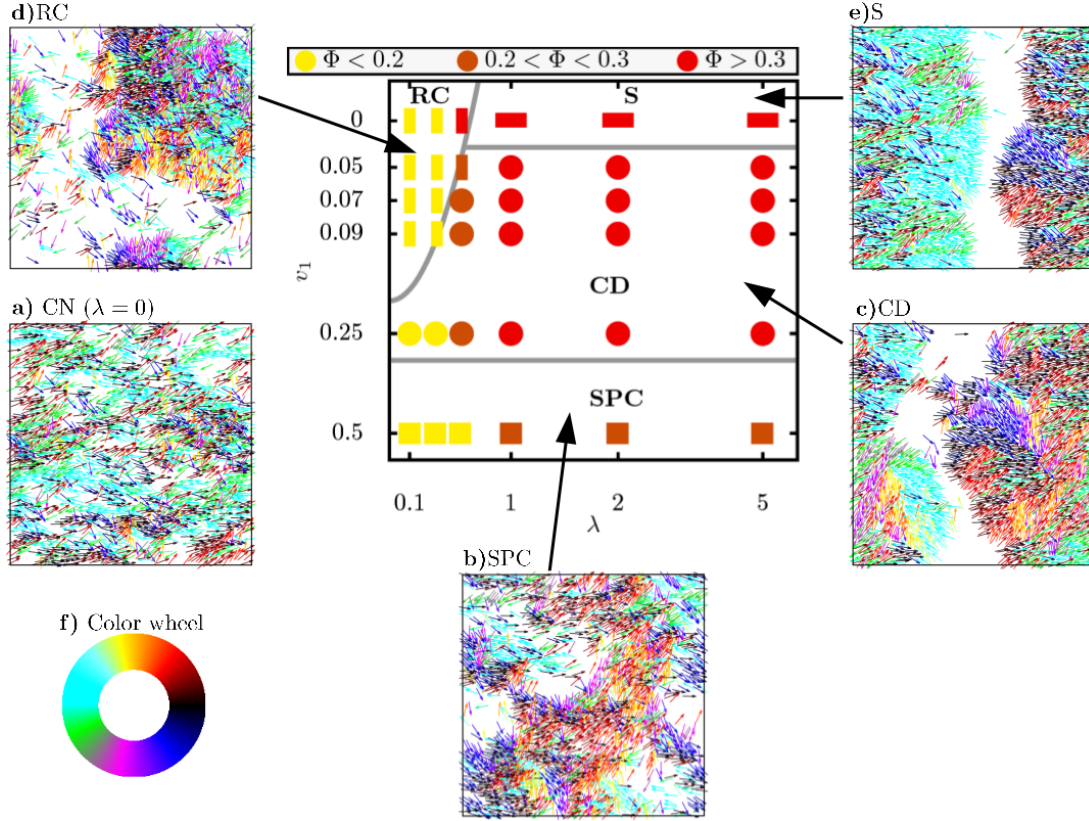


Figure 3.4: Phase diagram for various λ and v_1 , and simulation snapshots of self-propelled rod systems with $n_r = 9$ beads, $\rho_0 L_r^2 = 6.4$, $E_r/k_B T = 5$ and $Pe = 100$. **a)** Clustered nematic phase (CN), system with density-independent propulsion ($\lambda = 0$). **b)** Small polar clusters phase (SPC), system with $\lambda = 5$ and $v_1 = 0.5$. **c)** Cluster with domains phase (CD), system with $\lambda = 2$ and $v_1 = 0.05$. **d)** Round clusters phase (RC), system with $\lambda = 0.1$ and $v_1 = 0$. **e)** Stripes phase (S), system with $\lambda = 1$ and $v_1 = 0$. **f)** Color wheel that indicates rod orientation. In the phase diagram, squares represent polar clusters (PC), vertical rectangles represent round clusters (RC), horizontal rectangles represent bands (B), and circles represent clusters with domains (CD). The points are colored according to the value of the polar order parameter Φ , see the legend. Note that the base propulsion weight v_1 appears in the vertical axis top to bottom.

3.2 Density-dependent propulsion force: phase diagrams

base propulsion force, and \mathbf{F}_0 is the rod propulsion strength if no slowing-down were present. “We choose $v_0 + v_1 = 1$, such that for systems without neighbors $\mathbf{F}_p = \mathbf{F}_0$. The number of neighboring beads, m , is calculated on a bead basis. For each bead of rod i , we estimate the number of beads of neighboring rods that are inside an area of radius r_{cut} . We then sum over all beads of rod i to obtain the total number of neighboring beads.”

“Although passive rods are apolar, the rod-rod friction and in particular the density-dependent propulsion force leads to a polar interaction. For two rods in anti-parallel orientation the density-dependent deceleration lasts for $\tau_{\text{anti-parallel}} \approx L_r/2|\mathbf{v}_{\parallel}|$, while for two rods in parallel orientation the density-dependent deceleration lasts longer.”

“Density-dependent reduced propulsion force introduces a rich variety of dynamical structures, depending on aspect ratio a , deceleration ratio λ , and weight of the base propulsion force v_1 .” Here, we show the phases observed for the self-propelled rods and discuss the alignment mechanisms that density-dependent reduced propulsion introduces.

For rods with $n_r = 9$, corresponding to aspect ratio $a = 4.5$, Fig. 3.4 shows five different phases. “For density-independent propulsion force ($\lambda = 0$), the rods form a clustered nematic phase (CN). For systems with $\lambda > 0$ and large v_1 , the rods form small polar clusters (SPC). For intermediate v_1 , the rods form clusters with domains (CD). For small λ and intermediate and small v_1 , the rods form round clusters (RC). Finally, for large λ and $v_1 = 0$, the rods form stripes (S).”

Let us take a closer look at the structures that the rods form in the phases shown in Fig. 3.4. Rods in the small polar clusters phase (SPC) form motile polar clusters. In the clusters with domains phase (CD), the clusters are composed of large polar domains and tend to span the entire system. In the round clusters phase (RC), we observe round clusters with small polar domains. Here, the rods at the cluster borders are perpendicularly oriented with respect to the borders. Rods in the stripes phase (S) form elongated, system-spanning clusters. Rods both in bulk and at the border are perpendicular with respect to the aster border. Stripes have larger polar domains compared with round clusters, due to the increased rod alignment at increased lambda.

For rods with $n_r = 18$, corresponding to aspect ratio $a = 9$, Fig. 3.5 shows six different phases, with a larger local order than for the short rods. “For density-independent propulsion force ($\lambda = 0$), the rods form a clustered nematic phase (CN). For $\lambda > 0$ and large v_1 , the rods form an aligned phase (Al). For intermediate v_1 , the rods form polar clusters (PC). For small and intermediate λ and small v_1 , the rods form polar hedgehog clusters (PHC). For large λ and small v_1 , the rods form polar bands (PB). Finally, for $v_1 = 0$, the rods form asters (As).” Note that for systems with $n_r = 18$ beads, $\rho_0 L_r^2 = 12.8$, whereas for systems with $n_r = 9$ beads, $\rho_0 L_r^2 = 6.4$.

In the aligned phase (Al), rods form polar clusters, but the overall orientation is nematic. In the polar clusters phase (PC), rods form large polar dynamic clusters. In the polar hedgehog clusters phase (PHC), we find large polar worm-like clusters with perpendicular rods at the borders. In many cases, the rods at the borders form hedgehog-like structures. Rods in the polar bands phase (PB), form elongated stable polar clusters with perpendicular rods at the border. The stability of these bands is given by the perpendicular rods at the border. In the asters phase (As), rods form

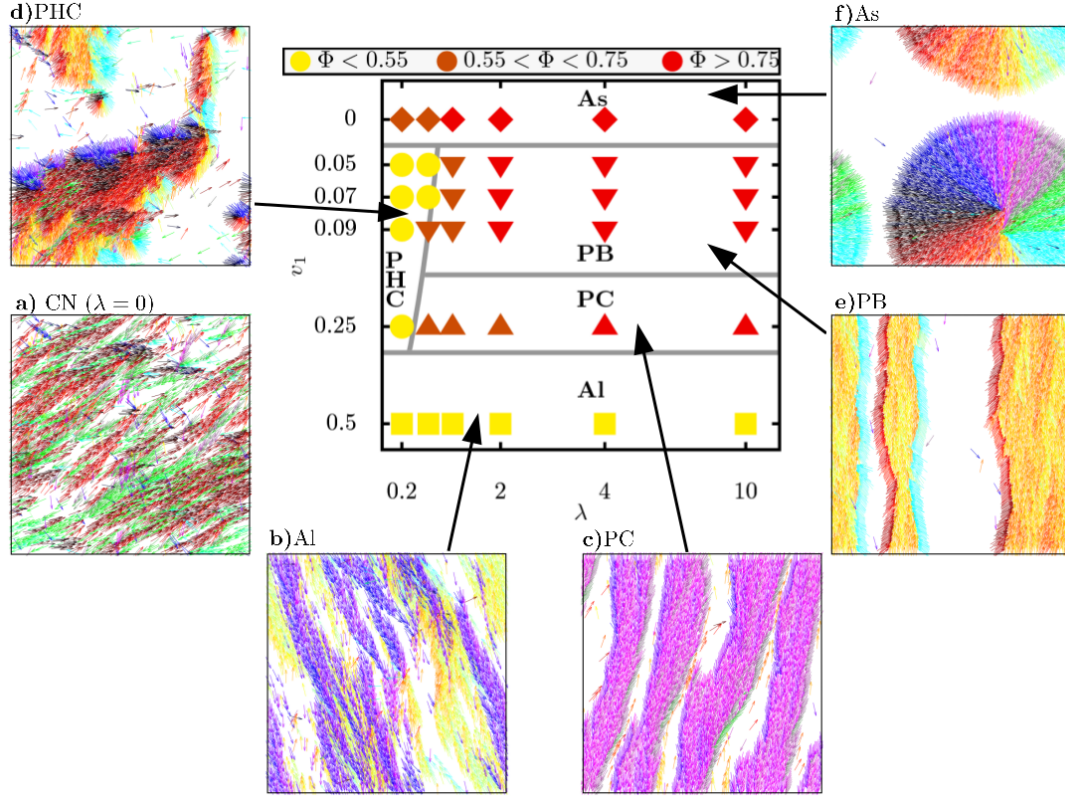


Figure 3.5: Snapshots and phase diagram of self-propelled rod systems with $n_r = 18$, $\rho_0 L_r^2 = 12.8$, $E_r/k_B T = 5$, and $Pe = 400$. **a)** Clustered nematic phase (CN), system with density-independent propulsion ($\lambda = 0$). **b)** Aligned phase (Al), system with $\lambda = 10$ and $v_1 = 0.5$. **c)** Polar clusters phase (PC), system with $\lambda = 10$ and $v_1 = 0.25$. **d)** Polar hedgehog clusters phase (PHC), system with $\lambda = 0.2$ and $v_1 = 0.09$. **e)** Polar bands phase (PB), system with $\lambda = 1$ and $v_1 = 0.09$. **f)** Asters phase (As), system with $\lambda = 0.4$ and $v_1 = 0$. In the phase diagram squares represent aligned rods (Al), circles represent polar hedgehog clusters (PHC), upward triangles represent polar clusters (PC), downward triangles represent polar bands (PB), and diamonds represent asters (As). The points are colored according to the value of the polar order parameter Φ , see the legend. Note that the base propulsion weight v_1 appears in the vertical axis top to bottom.

3.3 Density-dependent slowing-down enhances polarity

round clusters with large polar domains. Rods both in bulk and at the border are perpendicular with respect to the aster border.

The phenomena observed for short and long rods are the same, but the difference in aspect ratio causes the rods to form very different kind of structures. Long rods tend to form more polar and more ordered structures than short rods. The density-dependent self-propulsion enhances polar order parameter, see Sec. 3.3. The alignment and cluster formation observed for classical self-propelled rods ($\lambda = 0$) are caused by the rod-rod repulsive interaction, in our case the rod energy barrier E_r . For $\lambda > 0$, the density-dependent reduced propulsion allows the steric interaction to act longer, which enhances rod alignment. The local polar order parameter increases with increasing λ .

The density-dependent reduced propulsion enhances clustering in two ways, see Sec. 3.4. On the one hand, there is a more significant chance for the rods to align, since the rod energy barrier acts longer. As explained in Sec. 3.2, the density-dependent propulsion enhances the parallel rod orientation over the anti-parallel one. On the other hand, the slowing-down induces rod trapping. A rod that comes close to a cluster moves more slowly. This decreases the probability of a rod to exit the cluster. These two effects lead to the formation of loosely-packed clusters with domains.

As mentioned above, the density-dependent propulsion force introduces perpendicularity of the rods at the cluster borders. The density-dependent reduced propulsion increases the friction as the rod interact with each other. The increase in friction leads to perpendicularity for rods at the border. A more detailed explanation of this mechanism is given in Sec. 3.5. The rod perpendicularity at the borders increases with increasing slowing-down. For systems with $v_1 = 0$, rods in clusters become effectively passive. We observe asters and stripes. These structures are extreme cases of the perpendicularity effect since in these structures all the rods are perpendicular with respect to the borders.

Rods with $n_r = 18$, $Pe = 100$ and $E_r/k_B T = 5$ form polar clusters (PC), see Fig. A.1 in App. A. For these systems, we do not observe a nematic-to-polar transition caused by the density-dependent propulsion, because the system with $\lambda = 0$ is already polar.

3.3 Density-dependent slowing-down enhances polarity

“To quantify the increase of the rod alignment and polarity caused by the density-dependent self-propulsion we calculate the nematic and polar order parameters”

$$S = \left\langle \sum_{i \neq j}^N \frac{\cos(2(\theta_i - \theta_j))}{N(N-1)} \right\rangle \quad (3.2)$$

$$\Phi = \left\langle \sum_{i \neq j}^N \frac{\cos(\theta_i - \theta_j)}{N(N-1)} \right\rangle. \quad (3.3)$$

“The averages are taken over square cells of size $4L_r$. Here, $S = 0$ corresponds to an isotropic state, $\Phi = 0$ and $S = 1$ to a nematic state, and $\Phi = 1$ and $S = 1$ to a polar

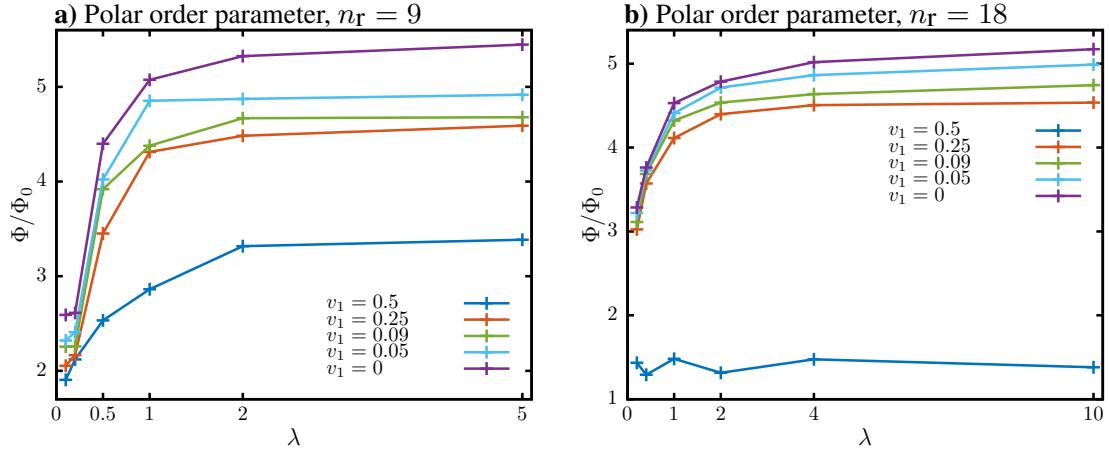


Figure 3.6: Polar order parameter Φ versus deceleration ratio λ for various values of v_1 . **a)** Systems with $n_r = 9$ beads, $\rho_0 L_r^2 = 6.4$, $E_r/k_B T = 5$, and $Pe = 100$. **b)** Systems with $n_r = 18$ beads, $\rho_0 L_r^2 = 12.8$, $E_r/k_B T = 5$, and $Pe = 400$. Φ_0 is the polar order parameter for the respective density-independent propulsion systems, for **a)** $\Phi_0 = 0.074$ and for **b)** $\Phi_0 = 0.168$. Figure reproduced from publication (B) Ref. [179] with permission from the American Physical Society ©2018 American Physical Society.

state.” The values for S , and Φ for various simulations are provided in Tabs. A.1 and A.2 in App. A.

For both, rods with $n_r = 9$ and rods with $n_r = 18$ beads, there is an increase in the polar order parameter with decreasing v_1 , see Fig. 3.6. For $\lambda \leq 2$, Φ increases with increasing λ . However, for $\lambda \geq 2$, the polar order parameter remains roughly constant, see Fig. 3.6a. There is a sharp increase in Φ for $\lambda \simeq 1$. Independent of v_1 , beyond the critical value of $\lambda \simeq 1$ the polar order reaches its maximum and Φ saturates. For systems with $\lambda = 1$, $m/a \approx 2.5$ which makes the term $v_0 \exp(-\lambda m)$ of the propulsion force vanish. This means that for $\lambda \geq 1$, the propulsion force is roughly $v_1 F_0$. All systems show similar behavior, except 18-bead rods in the aligned phase (A1, $v_1 = 0.5$), see Fig. 3.6b. Aligned-phase systems maintain a roughly constant polar order parameter as λ increases because the rod-rod interaction time for parallel and anti-parallel orientations are similar.

The increase in polar order parameter Φ/Φ_0 introduced by the density-dependent reduced propulsion force is similar for rods with 9 and 18 beads. However, Φ_0 for long rods is larger than for short rods. This means that systems with long rods have larger polar order parameter than systems with short rods.

3.3 Density-dependent slowing-down enhances polarity

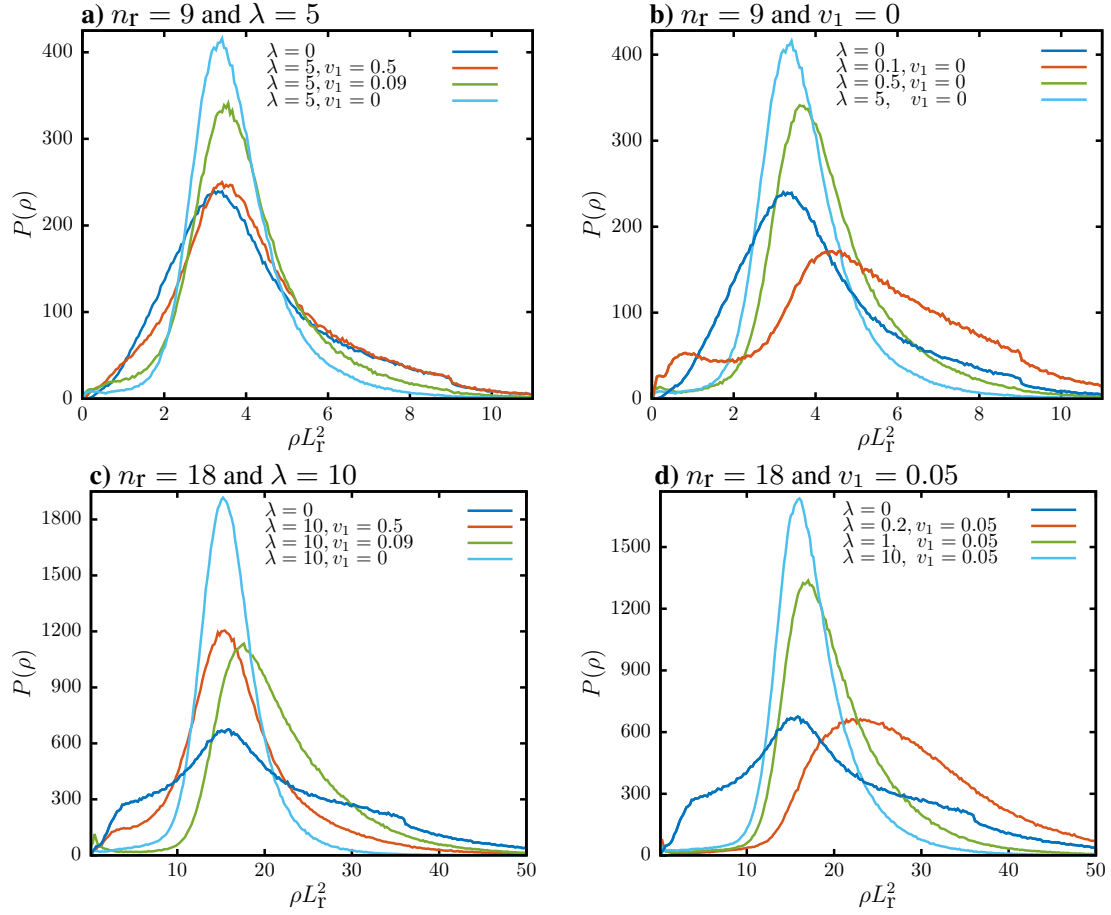


Figure 3.7: Density distribution $P(\rho)$ versus rod local density ρ . Upper row shows systems with $n_r = 9$, $\rho_0 L_r^2 = 6.4$, $E_r/k_B T = 5$, $Pe = 100$. Lower row shows systems with $n_r = 18$, $\rho_0 L_r^2 = 12.8$, $E_r/k_B T = 5$, $Pe = 400$. **a)** Systems with $\lambda = 5$, **b)** systems with $v_1 = 0$. **c)** Systems with $\lambda = 10$, **d)** systems with $v_1 = 0.05$. Figure reproduced from publication (B) Ref. [179] with permission from the American Physical Society ©2018 American Physical Society.

3.4 Density-dependent propulsion enhances clustering

“We quantify the effect of the density-dependent propulsion on the clustering process using the rod-density distributions $P(\rho)$ and the cluster size distributions $\Pi(M)$, see Figs. 3.7 and 3.8. The local rod densities are calculated using Voronoi tessellation, where the centers-of-mass of the rods are used as the tessellation seeds. The local density is then proportional to the inverse of the area of the Voronoi cells. Because many of our systems have very few rods in the low-density regions, the density distributions are, generally, single-peaked functions, see Fig. 3.7. A peak for $\rho = 0$ is lacking, because when using the Voronoi tessellation the density distribution is weighted by the rod density itself. For the cluster-size distributions, we consider two rods to be in the same cluster if their nearest distance is less than $2r_{\text{cut}}$ and their orientations differ by less than 15° .”

“Rods with $n_r = 9$ in the clustered-nematic phase (CN), form clusters of different sizes without a clear spatial separation or high and low-density regions, see Fig. 3.4a. Therefore, $P(\rho)$ shows a single but broad peak that is positively skewed, see Fig. 3.7a. The peak at $\rho L_r^2 \approx 3.8$ is only slightly below the rod density for a square stacked with rods side by side, $\rho L_r^2 = 4.5$. The peak position is independent of v_1 , and the peak increases with decreasing v_1 .” Density distributions for the small polar clusters (SPC) phase ($\lambda = 5$, $v_1 = 0.5$) are very similar to that of the clustered-nematic phase (CN). The density distributions for the cluster with domains (CD) phase ($\lambda = 5$, $v_1 = 0.09$), and for the stripes (S) phase ($\lambda = 5$, $v_1 = 0$) are narrower. The probability to find regions with $\rho L_r^2 \leq 2$ is negligible for systems with small v_1 . The density-dependent reduced propulsion enhances the probability of rods to join the cluster, reduces the probability of rods to leave the cluster, and induces perpendicularity. These effects lead to the formation of clusters with very sharp interfaces, $\rho L_r^2 \approx 2$ corresponds to the rod density at the cluster interface.

For systems with $v_1 = 0$, generally, the peak of the density distribution increases with increasing λ , see Fig. 3.7b. “The density distribution for the round cluster (RC) phase ($\lambda = 0.1$, $v_1 = 0$) is a bimodal distribution. The first peak corresponds to rods in the low-density region $\rho L_r^2 \approx 0.7$.” Round clusters show a more populated low-density region, see Fig. 3.4d, which is why we observe a peak for the low-density region. “The second peak of the density distribution corresponds to rods in the cluster $\rho L_r^2 \approx 4.5$.” For systems at the border between the round cluster (RC) and the stripes (S) phase ($\lambda = 0.5$, $v_1 = 0$), $P(\rho)$ has a single peak at $\rho L_r^2 \approx 4$, which corresponds to loosely packed rods, as discussed above. For stripes ($\lambda = 5$, $v_1 = 0$), the peak is at the same position as for the density-independent system, $\rho L_r^2 \approx 3.7$. For systems with $\lambda \leq 0.5$, $P(\rho L_r^2 \leq 2)$ is negligible, which corresponds to clusters with very sharp interfaces, as discussed above. For systems with $v_1 = 0$, as λ increases the systems transition from round clusters to stripes, and the low-density region is less populated by rods.

“Rods with $n_r = 18$ in the clustered nematic (CN) phase ($\lambda = 0$) form worm-like clusters of different sizes. As such, $P(\rho)$ is a broad distribution with a peak located at $\rho L_r^2 \approx 17$, see Fig. 3.7c. The peak position is roughly independent of v_1 . For systems with $\lambda = 10$, the peak of the density distribution increases with decreasing v_1 . The

3.4 Density-dependent propulsion enhances clustering

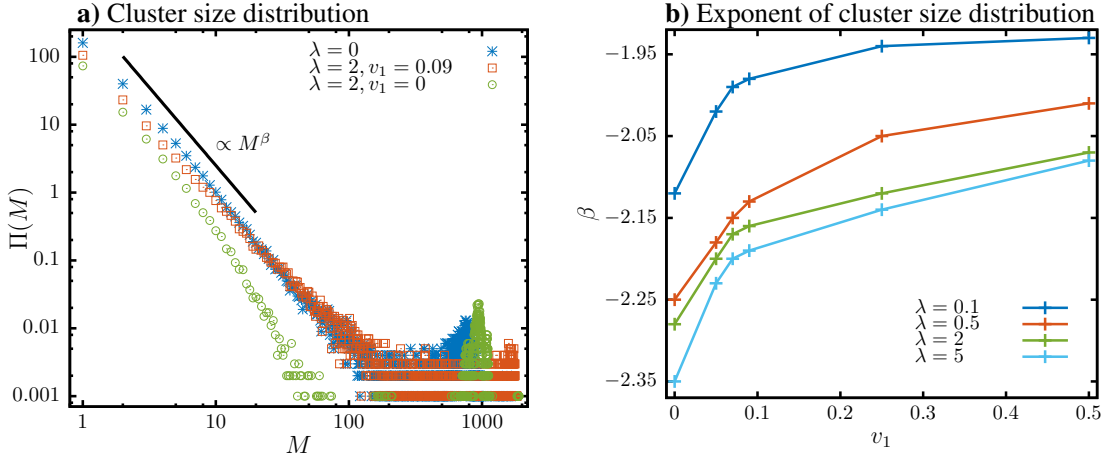


Figure 3.8: **a)** Cluster size distribution $\Pi(M)$ versus cluster size M for systems with $n_r = 9$, $\rho_0 L_r^2 = 6.4$, $E_r/k_B T = 5$, $Pe = 100$, for various values of λ and v_1 . **b)** Exponent of the cluster size distribution, β , versus the weight of the base propulsion, v_1 , for various values of λ . Figure reproduced from publication (B) Ref. [179] with permission from the American Physical Society ©2018 American Physical Society.

aligned (Al) phase ($\lambda = 10$, $v_1 = 0.5$) shows a better defined peak than the clustered nematic (CN) phase ($\lambda = 0$). The probability to find regions with $\rho L_r^2 \leq 10$ is negligible for polar bands (PB $\lambda = 10$, $v_1 = 0.09$) and asters (As $\lambda = 10$, $v_1 = 0$). The density-dependent reduced propulsion enhances the probability for rods to join the cluster, reduces the probability for rods to leave the cluster, and induces perpendicularity. These effects lead to the formation of clusters with very sharp interfaces, $\rho L_r^2 \approx 10$ corresponds to the rod density at the cluster interface.”

“For systems with $v_1 = 0.05$, generally, the peak of the density distribution increases with increasing λ , see Fig. 3.7d. The density-dependent distribution for the polar hedgehog clusters (PHC) phase ($\lambda = 0.2$, $v_1 = 0.05$) is broad and positively skewed. In this case, the peak is located at $\rho L_r^2 \approx 22$. This indicates that polar hedgehog clusters are more densely packed than the clusters formed in the clustered nematic phase. For systems with $\lambda > 0$, $P(\rho L_r^2 \leq 10)$ is negligible, which corresponds to sharp interfaces, see discussion above. In these systems, polar hedgehog clusters (PHC) and polar bands (PB), we find perpendicular rods at the cluster borders. The rod perpendicularity stabilizes cluster formation and prevents rods from escaping the cluster.”

Cluster-size distributions are shown in Fig. 3.8a. For small cluster sizes, M , the distribution decreases as a power law, $\Pi(M) \propto M^\beta$ [140,180]. “As the density-dependent reduced propulsion becomes more pronounced, the number of small clusters decreases. Rods form ”loose” system-spanning clusters as λ increases and v_1 decreases. The cluster size distribution for the clustered nematic (CN) phase ($\lambda = 0$), and for the cluster with domains (CD) phase ($\lambda = 2$, $v_1 = 0.09$). However, $\Pi(M)$ drastically changes for the stripes (S) phase ($\lambda = 2$, $v_1 = 0$). $\Pi(M)$ decreases and is shifted towards smaller M values, which indicates that the formation of small and intermediate clusters is

hindered. The cluster size distributions show a peak located at $M \simeq 1000$, which corresponds to system-spanning clusters formed by a large number of rods.”

“The exponent β of the cluster-size distribution decreases with increasing λ and decreasing v_1 , see Fig. 3.8b. β decays slowly with v_1 for small polar clusters ($v_1 > 0.09$), and sharply for round stripes, clusters, and clusters with domains ($v_1 \leq 0.09$).” The decrease of β with decreasing v_1 is caused by the fact that the density-dependent reduced propulsion not only helps the formation of large loosely packed clusters, but also disfavors the formation of small clusters.

3.5 Density-dependent propulsion induces perpendicularity

“For rods with small v_1 , the propulsion force strongly decreases as soon as the rod comes in contact with a cluster.” The decrease in the propulsion force of the rod means that the rod does not easily slide along the border of the cluster. “This enhances the probability for the rod to meet other with opposite orientation, thus leading to the formation of hedgehog-like aggregates at the cluster borders. Once the cluster border is filled with rods, the rods align perpendicularly rather than form hedgehog-like aggregates, to maximize packing.”

The density-dependent reduced propulsion induces jamming between rods. When a rod comes in contact with other rods due to the decrease in its propulsion the rod torque is also strongly reduced. Thus, if the rods do not meet in a parallel orientation, they do not align easily. This leads to small aggregates of rods which are created due to jamming. Such structures easily trap other neighboring rods, giving rise to small hedgehog-like clusters with perpendicular rods at the borders, see Fig. 3.9 at $t = 0.1\tau_0$. In our systems, like in other MIPS systems, there is positive feedback between the density-dependent slowing-down and the cluster formation [37]. For systems with $v_1 = 0$, as soon as rods cluster, the rods become passive, and the local structure is determined by steric alignment and optimal packing.

For systems with density-independent propulsion ($\lambda = 0$) the rods form elongated clusters [140]. In contrast, for systems with density-dependent reduced propulsion, we find perpendicular rods at the borders of the rod structures. This happens in particular for round clusters (RC), stripes (S), polar hedgehog clusters (PHC), polar bands (PB), and asters (As). In all phases with rod perpendicularity, initially motile pointed hedgehog-like clusters form, see Fig. 3.9 at $t = 0.1\tau_0$. Subsequently, for $t \leq 2\tau_0$, the clusters coalesce, and the stationary states can be very different: polar hedgehog clusters (PHC), polar bands (PB), and asters (As).

For systems with $v_1 > 0$, perpendicular rods are only observed at the cluster borders, e.g., borders of the polar hedgehog clusters (PHC), polar bands (PB), and round clusters (RC). For polar hedgehog clusters and polar bands ($v_1 > 0$), the rods in the center of the cluster are still propelled, which leads to rod alignment due to the classical SPR alignment mechanism. This is why systems with $v_1 > 0$ are overall polar.

For asters (As) and stripes (S), rods with neighbors are passive rods, such that there is no propulsion-induced alignment ($v_1 = 0$) and all rods are perpendicular with

3.5 Density-dependent propulsion induces perpendicularity

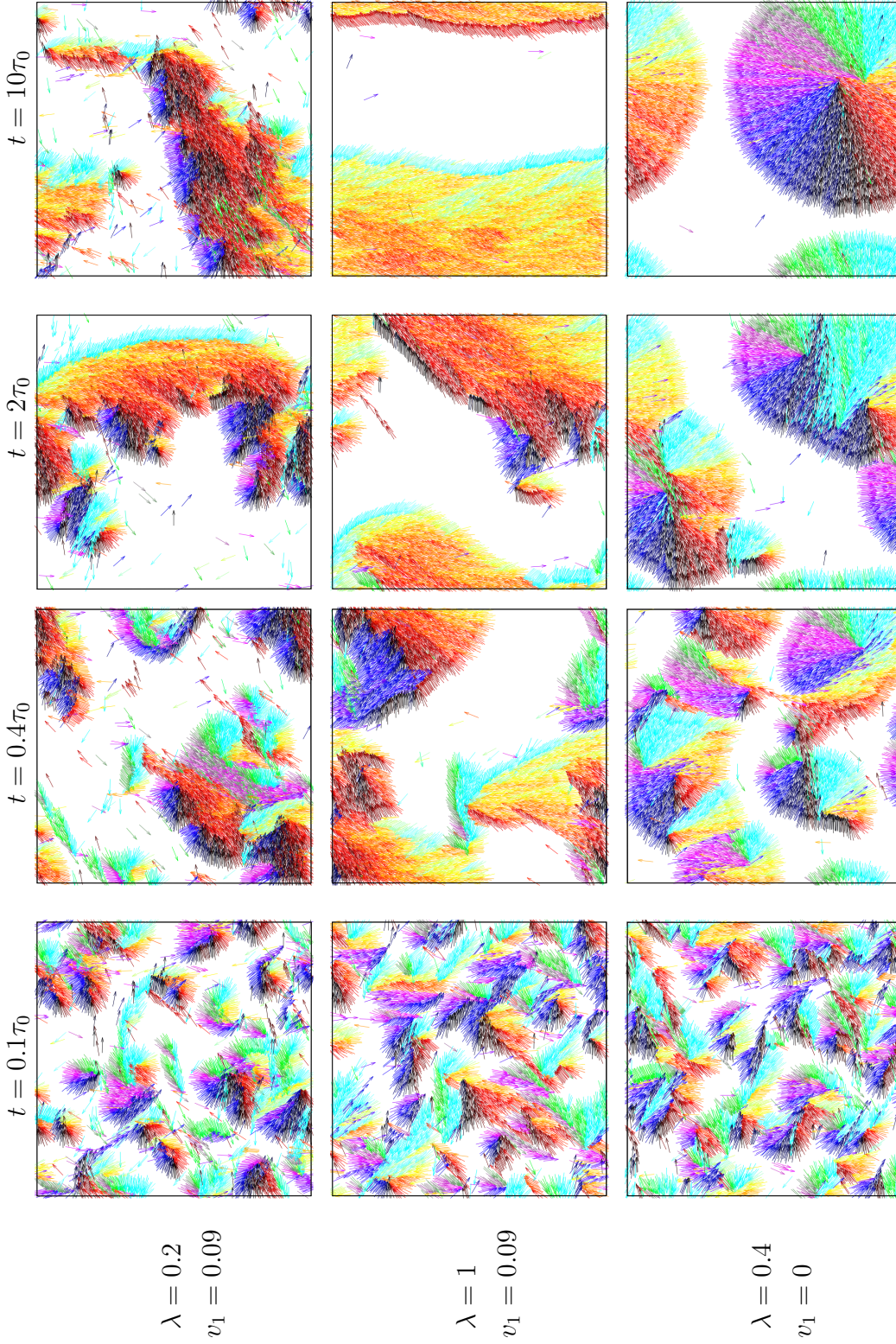


Figure 3.9: Snapshots of self-propelled rod systems at different times. Systems with $n_r = 18, \rho_0 L_r^2 = 12.8, E_r/k_B T = 5$, and $Pe = 400$. Top row shows the formation of polar hedgehog clusters (PHC). Intermediate row shows the formation of polar bands (PB). Bottom row shows the formation of asters (As). Figure reproduced from publication (B) Ref. [179] with permission from the American Physical Society ©2018 American Physical Society.

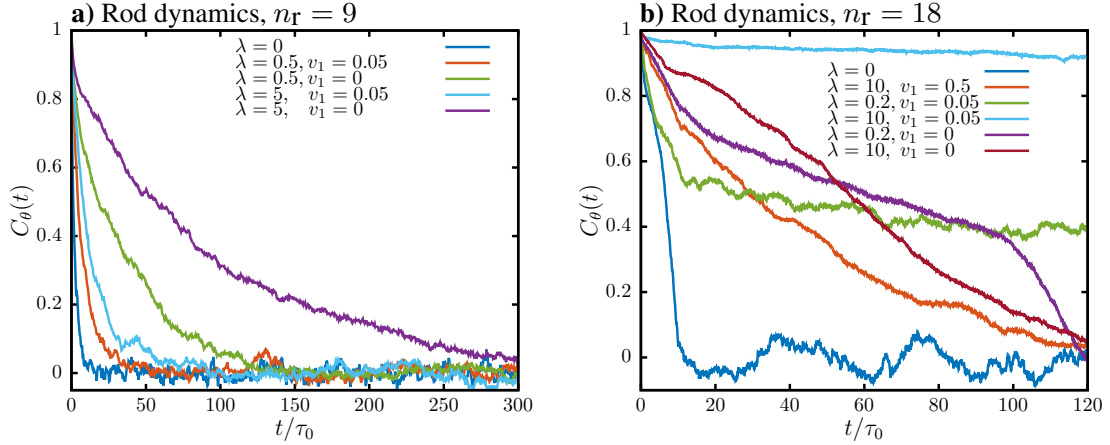


Figure 3.10: Rod orientation autocorrelation function $C_\theta(t)$ versus lag time t . **a)** Systems with $n_r = 9$, $\rho_0 L_r^2 = 6.4$, $E_r/k_B T = 5$, $Pe = 100$, for various values of λ and v_1 . **b)** Systems with $n_r = 18$, $\rho_0 L_r^2 = 12.8$, $E_r/k_B T = 5$, $Pe = 400$, for various values of λ and v_1 . Figure reproduced from publication (B) Ref. [179] with permission from the American Physical Society ©2018 American Physical Society.

respect to the borders. Asters and stationary clusters, in general, are typically not observed for classical SPRs. Round clusters have earlier been reported for rough SPRs that interlock [164]. For our asters and stripes ($v_1 = 0$), the alignment is caused by the locally dense packing and the rod-rod steric interactions.

3.6 Rod dynamics

So far we have only described the structure of clusters and interfaces. To study rod dynamics, we calculate the rod orientation autocorrelation function

$$C_\theta(t) = \langle \mathbf{l}_i(t' + t) \cdot \mathbf{l}_i(t') \rangle, \quad (3.4)$$

“where $\mathbf{l}_i(t')$ is the orientation vector of rod i at time t' , and t is the lag time.”

Due to the density-dependent interaction, rods will slow down when they sense other neighboring rods. “For rods with $n_r = 9$ beads, the rod orientation autocorrelation function decreases exponentially $C_\theta(t) = e^{-t/\tau}$ where τ is the relaxation time, see Fig. 3.10a. $C_\theta(t)$ decorrelates more slowly as λ increases and v_1 decreases. But v_1 has a stronger effect in the reduced propulsion of the autocorrelation function than λ , compare the curves for clusters with domains ($v_1 = 0.05$) with the curves for round clusters and stripes ($v_1 = 0$).”

“For systems of rods with $n_r = 18$, $C_\theta(t)$ is not always an exponentially decreasing function, see Fig. 3.10b. The functional form of the $C_\theta(t)$ strongly depends on the structure formed by the rods. For the clustered nematic (CN) phase ($\lambda = 0$), the rod orientation quickly becomes uncorrelated. For systems with density-dependent reduced

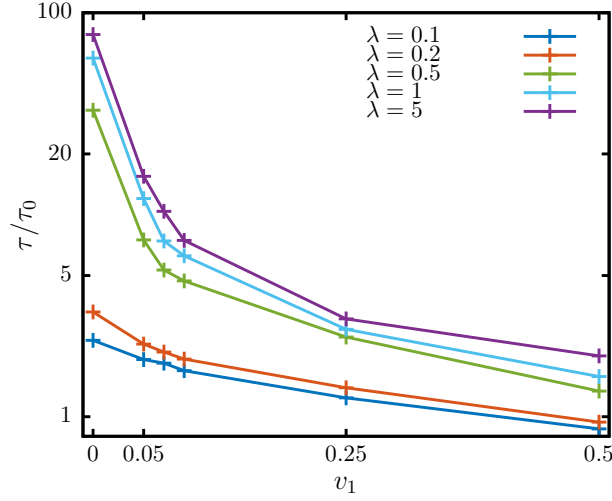


Figure 3.11: Exponent of the rod orientation autocorrelation fit τ versus the weight of the base propulsion v_1 . Systems with $n_r = 9$, $\rho_0 L_r^2 = 6.4$, $E_r/k_B T = 5$, $Pe = 100$, for various values of λ . Figure reproduced from publication (B) Ref. [179] with permission from the American Physical Society ©2018 American Physical Society.

propulsion, $C_\theta(t)$ decorrelates more slowly. The density-dependent reduced propulsion slows down rod dynamics, thus slowing down the relaxation of the orientation autocorrelation.” In polar bands (PB, $\lambda = 10$, $v_1 = 0.05$), the perpendicular rods at the border stabilize the bands and $C_\theta(t)$ roughly remains constant. For small polar clusters (PC, $\lambda = 10$, $v_1 = 0.5$), $C_\theta(t)$ decorrelates slowly. “For polar hedgehog clusters ($\lambda = 0.2$, $v_1 = 0.05$), $C_\theta(t)$ decorrelates quickly to a finite value, $C_\theta(t \gg \tau_0) \simeq 0.4$. Polar hedgehog clusters are dynamic at short times, rods can wiggle, but the perpendicular rods at the cluster borders stabilize the overall orientation. For asters (As) with small λ ($\lambda = 0.2$, $v_1 = 0$), $C_\theta(t)$ shows three linear regimes. A first regime with a fast decay, corresponding to single-rod dynamics in the dense region; a second slow decay, corresponding to rod collective behavior inside the aster; a third fast decay, corresponding to long-time behavior once the rod exits the aster. For asters (As) with large deceleration ratio ($\lambda = 10$, $v_1 = 0$), very few rods escape the asters. This leads to two decay regimes: a first quick decay, corresponding to single-rod dynamics in the dense region, and a second slow decay, corresponding to collective rod dynamics inside the aster.”

“For rods with $n_r = 9$ beads, the relaxation time τ increases with increasing λ and with decreasing v_1 , see Fig. 3.11.” For round clusters, small polar clusters and clusters with domains with small deceleration ratio ($\lambda \leq 0.2$), τ decreases at a constant rate. For stripes, clusters with domains and small polar clusters with large deceleration ratio ($\lambda \geq 0.2$), we find two different decays. For $v_1 < 0.09$, τ decreases sharply, whereas for $v_1 > 0.09$, τ decreases slowly. For systems with small v_1 the density-dependent reduced propulsion force is more pronounced, which leads to a sharp decrease in the rod dynamics

Chapter 4

Self-propelled complex rigid rings

The results of this chapter have been published in (A) (see list of publications on page 143), the text is reproduced with permission from the Royal Society of Chemistry. All verbatim quotes within this chapter are quotations of (A) and are indicated as “ ... ”. Such verbatim quotes can extend over several pages.

As a first step towards building a model for cell motility, we study complex self-propelled rigid rings. The self-propelled rings are composite particles made of passive rings, which have self-propelled rods on the inside. Here, we use self-propelled rods as a coarse-grained model for the cytoskeletal filaments involved in cell motility, such as actin filaments and actomyosin fibers. In experiments with crawling cells, it has been found that there are pushing forces at the front of the cell and retraction forces at the back [58, 117, 120]. The pushing forces are caused by actin polymerization at the leading edge of the lamellipodium, and the retraction forces are caused by stress fibers. In our systems, the pushing forces found at the edge of the cell are modeled using either attached pushing rods or non-attached rods. The retraction forces found at the back of crawling cells are modeled using attached pulling rods. Depending on the rod propulsion force, energy barrier, and penetrability coefficient the rod organization and dynamics will vary. These changes in the rings internal structure lead to rich motility patterns and dynamics. Here, we show that a minimal mechanistic model can capture the main motility patterns observed in cells.

In this chapter, we perform Brownian dynamic simulations with both mobile and stationary rings. We first quantify the rod self-organization and dynamics inside stationary rings. There are three main rod dynamics observed: circling in one direction, circling in both directions, and clustering. To quantify the rod self-organization, we use the polar order parameter. To quantify the rod dynamics, we use the orientation autocorrelation function. The second part of this chapter consists in studying the motility of the mobile rings. We correlate the different types of rod dynamics observed for stationary rings with the different types of ring motion: random motion, ballistic motion, circling, run-and-tumble, and run-and-circle motion.

”The systems studied in this chapter have rod numbers $N_r = 16, 40$ and 64 . Lengths are measured in units of rod length L_r , energies in units of $k_B T$, and times in units of $\tau_0 = 1/D_{r0}$, where D_{r0} is the rod rotational diffusion coefficient. The ring radius is $R_m = 5.6L_r$ and number of beads for each rod is $n_r = 9$. The energy barrier for rod-ring

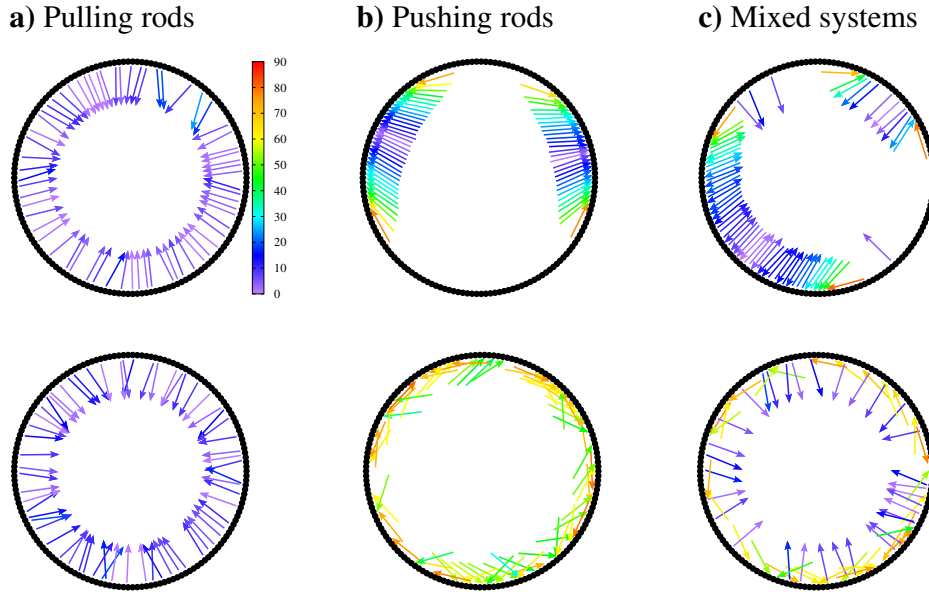


Figure 4.1: "Snapshots for $N_r = 64$ self-propelled attached rods inside stationary rigid rings with $Pe = 100$. The direction of the arrows represent the direction of propulsion. In mixed systems half the rods are pushing rods and half the rods are pulling rods. The rods are colored according to their orientation with respect to the radial direction; if the radial angle is 90° the rod is tangential to the ring and if the angle is 0° the rod is normal to the ring. In the upper row $E_r/k_B T = 10$ and $Q = 10$, and in the bottom row $E_r/k_B T = 1$ and $Q = 100$." Figure reproduced from publication (A) Ref. [141] with permission from the Royal Society of Chemistry.

interaction is $E_m = 250k_B T$, which prevents rods from escaping from the ring. The FENE potential spring length is $b_F = 0.28L_r$ and the spring stiffness is $k_F = 8k_B T/L_r^2$. The parameters used in our simulations are rod Péclet number $25 \leq Pe \leq 100$, rod energy barrier $k_B T \leq E_r \leq 10k_B T$, rod penetrability ratio $2.5 \leq Q \leq 100$, ring inverse overlap $0.2 \leq \zeta \leq 0.5$, and viscosity $\eta = 0.005k_B T\tau_0/L_r$."

4.1 Internal structure and rod dynamics of stationary rings

The rod organization inside the ring will dictate the overall ring motion, e.g., rings in which rods cluster very easily will move persistently. This means that isolating and analyzing the internal rod ordering and dynamics observed in stationary rings will be a crucial factor in studying the ring motion patterns. Once we know how the rods organize themselves, we will then be able to correlate the structures formed by the rods with the ring motion.

As stated before, in this chapter we consider three different types of rods: non-

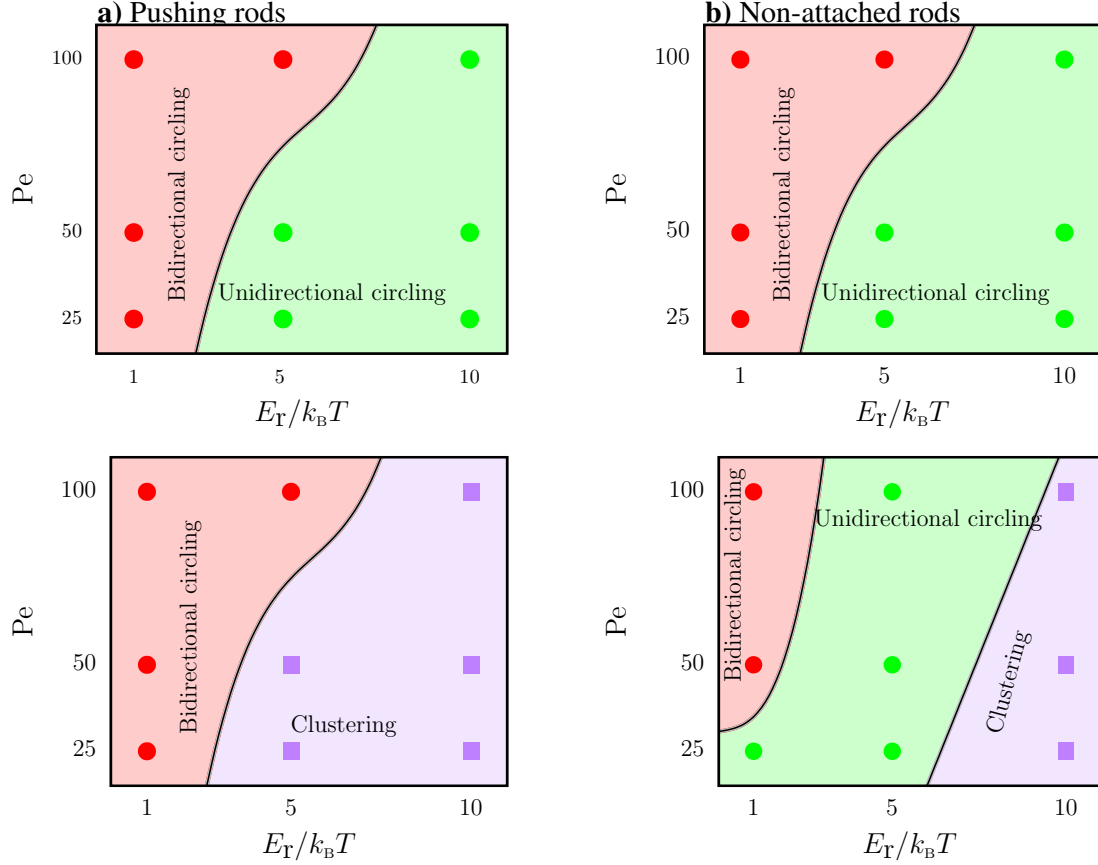


Figure 4.2: "Phase diagrams for self-propelled rods inside stationary rigid rings for various values of the energy barrier E_r and Péclet number Pe . Red circles represent systems with bidirectional circling of rods (clockwise and counter-clockwise), green circles represent systems with unidirectional circling of rods (clockwise or counter-clockwise), and purple squares represent systems with rod clusters, both stationary and mobile. The figures in the top row are for $N_r = 16$ and $\zeta = 0.2$, those in the bottom row for $N_r = 64$ and $\zeta = 0.2$." Figure reproduced from publication (A) Ref. [141] with permission from the Royal Society of Chemistry.

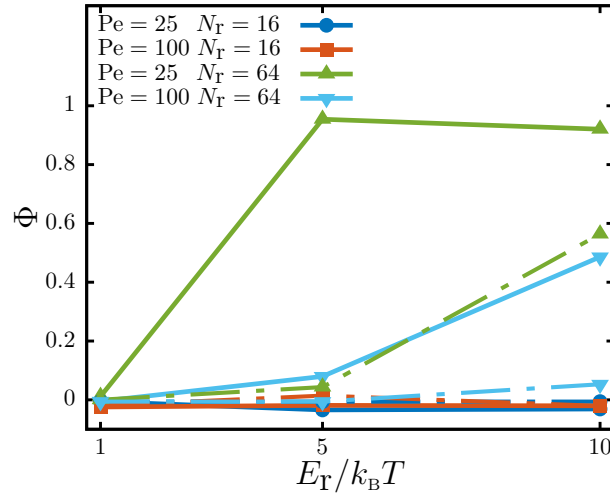


Figure 4.3: "Polar order parameter Φ versus energy barrier E_r , for various values of N_r and Pe . Stationary ring with $\zeta = 0.2$. Solid lines indicate polar order parameters for attached rods and dashed lines for non-attached rods." Figure reproduced from publication (A) Ref. [141] with permission from the Royal Society of Chemistry.

attached rods attached pushing rods and attached-pulling rods. For the stationary rings, we compare the results for non-attached rods and attached pushing rods, since both of them lead to pushing forces. "The structure of the rods inside a stationary ring depends on rod density, Péclet number, rod-ring attachment, and energy barrier, see Fig. 4.1. For both, attached pushing rods and non-attached rods, we observe three different rod dynamics inside the ring: unidirectional circling, bidirectional circling, and clustering, see Fig. 4.1. The regimes in which these internal phases exist are shown in the phase diagrams in Fig 4.2. Bidirectional circling exists for systems with high penetrability coefficients $Q \geq 20$ and $E_r/k_B T \leq 5$ for attached-pushing rods and for non-attached rods. Unidirectional circling is observed when the rods become less penetrable, and rod-crossing is suppressed, for $Q \leq 20$ for attached-pushing rods and non-attached rods. By increasing E_r further, the rods become impenetrable and consequently cluster. For all systems, rods cluster more easily when Q decreases and N_r increases."

To analyze the alignment of the rods inside the ring, the polar order parameter is employed, see Eq. 3.3 in Sec. 3.3. "Figure 4.3 shows that systems with equal numbers of attached-pushing rods have higher values of the polar order parameter for the same energy barriers and rod densities compared with non-attached rods. In case of attachment, the rods are more confined because they effectively move in one dimension. This is why attached-pushing rod systems with $N_r = 64$ already cluster for $Q \leq 20$, $E_r/k_B T \geq 5$ in Fig. 4.3. For $N_r = 64$ and $Pe = 25$, the polar order parameter for attached-pushing rods is non-monotonic for increasing energy barrier: Φ increases as $E_r/k_B T$ increases from 1 to 5, but slightly decreases as $E_r/k_B T$ increases further. For non-attached rods, the rods only cluster for systems with $N_r = 64$, $Pe = 25$ and

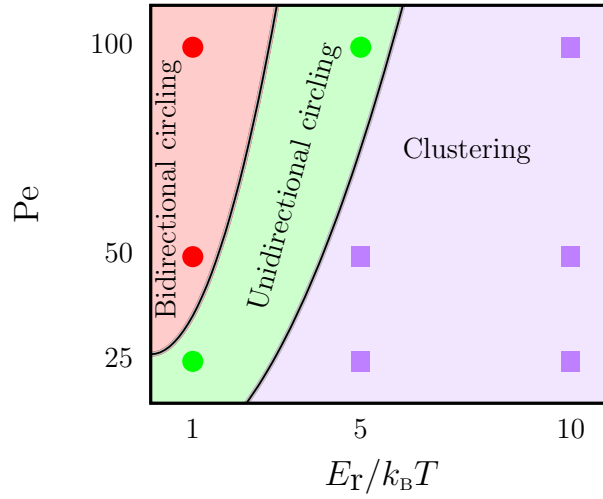


Figure 4.4: "Phase diagram for self-propelled non-attached rods inside stationary rings for various values of the energy barrier E_r and Péclet number Pe , for systems with $N_r = 64$ rods inside a stationary ring with $\zeta = 0.5$." Figure reproduced from publication (A) Ref. [141] with permission from the Royal Society of Chemistry.

$E_r/k_B T = 10$."

Attached-pulling rods orient themselves perpendicular to the ring, see Fig. 4.1. This is an effect of the strong repulsion between the rod and the ring. The bead of the rod closest to the ring, not only feels a strong repulsive interaction with the bead of the ring which is attached to but also to the neighboring ring beads. This means that energetically it is more favorable for the rods to be oriented perpendicular to the ring. Because of this, pulling rods have small tangential velocities, which means that pulling rods in stationary rings stay in the configuration in which they are initialized, i.e., random configuration. For attached pulling rods in stationary rings, there are no different phases and $\Phi \approx 0$.

"Another parameter that influences the collective behavior of the rods is the roughness of the ring. The roughness of the ring is directly related to the ring inverse overlap ζ , for a more detailed explanation see Sec. 2.7. As ζ increases, the separation between the ring beads increases. This leads to a larger friction between the rods and the ring. Thus the tangential velocity of the rods that are sliding along the ring decreases, see Fig. 2.4. For $\zeta = 0.5$, clustering occurs already for penetrability ratios $Q \leq 10$, while for smooth rings, $\zeta = 0.2$, clustering only occurs only for $Q \leq 5$, compare the phase diagrams in Fig. 4.4 and the bottom right diagram in Fig. 4.2. The boundary between bidirectional circling and unidirectional circling remains unchanged for smooth and rough rings. For systems with attached rods, we find that ζ does not play a major role in the inner structure of the complex ring."

The polar order parameter is also affected by the ring roughness, see Fig. 4.5. For intermediate energy barrier, $E_r/k_B T = 5$, the rods transit from unidirectional circling to a cluster if ζ increases from 0.2 to 0.5. The cluster formation causes an increase of the polar order parameter. Once the rods are impenetrable $E_r/k_B T = 10$, the polar

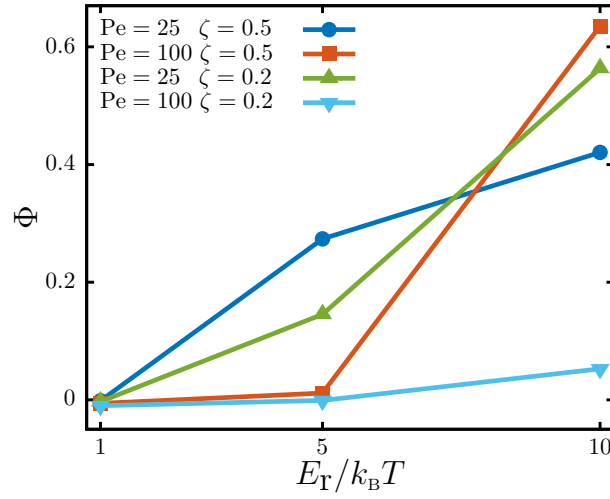


Figure 4.5: "Polar order parameter Φ versus energy barrier E_r , for various values of N_r and Pe . Stationary ring with $\zeta = 0.5$ and $N_r = 64$ non-attached-rods." Figure reproduced from publication (A) Ref. [141] with permission from the Royal Society of Chemistry.

order parameters for rods inside smooth and rough rings are similar for systems with $Pe = 100$. For smooth rings $\zeta = 0.2$ and rods with $Pe = 25$, the rods circle, whereas for rough rings $\zeta = 0.5$ the rods cluster.

So far, we have only analyzed rod organization, but we have yet to discuss the rod dynamics. The rod dynamics can be characterized using the rod orientation autocorrelation function, see Eq. 3.4 in Sec. 3.6. "For periodic systems, the period of the circular motion of the rods inside the ring is

$$T = \frac{2\pi R_m \mu}{\mathbf{F}_r \cdot \mathbf{e}_t}, \quad (4.1)$$

where R_m is the ring radius, \mathbf{F}_r is the rod propulsion force, \mathbf{e}_t is the unit vector along the tangential direction of the ring, and μ is the effective friction between rods and ring. The period T can also be extracted from the orientation autocorrelation functions, see Fig. 4.6."

"Figures 4.6a and b show orientation autocorrelation functions for circling attached-pushing rods and for clustering attached-pushing rods, respectively. Figures 4.6c and d show the analogous autocorrelation functions for non-attached rods. The error bars are calculated using the standard deviations for the averages over both time and rods."

"For circling rods, the orientation autocorrelation function oscillates with a constant period, and its amplitude decays with time, see Figs. 4.6a and 4.6c. The period for non-attached rods, Fig. 4.6c, is roughly the same as the one for attached-pushing rods, see Tab. 4.1. Thus, the attachment of the rods to the ring does not affect the rod tangential velocity, but it does affect the speed at which rod orientation decorrelates, see Tab. 4.1. The amplitudes of the orientation correlation functions for non-attached rods decay more quickly than for attached-pushing rods. This difference in the speed

4.1 Internal structure and rod dynamics of stationary rings

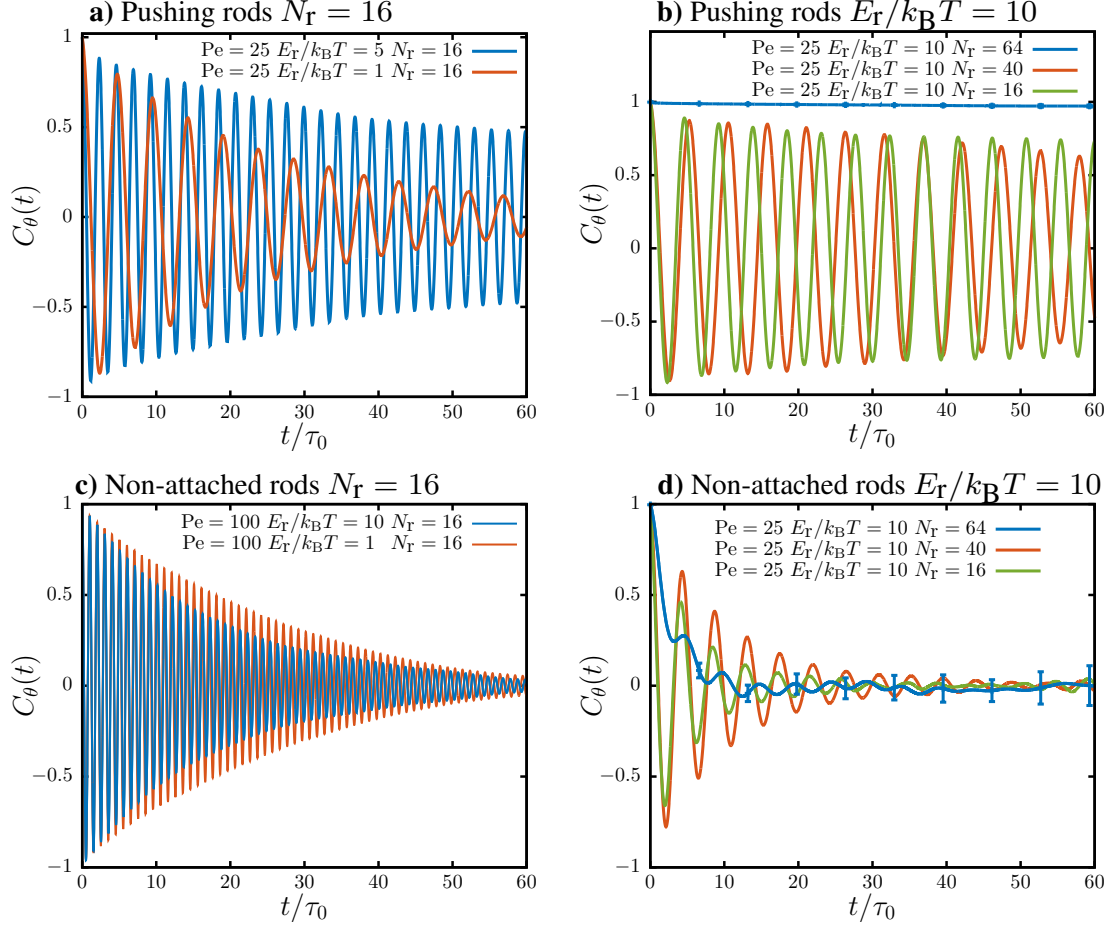


Figure 4.6: "Rod orientation autocorrelation function $C_\theta(t)$ versus lag time t , for various values of N_r , Pe and E_r . Stationary ring with $\zeta = 0.2$. **a)** Attached-pushing rods with $N_r = 16$ and $Pe = 25$. **b)** Attached-pushing rods with $Pe = 25$ and $E_r/k_B T = 10$. **c)** Non-attached rods with $N_r = 16$ and $Pe = 100$. **d)** Non-attached rods with $Pe = 25$ and $E_r/k_B T = 10$." Figure reproduced from publication (A) Ref. [141] with permission from the Royal Society of Chemistry.

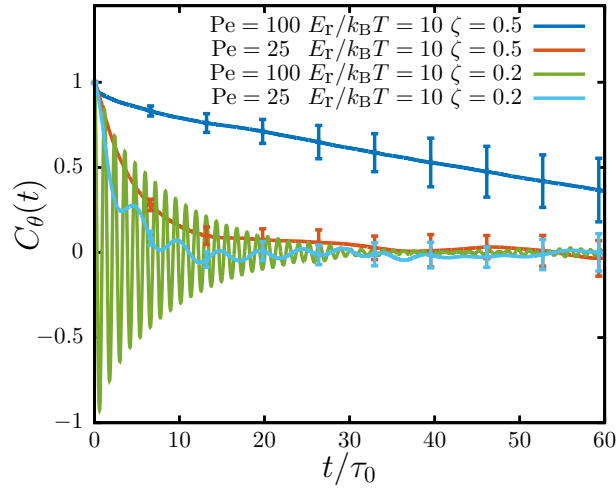


Figure 4.7: "Orientation autocorrelation function of non-attached rods $C_\theta(t)$ versus lag time t , for various values of Pe and ζ . Systems with $E_r/k_B T = 10$." Figure reproduced from publication (A) Ref. [141] with permission from the Royal Society of Chemistry.

of the decorrelation happens because non-attached rods slide and jump along the ring while attached rods can only slide. Systems where rods cluster show no periodic motion. Stationary clusters are observed for $E_r/k_B T = 10$ and $Pe = 25$ and $N_r = 64$, see Fig. 4.6b. Dynamic clusters are observed for $E_r/k_B T = 10$, $Pe = 25$ and $N_r = 64$ for non-attached rods, see Fig. 4.6d. While stationary clusters lead to a very slow decay of the orientation autocorrelation function, dynamic clusters show a rapid exponential decay overlaid with a sinusoidal dependence."

"The orientation autocorrelation function for all circling rod systems, both unidirectional and bidirectional, and for the dynamic-cluster systems shown in Fig. 4.6, have been fitted using

$$C_\theta(t) = e^{(-t/\tau)} \cos(t/T), \quad (4.2)$$

where t is the lag time, τ is the relaxation time, and T is the period. The exponential function accounts for the relaxation of the amplitude, and the sinusoidal function accounts for the periodicity of the circling. The results from these fits are shown in Tab. 4.1. For some of the systems with attached-pushing rods, no periodic motion is observed, whereas non-attached rods always show periodic motion."

"Although the period does not change with increasing roughness of the ring, some systems which show periodic motion for smooth rings, $\zeta = 0.2$, show no periodic motion for rough rings, $\zeta = 0.5$. This means that as the ring roughness increases the rods transit from unidirectional or bidirectional circling to clustering. Figure 4.7 shows orientation autocorrelation functions for systems with non-attached rods, $\zeta = 0.2$ and 0.5 , and $Pe = 25$ and 100 . For rods with $Pe = 25$ the systems transit from dynamic clusters towards more stationary clusters with increasing ζ . Therefore, autocorrelation functions for $\zeta = 0.5$ decay more slowly than for $\zeta = 0.2$; the relaxation times increase from $\tau_{ns} = 2.57\tau_0$ to $\tau_{nr} = 5.27\tau_0$, see Tab. 4.1. The dependence on the roughness

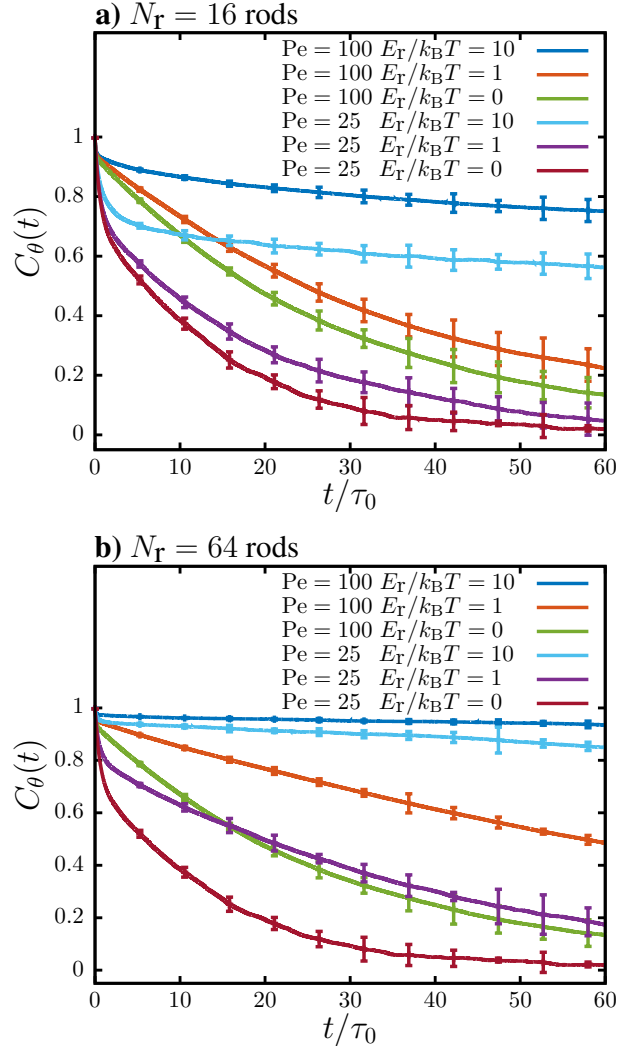


Figure 4.8: "Rod orientation autocorrelation $C_\theta(t)$ versus lag time t , for attached-pulling rods. **a)** Systems with $N_r = 16$, **b)** systems with $N_r = 64$. Error bars are calculated using the standard deviation of the average over time and rods for each system." Figure reproduced from publication (A) Ref. [141] with permission from the Royal Society of Chemistry.

Self-propelled rigid rings

| N_r | Pe | $E_r/k_B T$ | T_{as} | T_{ar} | T_{ns} | T_{nr} | τ_{as} | τ_{ns} | τ_{nr} |
|-------|-----|-------------|----------|----------|----------|----------|-------------|-------------|-------------|
| 16 | 25 | 1 | 4.79 | 4.91 | 3.78 | 3.95 | 23.46 | 4.53 | 7.38 |
| | | 10 | 4.62 | 4.72 | 4.14 | 4.29 | - | 5.52 | 8.18 |
| | 100 | 1 | 1.07 | 1.12 | 1.01 | - | - | 24.76 | - |
| | | 10 | 1.12 | 1.21 | 1.02 | 1.06 | - | 17.1 | 23.6 |
| 64 | 25 | 1 | 5.51 | 5.61 | 4.07 | 4.15 | 10.28 | 5.53 | 7.84 |
| | | 10 | - | - | 4.69 | - | - | 2.57 | 5.27 |
| | 100 | 1 | 1.13 | 1.15 | 1.04 | 1.08 | - | 15.49 | 20.37 |

Table 4.1: "Time periods extracted from the autocorrelation functions for rod orientation for systems with attached-pushing and non-attached rods with $Pe = 25$ and 100 , $E_r/k_B T = 1$ and 10 , and $N_r = 16$ and 64 . The periods T_{as} and T_{ar} are for attached-pushing rods in smooth and rough rings, respectively. The periods T_{ns} and T_{nr} are for non-attached rods in smooth and rough rings, respectively. The relaxation time τ_{as} characterizes the decorrelation for attached-pushing rods in a smooth ring, τ_{ns} for non-attached rods in a smooth ring, and τ_{nr} for non-attached rods in a rough ring. All time-related quantities are given in units of the single-rod relaxation time τ_0 . Systems for that no period is given do not show periodic motion." Table reproduced from publication (A) Ref. [141] with permission from the Royal Society of Chemistry.

of the rings is even more pronounced for systems with high Pe . For a smooth ring with $\zeta = 0.2$ and $Pe = 100$, a circling cluster is observed, and the envelope of the oscillating autocorrelation function decays quickly. For a rough ring with $\zeta = 0.5$, the cluster is more stationary, and a slow decay of the orientation autocorrelation function is observed."

Attached-pulling rods inside stationary rings show no phase transition. They always distribute randomly. The pulling rod dynamics show a dependence on the Péclet number, energy barrier and penetrability coefficient. "Figure 4.8 shows orientation autocorrelation functions for $N_r = 16$ and 40 interacting and non-interacting attached-pulling rods in smooth rings. The rod orientation decorrelates faster for lower rod

| E_r | N_r | Pe | a | b | c | τ_1/τ_0 | τ_2/τ_0 |
|---------|-------|-----|--------|-------|---------|-----------------|-----------------|
| 0 | - | 25 | 0.254 | 0.743 | 0.003 | 0.464 | 14.551 |
| | | 100 | 0.0563 | 0.906 | 0.036 | 0.069 | 27.41 |
| $k_B T$ | 16 | 25 | 0.27 | 0.721 | 0.005 | 0.60 | 21.5 |
| | | 100 | 0.051 | 0.887 | 0.061 | 0.0612 | 35.016 |
| | 64 | 25 | 0.1963 | 0.845 | -0.041 | 0.50 | 44.0 |
| | | 100 | 0.049 | 1.045 | -0.0949 | 0.0934 | 102.800 |

Table 4.2: "Fit parameters obtained using Eq. (4.3) for the data shown in Fig. 4.8." Table reproduced from publication (A) Ref. [141] with permission from the Royal Society of Chemistry.

4.2 Internal structure of mobile rings

density, smaller E_r , and lower Pe . We fit the orientation autocorrelation function using

$$C_\theta(t) = ae^{-t/\tau_1} + be^{-t/\tau_2} + c, \quad (4.3)$$

where τ_1 , and τ_2 are relaxation times. For non-interacting systems, $E_r = 0$, the decorrelation speed depends on Pe . For systems with $Pe = 25$, there are two degrees of freedom for the rods, the orientation of the rods and the position within the ring. For systems with $Pe = 100$, the rods tend to remain attached to the same bead of the ring throughout the simulation. Thus there is effectively only one degree of freedom." The values obtained from the fit of the pulling rods autocorrelation functions can be found in Tab. 4.2.

4.2 Internal structure of mobile rings

We now allow the rings to move. This way not only can we study how the self-propelled rod organization induces overall motion, but we can also analyze motility induced ordering. The relation between rod self-organization and ring motility is a feedback loop: rod clustering leads to ring motion, and ring motion induces rod clustering. "Mobile rings with confined self-propelled rods can both translate and rotate. Figure 4.9 shows snapshots for the inner structure of the ring, kymographs that characterize the rod density along the ring for each time step, and trajectories of the ring center. We find three major dynamic phases: random walks, persistent motion, and circling." To analyze the rod density inside the ring at different time steps we use kymographs. The kymographs are circular plots, where the radial axis represents the time axis, and the tangential axis represents the angular axis. The circumference with the smallest radius indicates the first time step, and the circumference with the largest radius indicates the last time step of the simulation. For a certain time step, certain radius in the kymograph, the tangential axis indicates the angular rod position along the ring. The color indicates the rod density along the ring: dark colors represent small rod densities, and bright colors represent large rod densities.

"We classify the motion of the center of the ring as random walk when the persistence length of the trajectory is smaller than the ring radius, and as persistent motion when the persistence length of the trajectory is larger than the ring radius. For random-walk motion, the kymographs show random patterns because the rods are distributed randomly along the ring and circle at all times. For circling motion, the kymographs show spirals because the rods form dynamic clusters that drift in angular direction. For persistent motion, the kymographs show a wedge because the rods form a stationary cluster with respect to the ring. Figure 4.10 shows the dynamic phases of the mobile rings for various E_r and Pe ."

"For attached-pushing rods, we observe random walk motion for systems with penetrable rods, $Q > 10$, see Fig. 4.10a. In these systems, the rods can cross easily and circle bidirectionally; the net force of the rods on the ring is very small. Persistent motion is observed for systems with impenetrable rods, $Q \leq 10$, and $E_r/k_B T = 5$ and 10. In these systems, the rods align and form stationary clusters, which transmit a large net force that propels the ring, see the trajectory in Fig. 4.9c. The direction of the

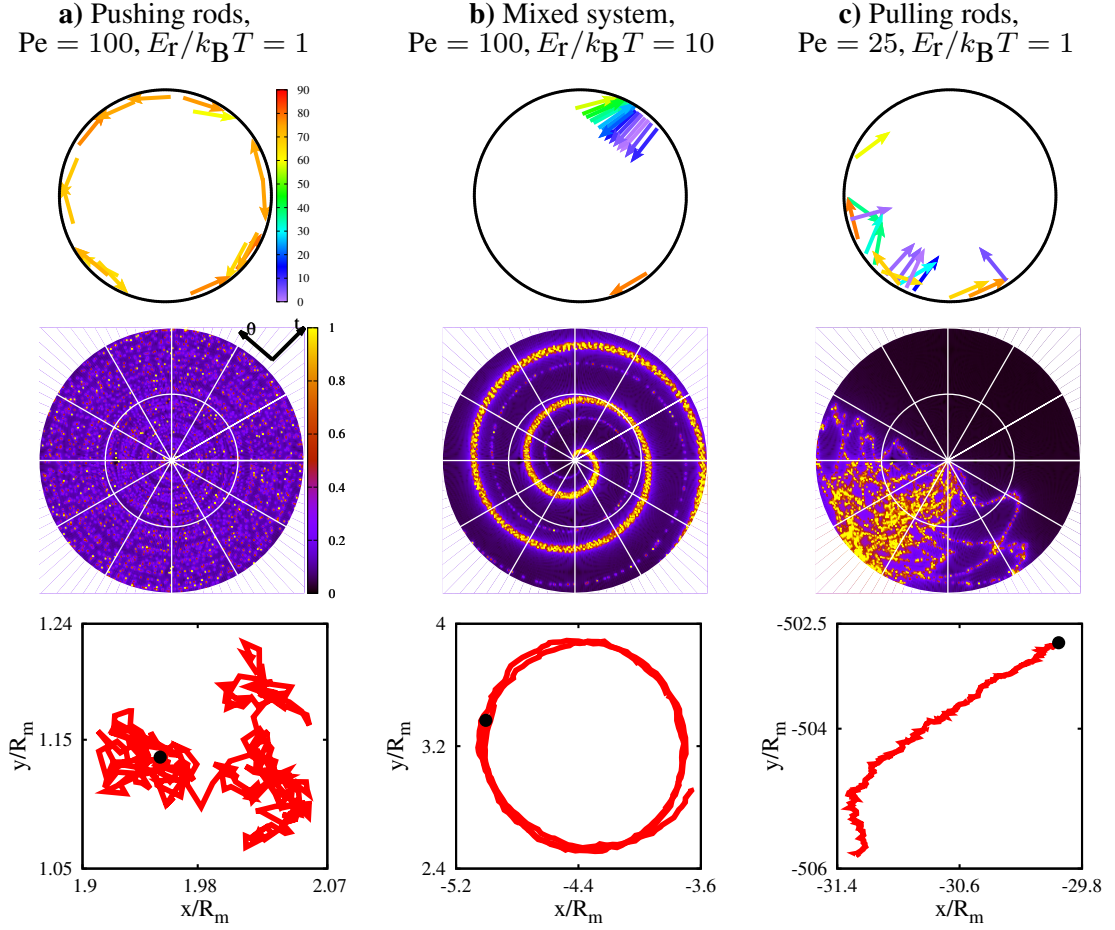


Figure 4.9: "Mobile rings with $N_r = 16$, $\eta = 0.005k_B T \tau_0 / L_r$ and $\zeta = 0.2$. The first row shows snapshots of the inside of the rings at the end of the simulation. Each rod is colored based on its orientation with respect to the radial direction. The middle row shows kymographs of the rods inside the rings, the radial axis represents the time axis, and the tangential axis represents the angular axis. The color indicates the rod density along the ring. The third row shows trajectories of the rings' centers. The final position is represented by a black circle. The rods are colored according to their orientation with respect to the radial direction; if the radial angle is 90 the rod is tangential to the ring and if the angle is 0 the rod is normal to the ring. **a)** Mobile rigid ring with attached-pushing rods. **b)** Mobile rigid ring with mixed rods. **c)** Mobile rigid ring with attached-pulling rods." Figure reproduced from publication (A) Ref. [141] with permission from the Royal Society of Chemistry.

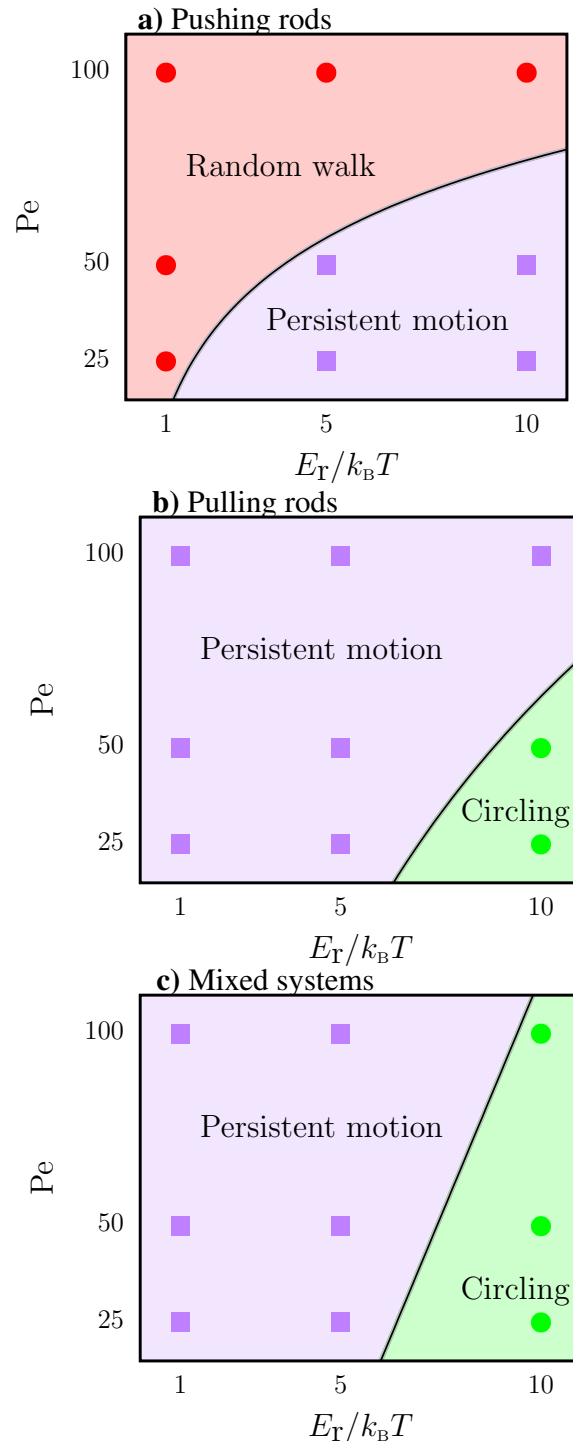


Figure 4.10: "Phase diagrams for complex self-propelled rigid rings for various values of the Péclet number Pe and the energy barrier E_r . Rings with $N_r = 40$ rods, $\eta = 0.005k_B T \tau_0 / L_r$ and $\zeta = 0.2$. Red circles represent systems that show random walk motion, green circles represent systems that circle, and purple rectangles show systems that show persistent motion. In mixed systems, half of the rods are pushing rods, the other half pulling rods." Figure reproduced from publication (A) Ref. [141] with permission from the Royal Society of Chemistry.

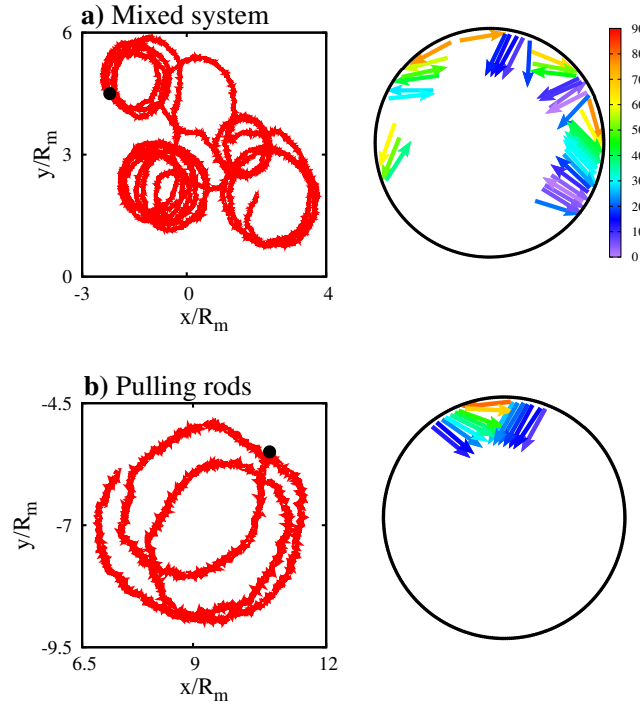


Figure 4.11: "Snapshots and trajectories for circling systems with $\eta = 0.005k_B T \tau_0 / L_r$ and $\zeta = 0.2$. **a)** Mixed system with $N_r = 40$, $Pe = 25$, $E_r/k_B T = 10$, and $Q = 2.5$. **b)** Pulling-rod system with $N_r = 16$, $Pe = 50$, $E_r/k_B T = 10$, and $Q = 5$. The rods are colored according to their orientation with respect to radial direction; if the radial angle is 90° the rod is tangential to the ring and if the angle is 0° the rod is normal to the ring." Figure reproduced from publication (A) Ref. [141] with permission from the Royal Society of Chemistry.

propulsion force of the clusters changes very slowly, thus making the overall motion of the ring very persistent. Some of the random-walk trajectories show run-and-tumble behavior, where the system switches between a motile phase with ballistic segments to a less motile phase with random motion."

"For attached-pulling rods, we observe persistent motion for $Q > 5$, see Fig. 4.10b. For impenetrable rods with high energy barriers and low penetrability coefficients, $E_r/k_B T = 10$ and $Q \leq 5$, the ring centers circle with a nearly constant radii in the range $0.7 R_m \leq R_{\text{circling}} \leq 6.5 R_m$. The circling of the ring happens because the rods exert a constant torque on the ring, which constantly changes the direction of the ring velocity, see Figs. 4.9b and 4.11b. The radius of the trajectory that the center of the ring experiences can be fitted by $R_{\text{circling}} = F D'_t / M D'_r$, [181] where D'_t and D'_r are the effective translational and rotational diffusion coefficients, and F and M are the absolute values of propulsion force and torque of a point particle. Due to the thermal noise that both the rods and the ring experience, the trajectories are not perfect circles. Compared with the rod distribution in stationary rings, the pulling-rod distribution in mobile rings is non-homogeneous. For attached-pulling rods the motility induced

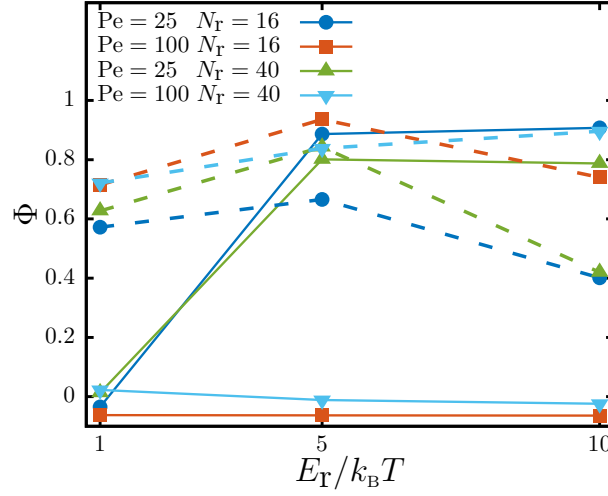


Figure 4.12: "Polar order parameter Φ versus energy barrier E_r , for various values of N_r and Pe . Mobile rings with $\eta = 0.005k_B T \tau_0/L_r$ and $\zeta = 0.2$. Solid lines are for systems with attached pushing rods and dashed lines are for systems with attached pulling rods." Figure reproduced from publication (A) Ref. [141] with permission from the Royal Society of Chemistry.

clustering is crucial for symmetry breaking."

"For mixed systems with both attached-pushing and attached-pulling rods, see Fig. 4.10c, we observe two different phases: persistent motion, and circling. Some of the circling trajectories show a run-and-circle behavior, where the system switches between ballistic segments and circling motion. Circling occurs for impenetrable systems $Q \leq 10$ with large energy barriers $E_r/k_B T = 10$. Persistent motion is observed for more penetrable systems, $Q > 10$ and $E_r/k_B T \leq 5$. Circling motion occurs due to attached-pushing rods pushing against clustered attached-pulling rods, and making the cluster slide along the ring, see Figs. 4.9b and 4.11a. When comparing attached-pulling systems with mixed systems, we find that the addition of attached-pushing rods slightly shifts the boundary between persistent motion and circling. The addition of pushing rods means larger tangential forces, which lead to more circling clusters. This is why the circling motion region is larger for mixed systems than for pulling-rod systems."

"Figure 4.12 shows polar order parameters for systems with $N_r = 16$ and 40 rods. For pushing rods, there is only clustering for systems with $Pe = 25$. For small energy barriers the rods circle bidirectionally, as the rods become more impenetrable with $E_r/k_B T = 5$ and $Q \leq 20$, the polar order parameter increases drastically. The polar order parameter remains constant as $E_r/k_B T$ increases from 5 to 10; this means that once the rods become impenetrable enough, $Q \leq 10$, the effect of E_r on the clusters is very small. Compared with the results for the stationary ring, see Fig. 4.3, the polar order parameter for $N_r = 16$ and large E_r is increased for the systems that show clustering, due to ring motility and ring-mediated rod alignment. It should be noted that the dashed lines represent non-attached rods in Fig. 4.3 and attached-pulling rods in Fig. 4.12."

”In penetrable pulling-rods with $E_r/k_B T = 1$, the polar order parameter Φ is finite, while for attached-pulling rods inside stationary rings Φ vanishes, see Fig. 4.12. For mobile rings, as soon as the rings start moving, the attached pulling rods cluster. This motility induced clustering gives rise to the finite value of the polar order parameter already for $E_r/k_B T = 1$. For intermediate energy barriers with $E_r/k_B T = 5$, the polar order parameters increase slightly, because the rods align within the clusters due to the repulsive interactions between them. For impenetrable rods with $E_r/k_B T = 10$, the polar order parameter decreases because the increased energy barrier causes the rods to thicken and separate from each other, thus making the clusters less compact.”

When we correlate the rod self-organization and dynamics found in Sec. 4.1 with the major dynamic phases found in Sec. 4.2, we find that: unidirectional and bidirectional circling of rods leads to random-walk motion. Stationary clusters, clusters which direction changes slowly, lead to persistent motion. Dynamic clusters which circle along the ring lead to circling motion.

4.3 Active Brownian motion

Although we have qualitatively studied the major dynamic phases observed for the mobile rings, we have yet to quantify the ring motility. In order to do so we analyze the ring dynamics using the mean-squared displacement $\text{MSD}(t) = \langle (\mathbf{r}(t') + t) - \mathbf{r}(t') \rangle^2$ of the position $\mathbf{r}(t)$ of the center of the ring. ”We find a ballistic regime at small and intermediate times $10^{-1.5}\tau_0 < t < 10^{1.5}\tau_0$, and a diffusive regime at long times, see Fig. 4.13. For smaller times than those shown in the plots, the MSD for active systems coincides with the MSD for passive systems, see system with $N_r = 16$, $\text{Pe} = 25$ and $E_r/k_B T = 10$ in Fig. 4.13a and system with $N_r = 40$, $\text{Pe} = 25$ and $E_r/k_B T = 5$ in Fig. 4.13c.”

”For pushing rods, the systems with $\text{Pe} = 25$ reach the second diffusive regime for the displayed time range, see Fig 4.13a. Systems with $N_r = 16$ cluster less easily than systems with $N_r = 40$. The MSD increases with increasing Pe and N_r , see system with $N_r = 40$, $\text{Pe} = 50$ and $E_r/k_B T = 5$. The system with $N_r = 16$, $\text{Pe} = 25$ and $E_r/k_B T = 10$ enters the ballistic regime later than for the rest of the systems and shows all three ABP regimes: diffusive, ballistic, and diffusive.”

”For pulling rods, all of the systems shown in Fig. 4.13b already are in the ballistic regime for the time range shown in the plot. The systems with $\text{Pe} = 100$ have a larger MSD in the ballistic regime and enter the long-time diffusive regime faster, see systems with $N_r = 16$, $\text{Pe} = 100$ and $E_r/k_B T = 10$, and $N_r = 40$, $\text{Pe} = 100$ and $E_r/k_B T = 5$. Overall, pulling rods show a more pronounced ballistic behavior than pushing rods or mixed systems.”

”Mixed systems have lower MSD and enter the long-time diffusive regime earlier than pushing-rod and pulling-rod systems, see Fig. 4.13c. The MSD increases with increasing Pe and N_r , see system with $N_r = 40$, $\text{Pe} = 100$ and $E_r/k_B T = 1$. The systems that enter the long-time regime first at $t \approx 10\tau_0$ are the ones with the most penetrable rods, $Q = 50$ and 100 , see systems with $N_r = 16$, $\text{Pe} = 100$ and $E_r/k_B T = 1$, and $N_r = 16$, $\text{Pe} = 50$ and $E_r/k_B T = 1$.”

We can effectively describe the mean-squared displacement using the ABP model

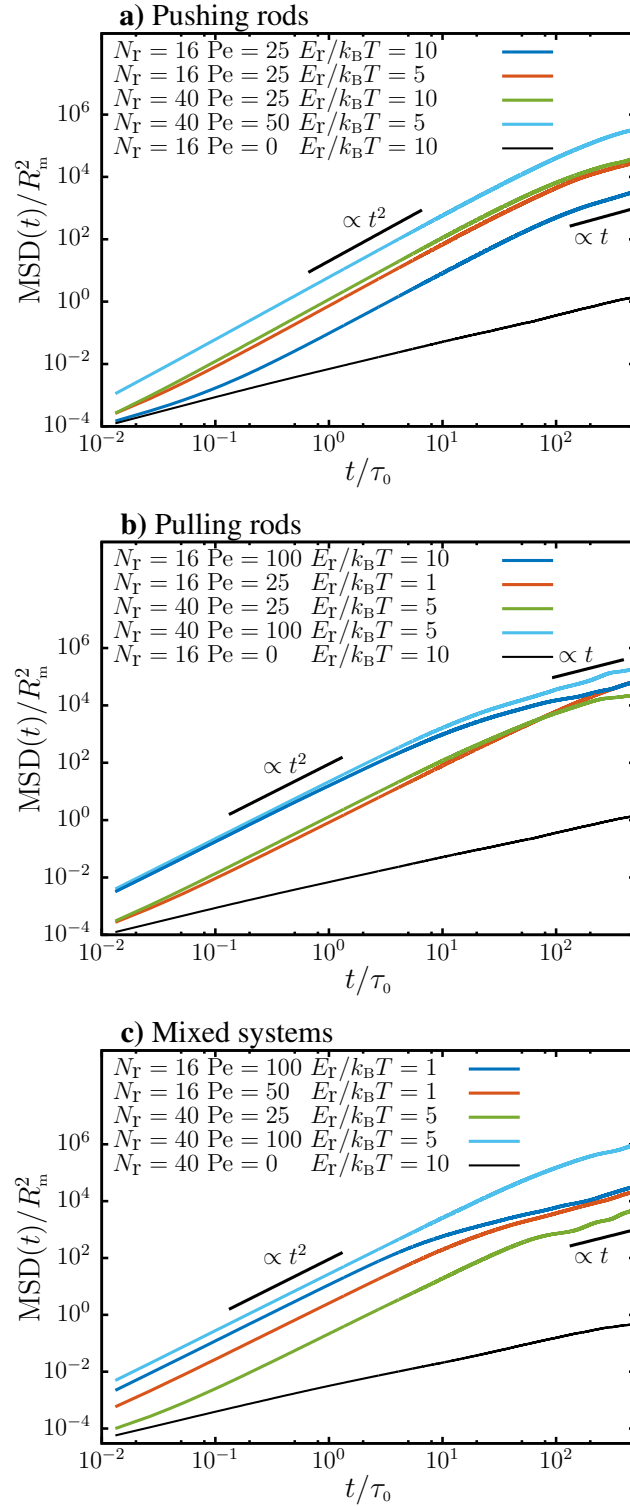


Figure 4.13: "Mean-squared displacement $MSD(t)$ versus lag time t , for various values of N_r , Pe , and E_r . Mobile rings with $\eta = 0.005k_B T\tau_0/L_r$ and $\zeta = 0.2$. **a)** Systems with attached pushing rods. **b)** Systems with attached-pulling rods. **c)** Systems with mixed rods." Figure reproduced from publication (A) Ref. [141] with permission from the Royal Society of Chemistry.

Self-propelled rigid rings

| System | N_r | Pe | $E_r/k_B T$ | $v \tau_0/L_r$ | τ_r/τ_0 | D_{eff}/D_t |
|---------|-------|-----|-------------|----------------|-----------------|----------------------|
| Pushing | 16 | 25 | 10 | 8.06 | 82.88 | 954 |
| | 16 | 25 | 5 | 23.29 | 86.05 | 8266 |
| Pulling | 16 | 100 | 10 | 105.5 | 9.32 | 18378 |
| | 40 | 100 | 5 | 128.51 | 19.36 | 56626 |
| Mixed | 16 | 50 | 1 | 43.87 | 17.38 | 5926 |
| | 16 | 100 | 1 | 90.72 | 6.38 | 9300 |
| | 40 | 25 | 1 | 12.71 | 42.13 | 2636 |

Table 4.3: "Parameters of the ABP model extracted from fits of Eq.2.30 to MSD curves in Fig 4.13. v is the ABP velocity, τ_r is the ABP rotational time, and D_{eff} is the diffusion coefficient for the long-time diffusion regime." Figure reproduced from publication (A) Ref. [141] with permission from the Royal Society of Chemistry.

[18, 139]. A more detailed explanation of the ABP model and its mean-squared displacement can be found in Sec. 2.4. For certain parameter values, our rings show the following types of motion: diffusive motion at short times; ballistic motion at intermediate times; diffusive motion at long times with a larger diffusion coefficient than that of the short-time diffusion. This behavior indicates that mobile rigid rings can be seen as active Brownian disks, where the values for propulsion force and the translational and rotational diffusion coefficients are determined by the rod dynamics and collective behavior.

"By fitting Eq. 2.30 to our MSD data, the values for the propulsion velocity v , the translational diffusion coefficient D_t , the rotational diffusion coefficient D_r , and the effective translational diffusion coefficient D_{eff} for the long-time diffusive regime can be extracted, see Tab. 4.3. D_t and v can be obtained for all simulated systems, as they are extracted from the passive systems and the ballistic regime of the active systems, respectively. τ_r and D_{eff} can only be extracted for systems that have reached the long-time diffusive regime. Depending on the dynamics of the inner structure, the time τ_r needed for each system to reach the diffusive regime at long times can be very long. This happens, in particular, for systems where rods cluster very easily where the $\text{MSD}(t)$ is purely ballistic."

"Pushing rods have the lowest velocities and take longest to reach the long-time diffusive regime, see Tab. 4.3; where we find roughly an order of magnitude difference between the values of v obtained for pushing rods and for pulling rods. All the ABP-like systems are characterized by a $D_{\text{eff}}/D_t \gg 1$ and $\tau_r/\tau_0 \gg 1$, because cluster reorientation and rod collective behavior lead to large D_{eff} ."

4.4 Beyond the active Brownian particle description

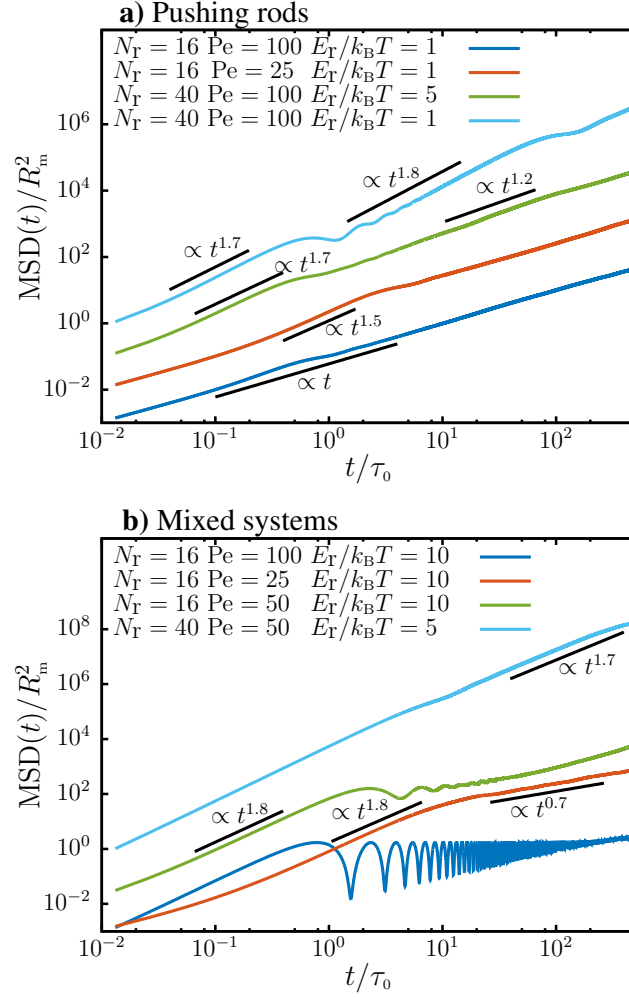


Figure 4.14: "Mean-squared displacement $MSD(t)$ versus lag time t , for various values of N_r , Pe , and E_r . Mobile rings with $\eta = 0.005k_B T\tau_0/L_r$ and $\zeta = 0.2$ that do not behave like active Brownian particles. Each curve has been shifted in the y axis by a factor 10 with respect to the previous curve. **a)** Systems with attached-pushing rods. **b)** Systems with mixed rods." Figure reproduced from publication (A) Ref. [141] with permission from the Royal Society of Chemistry.

4.4 Beyond the active Brownian particle description

”For certain parameter values, the complex self-propelled rings behave as active Brownian disks. However, the self-propelled rods act as internal degrees of freedom beyond those of an ABP. This means that the complex dynamics introduced by the self-propelled rods cannot always be explained by the ABP model, see Fig. 4.14. At short times the MSDs of non-ABP-like rings also coincide with those of passive rings.”

”For pushing rods with $N_r = 16$ no real ballistic regime is observed, see Fig 4.14a. For $N_r = 16$ and $Pe = 100$, the system is diffusive for $t/\tau_0 < 0.1$, there is a slight bump for $0.1 < t/\tau_0 < 1$, and the system becomes diffusive again for $t/\tau_0 > 1$. For the time range of $0.1 < t/\tau_0 < 1$ the system is superdiffusive at the beginning and then subdiffusive, so that the diffusion coefficients for $t/\tau_0 < 0.1$ and $t/\tau_0 > 1$ are roughly the same. For the system with $N_r = 16$ and $Pe = 25$, we observe a similar behavior as for the previous system. However, in this case, the bump is more pronounced, and it happens a bit later in time. We find a superdiffusive regime $t^{1.5}$ for intermediate times $10^{-0.5} < t/\tau_0 < 10^{0.5}$, followed by a subdiffusive regime. Because for this system the superdiffusive regime is more pronounced, the long-time diffusion coefficient is larger than the short-time diffusion coefficient. Both systems consist of $N_r = 16$ penetrable attached-pushing rods, $Q = 100$ and 25 respectively. The rods circle inside the ring, the forces transmitted to the ring are small, and therefore no ballistic regime is observed in the MSD. For pushing rods with $N_r = 40$, although there is still no ballistic regime, we find a superdiffusive regime with $t^{1.7}$. For the system with $N_r = 40$, $Pe = 100$ and $E_r/k_B T = 5$, the long-time regime is also superdiffusive with $t^{1.2}$. The trajectory shows circling at times $t/\tau_0 < 10^{-0.5}$ and a random walk-like behaviour at times $t/\tau_0 > 10^2$, where some segments show circling with drift; this mixture of behaviors leads to the overall superdiffusive MSD for long times. For the system with $N_r = 40$, $Pe = 100$ and $E_r/k_B T = 1$, we observe two superdiffusive regimes, the first for $10^{-1.5} < t/\tau_0 < 10^{-0.2}$, the second for $10^{0.2} < t/\tau_0 < 10^2$. In-between these two superdiffusive regimes, the system circles, this is seen in the MSD plateau at $t/\tau_0 \approx 10^{-0.2}$ and the regular wiggling that comes afterward. The first superdiffusive regime is seen for times shorter than what the ring needs to complete a circle, so although there are segments of persistent motion the motion is not fully ballistic. The trajectory of this system shows two less motile phases, where the ring tumbles, at the beginning and at the end of the trajectory and in-between segments of persistent motion made of circling. The fact that we observe two superdiffusive regimes separated by a plateau indicates that there are two reorientation processes of the rods inside the ring, which lead to several near-ballistic regimes. The overlap between the circling and the second superdiffusive regime shows that these two reorientation processes are not well separated in time.”

”For mixed systems, we also find several superdiffusive regimes and circling, see Fig 4.14b. The system with $N_r = 16$ and $Pe = 100$ has a ballistic regime for $t/\tau_0 < 10^{-0.2}$, right after the MSD plateaus, and it starts oscillating with an initial period of $\approx 1.6\tau_0$. The height at which the MSD plateaus represents the diameter of the circling, in this case, $2R_{\text{circling}} = 1.3R_m$, as shown in Fig. 4.9b. The initial period of the MSD

4.4 Beyond the active Brownian particle description

oscillations represents the time it takes the ring to complete a circle. The system with $N_r = 16$ and $Pe = 25$ has a first diffusive regime followed by a superdiffusive regime for $10^{-1} < t/\tau_0 < 10$, and a long-time subdiffusive regime $t/\tau_0 > 10$, see Fig. 4.15b. The long-time subdiffusive regime is caused by the alternation of a random walk and circling that persists at these times. The system with $N_r = 16$ and $Pe = 50$ has a first superdiffusive regime with $t^{1.8}$ and then circles for $t/\tau_0 > 10^{0.2}$ with a certain drift. The trajectory and kymograph for this system are shown in Fig. 4.15c. For long timescales $t/\tau_0 > 10$, the systems show a drift in the MSD because the ring does not circle in a certain spot but rather it performs a random walk while circling. The system with $N_r = 40$ and $Pe = 100$ has a first ballistic regime for $t/\tau_0 < 10$, and then a superdiffusive regime with $t^{1.7}$ for $t/\tau_0 > 10$. The trajectory shows less motile phases that are separated by long stretches of persistent motion. The long-time superdiffusive behavior is caused by the switching between the more and less motile phases.”

”Thus, the additional degrees of freedom of the rods inside the ring lead to a very rich dynamical behavior. In such cases, a possible explanation is velocity fluctuations, as predicted recently [182].

$$\begin{aligned} \text{MSD}(t) = & 2\langle v \rangle^2 \tau_r^2 \left(\frac{t}{\tau_r} - 1 + e^{-t/\tau_r} \right) \\ & + 2(\langle v^2 \rangle - \langle v \rangle^2) \tau_v^2 \left(\frac{t}{\tau_v} - 1 + e^{-t/\tau_v} \right), \end{aligned} \quad (4.4)$$

where v is the active particle velocity, and τ_r and τ_v are two characteristic timescales of the model, corresponding to the orientation and velocity fluctuations, respectively. This extended ABP model adds two new regimes (a ballistic and a diffusive regime), when the velocity fluctuations are large, i.e. $(\langle v^2 \rangle - \langle v \rangle^2)/\langle v \rangle^2 \gg 1$ and the timescales are well separated. We have calculated the velocity fluctuations in systems that deviate from the ABP behavior and have found them to be negligible. Therefore, although such a model is a step in the right direction, since it introduces more than one process which can lead to several ballistic regimes, velocity fluctuations do not capture the dynamics in our systems.”

”Figure 4.15 shows that our complex self-propelled rings exhibit run-and-circle motion. For attached-pulling rods, the trajectory resembles the run-and-tumble motion of E.coli with long ballistic segments, [154,183] see Fig 4.15a. For mixed attached-pushing and attached-pulling rods, the system circles continuously with small distortions which create a random walk, see Fig.4.15c. The kymograph shows the rod motion inside the ring: the spiral shows the motion of the circling cluster, but there are also some thick light and dark parts which indicate a running segment between the circling.”

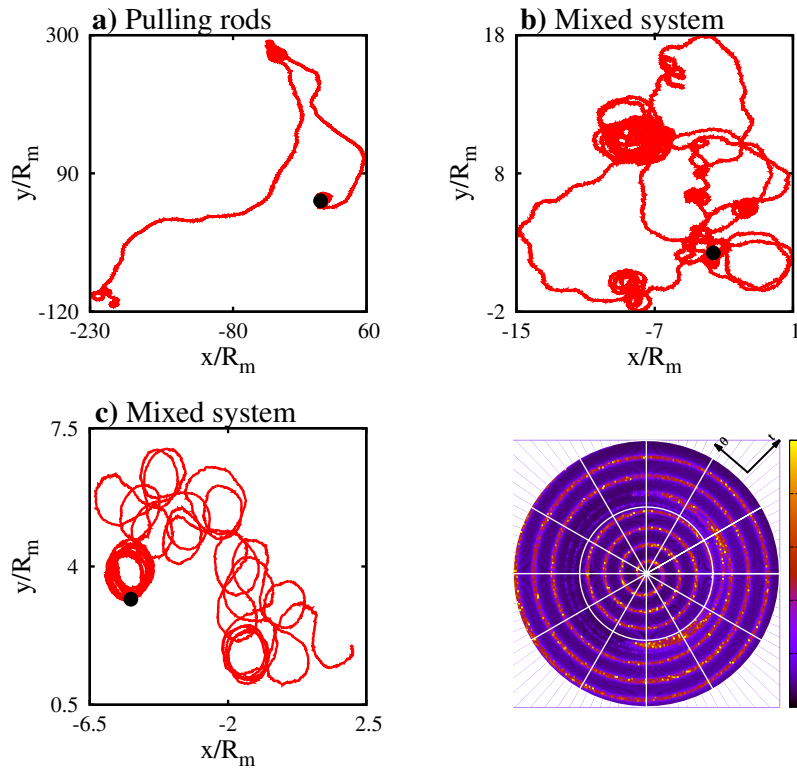


Figure 4.15: "Trajectories and kymograph for different run-and-circle rings with $N_r = 16$, $\eta = 0.005k_B T \tau_0 / L_r$ and $\zeta = 0.2$. **a)** Trajectory for a pulling-rod system with $Pe = 50$, $E_r/k_B T = 10$ and $Q = 5$. **b)** Trajectory for a mixed-rod system with $Pe = 25$, $E_r/k_B T = 10$ and $Q = 2.5$. **c)** Trajectory and kymograph of the rods inside the ring for a mixed-rod system with $Pe = 50$, $E_r/k_B T = 10$ and $Q = 5$. In the kymograph the radial axis represents the time and the tangential axis represents the position at the ring. The color shows the rod density along the ring." Figure reproduced from publication (A) Ref. [141] with permission from the Royal Society of Chemistry.

Chapter 5

Self-propelled complex deformable rings

In this chapter, we extend the rigid-ring model by making the ring deformable. We study and quantify the different shapes that the rings adopt. For systems with small ring friction and large enough rod propulsion, the rings show keratocyte and keratinocyte-like shapes [184, 185], as the ring friction increases the rings adopt neutrophil-like shapes [186], finally for systems with large ring friction and small Péclet number the rings adopt quasi-circular fluctuating shapes. In the first part of the chapter, we correlate ring shape and ring motility, and we find various motility patterns: random motion, ballistic motion, and run-and-circle motion. In the second part of the chapter, we quantify the interaction between a deformable ring and a wall. We compare the results for deformable and rigid self-propelled rings and pulling-rod systems with mixed systems. For rigid rings with attached-pulling rods, the system behaves as an ABP [187]. However, once the ring becomes deformable, the system shows cell-like behavior. Once a keratocyte-like ring hits a wall, it first flattens, and subsequently, a reorientation of the rods occurs. This rod reorientation leads to further shape changes of the ring that finally leaves the wall. The trajectories that we observe for keratocyte-like rings at walls are very similar to trajectories of keratocytes at interfaces between smooth and microgrooved surfaces [188, 189]. In the case of mixed systems, with both pushing and pulling rods, the rings stay at the walls. In the parameter regimes used for our simulations, changing the bending rigidity has little effect on the rings' behavior. In the third and final section of the chapter, we study rings at friction interfaces. We find that as a ring crosses an interface, the ring shape changes, which in turn leads to a deflection of the ring motion. For systems where the ring crosses from a large-friction region to a small-friction region, the ring reorients and follows the interface. In this chapter, we mostly show and discuss results for deformable rings with attached-pulling rods. However, shapes observed for rings with pushing and pulling rods are also briefly discussed.

For the deformable rings, we employ the following dimensionless ring parameters: the dimensionless ring friction $\bar{\gamma}_b = \gamma_b R_m^2 / (k_B T \tau_0)$, which is calculated on a bead basis, the dimensionless bending rigidity $\bar{\kappa} = \kappa / (k_B T R_m)$, the dimensionless compression modulus $\bar{k}_A = k_A R_m^4 / k_B T$, and the dimensionless spring stiffness $\bar{k}_S = k_S R_m^2 / k_B T$.

The systems studied here have rod numbers $N_r = 16, 40$ and 64 . Lengths are measured in units of rod length L_r , energies in units of $k_B T$, and times in units of $\tau_0 = 1/D_{r0}$, where D_{r0} is the rod rotational diffusion coefficient of a free rod. The ring equilibrium radius is $R_m = 5.6L_r$, the ring inverse overlap is $\zeta = 0.2$, and the number of beads for each rod is $n_r = 9$. The energy barrier for rod-ring interaction is $E_m = 250k_B T$, which prevents rods from escaping from the ring. The harmonic potential spring length is $b_H = 0.11L_r$ and the spring stiffness is $k_H = 50k_B T/R_m$. Further parameters used in our simulations are the rod Péclet number $25 \leq \text{Pe} \leq 100$, the attached-pulling rod energy barrier $E_r = E_{r,\text{pull}} = 1k_B T$, the attached-pushing rod energy barrier $E_{r,\text{push}} = 10k_B T$, the ring friction $1 \leq \bar{\gamma}_b \leq 25$, the bending rigidity $0.02 \leq \bar{\kappa} \leq 200$, the compression modulus $1 \leq \bar{k}_A \leq 100$, and the ring spring stiffness $\bar{k}_S = 1000$.

5.1 Deformable rings: phase diagrams and motility

The shapes of deformable rings are tightly correlated with their center-of-mass trajectories. For attached-pulling rods we observe three main shapes – fluctuating, neutrophil-like and keratocyte-like shapes – and three main motility patterns – persistent, random-walk, and run-and-tumble motion –, see Fig. 5.1. As in Sec. 4.2, we classify the motion of the center of the ring as random walk when the persistence length of the trajectory is smaller than the ring radius, and as persistent motion when the persistence length of the trajectory is larger than the ring radius.

In the case of fluctuating shapes (Fl), the rods are distributed homogeneously along the rings. The ring shapes are in general quasi-circular, and active fluctuations are observed. Due to the homogeneous rod distribution, the local forces transmitted to the rings are small. This leads to random-walk motion for the center-of-mass of the deformable ring. For neutrophil-like rings (N-l), the rods induce "triangular" shapes with folds at the backs and curved fronts. Pulling rods at the back of the rings are positioned either at the folds or the sides. The density of pulling rods at the front of the rings is negligible. Neutrophil-like rings show both persistent and run-and-tumble motion. The shapes and some of the motility patterns of our neutrophil-like rings are very similar to the shapes observed for motile neutrophils [186, 190]. Keratocyte-like rings (K-l) have half-circular shapes, curved at the front and flat at the back. Due to motility-induced clustering and the steric interaction between the pulling rods, the rods orient themselves normal to the back of the ring, see Sec. 4.1. The clusters of attached-pulling rods lead to flat ring segments. Compared with neutrophil-like rings, the rods in keratocyte-like rings have larger polar order parameters, since most of the rods point in the same direction. Therefore, the rods also exert larger net forces that propel the rings, which leads to fast persistent motion. The shapes observed for our keratocyte-like systems are very similar to the shapes observed for motile keratocyte and keratinocyte cells [184, 185].

For rigid self-propelled rings, rod clustering leads to ring motility and vice versa. For deformable rings, a new clustering mechanism, the ring deformability comes into

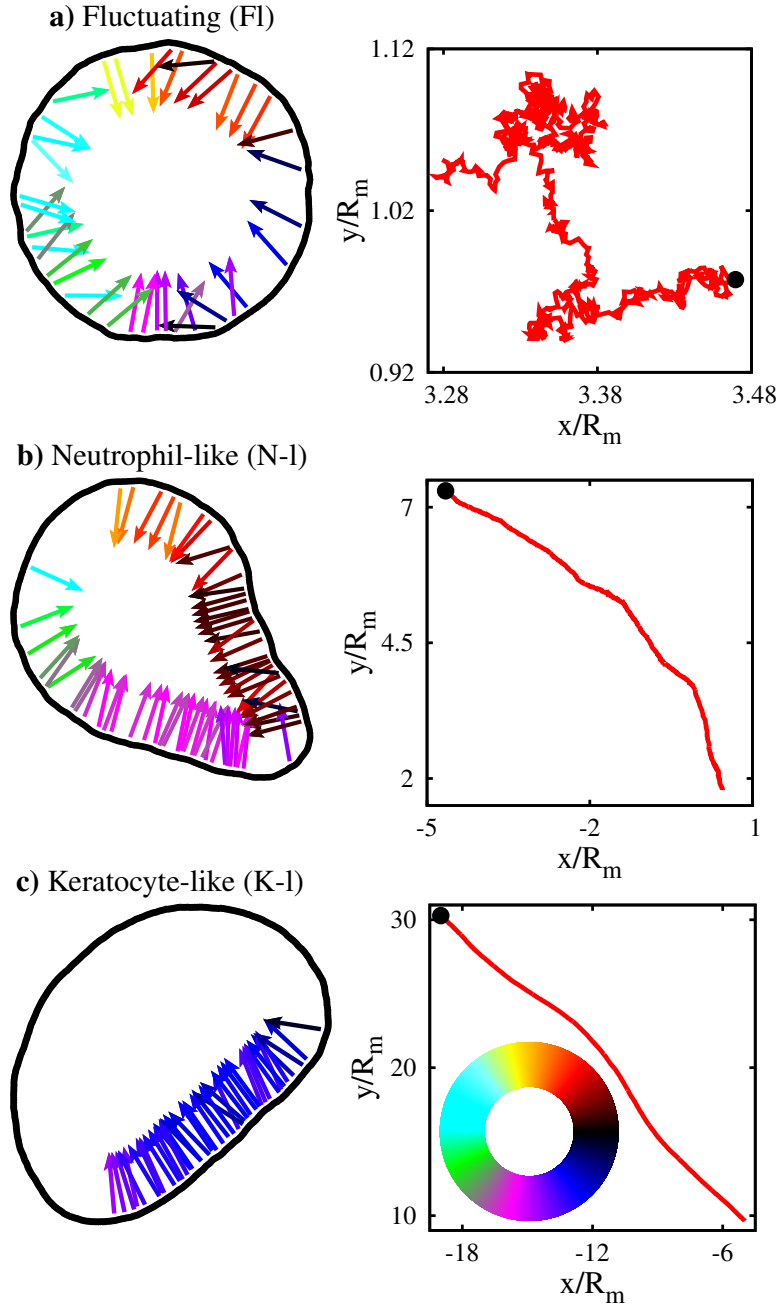


Figure 5.1: Deformable self-propelled rings with attached-pulling rods with $E_r/k_B T = 1$, $\bar{\kappa} = 2$ and $\bar{k}_S = 0.15$. The left column shows snapshots of the rings. The right column shows trajectories of the rings' centers. The final position is represented by a black circle. **a)** Fluctuating ring (Fl), system with $N_r = 40$, $Pe = 10$, $\bar{k}_A = 100$ and $\bar{\gamma}_b = 5$. **b)** Neutrophil-like ring (N-l), system with $N_r = 64$, $Pe = 50$, $\bar{k}_A = 1$, and $\bar{\gamma}_b = 10$. **c)** Keratocyte-like ring (K-l), system with $N_r = 40$, $Pe = 100$, $\bar{k}_A = 100$ and $\bar{\gamma}_b = 1$. Color wheel that indicates rod orientation.

play. Both clustering mechanisms, ring deformability, and ring motility dictate the ring dynamics which in turn strongly affects the stationary ring configuration. In our systems we have two different types of friction: the rod frictions $\gamma_{r\parallel}$ and $\gamma_{r\perp}$, which are kept constant in all our systems, and the ring friction γ_b which is varied. If the ring friction is small, the ring relaxes faster, and ring motility alignment is predominant. Furthermore, in many cases, all rods can be accommodated in a single cluster. This leads to keratocyte-like shapes if Pe is large enough and N_r is not too large. If the ring friction is large, the ring relaxes more slowly, and ring deformability is the predominant cluster mechanism. Therefore, often the ring is not able to deform quickly enough to accommodate all rods in a single cluster. Slow ring deformation leads to neutrophil-like or fluctuating shapes, depending on Pe .

For systems with $N_r = 16$, the phase diagrams for compression moduli $\bar{k}_A = 1$ and $\bar{k}_A = 100$, are similar. For systems with $\bar{k}_A = 1$ and $Pe = 10$, we observe fluctuating shapes. In these cases, the rod activity is small, which leads to small ring deformations. For $Pe \geq 25$ and $\bar{\gamma}_b < 10$, the rings form keratocyte-like shapes. For $\bar{\gamma}_b \geq 10$, the rings adopt fluctuating shapes. For systems with $\bar{k}_A = 100$, the parameter regime for keratocyte-like shapes increases. Thus, increasing ring stiffness stabilizes keratocyte-like shapes.¹

For systems with $N_r = 40$ and small ring stiffness $\bar{k}_A = 1$, the phase diagram is similar to the one obtained for rings with $N_r = 16$. For rings with 40 rods and $Pe = 100$, the deformations induced by the strongly-propelled rods are too large for the ring to adopt a fluctuating shape. Furthermore, because $\bar{\gamma}_b \geq 10$ the ring cannot accommodate all rods in a single straight segment. Therefore, the ring adopts a neutrophil-like shape. For systems with large ring stiffness $\bar{k}_A = 100$, the phase diagram is the same as obtained for rings with $N_r = 16$ rods. For large \bar{k}_A , large curvatures are suppressed, and neutrophil-like shapes are also suppressed.

For systems with $N_r = 64$ and small ring stiffness $\bar{k}_A = 1$, only rings with $25 \leq Pe \leq 50$ and $\bar{\gamma}_b = 1$ form keratocyte-like shapes. The parameter regime for neutrophil-like shapes increases. As the number of rods increases, it is more difficult to accommodate all rods in a single cluster. Therefore, neutrophil-like shapes dominate over keratocyte-like shapes. For systems with large ring stiffness $\bar{k}_A = 100$, neutrophil-like shapes are suppressed, and keratocyte-like shapes are stabilized.

5.1.1 Shape analysis

We quantify the ring shape using the gyration tensor [165]

$$\mathbf{Q} = \frac{1}{n_b} \sum_{i=1}^{n_b} (\mathbf{r}_i - \mathbf{r}_{CM}) \otimes (\mathbf{r}_i - \mathbf{r}_{CM}), \quad (5.1)$$

with \mathbf{r}_i the position vector of bead i and \mathbf{r}_{CM} the position vector of the center of mass of the ring. The gyration tensor calculates the ellipse that best fits to the ring. From the gyration tensor we extract the two eigenvalues λ_1 and λ_2 to evaluate the

¹Note that in this chapter we sometimes use ring stiffness to refer to the area constraint energy of the deformable ring.

5.1 Deformable rings: phase diagrams and motility

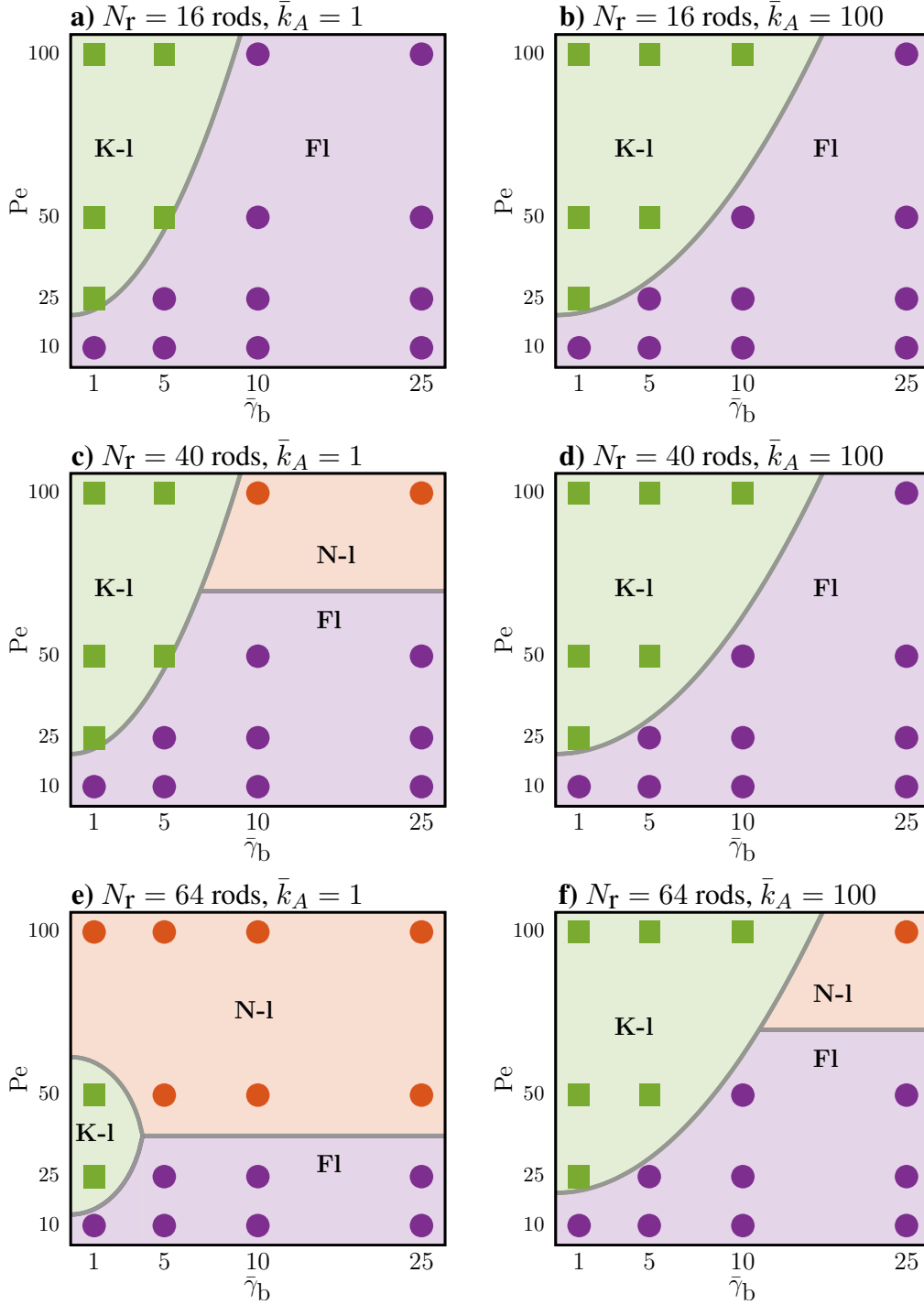


Figure 5.2: Phase diagrams for deformable rings with attached pulling rods for different Péclet numbers Pe , and ring frictions $\bar{\gamma}_b$. Systems with $N_r = 16, 40$ and 64 , $E_r/k_B T = 1$, $\bar{\kappa} = 2$, $\bar{k}_S = 0.15$ and $\bar{k}_A = 1$ and 100 . Purple circles represent fluctuating shapes (F1), orange circles represent neutrophil-like shapes (N-1), and green squares represent keratocyte-like shapes (K-1).

asphericity [165]

$$\Delta = \frac{(\lambda_1 - \lambda_2)^2}{(\lambda_1 + \lambda_2)^2}. \quad (5.2)$$

The asphericity vanishes for a circle, $\Delta = 0$, and is $\Delta = 1$ for a rod.

Another observable that characterizes the shape of vesicles and cells in three dimensions is the reduced volume [191], which is the ratio of the actual volume and the volume of a sphere which has the same area. For a sphere, the reduced volume is 1, and for any other configuration, the reduced volume is smaller than one. We analogously characterize the adhered membrane by using the reduced area

$$a_0 = \frac{4\pi A}{L^2}. \quad (5.3)$$

Here, A is the ring area, and L is the ring perimeter. For a circle $a_0 = 1$, whereas for any other shape $a_0 < 1$. It should be noted that from here onward we use Δ and a_0 to denote the time averages of the asphericity and reduced area, respectively. To represent the values at a specific time of the simulation, we use $\Delta(t)$ and $a_0(t)$.

By measuring reduced area and asphericity for all our systems and plotting them according to their shape type, we can characterize how much the ring shape varies for systems of the same shape type, see Fig. 5.3a. Fluctuating systems, whose shapes are closest to a circle, have the largest reduced areas and smallest asphericities. The maximum asphericity observed for fluctuating systems is $\Delta \approx 0.04$. For most fluctuating systems, $a_0 \propto -2\Delta$. Keratocyte-like systems have smaller reduced areas, $0.8 < a_0 < 0.97$, and larger asphericities, $0.01 < \Delta < 0.16$, compared with fluctuating cells. Keratocyte-like systems are more elongated than fluctuating systems and for most keratocyte-like rings $a_0 \propto -0.8\Delta$. Neutrophil-like rings have the lowest reduced areas, and their asphericities are similar to those obtained for keratocyte-like systems. We do not find a clear correlation of a_0 and Δ for neutrophil-like rings.

For deformable self-propelled rings, shape and motion are tightly correlated, see Fig. 5.3b. Depending on rod dynamics and collective behavior, the rings adopt certain shapes, which lead to certain motion patterns. We correlate the asphericity Δ and the path velocity v_s . Here, the path velocity is calculated as the velocity in a certain time window and multiplied by $\bar{\gamma}_b$, such that velocities for systems with different ring frictions can be normalized. Fluctuating systems have the smallest asphericities and the smallest path velocities because the circular symmetry is not broken. Systems that show persistent motion have broken circular symmetry; both keratocyte-like and neutrophil-like rings are elongated shapes. Although asphericities observed for neutrophil-like and keratocyte-like systems are similar, keratocyte-like rings tend to have higher path velocities than neutrophil-like rings. For keratocyte-like rings, the long axis is oriented perpendicular to the direction of motion, whereas, for neutrophil-like rings, the long axis is oriented parallel to the direction of motion. Having the long axis oriented perpendicularly to the direction of motion thus leads to more ballistic motion.

We also characterize the effect that the rod propulsion force and the ring friction have on the ring shape. As Pe increases, independent of the friction and the compression modulus, the ring deformation increases and the reduced area decreases, see Fig. 5.4a. There are two different groups of systems, rings with large and small ring stiffness. For

5.1 Deformable rings: phase diagrams and motility

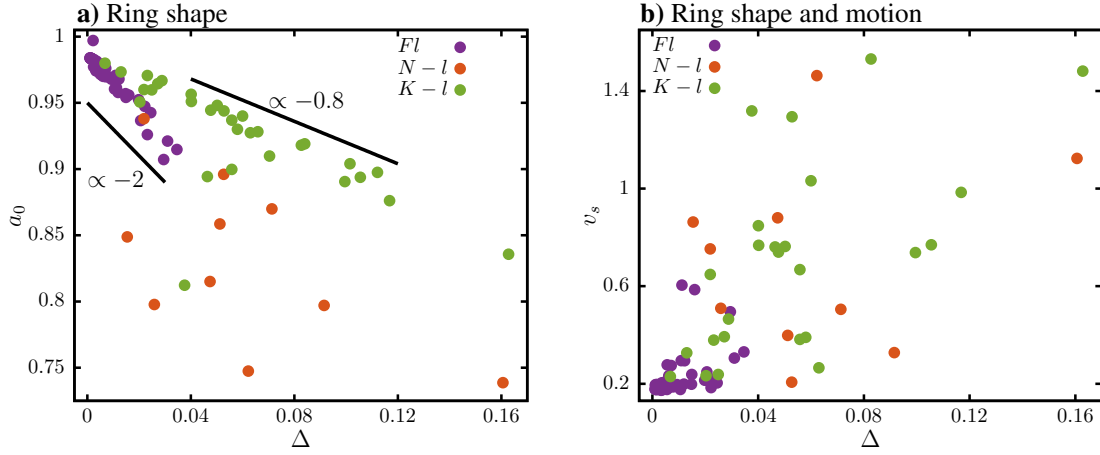


Figure 5.3: Scatter plots of shape observables and ring path velocities for various values of N_r , Pe , $\bar{\gamma}_b$, and \bar{k}_A , for rings with attached-pulling rods with $E_r/k_B T = 1$, $\bar{\kappa} = 2$ and $\bar{k}_S = 0.15$. **a)** Reduced area a_0 versus asphericity Δ . **b)** Ring path velocity v_s versus asphericity Δ .

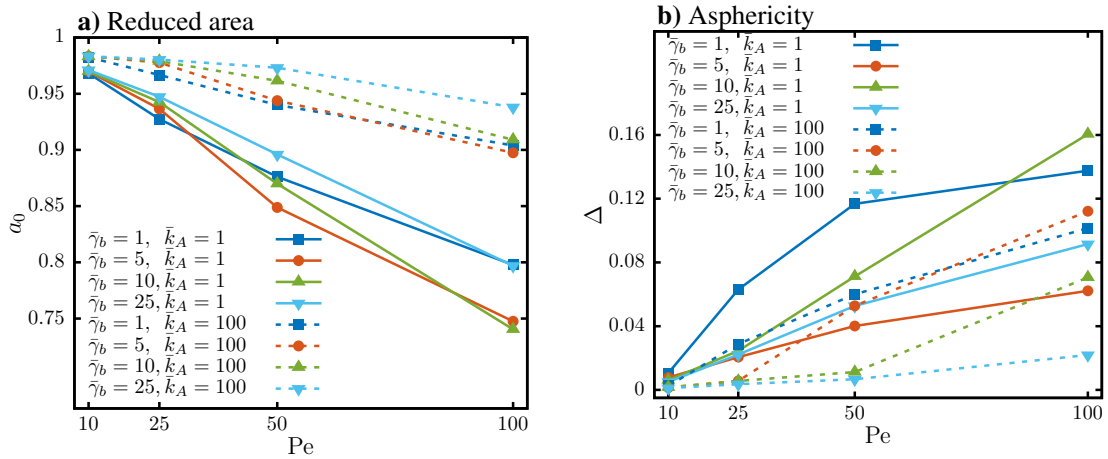


Figure 5.4: Shape observables versus Péclet number for deformable rings with attached-pulling rods with $N_r = 64$, $E_r/k_B T = 1$, $\bar{\kappa} = 2$ and $\bar{k}_S = 0.15$ for various values of $\bar{\gamma}_b$ and \bar{k}_A . Solid lines represent systems with $\bar{k}_A = 1$ and dashed lines represent systems with $\bar{k}_A = 100$. **a)** Reduced area a_0 versus Péclet number Pe . **b)** Asphericity Δ versus Péclet number Pe .

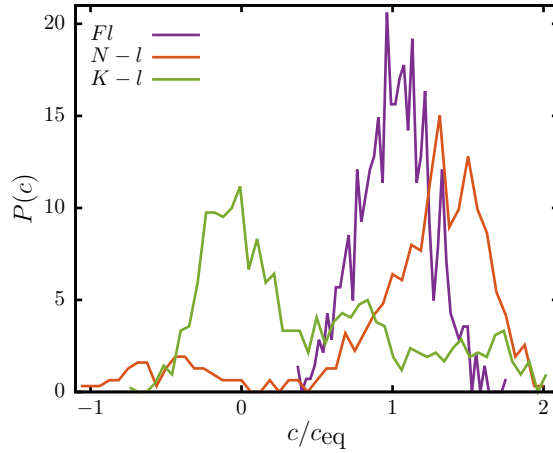


Figure 5.5: Curvature probability distribution $P(c)$ versus curvature c for deformable rings with attached-pulling rods with $N_r = 40$, $E_r/k_B T = 1$, $\bar{\kappa} = 2$, $\bar{k}_S = 0.15$ and $\bar{k}_A = 1$. The fluctuating systems has $Pe = 10$ and $\bar{\gamma}_b = 25$. The neutrophil-like systems has $Pe = 100$ and $\bar{\gamma}_b = 10$. The keratocyte-like systems has $Pe = 50$ and $\bar{\gamma}_b = 1$. Instead of plotting the curvature we plot the ratio between c , calculated with a bead window of $n = 5$, and the equilibrium curvature $c_{eq} = 1/R_m$.

rings with $\bar{k}_A = 100$, $0.9 \lesssim a_0 \lesssim 0.95$ for $Pe=100$, whereas for rings with $\bar{k}_A = 1$, $0.75 \lesssim a_0 \lesssim 0.8$ for $Pe=100$. This shows that the ring stiffness plays a much more crucial role in determining the ring reduced area than the ring friction. As Pe increases, independent of the ring friction and the ring stiffness, also the asphericity increases, see Fig. 5.4b. For large rod propulsion $Pe \geq 50$, the systems with small and large ring stiffnesses can show similar asphericities. There are two competing effects when determining the ring asphericity: ring stiffness and formation of keratocyte-like or neutrophil-like shapes. On the one hand, increased ring stiffness suppresses ring deformation for a particular shape. On the other hand, it stabilizes more elongated keratocyte-like shapes.

We characterize local shapes by measuring the local curvatures [165]

$$c = \sum_{-n}^n \frac{\mathbf{r}'_i \times \mathbf{r}''_i}{|\mathbf{r}'_i|^3}, \quad (5.4)$$

where \mathbf{r}_i is the position vector of bead i , and \mathbf{r}'_i and \mathbf{r}''_i are the first and second derivatives of the position vector of bead i with respect to the ring contour length. Due to the noise in our simulations the ring experiences thermal fluctuations, therefore we calculate the curvature over a window of $2n + 1$ beads.

We measure the curvature probability distribution for typical fluctuating, neutrophil-like and keratocyte-like rings, see Fig. 5.5. The fluctuating ring has the narrowest distribution with a peak at $c \approx c_{eq}$, because it is a quasi-circular system with radius of $R_{ring} \approx R_m$. The keratocyte-like system has a broader distribution that is positively skewed. The pulling rods clustering and forming the flat back of the ring lead to significant contributions to $P(c)$ for small positive and negative curvatures.

5.1 Deformable rings: phase diagrams and motility

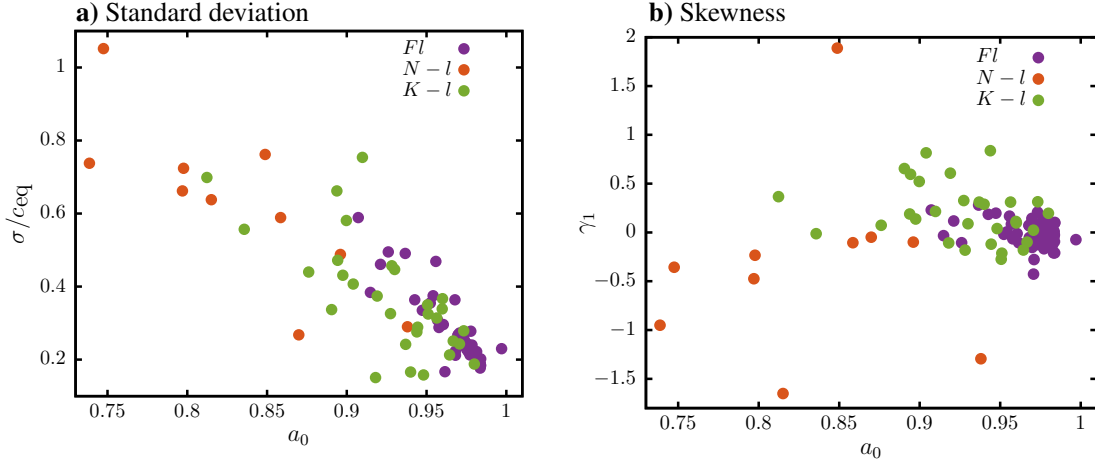


Figure 5.6: Standard deviation and skewness for the curvature probability distribution for all possible values of N_r , Pe , $\bar{\gamma}_b$, and \bar{k}_A , for rings with attached-pulling rods with $E_r/k_B T = 1$, $\bar{\kappa} = 2$ and $\bar{k}_S = 0.15$. **a)** Standard deviation σ versus reduced area a_0 . The standard deviation σ has units, in this case units of curvature, so we divide σ by the equilibrium curvature c_{eq} . **b)** Skewness γ_1 versus reduced area a_0 . The skewness γ_1 is here calculated using the third standardized moment of the distribution, and as such, γ_1 is unitless.

The neutrophil-like systems show a broad distribution, which is negatively skewed and centered around $c \approx 1.5c_{eq}$. The shift towards positive curvature in the peak of the distribution is caused by the formation of the fold at the back of the ring.

We compare the curvature of the different types of systems, fluctuating, neutrophil-like and keratocyte-like rings, using the standard deviation and skewness of the curvature probability distributions, see Fig. 5.6a and App. C. There seems to be a correlation between reduced area and the standard deviation of the curvature distribution. As the systems become less circular, a_0 decreases and σ increases. Fluctuating systems have the smallest standard deviations because they are quasi-circular systems with small deformations. The systems with the largest standard deviations are neutrophil-like systems, because of the different curvatures of the fold and the rest of the ring membrane. Rings which show pronounced folds have positive curvatures at the front and the back of the ring, and negative curvatures at the sides. Figure 5.6b shows the skewness for the different types of rings. Fluctuating rings have small γ_1 and their curvature distributions are centered around 0. Neutrophil-like and keratocyte-like rings have large skewness. For most keratocyte-like rings γ_1 is positive. Neutrophil-like rings show the largest γ_1 values, their curvature distributions are negatively skewed.

5.1.2 Motility analysis

The motility analysis is mainly based on the mean-squared displacements of the ring. For each frame, we calculate the ring center-of-mass using ring beads only, which is then used to calculate the mean-squared displacement $MSD(t) = \langle (\mathbf{r}_{cm}(t' + t) - \mathbf{r}_{cm}(t'))^2 \rangle$,

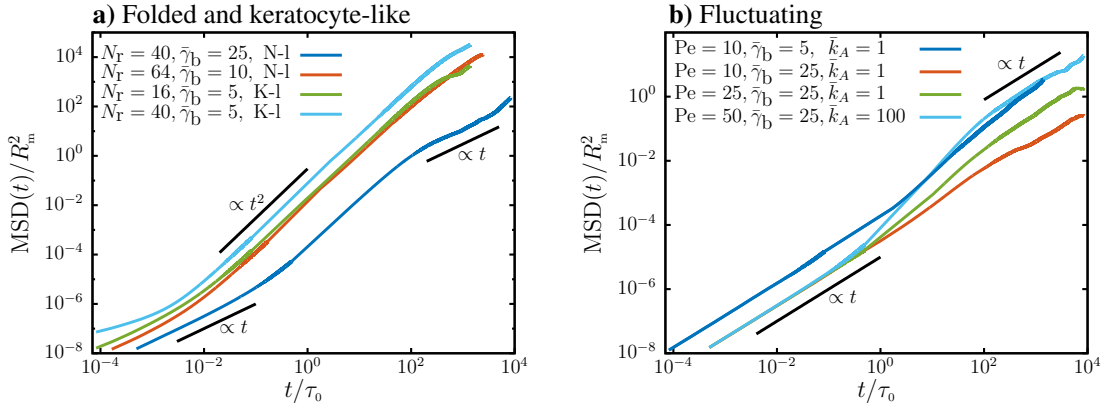


Figure 5.7: Mean-squared displacement $\text{MSD}(t)$ versus lag time t , for deformable rings with attached-pulling rods with $E_r/k_B T = 1$, $\bar{\kappa} = 2$ and $\bar{k}_S = 0.15$. **a)** Neutrophil-like and keratocyte-like systems with $\text{Pe} = 100$ and $\bar{k}_A = 1$. **b)** Fluctuating systems with $N_r = 40$.

where \mathbf{r}_{cm} is the position vector of the ring center-of-mass.

Figure 5.7a shows MSDs for neutrophil-like and keratocyte-like rings. For the systems with $\bar{\gamma}_b \leq 10$, the MSDs show a first diffusive regime for $t \leq 0.007\tau_0$ and a ballistic regime for $t > 0.007\tau_0$. Keratocyte-like rings ($\bar{\gamma}_b = 5$) have the highest MSDs. Small ring friction leads to high ring self-propulsion velocities, which cause persistent, ballistic motion. For example, the keratocyte-like ring with $N_r = 40$ and $\bar{\gamma}_b = 5$ has a propulsion velocity $v = 0.26R_m/\tau_0$, its trajectory is shown in Fig. 5.8a. The keratocyte-like ring with $N_r = 16$ and $\bar{\gamma}_b = 5$ has a propulsion velocity of $v = 0.11R_m/\tau_0$. For the same ring shape, larger numbers of rods lead to higher MSDs and higher velocities. As discussed in Sec. 5.1.1 neutrophil-like rings lead to less persistent motion than keratocyte-like rings, because the elongated axis is oriented parallel to the direction of motion. For example, the neutrophil-like ring with $\bar{\gamma}_b = 10$ has a lower MSD than the keratocyte-like systems, even though it has more rods, $N_r = 64$. The neutrophil-like ring with $\bar{\gamma}_b = 25$ has a thermal diffusive regime for $t \leq 0.2\tau_0$, a ballistic regime for $0.2 < t/\tau_0 < 200$, and an active diffusive regime for $t > 200\tau_0$, see Fig. 5.8b. This means that for certain parameters the deformable ring can be described as an ABP. The effective diffusion coefficient is $D_{\text{eff}}/D_t = 2.4 \cdot 10^4$. The ring performs run-and-tumble motion. This trajectory resembles some of the run-and-tumble and run-and-circle trajectories observed for the rigid self-propelled rings, see Sec. 4.4. The other systems shown in Fig. 5.7a can also be described as ABPs.

The MSDs for fluctuating rings are shown in Fig. 5.7b. The rod distribution along the ring is more homogeneous, which leads to smaller ring propulsion forces. The ballistic regime for these systems typically follows $\text{MSD} \propto t^\beta$ with $\beta < 2$, since the thermal and active diffusive regimes are not well separated in time. The rings with $\bar{\gamma}_b = 25$ have $D_t = 8 \cdot 10^{-6}R_m^2/\tau_0$, whereas the ring with $\bar{\gamma}_b = 5$ has $D_t = 4.2 \cdot 10^{-5}R_m^2/\tau_0$. Larger ring frictions lead to smaller thermal translational diffusion coefficients. The rings with $\text{Pe} \leq 25$ barely show ballistic regimes. For these systems, the rod propulsion is so small that their MSDs are very similar to the MSDs of deformable passive rings.

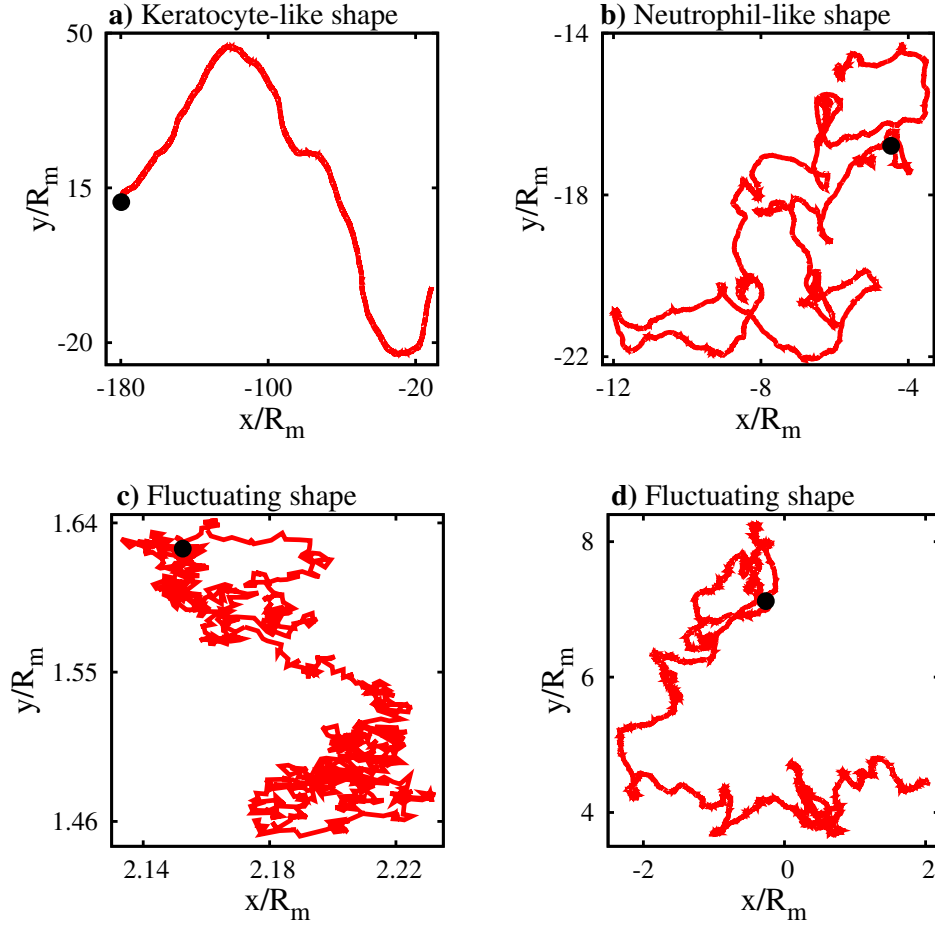


Figure 5.8: Ring center-of-mass trajectories for systems with attached-pulling rods with $N_r = 40$, $E_r/k_B T = 1$, $\bar{\kappa} = 2$ and $\bar{k}_S = 0.15$. The final position is represented by a black circle. **a)** Neutrophil-like system with $Pe = 100$, $\bar{k}_A = 1$ and $\bar{\gamma}_b = 25$. **b)** Keratocyte-like system with $Pe = 100$, $\bar{k}_A = 1$ and $\bar{\gamma}_b = 5$. **c)** Fluctuating system with $Pe = 10$, $\bar{k}_A = 1$ and $\bar{\gamma}_b = 25$. **d)** Fluctuating system with $Pe = 50$, $\bar{k}_A = 100$ and $\bar{\gamma}_b = 25$

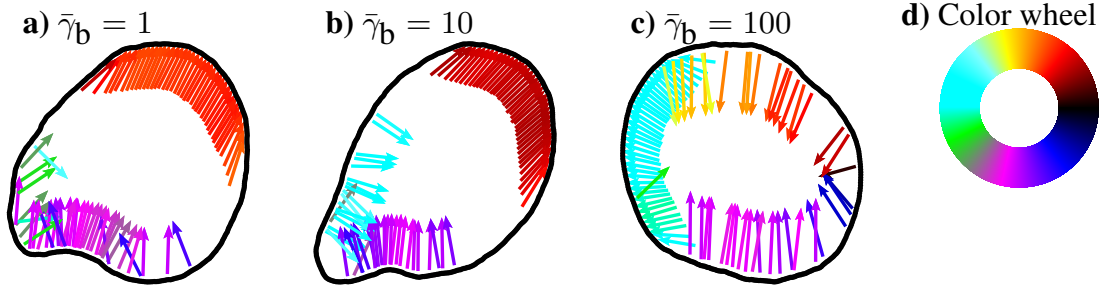


Figure 5.9: Snapshots of deformable self-propelled rings with mixed rods. Systems with $N_r = 80$, $E_{r,pull}/k_B T = 1$, $E_{r,push}/k_B T = 10$, $Pe = 50$, $\bar{\kappa} = 2$, $\bar{k}_A = 1$ and $\bar{k}_S = 0.15$ and various values of the ring friction $\bar{\gamma}_b$. **a)** System with $\bar{\gamma}_b = 1$. **b)** System with $\bar{\gamma}_b = 10$. **c)** System with $\bar{\gamma}_b = 100$. **d)** Color wheel that indicates rod orientation.

In fact, the trajectory for the ring with $Pe = 10$ and $\bar{\gamma}_b = 25$, shown in Fig 5.8c resembles a random walk. The MSD for the ring with $Pe = 50$ can be described using the ABP model. The propulsion velocity is $v = 6 \cdot 10^{-3} R_m / \tau_0$, and the effective diffusion coefficient is $D_{eff} = 1.1 \cdot 10^4 D_t$. Compared with the values obtained for the neutrophil-like and keratocyte-like rings, both v and D_{eff} are smaller for fluctuating rings. The run-and-tumble trajectory for the fluctuating system with $Pe = 50$ is shown in Fig. 5.8d.

The motility patterns observed for deformable rings are very similar to those seen for rigid self-propelled rings, see chapter 4. In both cases, the rings show random-walk, persistent, and run-and-tumble motion. Their MSDs can be described using the ABP model. The main difference between the systems is that ring deformability decreases the probability to observe circling ring motion. In particular, for deformable self-propelled rings, we do not observe pure circling systems, because the ring deformability stabilizes rod clusters that do not circle.

5.1.3 Mixed systems

So far, we have only studied deformable rings with attached-pulling rods. To model the forces exerted on the lipid bilayer by the polymerizing actin in the lamellipodium explicitly, we add attached pushing rods to our systems. These mixed systems studied here have the same number of attached-pushing rods as attached-pulling rods. Attached pushing-rods do not interact directly with attached-pulling rods; attached-pushing rods interact with other attached-pushing rods with a large energy barrier $E_{r,push}/k_B T = 10$, whereas attached-pulling rods interact with other attached-pulling rods with a small energy barrier $E_{r,pull}/k_B T = 1$.

As for system with attached-pulling rods, in mixed systems, the ring friction plays a crucial role in determining the stationary shape of the system. For $\bar{\gamma}_b = 1$, where motility alignments is more important than deformability alignment, the rings adopt keratocyte-like shapes, see Fig. 5.9a. The pulling rods positioned at the back of the ring form a flat stretch, while the pushing rods at the front cause a more pointed front.

Keratocyte-like shapes are less stable for mixed systems than for pulling systems and are found in a smaller region of the parameter space. For mixed systems, the rings only adopt keratocyte-like shapes for $\bar{\gamma}_b = 1$, whereas for pulling rods we find keratocyte-like shapes for $\bar{\gamma}_b \leq 10$. As the ring friction increases to $\bar{\gamma}_b = 10$, the ring adopts a neutrophil-like shape, see Fig. 5.9b, where the pulling rods are located at the back and the sides. Due to the larger ring friction, the ring is not able to form a flat back, which leads to a fold at the back of the ring. As the ring friction further increases to $\bar{\gamma}_b = 100$, the ring shows an elongated ellipsoidal shape, see Fig. 5.9c. For these systems, the pulling rods are mainly at the sides of the ring and the pushing rods cluster at the front. For systems with larger number of rods $N_r = 128$, the pushing rods form two clusters, and the pulling rods stay at the sides, which leads to even more elongated shapes. In the case of the two-clustered pushing-rods systems, the rings show very little motility.

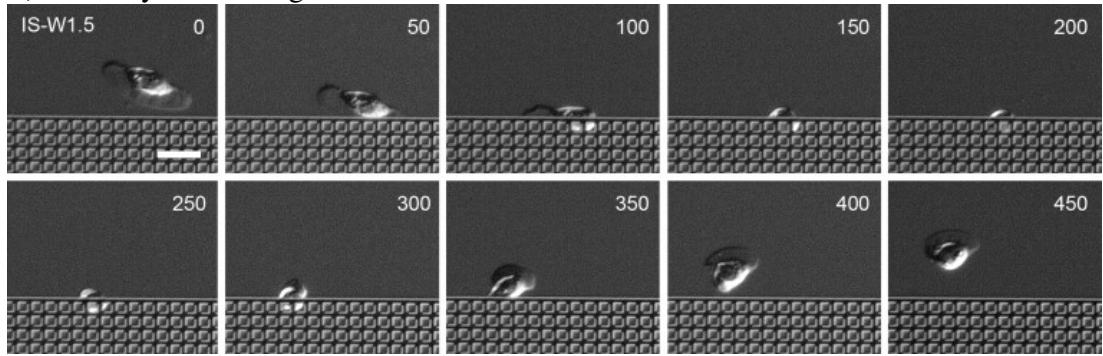
5.2 Deformable rings at walls

Previous studies have shown that the substrates on which cells crawl deeply affect cell motion. Miyoshi et al. found that keratocytes can be deflected or scattered at interfaces between smooth and microgrooved surfaces [188,189], see Fig. 5.10. In these experiments, half of the substrate was microgrooved with pillars and the other half was a smooth substrate. Keratocytes were positioned on the non-grooved region of the substrate facing the interface. Depending on the pillar width w and separation between the pillars s , keratocytes either were deflected at the substrate interface or got stuck in it, see Fig. 5.10a. For the keratocytes which were scattered, they found that the angle of exit from the interface is independent of the angle of entry. Keratocytes always left the interface along the same angular cone, see Fig. 5.10b. In this section, we perform scattering experiments with keratocyte-like rings. We let our rings run against a steric wall and analyze the results. It should be noted that angles are calculated with respect to the y-axis, along which the wall is also oriented. Thus, $\theta_i \approx 90^\circ$ corresponds to a ring that moves perpendicularly to the wall, while $\theta_i \approx 0^\circ$ corresponds to a ring that moves parallel to the wall.

The ring is initialized close to the wall with an initial angle $\theta_i = 88^\circ$, see Fig. 5.11a. As the first ring beads encounter the wall, a flattening of the ring front is observed, while the shape of the rest of the ring remains roughly unchanged, see Fig. 5.11b. As the ring continues to flatten, the rods slide closer to the wall. This leads to a more triangular shape, see Fig. 5.11c. Subsequently, the ring develops a fold close to the wall, making most of the rods collect there; during this process, the ring becomes rounder, see Fig. 5.11d. The ring starts to leave the wall in a neutrophil-like configuration with an orientation θ_{o1} , see Fig. 5.11e. After the fold has disappeared from the back of the ring, the system resumes a more elongated and keratocyte-like shape, see Fig. 5.11f. Finally, the ring adopts its stationary shape again, leading to a new rod and ring orientation θ_{o2} , see Fig. 5.11g.

Figure 5.12 shows the trajectories of the centers-of-mass of deformable rings that hit the wall under different initial angles. In the beginning, the trajectories are straight lines pointing towards the wall. As the rings are scattered from the wall, the trajectories

a) Keratocyte at microgrooved interface



b) Keratocyte trajectory

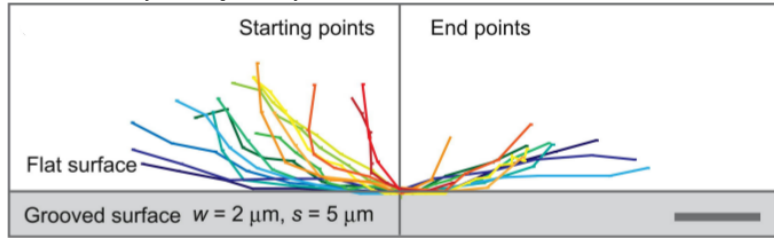


Figure 5.10: Keratocytes at interfaces between smooth and microgrooved surfaces. **a)** Half of the substrate was microgrooved with pillars and the other half was a smooth substrate. Keratocytes were positioned in the smooth region of the substrate facing the interface. For $w = 2\mu\text{m}$ and $s = 5\mu\text{m}$ the keratocyte is scattered by the interface. Figure reproduced from Ref. [189] with permission from Elsevier. **b)** Trajectories of keratocytes that are scattered at an interface with $w = 2\mu\text{m}$ and $s = 5\mu\text{m}$ for different initial angles. Figure reproduced from Ref. [188] with permission from Elsevier.

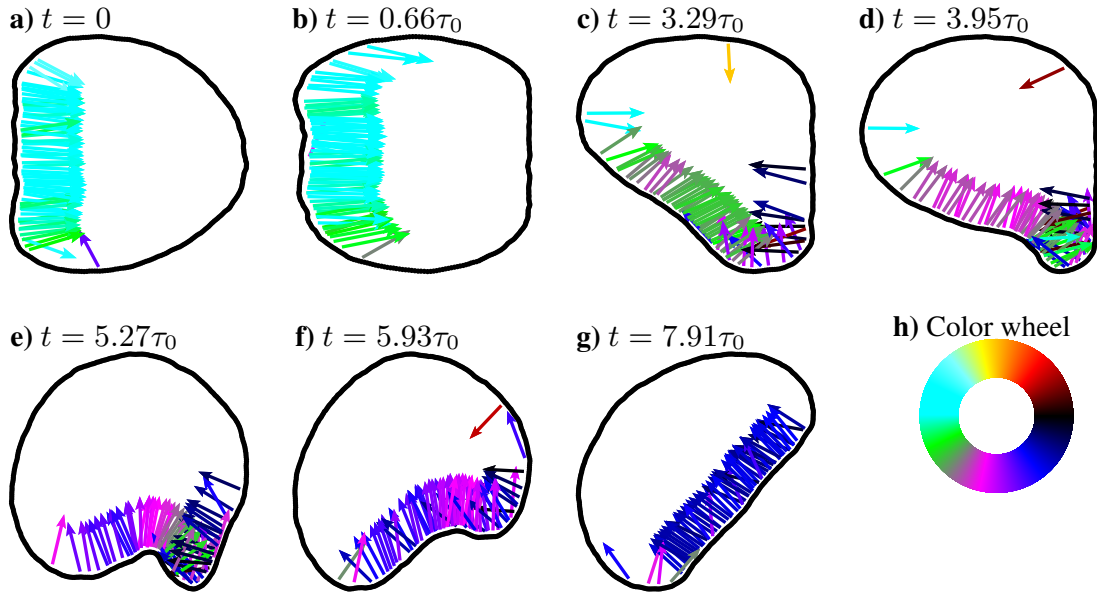


Figure 5.11: Snapshots of a deformable self-propelled ring interacting with a wall. System with $N_r = 64$, $E_r/k_B T = 1$, $Pe = 50$, $\bar{\gamma}_b = 1$, $\bar{\kappa} = 2$, $\bar{k}_A = 1$, $\bar{k}_S = 0.15$ and $\zeta = 0.2$. Snapshots of the ring and rods at different times of the simulations. Initial angle of the trajectory with respect to the wall $\theta_i = 88^\circ$, corresponds to snapshot **a)**. Angle just after leaving the wall $\theta_{o1} = 17^\circ$, corresponds to snapshot **e)**. Angle after reorientation and once the ring has recovered the stationary shape $\theta_{o2} = 41^\circ$, corresponds to snapshot **g)**. **h)** Color wheel that indicates rod orientation.

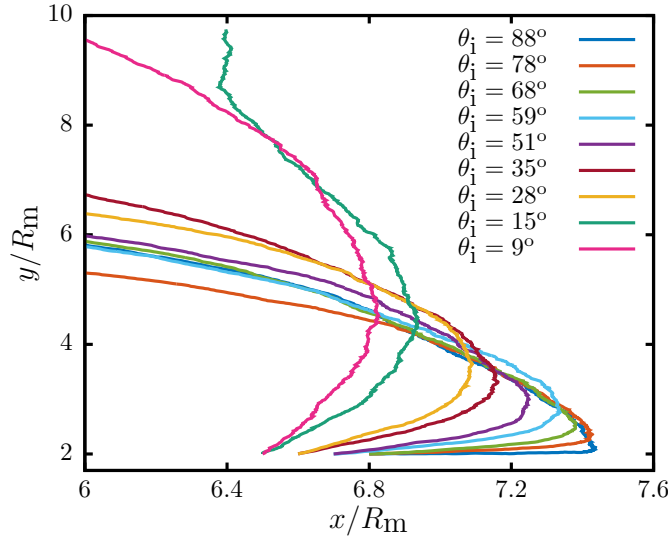


Figure 5.12: Trajectory of center-of-mass of a deformable ring with attached-pulling rods interacting with a wall. The wall is located at $x = 8R_m$. System with $N_r = 64$, $E_r/k_B T = 1$, $Pe = 50$, $\bar{\gamma}_b = 1$, $\bar{\kappa} = 2$, $\bar{k}_A = 1$, $\bar{k}_S = 0.15$ and $\zeta = 0.2$. Initial angles of the trajectories with respect to the wall range from $9.18^\circ \leq \theta_i = 88^\circ$.

become curved. Finally, as the rings recover their stationary shapes, the trajectories again become straight lines. For $28^\circ \leq \theta_i \leq 88^\circ$, the trajectories of the ring after reflection are very similar. In agreement with the experimental data, as long as θ_i is not too small $\theta_i \geq 28^\circ$, the angle of exit θ_{o1} remains unchanged. For initial angles that are almost tangential to the wall $\theta_i \leq 15^\circ$, also the angles of exit are small.

5.2.1 Trajectory and shape analysis for rings close to walls

We first study the ring trajectory by measuring the minimum distance d_{\min} of the center-of-mass of the ring with respect to the wall for different angles, see Fig. 5.13. The minimum distance between the ring and the wall d_{\min} increases as the initial angle decreases, while an almost perpendicular impact at large angles maximize the ring deformation at the wall and leads to small values d_{\min} . As \bar{k}_A increases the ring becomes less deformable, which increases the distance between the ring center and the wall. Furthermore, the effect of θ_i on d_{\min} decreases for increasing ring friction, compare systems with $Pe = 50$ and $\bar{k}_A = 1$ and $Pe = 50$ and $\bar{k}_A = 100$. For rings with tangential orientation with respect to the wall, the ring barely interacts with the wall. Therefore, the deformability of the ring only plays a small role. For rings with perpendicular orientation with respect to the wall, the ring fully interacts with the wall. Therefore, the deformability of the ring plays a crucial role. Similarly, as $\bar{\gamma}_b$ increases, the ring relaxation time increases. Therefore, the ring deforms less and d_{\min} increases with increasing $\bar{\gamma}_b$. The system with $Pe = 100$, $\bar{\gamma}_b = 1$ and $\bar{k}_A = 100$ shows the smallest values of d_{\min} . Although it has a stronger compression modulus than the

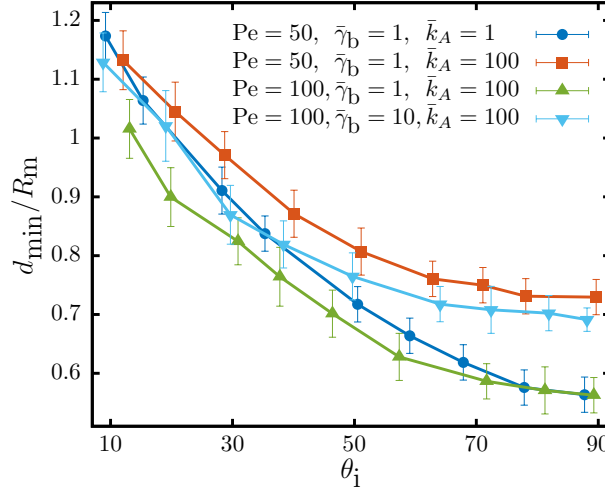


Figure 5.13: Minimum distance between the center-of-mass and the wall d_{\min} versus initial angle θ_i , for various values of Pe , $\bar{\gamma}_b$ and \bar{k}_A . System with $N_r = 64$, $E_r/k_B T = 1$, $\bar{k}_S = 0.15$ and $\zeta = 0.2$.

system with $Pe = 50$ and $\bar{k}_A = 1$, the rod activity is also larger. This leads to larger ring deformations and therefore a smaller distance between the ring center and the wall.

We also compare the angles of exit, both after leaving the wall θ_{o1} and after reorientation θ_{o2} , with the initial angle for two area compression moduli and two ring frictions. Interestingly, θ_{o1} is independent of \bar{k}_A , see Fig. 5.14a. The ring always leaves the wall with a more tangential orientation than the initial one, $\theta_{o1} < \theta_i$ for all θ_i . The deformability of the ring does not affect the scattering of the ring. For small initial angles $\theta_i \leq 15^\circ$, θ_{o1} decreases so that $\theta_{o1} < \theta_i$ holds. For $\theta_i \geq 28^\circ$, θ_{o1} roughly remains constant $\theta_{o1} \approx 21^\circ$ and is independent of $\bar{\gamma}_b$. The angle of exit after complete reorientation when the ring has resumed its stationary shape, θ_{o2} , shows a peak for intermediate initial angles $\theta_i \approx 50^\circ$. The peak of θ_{o2} also strongly depends on \bar{k}_A . The system with $\bar{k}_A = 1$, which is more deformable, shows larger values of θ_{o2} than the system with $\bar{k}_A = 100$. For the system with $\bar{k}_A = 1$, the ring always reorients more perpendicularly $\theta_{o2} > \theta_{o1}$ for all θ_i . For the system with $\bar{k}_A = 100$, $\theta_{o2} > \theta_{o1}$ only for $29^\circ \leq \theta_i \leq 63^\circ$. For larger or smaller values of θ_i , $\theta_{o2} = \theta_{o1}$, which means that no reorientation occurs after the ring leaves the wall. Ring deformability thus, plays a critical role in the ring reorientation after leaving the wall.

The angle of exit θ_{o1} depends on the ring friction $\bar{\gamma}_b$, see Fig. 5.14b. The ring leaves the wall with a more tangential orientation for larger ring friction. For the system with $\bar{\gamma}_b = 10$, we find $\theta_{o1} \approx 18^\circ$ for all initial angles. Whereas, for $\bar{\gamma}_b = 1$, $\theta_{o1} \approx 27^\circ$ for most initial angles. For the rings with $\bar{\gamma}_b = 1$, the ring always leaves the wall with a more tangential orientation than the initial one, $\theta_{o1} < \theta_i$. The value of the exit angle θ_{o1} remains roughly constant for $\theta_i \geq 36^\circ$. However, for small initial angles $\theta_i \leq 20^\circ$, θ_{o1} decreases. The exit angle after reorientation θ_{o2} has a peak for intermediate initial angles $\theta_i = 57^\circ$ and $\theta_i = 50^\circ$, for the systems with $\bar{\gamma}_b = 1$ and 10 , respectively. For

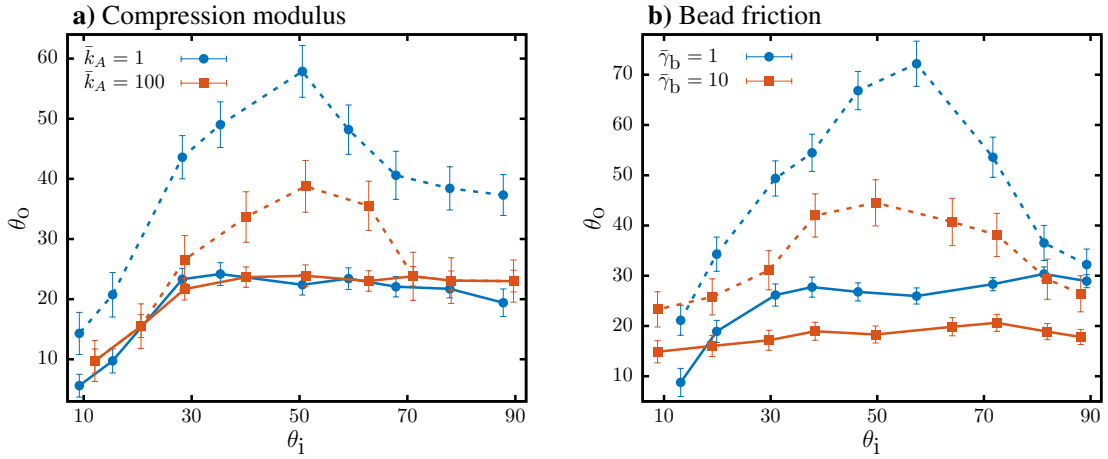


Figure 5.14: Angle of exit of the ring θ_o versus ring initial θ_i for a deformable ring with attached-pulling rods interacting with a wall. Systems with $N_r = 64$, $E_r/k_B T = 1$, $\bar{\kappa} = 2$, $\bar{k}_S = 0.15$ and $\zeta = 0.2$. Solid lines represent the angle of exit just after the ring leaves the wall θ_{o1} , dashed lines represent the angle of exit after the ring reorients and recovers the stationary shape θ_{o2} . **a)** Systems with $\text{Pe} = 50$ and $\bar{\gamma}_b = 1$, for various values of the compression modulus \bar{k}_A . **b)** Systems with $\text{Pe} = 100$ and $\bar{k}_A = 100$, for various values of the ring friction $\bar{\gamma}_b$.

systems with smaller ring friction, the ring relaxes more quickly, such that the rods are able to reorient and change the shape of the ring more than for a system with larger ring friction, which leads to larger values of θ_{o2} .

Figure 5.15 shows the dependence of the ring reorientation after leaving the wall for various ring elastic parameters and rod propulsions. For all systems and all initial angles $\theta_{o2} \geq \theta_{o1}$. This shows that either the system does not reorient further after leaving the wall, $\theta_{o2} = \theta_{o1}$, or that the final angle is more perpendicular with respect to the wall. The systems where no further reorientation occurs are the systems with $\text{Pe} = 50$ and $\bar{k}_A = 100$, where the ratio of rod propulsion energy to ring elastic energy is small enough. For most of the systems, $\theta_{o2} = \alpha \theta_{o1}$ with $1 < \alpha \leq 2$. All systems, except the two systems with $\text{Pe} = 50$ and $\bar{k}_A = 100$, have some points which lie in the plot region $\theta_{o2} = \alpha \theta_{o1}$ with $2 < \alpha \leq 3$. In general, the ratio between exit angles θ_{o2}/θ_{o1} increases with decreasing $\bar{\gamma}_b$ and \bar{k}_A , and increasing Pe . With increasing ring deformability and rod propulsion ring reorientation after leaving the wall is enhanced.

So far, we have only discussed the ring trajectories. However, because the ring is flexible, the wall scatters the ring and also changes its shape, see Fig. 5.11. We measure the ring asphericity at each time step for different values of \bar{k}_A and θ_i , see Fig. 5.16a. As the ring deforms and elongates when it first encounters the wall $\Delta(t)$ increases. After the rods rearrange and the ring starts to leave the wall its shape becomes more round, thus decreasing $\Delta(t)$. Finally, after the ring has left the wall and has recovered its stationary shape, $\Delta(t)$ recovers its original value. This process leads to a double-peaked structure for $\Delta(t)$. The first peak, which is positive, corresponds to the ring's early contact the wall. The second peak, which is negative, occurs as the ring leaves

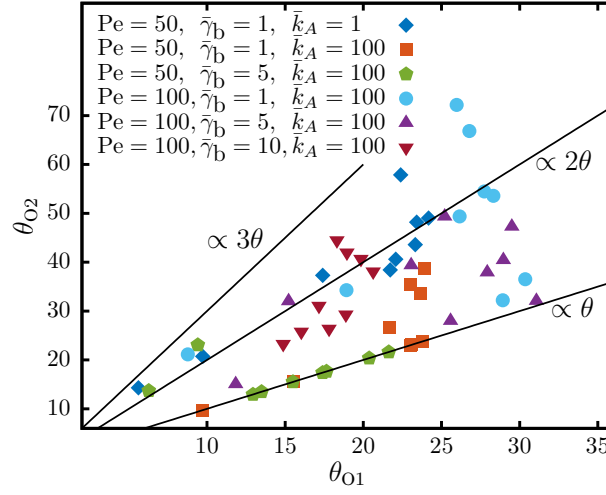


Figure 5.15: Angle of exit after reorientation θ_{o2} versus angle of exit after leaving the wall θ_{o1} , for all possible values of Pe , $\bar{\gamma}_b$, and \bar{k}_A . Systems with attached-pulling rods with $N_r = 64$, $E_r/k_B T = 1$, $\bar{\kappa} = 2$ and $\bar{k}_S = 0.15$ and $\zeta = 0.2$.

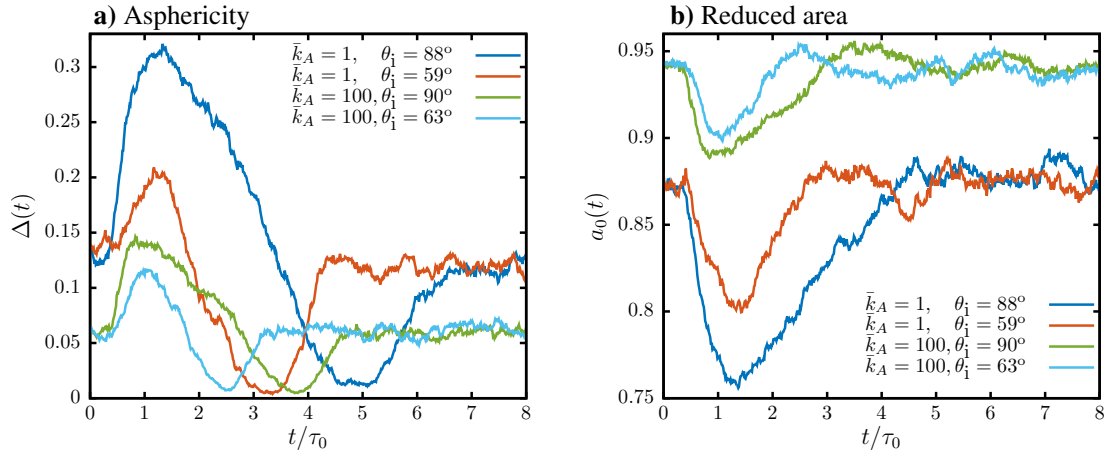


Figure 5.16: Ring shape dynamics for various values of \bar{k}_A and θ_i . Systems with $N_r = 64$, $E_r/k_B T = 1$, $Pe = 50$, $\bar{\gamma}_b = 1$, $\bar{\kappa} = 2$, $\bar{k}_S = 0.15$ and $\zeta = 0.2$. **a)** Asphericity $\Delta(t)$ versus time t . **b)** Reduced area $a_0(t)$ versus time t .

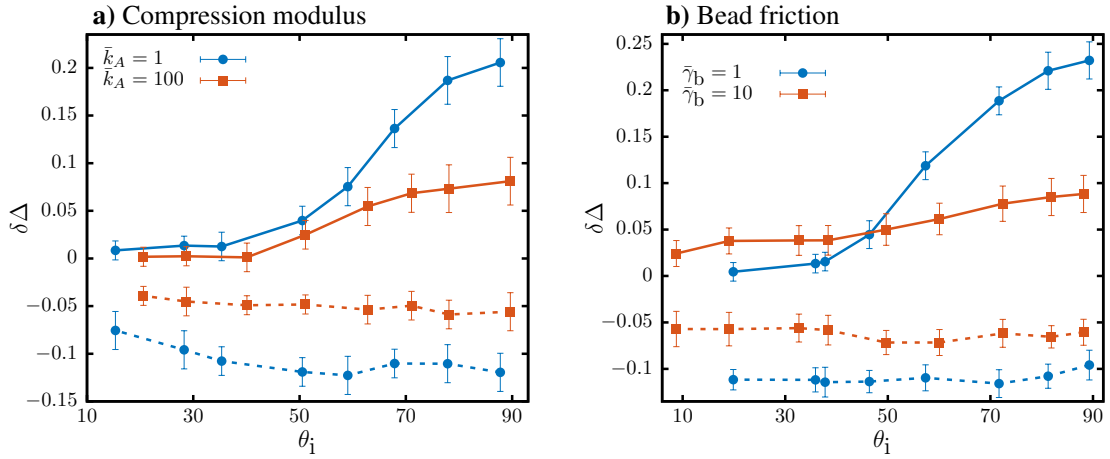


Figure 5.17: Asphericity peak height $\delta\Delta$ versus initial angle θ_i . Solid lines represent the height of the first asphericity peak, dashed lines represent the height of the second asphericity peak. Systems with $N_r = 64$, $E_r/k_B T = 1$, $\bar{\gamma}_b = 1$, $\bar{\kappa} = 2$, $\bar{k}_S = 0.15$ and $\zeta = 0.2$. **a)** Systems with $Pe=50$ and $\bar{\gamma}_b = 1$, for various values of \bar{k}_A . **b)** Systems with $Pe=100$ and $\bar{k}_A = 100$, for various values of $\bar{\gamma}_b$.

the wall. The heights of the peaks decrease both with decreasing θ_i and with increasing \bar{k}_A , because either the force compressing the ring or the ring compressibility decreases. Furthermore, as θ_i decreases and \bar{k}_A increases, the second peak shifts to smaller values of t .

The reduced area shows a single peak, see Fig. 5.16b. a_0 decreases as the ring first encounters the wall and increases again as the ring leaves the wall. When the ring recovers its stationary shape, a_0 stabilizes and plateaus. As for the asphericity, the peak height for the reduced area increases with decreasing \bar{k}_A and with increasing θ_i . Although the position of the peak does not depend on θ_i , the time it takes the ring to recover its stationary shape decreases with decreasing θ_i . For systems with smaller θ_i , rings with a more tangential orientation, the part of the ring that interacts with the wall is smaller, which leads to smaller ring deformations. Thus, the ring recovers its stationary shape faster.

Figure 5.17a shows the asphericity peak heights, both for the positive $\delta\Delta_1$ and negative peak $\delta\Delta_2$, versus the initial angle of the ring for systems with different compression moduli. The first peak increases with increasing θ_i . For more perpendicular orientations of the ring, the deformation is larger, which leads to an increase of $\delta\Delta_1$ when the ring encounters the wall. For small values of the initial angle $\theta_i \leq 35^\circ$, $\delta\Delta_1$ remains constant. For the system with $\bar{k}_A = 1$, the increase in $\delta\Delta_1$ is larger than for the system with $\bar{k}_A = 100$, due to the increased ring deformability. For the system with $\bar{k}_A = 1$, $\delta\Delta_2$ decreases with increasing θ_i . This shows that rings that are oriented more perpendicularly elongate more when they first encounter the wall, but "over-correct" and leave the wall with a more circular shape. For the system with $\bar{k}_A = 100$, $\delta\Delta_2$ roughly remains constant. The over-correction of the ring shape as a ring leaves the wall disappears, due to the increased ring stiffness.

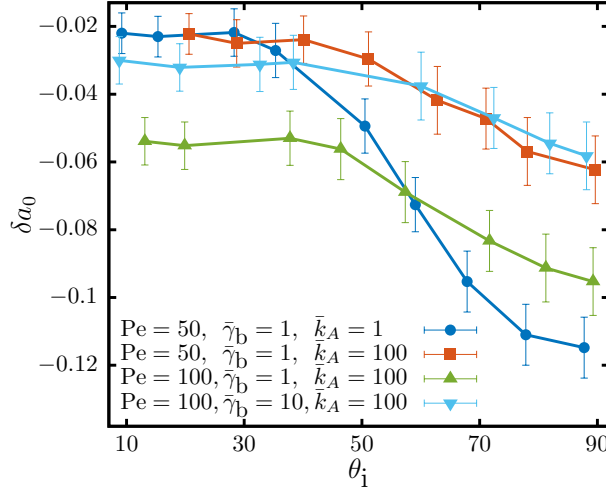


Figure 5.18: Reduced area peak height δa_0 versus initial angle θ_i . Systems with $N_r = 64$, $E_r/k_B T = 1$, $\bar{\kappa} = 2$, $\bar{k}_S = 0.15$ and $\zeta = 0.2$, for various values of $\bar{\gamma}_b$ and \bar{k}_A .

Figure 5.17b shows the dependence of the asphericity on the initial angle for different ring frictions. Decreasing $\bar{\gamma}_b$ increases the asphericity peak height $\delta\Delta$; the ring deforms more because it can deform more quickly. As for the systems with different compression modulus, $\delta\Delta_1$ plateaus for small θ_i and increases with increasing θ_i . For the system with $\bar{\gamma}_b = 1$, the increase in $\delta\Delta_1$ with increasing θ_i is larger than for the system with $\bar{\gamma}_b = 10$. As the ring friction decreases, the ring relaxes more quickly, thus leading to larger ring deformations and larger changes in the asphericity. $\delta\Delta_2$ remains roughly constant for all θ_i values. For the system with $\bar{\gamma}_b = 1$, $\delta\Delta_2 \approx -0.11$, whereas for the system with $\bar{\gamma}_b = 10$, $\delta\Delta_2 \approx -0.05$. With smaller ring friction, the ring leaves the wall with a more circular shape.

Figure 5.18 shows the height of the peak of $a_0(t)$ as a function of θ_i . For all systems, we find a plateau of δa_0 for tangential ring orientations and a decrease of δa_0 as the ring orientation becomes more perpendicular. The value of δa_0 in the plateau regime $\delta a_0 \approx -0.02$ is independent of \bar{k}_A . The steepness at which δa_0 decreases, grows with decreasing \bar{k}_A because decreasing ring stiffness leads to larger ring deformations. With increasing $\bar{\gamma}_b$ the region at which δa_0 plateaus increases and the height of the plateau decreases, because increasing ring friction suppresses ring deformations. For the system with $Pe = 100$ and $\bar{\gamma}_b = 1$, $\delta a_0 \approx -0.055$ for $\theta_i \leq 46^\circ$. Whereas for the system with $Pe = 100$ and $\bar{\gamma}_b = 10$, $\delta a_0 \approx -0.03$ for $\theta_i \leq 64^\circ$. The steepness at which δa_0 decreases grows with decreasing $\bar{\gamma}_b$.

5.2.2 Bending rigidity dependence of rings interacting with walls

In Sec. 2.6, we show that for a semiflexible ring that changes shape from a circle to an ellipse – unless the eccentricity of the ellipse is very large $e \gtrsim 0.97$ – the area constraint

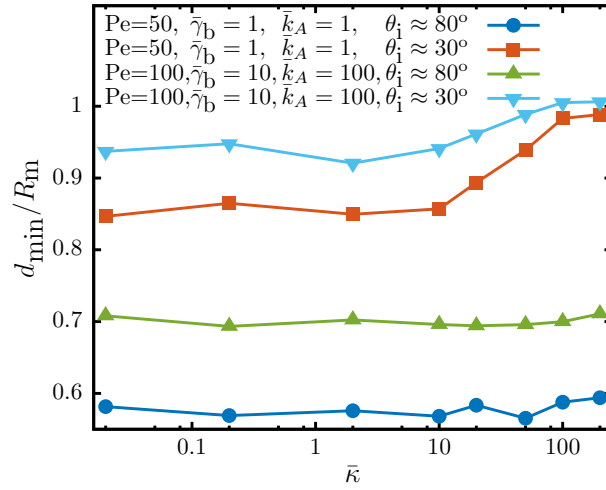


Figure 5.19: Minimum distance between the center-of-mass and the wall d_{\min} versus bending rigidity $\bar{\kappa}$, for various values of Pe , $\bar{\gamma}_b$, \bar{k}_A and θ_i . Systems with $N_r = 64$, $E_r/k_B T = 1$, $\bar{k}_S = 0.15$ and $\zeta = 0.2$.

energy is the dominant term. This indicates that for the keratocyte-like systems the overall shape is controlled by \bar{k}_A and the role of $\bar{\kappa}$ is to control the local curvature. However, the calculations in Sec. 2.6 are an approximation, since the keratocyte-like shape is not an ellipse. Here, we study the role of the bending rigidity for self-propelled rings interacting with a wall. We study two types of systems that adopt keratocyte-like shapes for $\theta_i \approx 80^\circ$ and 30° . The first system has $N_r = 64$, $E_r/k_B T = 1$, $Pe = 50$, $\bar{\gamma}_b = 1$, $\bar{k}_A = 1$, $\bar{k}_S = 0.15$ and $\zeta = 0.2$, the second system has $N_r = 64$, $E_r/k_B T = 1$, $Pe = 100$, $\bar{\gamma}_b = 10$, $\bar{k}_A = 100$, $\bar{k}_S = 0.15$ and $\zeta = 0.2$.

Figure 5.19 shows the minimum distance between the center-of-mass of the as a function of the bending rigidity. As expected, d_{\min} increases with increasing \bar{k}_A and $\bar{\gamma}_b$, and decreasing θ_i . For the systems with $\theta_i \approx 80^\circ$, d_{\min} remains constant for all $\bar{\kappa}$ values. For the systems with $\theta_i \approx 30^\circ$, d_{\min} remains constant for $\bar{\kappa} < 10$ and increases for $\bar{\kappa} \geq 10$. For large bending rigidity $\bar{\kappa} \geq 10$, d_{\min} increases more quickly with increasing $\bar{\kappa}$ for the rings with $Pe = 50$ and $\bar{k}_A = 1$ than for the rings $Pe = 100$.

We also study the changes in shape as a function of the bending rigidity. For all $\bar{\kappa}$ values simulated here, the asphericity shows a positive and negative peak as a function of time. To characterize the change as the ring interacts with the wall, we calculate the height of the positive and negative peak and plot them with respect to the bending rigidity. Figure 5.17a shows the heights of the asphericity peaks for systems with $\theta_i \approx 80^\circ$. For both systems, $\delta\Delta$ is constant for $\bar{\kappa} < 10$. For $\bar{\kappa} \geq 10$ a slight decrease of $\delta\Delta_1$ and an increase of $\delta\Delta_2$ are observed. Thus, as expected the changes in asphericity slightly decrease, which indicates that as the bending rigidity increases the ring becomes stiffer and less deformable. For the systems with $\theta_i \approx 30^\circ$, the overall values of $\delta\Delta$ are smaller, because the ring interacts more tangentially with the wall. For the system with $Pe = 50$ and $\bar{k}_A = 1$, $\delta\Delta_1$ slowly decreases with increasing $\bar{\kappa}$ and for $\bar{\kappa} \geq 50$, $\delta\Delta_1 \approx 0$. For the system with $Pe = 100$ and $\bar{k}_A = 100$, $\delta\Delta_1$ is constant for $\bar{\kappa} < 50$ and slightly

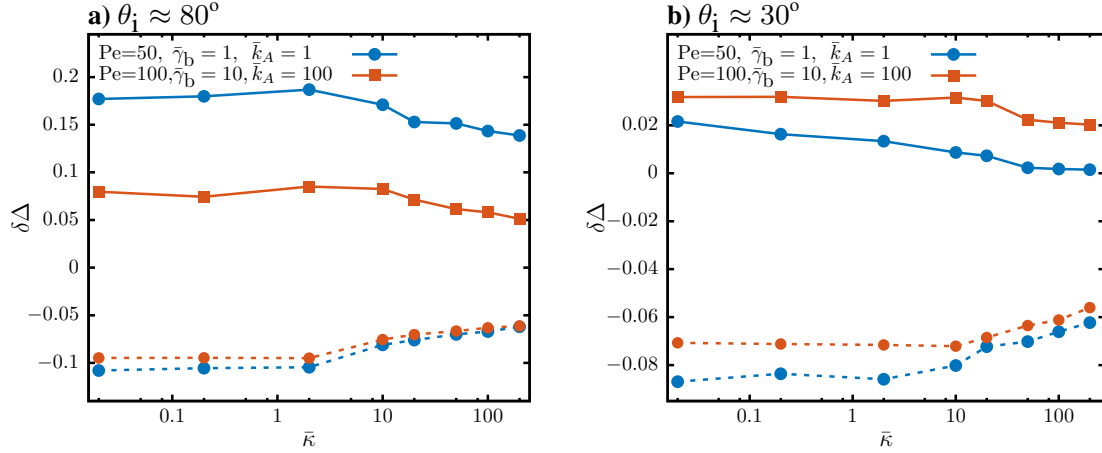


Figure 5.20: Asphericity peak height $\delta\Delta$ versus bending rigidity $\bar{\kappa}$, for deformable self-propelled rings interacting with walls. Systems with $N_r = 64$, $E_r/k_B T = 1$, $\bar{k}_S = 0.15$ and $\zeta = 0.2$ for various values of Pe , $\bar{\gamma}_b$ and \bar{k}_A . Solid lines represent the height of the first asphericity peak $\delta\Delta_1$, dashed lines represent the height of the second asphericity peak $\delta\Delta_2$. **a)** Systems with initial angle $\theta_i \approx 80^\circ$. **b)** Systems with initial angle $\theta_i \approx 30^\circ$.

decreases for $\bar{\kappa} \geq 50$. This more detailed analysis of the simulation data supports the calculations in Sec. 2.6 that show the dominant contribution to the overall ring shape and ring elasticity is the compression or area constraint energy. Overall changes in the bending rigidity minimally affect the interaction between deformable rings and walls. Only for $\bar{\kappa} \geq 50$, we see small changes in the ring system trajectory and shape for different bending rigidities.

5.2.3 Interaction of mixed systems with walls

Deformable rings with both pushing and pulling rods stay at walls, see Fig. 5.21. Due to the addition of pushing rods, the ring continuously exerts a pushing force towards the wall. The ring is initialized next to the wall with an initial angle $\theta_i = 89^\circ$, see Fig. 5.21a. As the first ring beads encounter the wall, a flattening of the ring front is observed, while the rest of the ring shape remains unchanged, see Fig. 5.11b. As the ring continues to flatten, the cluster of pushing rods slides up the wall, whereas the pulling rods propel the ring parallel to the wall, see Figs. 5.21c-e. Finally, the ring adopts its stationary shape, see Figs. 5.21f-g.

Figure 5.22 shows the trajectories of the center-of-mass of deformable rings with both pushing and pulling rods with different initial angles. In the beginning, the trajectory is a straight line pointing towards the wall. As the pushing rods slide towards the front of the ring and the pulling rods slide towards the wall, the shape change of the ring shifts the position of the center-of-mass away from the wall. After the ring has adopted its stationary shape, the center-of-mass remains at a constant distance from the wall. The trajectories for $\theta_i \geq 28^\circ$ are qualitatively very similar. For small initial

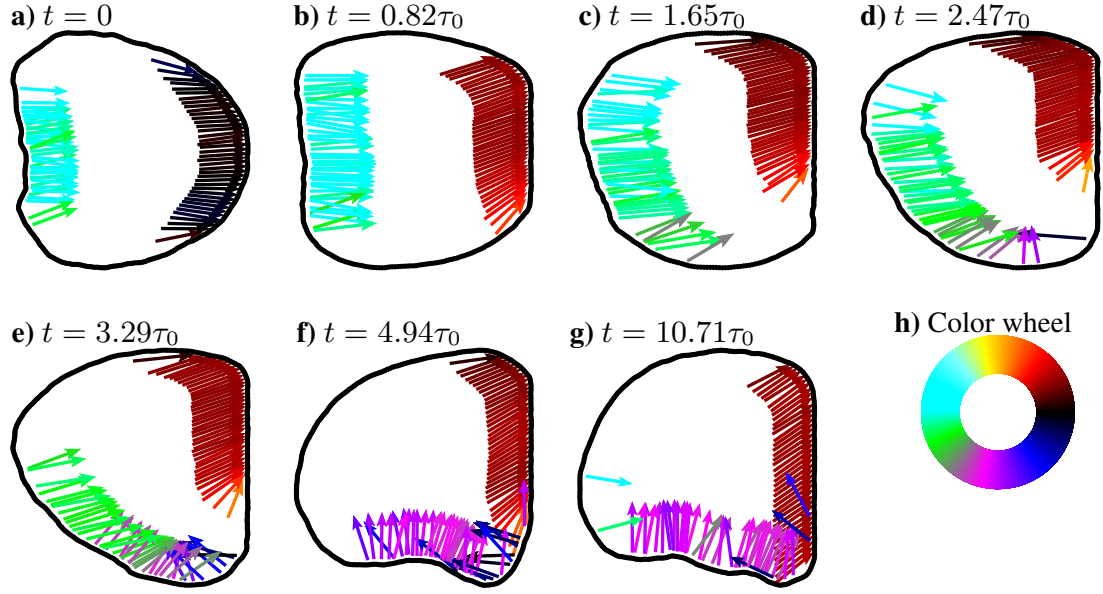


Figure 5.21: Snapshots of a deformable self-propelled ring with mixed rods interacting with a wall. System with $N_r = 80$ mixed rods, $E_{r,pull}/k_B T = 1$, $E_{r,push}/k_B T = 10$, $Pe = 50$, $\bar{\gamma}_b = 1$, $\bar{\kappa} = 2$, $\bar{k}_A = 1$, $\bar{k}_S = 0.15$ and $\zeta = 0.2$. Snapshots of the ring and rods at different times of the simulations. The initial angle of the trajectory with respect to the wall of $\theta_i = 89^\circ$ corresponds to snapshot (a). **h)** Color wheel that indicates rod orientation.

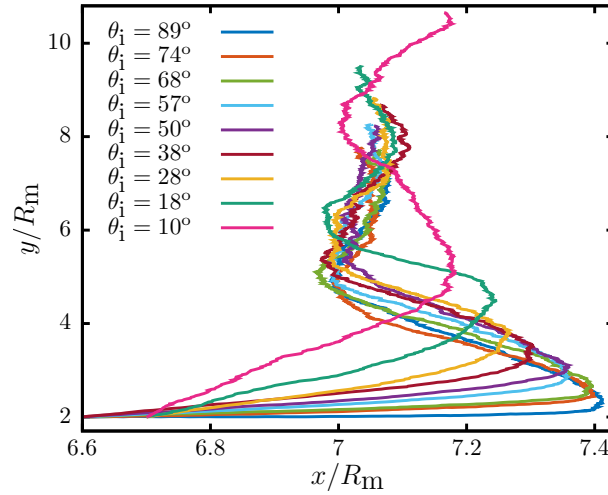


Figure 5.22: Trajectories of centers-of-mass of deformable self-propelled rings with mixed rods interacting with a wall. The wall is located at $x = 8R_m$. System with $N_r = 80$ mixed rods, $E_{r,pull}/k_B T = 1$, $E_{r,push}/k_B T = 10$, $Pe = 50$, $\bar{\gamma}_b = 1$, $\bar{\kappa} = 2$, $\bar{k}_A = 1$, $\bar{k}_S = 0.15$ and $\zeta = 0.2$. Initial angles of the trajectories with respect to the wall range from $9.51 \leq \theta_i = 89^\circ$.

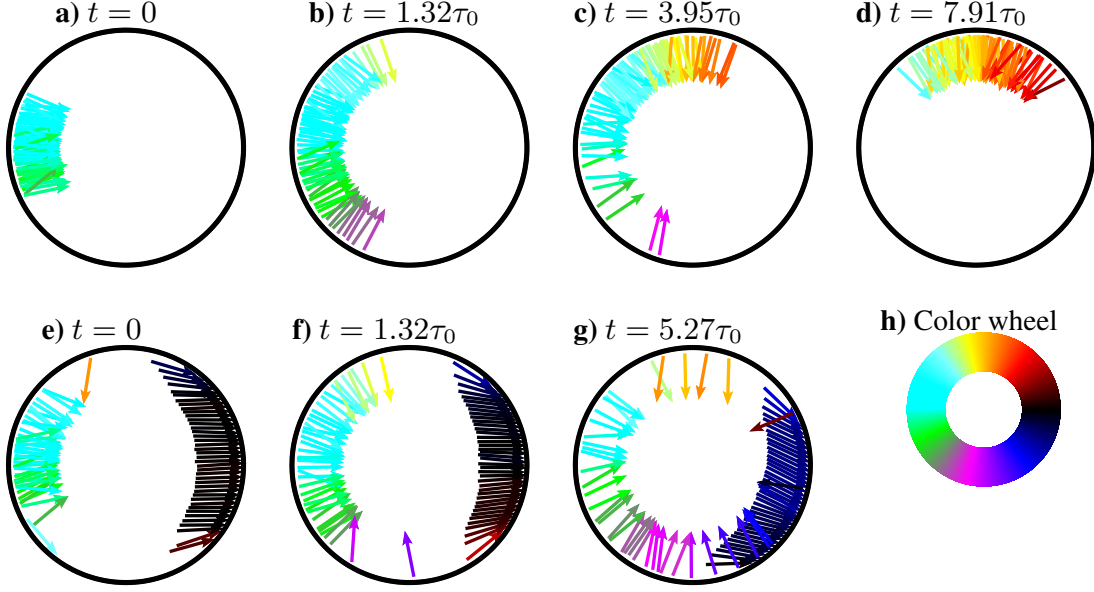


Figure 5.23: Snapshots of a rigid self-propelled ring interacting with a wall. **a)-d)** system with $N_r = 64$ pulling rods, $E_r/k_B T = 1$, $Pe = 50$, $\zeta = 0.2$ and $\theta_i = 89^\circ$. **e)-g)** system with $N_r = 80$ mixed rods, $E_{r,pull}/k_B T = 1$, $E_{r,push}/k_B T = 10$, $Pe = 50$, $\zeta = 0.2$ and $\theta_i = 89^\circ$. **h)** Color wheel that indicates rod orientation.

angles $\theta_i \leq 18^\circ$, due to the smaller interaction between the ring and the wall, it takes longer for the ring to reach its stationary shape. This leads to larger oscillations of the position of the center-of-mass around the final stationary distance to the wall.

For comparison, we analyze the behavior of rigid rings at walls both for systems with attached-pulling rods and with mixed rods, see Fig. 5.23. The snapshots for a rigid ring with attached pulling rods are shown in Fig. 5.23a to d, and the trajectories are shown in Fig. 5.24. The ring is initialized next to the wall with an initial orientation $\theta_i = 89^\circ$. Initially, all pulling rods are tightly clustered at the back of the ring, see Fig. 5.23a. As the ring hits the wall, due to the lack of motility-induced clustering the rods start to diffuse along the ring, see Fig. 5.23b. The cluster reforms, such that it is oriented more or less parallel to the wall, see Fig. 5.23c. This reorientation of the cluster can cause the ring to leave the wall, see Fig. 5.23d. Figure 5.24 shows that rigid rings with attached-pulling rods behave as ABPs when interacting with walls [187]. The ring behavior does not depend on the initial angle θ_i . The ring hits the wall and stays there until the cluster of pulling rods has reoriented. Once the reorientation has occurred, the ring leaves the wall. Often rigid rings after having left the wall, reorient again towards it, leading to a second interaction between the ring and the wall. This shows that ring deformability is a crucial parameter for determining the behavior of the rings at walls or obstacles. Deformable self-propelled rings with attached pulling rods exhibit keratocyte-like behavior when interacting with walls, whereas rigid self-propelled rings with attached-pulling rods behave as ABPs.

Snapshots and trajectories for rigid rings with mixed rods close to walls are shown

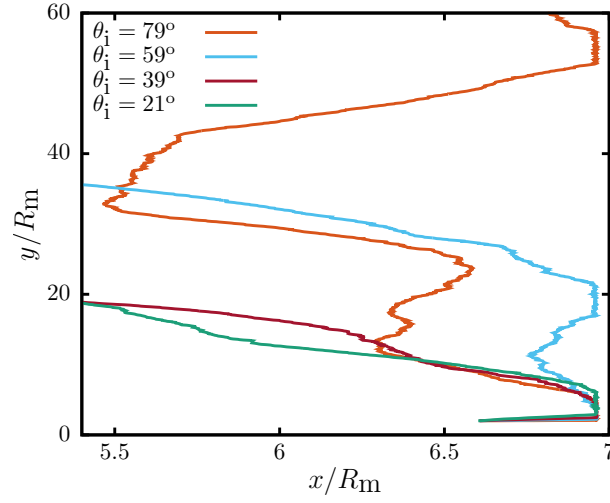


Figure 5.24: Center-of-mass trajectories of rigid rings with attached-pulling rods interacting with a wall. The wall is located at $x = 8R_m$. System with $N_r = 64$ pulling rods, $E_r/k_B T = 1$, $Pe = 50$ and $\zeta = 0.2$. Initial angles of the trajectories with respect to the wall range from $9.92 \leq \theta_i = 89^\circ$.

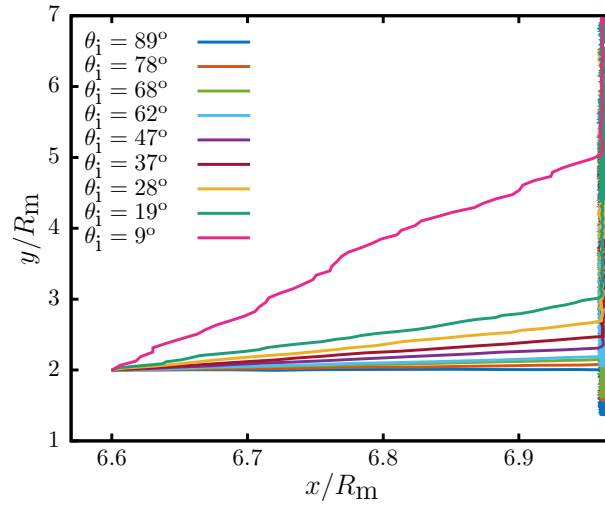


Figure 5.25: Center-of-mass trajectories of rigid rings with mixed rods interacting with a wall. The wall is located at $x = 8R_m$. System with $N_r = 80$ mixed rods, $E_{r,pull}/k_B T = 1$, $E_{r,push}/k_B T = 10$, $Pe = 50$ and $\zeta = 0.2$. Initial angles of the trajectories with respect to the wall range from $8.59 \leq \theta_i = 89^\circ$.

in Figs. 5.23e to g and 5.25, respectively. As for deformable rings with mixed rods, the addition of pushing rods stabilizes the rigid ring at the wall. The ring is initialized next to the wall with an initial orientation of $\theta_i = 89^\circ$. At the beginning of the simulation, the pushing rods form a cluster at the front and the pulling rods cluster at the back of the ring, see Fig. 5.23e. As the ring meets the wall, the pushing rods remain at the front of the ring, and the pulling rods start to diffuse along the ring, because the ring is no longer motile in the direction perpendicular to the wall, see Fig. 5.23f. The ring stays at the wall since the pushing rods remain clustered next to the wall. Depending on where the cluster of pulling rods forms, the ring will move in one or the other direction along the wall, see Fig. 5.23g.

5.3 Deformable rings at friction interfaces

Cells change shape according to the cell-substrate adhesion strength [10,12,192], follow stiffness interfaces, and move on adhesion tracks [11]. Barnhart et al. studied the effect of adhesion strength on keratocyte motility and shape [12]. They modified the adhesive properties of the substrate using a functionalized copolymer [193], the strength of the cell-substrate attachment increased with increasing copolymer density. This allowed them to create substrates with interfaces between regions of different adhesion strengths. At low adhesion strengths, the keratocyte shows a round shape with area $\approx 350\mu\text{m}^2$ and moves with velocity $\approx 0.17\mu\text{m/s}$, see top row of Fig. 5.26. A keratocyte crossing from a low adhesion strength region to a medium adhesion strength region increases its area and aspect ratio. At medium adhesion strengths the keratocyte becomes fan-shaped with area $\approx 550\mu\text{m}^2$ and velocity $\approx 0.17\mu\text{m/s}$. A keratocyte crossing from a medium adhesion strength region to a high adhesion strength region further increases its area and aspect ratio, but decreases its speed, see top row of Fig. 5.26. At high adhesion strengths, the keratocyte shape is rapidly changing due to traveling wave-like protrusions at the front of the cell. Its area is $\approx 620\mu\text{m}^2$ and it moves with velocity $\approx 0.05\mu\text{m/s}$.

We show preliminary results for self-propelled deformable rings with attached-pulling rods at friction interfaces. The friction change occurs along the x-axis. Here, changing the substrate properties in experiments corresponds to changing the ring friction $\bar{\gamma}_b$ in our minimal model.² To model the friction interface, we use a sigmoid function

$$\bar{\gamma}_b = \bar{\gamma}_{b,l} + \frac{(\bar{\gamma}_{b,r} - \bar{\gamma}_{b,l})}{1 + e^{-b(x-x_{\text{int}})}}, \quad (5.5)$$

where $\bar{\gamma}_{b,l}$ is the ring friction for small x , $\bar{\gamma}_{b,r}$ is the ring friction for large x , x_{int} is the center of the interface, and b characterizes the steepness of the slope. In our simulations, we use $x_{\text{int}} = 3.5R_m$, and $b = 100/R_m$, which corresponds to an interface width $w_{\text{int}} \approx 0.1R_m$, which is much smaller than the ring equilibrium radius. Figure 5.27 shows friction profiles for two friction interfaces. The curve with $\bar{\gamma}_{b,l} = 1$, $\bar{\gamma}_{b,r} = 10$ represents a system where a ring transitions from a region of small friction

²It is important to note that although the ring friction changes at the interface, the rod friction remains constant in our simulations.

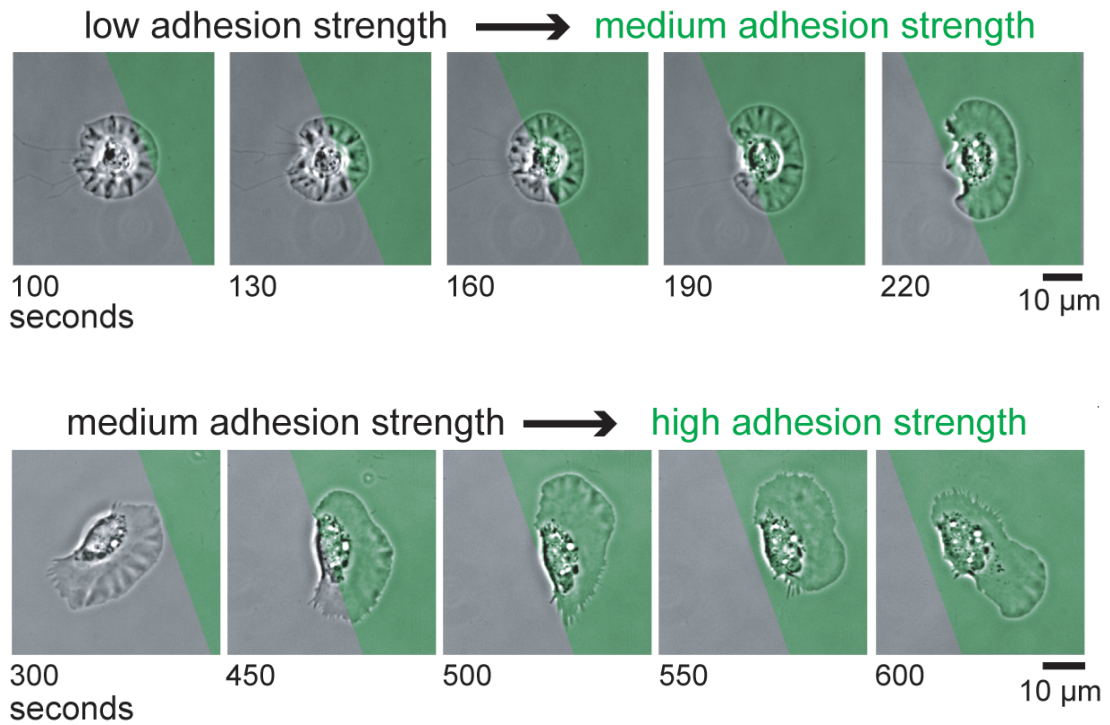


Figure 5.26: Keratocytes at interfaces between substrates with different adhesion strengths. The top row shows a keratocyte crossing from a region of low adhesion strength, where the keratocyte is round, to a region of medium adhesion strength, where the keratocyte is fan-shaped. The bottom row shows a keratocyte crossing from a region of medium adhesion strength, where the keratocyte is fan-shaped, to a region of high adhesion strength, where the keratocyte shows travelling protrusion at the cell front. The adhesive properties of the substrate are modified by using a functionalized copolymer [193], the strength of the cell-substrate attachment increased with increasing copolymer density. Figure reproduced from Ref. [12].

5.3 Deformable rings at friction interfaces

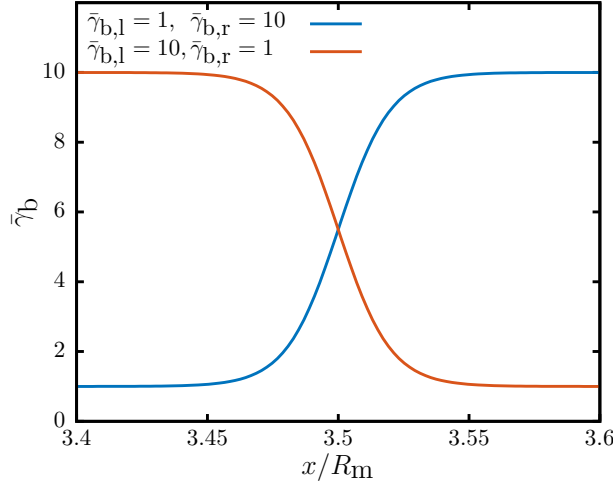


Figure 5.27: Bead friction $\bar{\gamma}_b$ for deformable rings versus position along the x-axis. The profile of the ring friction at the friction interface is given by a sigmoid function. The interface is centered around $x = 3.5R_m$ and has a width of $\approx 0.1R_m$.

to a region of large friction. The curve with $\bar{\gamma}_{b,l} = 10$, $\bar{\gamma}_{b,r} = 1$ represents a system where the ring transitions from a region of large friction to a region of small friction.

Figure 5.28 shows center-of-mass trajectories of deformable rings that move from regions with small ring friction to regions with large ring friction.³ The center-of-mass of the ring is initialized at small x close to the interface with an initial angle $\theta_i = 88^\circ$ with respect to the y-axis, see Fig. 5.28c at time $t = 0$. The system is initialized in the stationary shape corresponding to ring friction $\bar{\gamma}_{b,l}$. As the ring moves along the x-axis, the beads at the front of the ring reach the friction interface first, and their velocities decrease. Since the rod propulsion remains unchanged, the back of the ring continues to move with roughly its initial velocity. This leads to a decrease of the ring area and an elongation along the y-axis. The ring stiffness opposes the area decrease at the interface and leads to a reorientation of the ring, see Fig. 5.28c at times $t = 1.58$ and $7.91\tau_0$. After the ring has completely entered the large-friction region, it adapts to the new stationary shape corresponding to ring friction $\bar{\gamma}_{b,r}$, which can lead to further reorientation, see Fig. 5.28c at time $t = 26.35\tau_0$.

The larger the friction change, the more the ring is deflected, see Fig. 5.28a. For systems where the friction change is small $\gamma_{b,r} = 5$, a change in orientation only occurs once the entire ring has completely entered the large-friction region. The stationary shapes in the small and large-friction regions are similar; therefore the deflection is small. For systems where the friction change is large $\gamma_{b,r} = 25$, a change in orientation occurs as soon as the front of the ring comes in contact with the interface. The stationary shapes in the small and large-friction regimes are very different; therefore the deflection of the ring motion is large. A deflection occurs independently of the initial

³The that angles are calculated with respect to the y-axis and their values are given in degrees. $\theta_i \approx 90^\circ$ corresponds to a ring that is oriented perpendicular with respect to the interface. $\theta_i \approx 0^\circ$ corresponds to a ring that is oriented parallel with respect to the interface.

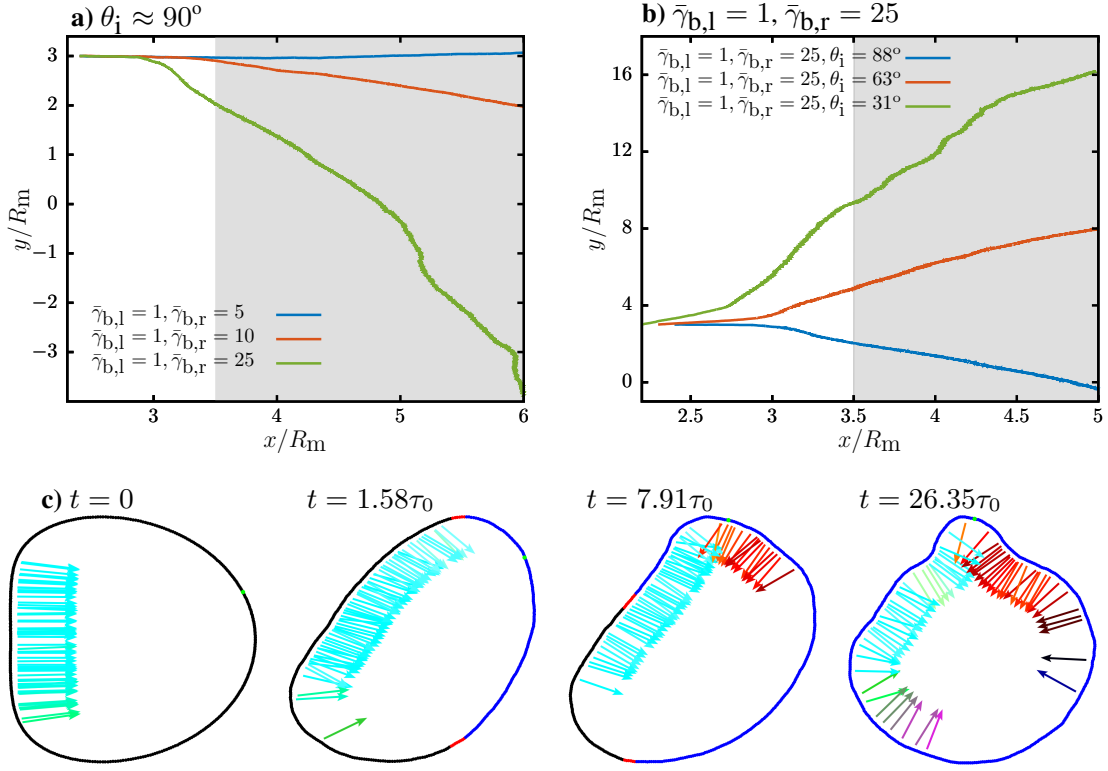


Figure 5.28: Center-of-mass trajectories and snapshots of deformable rings with attached-pulling rods at friction interfaces. Rings moving from a smaller to larger ring-friction region. Systems with $N_r = 64$, $E_r/k_B T = 1$, $Pe = 100$, $\bar{\kappa} = 2$, $\bar{k}_A = 100$, $\bar{k}_S = 0.15$ and $\zeta = 0.2$. **a)** Center-of-mass trajectories for deformable rings at friction interfaces. Systems with various $\bar{\gamma}_{b,r}$ and $\theta_i \approx 90^\circ$. **b)** Center-of-mass trajectories for deformable rings at friction interfaces. Systems with varying initial angle θ_i . The friction interface is located along the y -axis at $x = x_{int}$. White background represents the region $x < x_{int}$, and gray background represents the region $x > x_{int}$. **c)** Snapshots of a self-propelled deformable ring at a friction interface. System with $\bar{\gamma}_{b,l} = 1$, $\bar{\gamma}_{b,r} = 25$, and $\theta_i = 88^\circ$. Ring beads are colored black if they are located in the small-friction region, blue if they are located in large-friction region, and red if they are located at the friction interface. One specific bead of the ring is colored in green. The rods are colored according to their orientation.

orientation of the ring, see Fig. 5.28 b.

For systems where the ring moves from a large ring-friction region to a small ring-friction region, we also observe a deflection of the ring center-of-mass motion, see Fig. 5.29. For systems where the initial angle is perpendicular to the interface $\theta_i \approx 90^\circ$, the ring crosses the interface to the small-friction region, see Fig. 5.29a. For systems with $\bar{\gamma}_{b,l} \geq 10$, we observe bumps in the trajectory after the ring crosses the interface. However, for these systems, the initial ring shape is either a neutrophil or a non-stable keratocyte, see Fig. 5.29c at time $t = 0$. As the ring crosses the interface, the rods cluster at the back of the ring, forming a sharper end, see Fig. 5.29c at time $t = 31.09\tau_0$. As soon as the back of the ring enters the new region, the rods quickly rearrange and form a stable flat back, see Fig. 5.29c at times $t = 32.10$ and $33.21\tau_0$. The bump in the trajectory is caused by the quick change in the ring morphology.

For systems where the ring is initialized more tangentially, the ring cannot cross to the small-friction region, see Fig. 5.29 b. As soon as the ring reaches the interface, it reorients its direction of motion along the interface. Typically half of the ring remains in the large-friction region and half of the ring enters the small-friction region. The complete deflection at the interface is caused by the tank-treading motion of the ring with respect to the ring center-of-mass, see Fig. 5.30. As soon as the first beads of the ring are located on the small-friction region their velocity increases. Due to the increase in velocity for some ring beads and the ring orientation, the rings beads start to rotate in a counter-clockwise manner.

Figure 5.30 quantifies the rotation of the ring beads with respect to the ring center for systems where the ring motion follows the interface. Once the ring reaches the interface, the rotational velocity roughly remains constant. The angle of the zeroth bead θ_{bead} increases linearly with the distance d of the ring center-of-mass along the interface. We express this relation as $\theta_{\text{bead}} = a d + \theta_{\text{ini}}$, where θ_{ini} is the angle of the zeroth bead as the ring comes in contact with the interface, and a is the slope. $d(t) = \text{sign}(t) \sqrt{(x_{\text{cm}}(t) - x'_{\text{cm}})^2 + (y_{\text{cm}}(t) - y'_{\text{cm}})^2}$, where $x'_{\text{cm}} = x_{\text{cm}}(t')$ and $y'_{\text{cm}} = y_{\text{cm}}(t')$ represent the position of the center-of-mass as the first bead of the ring comes in contact with the interface and $t = t'$ is the time when the first bead of the ring comes in contact with the interface. $\text{sign}(t) = -1$ if $t < t'$ and $\text{sign}(t) = 1$ if $t \geq t'$.

For the systems with $\bar{\gamma}_{b,l} = 5$, the tank-treading motion is independent of the initial ring orientation, $a = 0.28$ and $0.24/R_m$, for $\theta_i \approx 60^\circ$ and 30° , respectively. For the systems with $\bar{\gamma}_{b,l} = 10$, the angular velocity is higher for $\theta_i \approx 60^\circ$, $a = 0.5/R_m$, than for $\theta_i \approx 30^\circ$, $a = 0.33/R_m$. Overall a increases as the change in friction increases. The rotation of the ring beads with respect to the ring center is similar to the tank-treading observed for vesicles and red blood cells in shear flow [194, 195].

Figure 5.31 shows the ring asphericity as the ring crosses the interface. The initial and final asphericities correspond to those of the stationary shapes on both sides of the interface. This means that the ring has no long-time memory because it eventually adopts the shape dictated by the substrate on which it is placed, independently of previous configurations. For systems where the ring crosses from a small ring-friction region to a large ring-friction region, the asphericity shows a positive peak as the first beads of the ring come in contact with the friction interface, see Fig. 5.31a. On the one hand, the front of the ring is moving more slowly, on the other hand, the back of

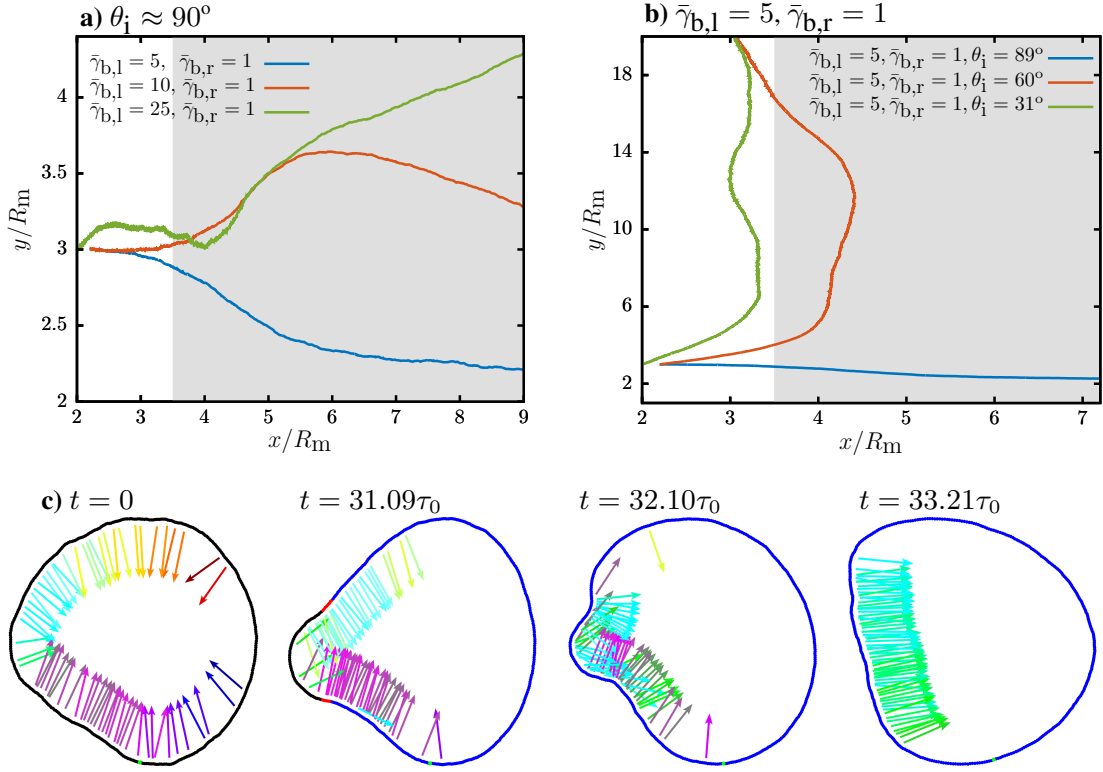


Figure 5.29: Center-of-mass trajectories and snapshots of deformable rings with attached-pulling rods at friction interfaces. The rings move from a larger ring-friction to smaller ring-friction region. Systems with $N_r = 64$, $E_r/k_B T = 1$, $Pe = 100$, $\bar{\kappa} = 2$, $\bar{k}_A = 100$, $\bar{k}_S = 0.15$ and $\zeta = 0.2$. **a)** Center-of-mass trajectories for deformable rings at friction interfaces. Systems with various $\bar{\gamma}_{b,l}$ and $\theta_i \approx 90^\circ$. **b)** Center-of-mass trajectories for deformable rings at friction interfaces. Systems with various initial angle θ_i . The friction interface is located along the y-axis at $x = x_{\text{int}}$. White background represents the region $x < x_{\text{int}}$, and gray background represents the region $x > x_{\text{int}}$. **c)** Snapshots of a self-propelled deformable ring at a friction interface. System with $\bar{\gamma}_{b,l} = 25$, $\bar{\gamma}_{b,r} = 1$, and $\theta_i = 71^\circ$. Ring beads are colored black if they are located in the large-friction region, blue if they are located in the small-friction region, and red if they are located at the friction interface. One specific bead of the ring is colored in green. The rods are colored according to their orientation.

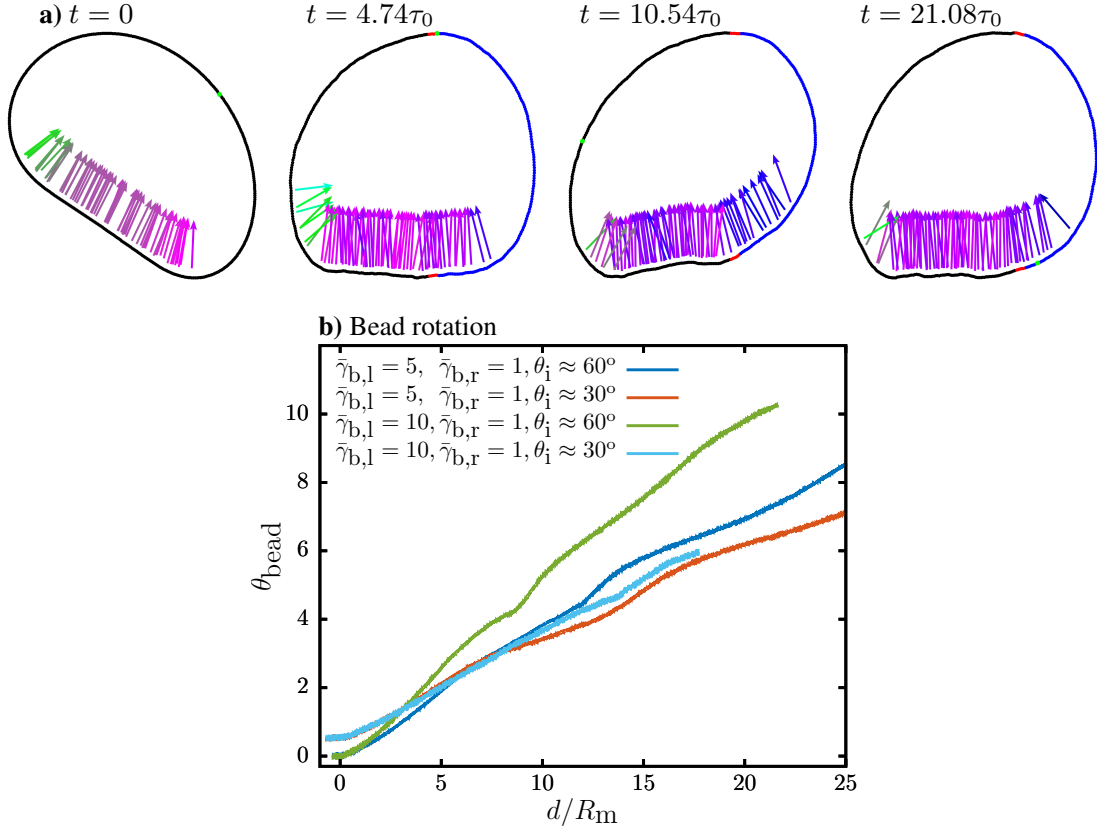


Figure 5.30: Ring tank-treading. **a)** Snapshots of a self-propelled deformable ring at a friction interface. System with $\bar{\gamma}_{b,l} = 5$, $\bar{\gamma}_{b,r} = 1$, and $\theta_i = 31^\circ$. Ring beads are colored black if they are located in the large-friction region, blue if they are located in the small-friction region, and red if they are located at the friction interface. One specific bead of the ring is colored in green. The rods are colored according to their orientation. **b)** Angle of a specific bead θ_{bead} versus distance d of the ring center-of-mass along the interface. System with $N_r = 64$, $E_r/k_B T = 1$, $Pe = 100$, $\bar{\kappa} = 2$, $\bar{k}_A = 100$, $\bar{k}_S = 0.15$ and $\zeta = 0.2$. Systems with various $\bar{\gamma}_{b,l}$, and $\bar{\gamma}_{b,r}$, and initial angles θ_i .

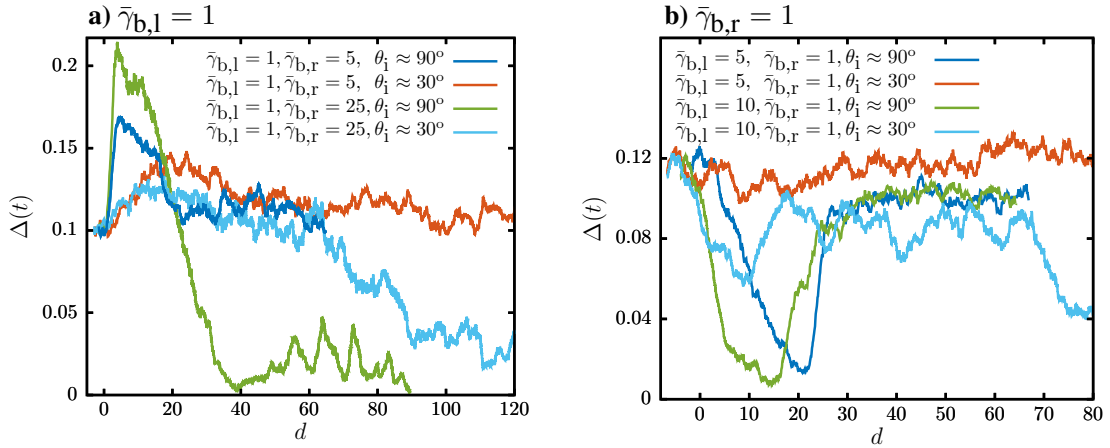


Figure 5.31: Shape dynamics for deformable rings with attached pulling rods at friction interfaces. Systems with $N_r = 64$, $E_r/k_B T = 1$, $Pe = 100$, $\bar{\kappa} = 2$, $\bar{k}_A = 100$, $\bar{k}_S = 0.15$ and $\zeta = 0.2$. **a)** Asphericity $\Delta(t)$ versus distance d of the ring center-of-mass along the interface for $\bar{\gamma}_{b,l} = 1$, and various values of $\bar{\gamma}_{b,r}$ and θ_i . **b)** Asphericity $\Delta(t)$ versus distance d of the ring center-of-mass along the interface for $\bar{\gamma}_{b,r} = 1$, and various values of $\bar{\gamma}_{b,l}$ and θ_i .

the ring, where the rods are placed, keeps moving almost with its initial velocity. This squeezes the ring along the y-axis, thus increasing its asphericity. The peak increases with increasing change in friction, and decreases as the initial ring orientation becomes more tangential. For rings with $\theta_i < 90^\circ$, the rods are initially not oriented in the direction of the first beads that cross the interface. Thus, the ring elongates less, and the asphericity peak decreases. Furthermore, the friction change is more gradual, which leads to a slower change of the ring shape, and therefore a slower relaxation of the asphericity. However, the final value of the asphericity is independent of the initial ring orientation θ_i .

For systems where the ring crosses from a large ring-friction region to a small ring-friction region and $\theta_i \approx 90^\circ$, the asphericity shows a negative peak as the ring crosses the interface, see Fig. 5.31b. During this process, the ring typically adopts a roundish shape with a pointed end, see Fig. 5.29c. After the ring has crossed the interface, the rods cluster and form a flat back. For systems with $\theta_i \approx 30^\circ$, we see no asphericity peak, because these are rings that stay at the interface. The asphericity fluctuates around a certain value, according to the percentage of beads which lie on the small-friction and the large-friction regions.

Chapter 6

Conclusions and Outlook

Our simulations focus on explaining collective behavior and complex dynamics observed in biological active matter systems. We have studied active self-propelled systems where the propulsion can adapt to its environment. While SPRs with density-dependent slowing down partially capture the behavior observed for bacteria with density-dependent reduced propulsion, SPRs in ring-like confinements can be considered as a minimal, soft matter model for cell motility.

6.1 Collective behavior of self-propelled rods with density-dependent reduced propulsion

We have studied self-propelled rods with density-dependent propulsion force in quasi-two-dimensional systems with periodic boundary conditions. The rods are discretized into beads that interact via a capped repulsive potential, which mimics self-avoiding rods in a thin, three-dimensional slab or next to a surface. Therefore, we use Brownian dynamics simulations and investigate the effect of the density-dependent propulsion force on the rod collective behavior. We find a very rich phase behavior with phases that are not observed for SPRs with constant propulsion.

Density-dependent reduced propulsion enhances polarity. SPRs with density-dependent reduced propulsion favor polar alignment over anti-polar orientations (stripes, polar clusters, polar hedgehog clusters and polar bands). The polar global order parameter Φ increases with increasing deceleration ratio λ and decreasing weight v_1 of the base propulsion force. As λ increases, the size of the polar clusters or the size of the polar domains increases.

Density-dependent reduced propulsion enhances cluster formation, as expected in MIPS systems. Clustered-nematic phases ($\lambda = 0$), which are phases composed of small clusters, become phases with large clusters when the density-dependent slowing-down is activated. The cluster size grows with decreasing v_1 , the propulsion force of rods decreases with the number of neighbors. This allows for the rod steric interaction to act longer, thus helping cluster formation. Because the propulsion force of rods with neighbors is small, there are few crossing events. This leads to the formation

Conclusions and Outlook

of system-spanning clusters which are loosely packed (cluster with domains, round clusters, stripes, polar hedgehog clusters, polar bands, and asters).

SPRs with density-independent propulsion form giant worm-like clusters. The density distribution function for systems with clusters shows two well-separated peaks [140]. The first peak represents the low-density region. The second peak represents the high-density region. In our systems, the density distribution shows only one peak, which corresponds to the high-density region (cluster with domains, stripes, polar hedgehog clusters, polar bands, and asters), because of the Voronoi tessellation used to calculate the cells enclosing the rods. In general, as λ increases and v_1 decreases, the peak of the distribution increases. The density-dependent propulsion heavily shifts the coexistence between the low-density region and the high-density region towards the high-density region. Thus leaving the low-density region nearly empty of rods.

Density-dependent reduced propulsion introduces perpendicularity in the rods at the cluster borders (round clusters, stripes, polar hedgehog clusters, polar bands, and asters). As v_1 decreases, the angle between the rods at the cluster borders and in bulk increases until the rods at the borders are oriented completely perpendicular. In contrast, SPRs with density-independent propulsion do not show perpendicularity [140].

For systems with $v_1 = 0$, rods with neighbors essentially become passive. This leads to the formation of asters or stripes. There is a clear transition between systems with $v_1 > 0$ and systems with $v_1 = 0$. For systems with $v_1 > 0$, the rods in the center of the cluster are propelled, and this leads to overall polar structures, e.g., polar bands. For systems with $v_1 = 0$, the propulsion for the rods in the center of the cluster disappears, and the global polarity of the systems disappears. Previous studies with two-dimensional constant-propulsion SPRs have shown aster-like clusters for large systems [196]. The aster-like clusters eject streams of rods to relieve the stresses created in the cluster. In our systems, there is no periodic streaming of rods. The possibility for our rods to cross each other and the density-dependent propulsion force diminish stresses in the asters. In a previous study where the collective behavior of classical SPRs with a hard repulsive potential was investigated, a low-density region is observed. In our systems, we see the low-density region is empty of rods, due to the density-dependent reduced propulsion.

In our systems, there is positive feedback between the density-dependent slowing-down and the cluster formation, like it happens in other MIPS systems [37]. On the contrary, for classical SPRs the rods cluster due to alignment only, and not by jamming as in MIPS. The emptiness of the gas phases found in our systems can be explained as a mixture of MIPS and rod perpendicularity observed at cluster borders.

Previous theoretical studies of systems with density-dependent reduced propulsion have been performed for self-propelled particles with Vicsek-type interactions [178]. They show similar dynamic phases to the ones observed in our systems: stripy, aster, moving clumps, and lane phases. Point particles with Vicsek interaction do not show clumps or aster formation; like for SPRs, such structures are only formed when a density-dependent reduced propulsion mechanism is present. Thus, for disks slowing-down due to steric interactions and density-dependent reduced propulsion both act in a similar way, inducing motility-induced clustering. For rods, steric interactions lead to

alignment, whereas density-dependent reduced propulsion leads to jamming. The stripy and lane phases are present in systems with Vicsek interaction and density-independent propulsion. However, it is not possible to observe polar bands or stripes for classical SPRs. No perpendicularity was observed for the system with point particles, which is the reason why the low-density regions in the system with point particles are more populated.

6.2 Self-propelled rods in rigid rings: cell-like motility patterns

Composite active particles that consist of penetrable self-propelled rods describing growing actin filaments of the cytoskeleton confined within passive rigid rings, mimicking a cell membrane, in two dimensions allow us to study both the internal structure and motility of model cells. The effective friction between rods and rings can be quantified and adjusted. We have studied non-attached rods, attached-pushing rods, and attached-pulling rods. The collective motion of the rods confined within a ring gives rise to the complex motion of the composite ring. This system can be considered as a minimal model for cell motility because it captures pushing and pulling forces, and alignment between filaments.

For rods within stationary rings, we find unidirectional circling, bidirectional circling, and clustering. Attached-pushing rods cluster more easily than non-attached rods. Compared with previous studies for the formation of hedgehog-like clusters of self-propelled rods near walls [143], the clusters formed in our systems are stable, which might be caused by both ring curvature and roughness. For non-attached rods, increasing the roughness of the ring extends the parameter region for the clustering phase.

For rods within mobile rings, we observe random walks, circling, persistent motion, and run-and-circle motion. Random-walk motion is observed for pushing-rod systems, persistent motion is observed for pulling-rod and pushing-rod systems, and circling motion is observed pulling-rod and mixed systems. In some cases, the mean-squared displacement of the rings can be explained by the ABP model [18,139]. For such cases, we find a thermal diffusive regime at short times, followed by a ballistic regime and a long-time active diffusive regime. For other parameter regimes, the dynamics of our complex self-propelled rings is much richer than for ABPs. For example, we observe superdiffusive and subdiffusive regimes and circling. In other non-ABP like systems, we observe more than one superdiffusive regime, which we attribute to a crossover between a diffusive and a second ballistic regime or to a crossover between circling and a second ballistic regime.

For all three types of systems with pushing, pulling and mixed rods, run-and-circle trajectories are observed. For some parameters the run-and-circle trajectories have less motile phases, circling phases, connected between long persistent motion stretches. The trajectories obtained in such systems are similar to the run-and-tumble motion of *E.coli* [183,197]. If the length of the segments decreases and the frequency of the circling increases, the trajectory becomes a random walk with circling phases, which resembles motion patterns seen for mesenchymal cells [184,198]. Finally, if the circling

frequency further increases, the trajectory becomes a random walk where the segments are composed of circling patterns.

Our results imply that not only treadmilling of cytoskeletal filaments and chemical signaling but also mechanical processes, such as filament-filament interaction and motility-mediated alignment of the filaments, determine the cell motility.

6.3 Self-propelled rods in deformable rings as model cells

In general, pushing forces due to actin polymerization are thought to be the critical ingredient in mesenchymal cell motility. Recent papers have found that contractile pulling forces, at the back of the cell, also play a crucial role in cell migration [199,200]. A recent paper by Nickaen et al. [146] proposed a model for keratocytes where only a homogeneous actin polymerization and myosin concentration were taken into account. The main forces present in their work were thus pulling forces. Their model reproduced keratocyte-like shapes that were capable of rotation.

We extend the model for complex self-propelled rigid rings by allowing the rings to deform. Here, we consider mainly systems with attached-pulling rods, although we also briefly describe the main results for systems with mixed rods. The collective motion of the rods confined within the rings gives rise to out-of-equilibrium shapes and complex motion patterns. This system can be considered as a minimal model for cell motility because it captures both pushing and pulling forces, alignment between filaments, and can reproduce cell-like shapes and motility patterns.

Rod self-propulsion leads to rod alignment and ring motility. In addition, ring deformation enhances rod clustering. For large ring friction, the ring shape relaxes slowly, and the deformability alignment is dominant over the motility alignment. For small ring friction, the ring shape relaxes quickly, and the motility alignment is dominant over the deformability alignment. For attached-pulling rod systems, we find quasi-circular fluctuating shapes for large ring frictions and small rod propulsion forces. Fluctuating shapes, in general, show random-walk motion, because they have no clear broken symmetry. For systems with large ring frictions and large rod propulsion forces, we find neutrophil-like shapes [186] that show persistent and run-and-tumble motion. In neutrophil-like systems, the long axis is oriented along the direction of motion. For systems with large rod propulsion forces and small ring frictions, we find keratocyte-like shapes, similar to keratocytes [12] and keratinocytes [185], which show very persistent motion. Here, the long axis is oriented perpendicular to the direction of motion. Increasing ring stiffness stabilizes the formation keratocyte-like rings and suppresses the formation of neutrophil-like rings.

For mixed systems, rings with both attached-pushing and attached-pulling rods, the pushing rods cluster at the front of the rings and the pulling rods cluster at the back or the sides of the rings. For systems with large ring frictions, we find elongated rings; for systems with intermediate ring frictions, we find neutrophil-like shapes; and for systems with small ring frictions, we find keratocyte-like systems. The addition of pushing rods to the rings renders the keratocyte-like shapes less stable, as such we find

fewer keratocyte-like and more neutrophil-like shapes for rings with mixed rods.

Our model hints that retraction forces are key to maintaining cell shapes in mesenchymal motility. If the actin polymerization is considered homogeneous along the plasma membrane, it can be implicitly modeled in the deformable ring. The explicitly modeled pulling forces then represent contractile actomyosin forces, such as actin retrograde flow or forces derived from stress fibers.

We quantify the ring shape by using the asphericity and the reduced area. Fluctuating systems have the largest reduced areas and the smallest asphericities. Neutrophil-like rings have smaller reduced areas and show similar asphericities to those of keratocyte-like rings. Keratocyte-like rings have the smallest reduced areas. In general, as the rod propulsion force increases, the rods can deform the rings more efficiently, which leads to a decreased reduced area and an increased asphericity. Rings with fluctuating shapes show minimal path velocities because the overall shape is quasi-circular, while neutrophil-like and keratocyte-like rings show significant path velocities.

Deformable self-propelled rings show similar motion patterns as rigid self-propelled rings: random-walk motion, persistent motion, and run-and-tumble motion. Ring deformability stabilizes rod clusters, which in turn suppresses circling ring motion. However, we still find run-and-tumble motion for neutrophil-like and fluctuating rings. From a motility point of view, the mean-squared-displacement of our deformable self-propelled rings can always be described using the ABP model: a thermal-diffusion regime at short times is followed by a ballistic regime at intermediate times, and an active-diffusion regime at long times. Keratocyte-like systems show the most persistent motion, their ballistic regimes of the MSDs extend to long times. Neutrophil-like systems also show long-time ballistic regimes, although their velocities are smaller than those observed for keratocyte-like systems. Having the elongated axis oriented perpendicular to the direction of motion thus leads to more pronounced and faster ballistic motion. Many fluctuating systems show no ballistic motion, and their trajectories resemble random walks.

6.4 Cell scattering at walls and interfaces

The motion of keratocytes at interfaces between smooth and microgrooved surfaces has been studied experimentally [188, 189]. Our simulations for keratocyte-like rings with attached-pulling rods qualitatively reproduce these experimental results. In our simulations, the microgrooved interface is modeled as a wall. During the interaction with the wall, the rings deform, and the rods reorient, such that the rings eventually leave the wall. Typically the shapes of the rings just after leaving the wall are not yet stationary shapes, which leads to further ring deformation and reorientation.

If the initial direction of motion is not too tangential, the rings always leave the wall within the same angular cone, in agreement with the experiments [188, 189]. In our simulations, the compression modulus does not affect the exit angle. However, with increasing ring friction the ring leaves the wall with a more tangential orientation. The reorientation after the ring leaves the wall increases with decreasing compression modulus and ring friction.

When studying dynamic shape changes as the rings are scattered, the asphericity

Conclusions and Outlook

shows two peaks. The first peak is positive and occurs as the ring first hits the wall. The ring elongates due to the pulling rods at the back of the ring. The second peak is negative and occurs as the ring leaves the wall. It indicates that the ring leaves the wall with a rounder shape than its stationary one. Finally, the ring recovers its stationary shape once it is far enough away from the wall. The reduced area shows only a negative peak, which corresponds to the elongation of the ring at the wall. In our parameter range, the shapes of deformable rings are mainly determined by the area constraint energy and not by the bending energy. Only for high values of the bending rigidity, $\bar{\kappa} \gtrsim 100$, the minimum distance between the ring and the wall increases and the height of the positive asphericity peak decreases.

Rigid rings with attached-pulling rods behave as ABPs when interacting with walls. This proves that ring deformation is crucial to obtaining cell-like behavior and for the ring to be deflected by the wall. Mixed systems, both for deformable and rigid rings, always stay at the wall. The addition of attached-pushing rods prevents the rings from leaving the wall.

The effect of substrate mechanical properties on keratocytes has been studied experimentally [10, 12, 192]. Of particular interest to us are keratocytes at adhesion strength interfaces [12]. On each side of the interface, the keratocyte adopts the stationary shape corresponding to the adhesion strength of the region it is placed in. As such, keratocytes crossing from low to medium adhesion strength change from a round shape to a fan-like shape. Upon crossing an interface, the trajectory of the cell is deflected. In our simulations, a ring assumes the stationary shape corresponding to the ring friction of the region it is placed in. As a ring crosses the interface, its shape changes, which leads to a deflection of the ring's center-of-mass trajectory. Let us consider a system where a ring crosses from a small-friction to a large-friction region. As the first beads of the ring come in contact with the interface, their velocity decreases. Meanwhile, the back of the ring, where the rods are located, is propelled with its initial velocity. Together with the area constraint, this leads to a reorientation of the ring. Deflection of the ring trajectory occurs independently of the initial ring orientation and increases as the friction change between the two regions increases.

For systems where a ring crosses from a large-friction to a small-friction region, we observe two different behaviors. For rings which are initially oriented perpendicularly with respect to the interface, the ring crosses the interface, and its trajectory is deflected. For rings which initially have a more tangential orientation, the rings reorient parallel to and move along the interface. This is caused by the tank-treading motion of the ring. This rotation is similar to the tank-treading motion observed for vesicles and red blood cells in shear flow.

6.5 Outlook

Our density-dependent self-propelled rod simulations show new and complex structures and rod dynamics. However, the phases observed do not fully reproduce the patterns observed in bacterial colonies for genetically modified *E. coli* with density-dependent reduced propulsion [166–168]. Furthermore, swarming *Bacillus subtilis* show density-dependent enhanced swimming velocity [201]. Bacterial rafts, small bacterial clusters,

swim faster than single bacteria. A possible research line in the future is to implement a speeding-up density-dependent propulsion, to see whether or not density-dependent enhanced-propulsion force SPRs can capture swarming behavior.

We have presented a minimalistic soft-matter active particle approach to modeling cell motility. Although the model is minimal, it captures cell-like shapes and motility patterns. On a qualitative level, we have shown that pulling forces are sufficient to recover cell-like motility patterns and shapes of crawling cells. This supports that pulling forces are a vital ingredient in mesenchymal cell motility. In the future, we want to quantitatively compare our shapes and trajectories with experimental shapes and trajectories of keratinocytes, keratocytes, and neutrophils. Access to experimental data allows us to test and further develop our model for different situations with motile cells: adding new substrate characteristics, such as adhesion and stiffness, as well as inhomogeneities and protein gradients along the membrane.

So far, we have only worked with single deformable cells. An obvious next step is to study systems with many deformable rings. A natural extension of the scattering simulations between a deformable ring and a wall would be scattering events of two deformable rings. Of particular interest are scattering events between keratocyte-like rings, because keratocytes are classical model systems to study cell motility. It would be particularly interesting to see whether pulling or mixed systems are better at reproducing the experimental data. Keratinocytes, which are very adhesive cells, are the predominant cells in the epidermis. When two keratinocytes come together, they form a small colony which can rotate [202, 203]. Adding an attractive potential between the polymer rings would allow different deformable rings to adhere. It is probable that such a system with adhered rings containing attached-pulling rods could reproduce the rotations and oscillations observed in small keratinocyte colonies.

We have focused on the shape and motion aspect of our motile cells. However, our model also allows us to study of out-of-equilibrium fluctuations. In the past few years, active fluctuations have become more and more interesting for the biophysics community [204–207]. In recent years, there have been studies predicting negative tension and enhanced fluctuations at long distances in active systems [205, 208]. The complex self-propelled deformable rings allow us to systematically study the effect that activity, clustering and pushing and pulling forces have on fluctuations. Preliminary results show that pushing rods lead to an increase of the ring tension, thus decreasing fluctuations at long distances. However, pulling rods decrease the tension along the ring, thus leading to enhanced fluctuations with long wavelengths.

Appendix A

Density-dependent rods: Systems with $n_r = 18$ and $Pe = 100$ and tables for polar and nematic order parameter

Here, we show the the values for S , and Φ for various parameter combinations for rods with $n_r = 9$, $\rho_0 L_r^2 = 6.4$, $E_r/k_B T = 5$, $Pe = 100$, and for rods with $n_r = 18$, $\rho_0 L_r^2 = 12.8$, $E_r/k_B T = 5$, $Pe = 400$, see Tabs. A.1 and A.2, respectively.

In chapter 3, we analyze systems with $n_r = 9$, $E_r/k_B T = 5$, and $Pe = 100$, and $n_r = 18$, $E_r/k_B T = 5$, and $Pe = 400$. We have also simulated systems with $n_r = 18$, $E_r/k_B T = 5$, and $Pe = 100$. The phases we observe for systems with $Pe=100$ and $Pe=400$ are very similar, compare snapshots for rods with $n_r = 18$ in Fig. 3 in the main text with Fig. A.1. The only difference between these two systems is that rods with $Pe = 100$ do not show an aligned phase (A1). This is due to the fact, that rods with $Pe = 100$ for polar clusters (PC) for systems with density-independent propulsion ($\lambda = 0$).

The density-dependent propulsion phase diagram for rods with $Pe = 100$ is very similar to that calculated for systems with $Pe = 400$, see Fig. 3b in the main text and Fig. A.1. For systems with $n_r = 18$, $Pe = 100$, and $v_1 = 0.5$ the rods form polar clusters, see Fig. A.1b. For systems with $\lambda \leq 1$ and $0.05 \leq v_1 \leq 0.25$, the rods form polar hedgehog clusters, see Fig. A.1c. For systems with $\lambda \geq 1$ and $0.05 \leq v_1 \leq 0.25$, the rods form polar bands, see Fig. A.1d. For systems with $v_1 = 0$, the rods form asters, see Fig. A.1e. The nematic and polar order parameter for the density-dependent systems with $n_r = 18$, and $Pe = 100$ can be found in Tab. A.3.

Density-dependent rods: Systems with $n_r = 18$ and $Pe = 100$ and tables for polar and nematic order parameter

| | | λ | | | | | |
|-------|--------|-----------|-------|-------|-------|-------|-------|
| v_1 | | 0.1 | 0.2 | 0.5 | 1 | 2 | 5 |
| 0.5 | S | 0.151 | 0.154 | 0.219 | 0.246 | 0.274 | 0.284 |
| | Φ | 0.141 | 0.157 | 0.187 | 0.212 | 0.245 | 0.252 |
| 0.25 | S | 0.152 | 0.155 | 0.231 | 0.284 | 0.319 | 0.336 |
| | Φ | 0.152 | 0.161 | 0.255 | 0.319 | 0.331 | 0.339 |
| 0.09 | S | 0.154 | 0.157 | 0.288 | 0.326 | 0.343 | 0.354 |
| | Φ | 0.166 | 0.167 | 0.289 | 0.324 | 0.345 | 0.348 |
| 0.07 | S | 0.155 | 0.159 | 0.309 | 0.349 | 0.361 | 0.378 |
| | Φ | 0.169 | 0.175 | 0.294 | 0.338 | 0.352 | 0.357 |
| 0.05 | S | 0.157 | 0.162 | 0.359 | 0.394 | 0.405 | 0.416 |
| | Φ | 0.172 | 0.178 | 0.297 | 0.359 | 0.360 | 0.363 |
| 0 | S | 0.159 | 0.164 | 0.453 | 0.556 | 0.565 | 0.579 |
| | Φ | 0.192 | 0.193 | 0.325 | 0.375 | 0.394 | 0.404 |

Table A.1: Polar and nematic order parameters, Φ and S , respectively, for systems with density-dependent propulsion, with $n_r = 9$, $\rho_0 L_r^2 = 6.4$, $E_r/k_B T = 5$, $Pe = 100$, and varying v_0 and λ values. For the system with constant propulsion, $S = 0.363$ and $\Phi = 0.074$. Table reproduced from publication (B) Ref. [179] with permission from the American Physical Society, ©2018 American Physical Society.

| | | λ | | | | | |
|-------|--------|-----------|-------|-------|-------|-------|-------|
| v_1 | | 0.2 | 0.4 | 1 | 2 | 4 | 10 |
| 0.5 | S | 0.713 | 0.721 | 0.845 | 0.853 | 0.871 | 0.871 |
| | Φ | 0.241 | 0.217 | 0.201 | 0.229 | 0.232 | 0.199 |
| 0.25 | S | 0.375 | 0.571 | 0.718 | 0.748 | 0.797 | 0.827 |
| | Φ | 0.508 | 0.613 | 0.691 | 0.739 | 0.757 | 0.762 |
| 0.09 | S | 0.388 | 0.463 | 0.557 | 0.632 | 0.667 | 0.682 |
| | Φ | 0.523 | 0.619 | 0.726 | 0.762 | 0.779 | 0.797 |
| 0.07 | S | 0.394 | 0.473 | 0.587 | 0.653 | 0.673 | 0.693 |
| | Φ | 0.536 | 0.625 | 0.736 | 0.787 | 0.801 | 0.822 |
| 0.05 | S | 0.428 | 0.482 | 0.652 | 0.662 | 0.685 | 0.717 |
| | Φ | 0.541 | 0.626 | 0.741 | 0.792 | 0.817 | 0.838 |
| 0 | S | 0.556 | 0.677 | 0.739 | 0.751 | 0.774 | 0.781 |
| | Φ | 0.552 | 0.632 | 0.761 | 0.804 | 0.843 | 0.869 |

Table A.2: Polar and nematic order parameters, Φ and S , respectively, for systems with density-dependent propulsion, with $n_r = 18$, $\rho_0 L_r^2 = 12.8$, $E_r/k_B T = 5$, $Pe = 400$, and varying v_0 and λ values. For the system with constant propulsion, $S = 0.701$ and $\Phi = 0.168$. Table reproduced from publication (B) Ref. [179] with permission from the American Physical Society, ©2018 American Physical Society.

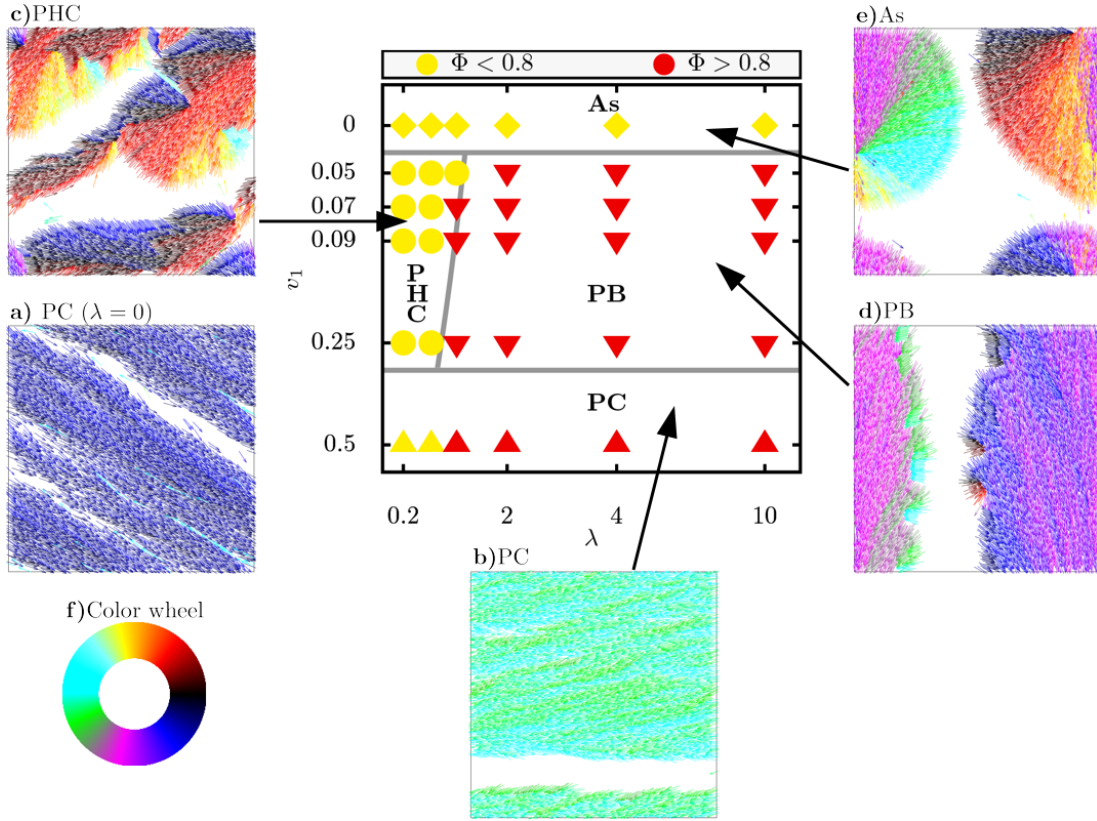


Figure A.1: Snapshots and phase diagram of self-propelled rod systems with $n_r = 18$, $\rho_0 L_r^2 = 12.8$, $E_r/k_B T = 5$, and $Pe = 100$. **a)** Polar clusters phase (PC), system with constant propulsion, i.e., $\lambda = 0$ highlighted by orange circle. **b)** Polar clusters phase (PC), system with $\lambda = 5$, and $v_1 = 0.5$. **c)** Polar hedgehog clusters phase (PHC), system with $\lambda = 0.2$, and $v_1 = 0.07$. **d)** Polar bands phase (PB), system with $\lambda = 1$, and $v_1 = 0.07$. **e)** Asters phase (As), system with $\lambda = 0.2$, and $v_1 = 0$. **f)** Color wheel indicates rod orientation. Figure reproduced from publication (B) Ref. [179] with permission from the American Physical Society, ©2018 American Physical Society..

Density-dependent rods: Systems with $n_r = 18$ and $Pe = 100$ and tables for polar and nematic order parameter

| | | λ | | | | | |
|-------|--------|-----------|-------|-------|-------|-------|-------|
| v_1 | | 0.2 | 0.4 | 1 | 2 | 4 | 10 |
| 0.5 | S | 0.758 | 0.769 | 0.837 | 0.812 | 0.857 | 0.841 |
| | Φ | 0.756 | 0.796 | 0.821 | 0.898 | 0.914 | 0.956 |
| 0.25 | S | 0.551 | 0.586 | 0.739 | 0.689 | 0.771 | 0.799 |
| | Φ | 0.675 | 0.689 | 0.813 | 0.825 | 0.828 | 0.839 |
| 0.09 | S | 0.575 | 0.612 | 0.701 | 0.727 | 0.781 | 0.804 |
| | Φ | 0.681 | 0.718 | 0.821 | 0.834 | 0.839 | 0.862 |
| 0.07 | S | 0.583 | 0.612 | 0.703 | 0.734 | 0.782 | 0.822 |
| | Φ | 0.688 | 0.737 | 0.825 | 0.846 | 0.862 | 0.881 |
| 0.05 | S | 0.595 | 0.626 | 0.720 | 0.731 | 0.734 | 0.825 |
| | Φ | 0.692 | 0.746 | 0.832 | 0.855 | 0.879 | 0.928 |
| 0 | S | 0.691 | 0.741 | 0.749 | 0.753 | 0.761 | 0.781 |
| | Φ | 0.718 | 0.729 | 0.748 | 0.773 | 0.782 | 0.788 |

Table A.3: Polar and nematic order parameters Φ and S , respectively, for systems with density-dependent propulsion, with $n_r = 18$, $\rho_0 L_r^2 = 12.8$, $E_r/k_B T = 5$, $Pe = 100$, and varying v_0 and λ values. For the system with constant propulsion $S = 0.743$ and $\Phi = 0.734$. Table reproduced from publication (B) Ref. [179] with permission from the American Physical Society, ©2018 American Physical Society.

Appendix B

Self-propelled rods inside a channel

We have also simulated self-propelled rods with $n_r = 9$ inside a channel. There are walls in the x-axis so that the rods can not escape, while in the y-axis there are periodic boundary conditions. We also implement a friction between the rods and the wall γ_{wall} .

Figure B.1 shows self-propelled rods inside a channel for different values of the Péclet number and the wall friction. For a system of passive rods the density is homogeneous, but for active systems as Pe increases most of the rods can be found close to the channel walls. For systems with small wall friction $\gamma_{\text{wall}} < 0.2$, the rods close to the wall are oriented parallel to the wall. For large values of the wall friction $\gamma_{\text{wall}} \geq 0.2$, the rods at the wall form hedgehog like clusters. For systems with $\gamma_{\text{wall}} = 0.23$, the rods close to the wall are oriented perpendicular to the wall. Only the rods at the wall show perpendicularity, the rods clustered after the column of perpendicular rods show parallel alignment. Thus, the rod perpendicularity is caused by the friction.

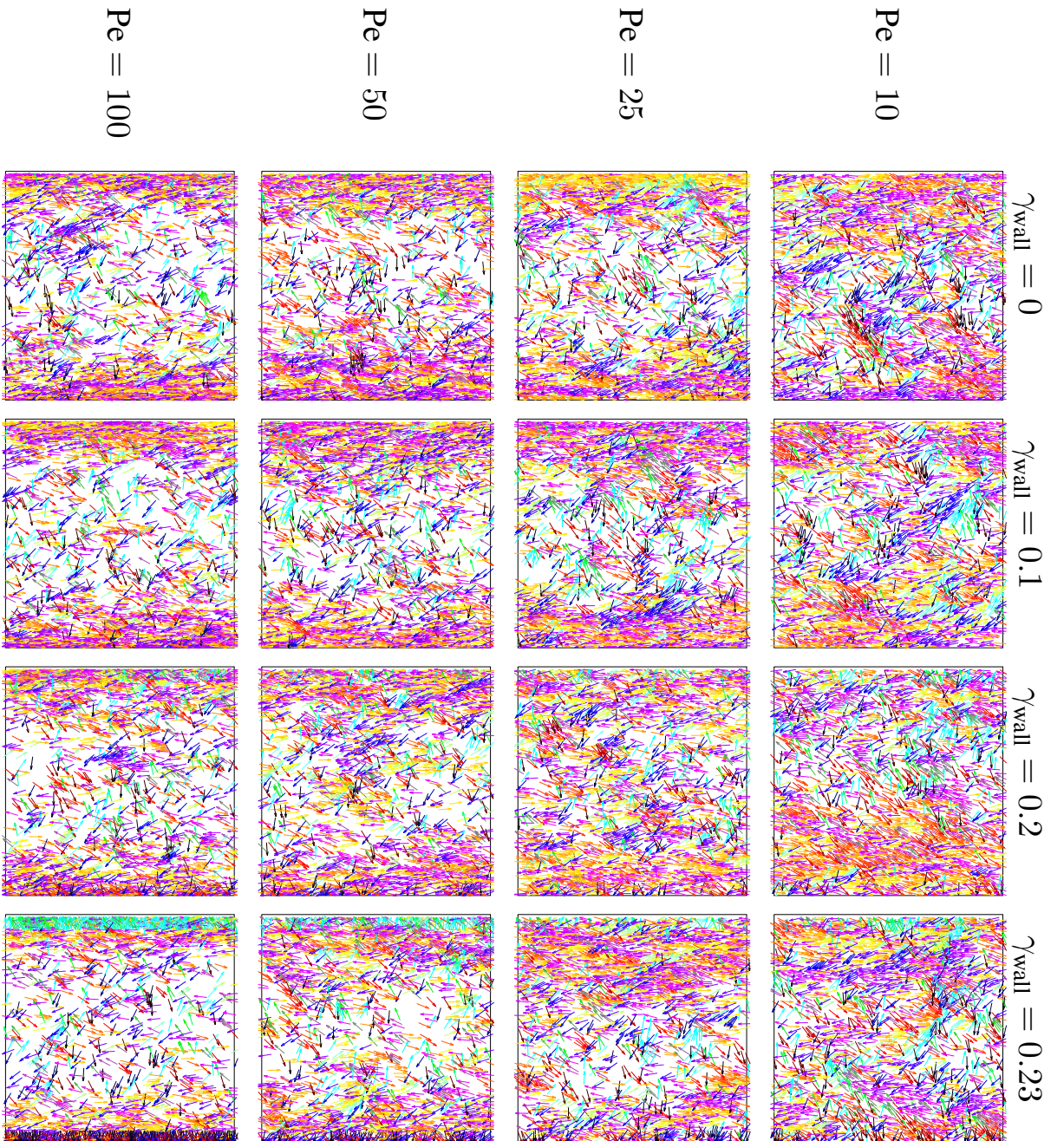


Figure B.1: Snapshots of self-propelled rods inside a channel for various values of the Péclet number Pe and the wall friction γ_{wall} . Systems with $n_r = 9$, $N_r = 2048$ and $E_r/k_B T = 1.5$.

Appendix C

Moments of a distribution

In probability theory, the n -th raw moment of a probability density function is

$$\mu_n = \mathbf{E}[X^n] = \int_{-\infty}^{\infty} x^n dF(x), \quad (\text{C.1})$$

where x is a random variable, $F(x)$ is the cumulative probability distribution function and \mathbf{E} is the expectation operator. The first raw moment of a distribution is the mean $\mu = \mathbf{E}[X]$.

There are other two type of moments: the central moments and the standardized moments. The central moments or moments about the mean are calculated using

$$\mu'_n = \mathbf{E}[(X - \mu)^n] = \int_{-\infty}^{\infty} x^n dF(x), \quad (\text{C.2})$$

The second central moment of a distribution is the variance. Its square root, the standard deviation is $\sigma = \sqrt{\mathbf{E}[X - \mu]^2}$.

The standardized moments of a distribution are the ratio between the n -th central moment and the n -th power of the standard deviation

$$\tilde{\mu}_n = \frac{\mu_n}{\sigma^n} = \frac{\mathbf{E}[(X - \mu)^n]}{(\mathbf{E}[X - \mu]^2)^{\frac{n}{2}}} \quad (\text{C.3})$$

The first standardized moment of a distribution is always 0, because the first moment about the mean is 0. The second standardized moment of a distribution is always 1, because the second moment about the mean is the variance. The third standardized moment is the skewness $\tilde{\mu}_3 = \gamma_1$, which is a measure of the asymmetry of a distribution about the mean. A positive skewness indicates that the right tail of the distribution is heavier than the left tail. The fourth standardized moment is the kurtosis, which is a measure of how heavy the tails of a distribution are. The kurtosis measures what portion of the data lies outside the region of the peak.

Bibliography

- [1] S. Ramaswamy, *Active matter*, J. Stat. Mech. Theory Exp. **2017**, 054002 (2017).
- [2] M. Marchetti et al., *Hydrodynamics of soft active matter*, Rev. Mod. Phys. **85**, 1143 (2013).
- [3] G. DeMagistris and D. Marenduzzo, *An introduction to the physics of active matter*, Physica A **418**, 65 (2015).
- [4] V. Schaller, C. Weber, C. Semmrich, E. Frey, and A. Bausch, *Polar patterns of driven filaments*, Nature **467**, 73 (2010).
- [5] Y. Sumino et al., *Large-scale vortex lattice emerging from collectively moving microtubules*, Nature **483**, 448 (2012).
- [6] F. Keber et al., *Topology and dynamics of active nematic vesicles*, Science **345**, 1135 (2014).
- [7] T. Sanchez, D. Chen, S. DeCamp, M. Heymann, and Z. Dogic, *Spontaneous motion in hierarchically assembled active matter*, Nature **491**, 431 (2012).
- [8] S. J. DeCamp, G. S. Redner, A. Baskaran, M. F. Hagan, and Z. Dogic, *Orientational order of motile defects in active nematics*, Nat. Mater. **14**, 1110 (2015).
- [9] S. Khler, V. Schaller, and A. Bausch, *Collective Dynamics of Active Cytoskeletal Networks*, PLoS One **6**, 23798 (2011).
- [10] E. Barnhart, K. Lee, G. Allen, J. Theriot, and A. Mogilner, *Balance between cell-substrate adhesion and myosin contraction determines the frequency of motility initiation in fish keratocytes*, Proc. Natl. Acad. Sci. U.S.A. **112**, 5045 (2015).
- [11] G. Csucs, K. Quirin, and G. Danuser, *Locomotion of fish epidermal keratocytes on spatially selective adhesion patterns*, Cytoskeleton **64**, 856 (2007).
- [12] E. Barnhart, K. Lee, K. Keren, A. Mogilner, and J. Theriot, *An adhesion-dependent switch between mechanisms that determine motile cell shape*, PLoS Biol. **9**, e1001059 (2011).
- [13] N. Evans, R. Oreffo, E. Healy, P. Thurner, and Y. Man, *Epithelial mechanobiology, skin wound healing, and the stem cell niche*, J. Mech. Behav. Biomed. Mater. **28**, 397 (2013).

- [14] X. Serra-Picamal et al., *Mechanical waves during tissue expansion*, Nat. Phys. **8**, 628 (2012).
- [15] Y. Matsubayashi, W. Razzell, and P. Martin, *White wave analysis of epithelial scratch wound healing reveals how cells mobilise back from the leading edge in a myosin-II-dependent fashion*, J. Cell Sci. **124**, 1017 (2011).
- [16] J. Palacci, S. Sacanna, A. Steinberg, D. Pine, and P. Chaikin, *Living Crystals of Light-Activated Colloidal Surfers*, Science **339**, 936 (2013).
- [17] R. Golestanian, T. Liverpool, and A. Ajdari, *Propulsion of a Molecular Machine by Asymmetric Distribution of Reaction Products*, Phys. Rev. Lett. **94**, 220801 (2005).
- [18] J. R. Howse et al., *Self-motile colloidal particles: from directed propulsion to random walk*, Phys. Rev. Lett. **99**, 048102 (2007).
- [19] I. Buttinoni, G. Volpe, F. Kmmel, G. Volpe, and C. Bechinger, *Active Brownian motion tunable by light*, J. Phys.: Condens. Matter **24**, 284129 (2012).
- [20] A. Cavagna et al., *Scale-free correlations in starling flocks*, Proc. Natl. Acad. Sci. U.S.A. **107**, 11865 (2010).
- [21] W. Bialek et al., *Statistical mechanics for natural flocks of birds*, Proc. Natl. Acad. Sci. U.S.A. **109**, 4786 (2012).
- [22] G. Kattas, X. Xu, and M. Small, *Dynamical Modeling of Collective Behavior from Pigeon Flight Data: Flock Cohesion and Dispersion*, PLoS Comput. Biol. **8**, 1002449 (2012).
- [23] F. Fish, *Kinematics of ducklings swimming in formation: Consequences of position*, J. Exp. Zool. **273**, 1 (1995).
- [24] A. McNeill, *Hitching a lift hydrodynamically - in swimming, flying and cycling*, J. Biol. **3**, 7 (2004).
- [25] D. Hoare, J. Krause, N. Peuhkuri, and J. Godin, *Body size and shoaling in fish*, abbreviation J. Fish Biol. **57**, 1351 (2000).
- [26] J. Landa, *Bioeconomics of schooling fishes: selfish fish, quasi-free riders, and other fishy tales*, Environ. Biol. Fish. **53**, 353 (1998).
- [27] https://en.wikipedia.org/wiki/Shoaling_and_schooling.
- [28] G. Fenteany, P. A. Janmey, and T. P. Stossel, *Signaling pathways and cell mechanics involved in wound closure by epithelial cell sheets*, Curr. Biol. **10**, 831 (2000).
- [29] https://en.wikipedia.org/wiki/Swarming_motility.
- [30] C. Jarzynski, *Nonequilibrium Equality for Free Energy Differences*, Phys. Rev. Lett. **78**, 2690 (1997).

BIBLIOGRAPHY

- [31] E. Bertin et al., *Mesoscopic theory for fluctuating active nematics*, New J. Phys. **15**, 085032 (2013).
- [32] G. Crooks, *Entropy production fluctuation theorem and the nonequilibrium work relation for free energy differences*, Phys. Rev. E **60**, 2721 (1999).
- [33] E. Bertin, A. Baskaran, H. Chate, and M. Marchetti, *Comparison between Smoluchowski and Boltzmann approaches for self-propelled rods*, Phys. Rev. E **92**, 042141 (2015).
- [34] L. Giomi, M. J. Bowick, X. Ma, and M. C. Marchetti, *Defect Annihilation and Proliferation in Active Nematics*, Phys. Rev. Lett. **110**, 228101 (2013).
- [35] G. Kokot et al., *Active turbulence in a gas of self-assembled spinners*, Proc. Natl. Acad. Sci. U.S.A. **114**, 12870 (2017).
- [36] J. Stenhammar, R. Wittkowski, D. Marenduzzo, and M. E. Cates, *Activity-Induced Phase Separation and Self-Assembly in Mixtures of Active and Passive Particles*, Phys. Rev. Lett. **114**, 018301 (2015).
- [37] M. E. Cates and J. Tailleur, *Motility-Induced Phase Separation*, Annu. Rev. Condens. Matter Phys. **6**, 219 (2015).
- [38] M. E. Cates and J. Tailleur, *When are active Brownian particles and run-and-tumble particles equivalent? Consequences for motility-induced phase separation*, EPL **101**, 20010 (2013).
- [39] T. E. Angelini et al., *Glass-like dynamics of collective cell migration*, Proc. Natl. Acad. Sci. U.S.A. **108**, 4714 (2011).
- [40] D. Bi, X. Yang, M. C. Marchetti, and M. L. Manning, *Motility-Driven Glass and Jamming Transitions in Biological Tissues*, Phys. Rev. X **6**, 021011 (2016).
- [41] D. Bi, J. H. Lopez, J. M. Schwarz, and M. L. Manning, *A density-independent rigidity transition in biological tissues*, Nat. Phys. **11**, 1074 (2015).
- [42] C. Ioannou, C. Tosh, L. Neville, and J. Krause, *The confusion effect from neural networks to reduced predation risk*, Behav. Ecol. **19**, 126 (2008).
- [43] J. Jeschke and R. Tollrian, *Prey swarming: which predators become confused and why?*, Animal Behav. **74**, 387 (2007).
- [44] T. Pitcher, A. Magurran, and I. Winfield, *Fish in larger shoals find food faster*, Behav. Ecol. Sociobiol. **10**, 149 (1982).
- [45] C. Peichel, *Social Behavior: How Do Fish Find Their Shoal Mate?*, Curr. Biol. **14**, R503 (2004).
- [46] S. Zhou, A. Sokolov, O. D. Lavrentovich, and I. S. Aranson, *Living liquid crystals*, Proc. Natl. Acad. Sci. U.S.A. **111**, 1265 (2014).

- [47] T. Gao, R. Blackwell, M. A. Glaser, M. D. Betterton, and M. J. Shelley, *Multiscale Polar Theory of Microtubule and Motor-Protein Assemblies*, Phys. Rev. Lett. **114**, 048101 (2015).
- [48] J. Prost, *The physics of liquid crystals. Vol. 83*, Oxford university press.
- [49] <https://www.mechanobio.info/cytoskeleton-dynamics/what-is-the-cytoskeleton/what-are-actin-filaments/how-do-actin-filaments-grow>.
- [50] <https://www.mechanobio.info/cytoskeleton-dynamics/what-is-the-cytoskeleton/what-are-actin-filaments/what-factors-influence-actin-filament-length-and-treadmilling>.
- [51] S. Burlacu, P. Janmey, and J. Borejdo, *Distribution of actin filament lengths measured by fluorescence microscopy*, Am. J. Physiol. **262**, C569 (1992).
- [52] R. Wade and A. Hyman, *Microtubule structure and dynamics*, Curr. Opin. Cell Biol. **9**, 12 (1997).
- [53] J. Block, V. Schroeder, P. Pawelzyk, N. Willenbacher, and S. Kster, *Physical properties of cytoplasmic intermediate filaments*, Biochim. Biophys. Acta-Molecular Cell Research **1853**, 3053 (2015).
- [54] A. Mogilner and G. Oster, *Cell motility driven by actin polymerization.*, Biophys. J **71**, 3030 (1996).
- [55] E. Bearer, *Role of Actin Polymerization in Cell Locomotion: Molecules and Models*, Am. J. Respir. Cell Mol. Biol. **8**, 582 (1993).
- [56] M. Nemethova, S. Auinger, and J. Small, *Building the actin cytoskeleton: filopodia contribute to the construction of contractile bundles in the lamella*, J. Cell. Biol. **180**, 1233 (2008).
- [57] H. Mellor, *The role of formins in filopodia formation*, Biochim. Biophys. Acta-Molecular Cell Research **1803**, 191 (2010).
- [58] S. Tojkander, G. Gateva, and P. Lappalainen, *Actin stress fibers: assembly, dynamics and biological roles*, J. Cell Sci. **125**, 1855 (2012).
- [59] S. Pellegrin and H. Mellor, *Actin stress fibres*, J. Cell Sci. **120**, 3491 (2007).
- [60] E. Foley and T. Kapoor, *Microtubule attachment and spindle assembly checkpoint signaling at the kinetochore*, Nat. Rev. Mol. Cell Biol. **14**, 25 (2013).
- [61] M. Glotzer, *The 3Ms of central spindle assembly: microtubules, motors and MAPs*, Nat. Rev. Mol. Cell Biol. **10**, 9 (2009).
- [62] P. Baas, *Microtubules and axonal growth*, Curr. Opin. Cell Biol. **9**, 29 (1997).
- [63] E. Dent, S. Gupton, and F. Gertler, *The Growth Cone Cytoskeleton in Axon Outgrowth and Guidance*, Cold Spring Harb. Perspect. Biol. **3** (2011).

BIBLIOGRAPHY

- [64] K. Green and C. Gaudry, *Are desmosomes more than tethers for intermediate filaments?*, Nat. Rev. Mol. Cell Biol. **1**, 208 (2000).
- [65] D. Garrod and M. Chidgey, *Desmosome structure, composition and function*, Biochim. Biophys. Acta-Biomembranes **1778**, 572 (2008).
- [66] E. Smith and E. Fuchs, *Defining the Interactions Between Intermediate Filaments and Desmosomes*, J Cell Biol. **141**, 1229 (1998).
- [67] R. Dominguez and K. Holmes, *Actin Structure and Function*, Annu. Rev. Biophys. **40**, 169 (2011).
- [68] R. Phillips, J. Kondev, J. Theriot, H. Garcia, and N. Orme, *Physical biology of the cell*, Garland Science.
- [69] E. Firat-Karalar and M. Welch, *New mechanisms and functions of actin nucleation*, Curr. Opin. Cell Biol. **23**, 4 (2011).
- [70] M. Chesarone and B. Goode, *Actin Nucleation and Elongation Factors: Mechanisms and Interplay*, Curr. Opin. Cell Biol. **21**, 28 (2009).
- [71] J. Neuhaus, M. Wanger, T. Keiser, and A. Wegner, *Treadmilling of actin*, J. Muscle Res. Cell Motil. **4**, 507 (1983).
- [72] B. Bugyi and M. Carlier, *Control of Actin Filament Treadmilling in Cell Motility*, Annu. Rev. Biophys. **39**, 449 (2010).
- [73] B. L. Goode, J. A. Eskin, and B. Wendland, *Actin and Endocytosis in Budding Yeast*, Genetics **199**, 315 (2015).
- [74] M. Vinzenz et al., *Actin branching in the initiation and maintenance of lamellipodia*, J. Cell. Sci. **125**, 2775 (2012).
- [75] I. Rouiller et al., *The structural basis of actin filament branching by the Arp2/3 complex*, J. Cell Biol. **180**, 887 (2008).
- [76] J. Bartles, *Parallel Actin Bundles and Their Multiple Actin-bundling Proteins*, Curr. Opin. Cell Biol. **12**, 72 (2000).
- [77] E. Goley and M. Welch, *The ARP2/3 complex: an actin nucleator comes of age*, Nat. Rev. Mol. Cell Biol. **7**, 713 (2006).
- [78] H. Higgs and T. Pollard, *Regulation of Actin Polymerization by Arp2/3 Complex and WASp/Scar Proteins*, J. Biol. Chem. **274**, 32531 (1999).
- [79] R. Mullins, J. Heuser, and T. Pollard, *The interaction of Arp2/3 complex with actin: Nucleation, high affinity pointed end capping, and formation of branching networks of filaments*, Proc. Natl. Acad. Sci. U.S.A. **95**, 6181 (1998).
- [80] B. L. Goode and M. J. Eck, *Mechanism and Function of Formins in the Control of Actin Assembly*, Annu. Rev. Biochem. **76**, 593 (2007).

-
- [81] S. Shekhar et al., *Formin and capping protein together embrace the actin filament in a mge ois*, Nat. Comm. **6**, 8730 (2015).
 - [82] T. Pollard, *Formins initiate new actin filaments*, Nat. Cell Biol. **4**, E191 (2002).
 - [83] S. Mostowy, *Multiple Roles of the Cytoskeleton in Bacterial Autophagy*, PLOS Pathog. **10**, 1 (2014).
 - [84] B. Mickey and J. Howard, *Rigidity of microtubules is increased by stabilizing agents.*, J. Cell Biol. **130**, 909 (1995).
 - [85] J. Bragues, V. Nuzzo, E. Mazur, and D. Needleman, *Nucleation and Transport Organize Microtubules in Metaphase Spindles*, Cell **149**, 554 (2012).
 - [86] S. Heins et al., *The rod domain of NF-L determines neurofilament architecture, whereas the end domains specify filament assembly and network formation.*, J. Cell Biol. **123**, 1517 (1993).
 - [87] http://www.thepinsta.com/a-amp-ampp-chs-10-11-week-8-biology-223-with-tattersall-at-XxrvtEVsppPkijaPb2ORhPGBcAfnODG*ZnZEM|GhqV0crIq5GnEFh1FeNDV2MS2IaG8FjzgzR705e5P5CzxZONsNVM0c3BcSAMvE18QvWAdL1uU7BKwilF368RQvOE3ymt3WDX4GUb8bkPKPspzIBxUJFM1vWcQNIV34VhuF40XliYgnMKxsoJ98LYugOLopMxwlWPRXkPBDq1*VHnwKQAC9VR5P0rJjDljQPmINarhlru5Q/.
 - [88] L. H. et al., *Molecular cell biology*, W. H. Freeman.
 - [89] M. Schliwa and G. Woehlke, *Molecular motors*, Wiley-VCH Verlag, 2003.
 - [90] G. Woehlke et al., *Microtubule Interaction Site of the Kinesin Motor*, Cell **90**, 207 (1997).
 - [91] N. Hirokawa, R. Nitta, and Y. Okada, *The mechanisms of kinesin motor motility: lessons from the monomeric motor KIF1A*, Nat. Rev. Mol. Cell Biol. **10**, 877 (2009).
 - [92] A. Roberts, T. Kon, P. J. Knight, K. Sutoh, and S. A. Burgess, *Functions and mechanics of dynein motor proteins*, Nat. Rev. Mol. Cell Biol. **14**, 713 (2013).
 - [93] J. R. Kardon and R. D. Vale, *Regulators of the cytoplasmic dynein motor*, Nat. Rev. Mol. Cell Biol. **10**, 854 (2009).
 - [94] M. J. Tyska and D. M. Warshaw, *The myosin power stroke*, Cell Motil. Cytoskeleton **51**, 1 (2002).
 - [95] J. T. Finer, R. M. Simmons, and J. A. Spudich, *Single myosin molecule mechanics: piconewton forces and nanometre steps*, Nature **368**, 113 (1994).
 - [96] S. V. Kim and R. A. Flavell, *Myosin I: From yeast to human*, Cell. Mol. Life Sci. **65**, 2128 (2008).
 - [97] M. Vicente-Manzanares, X. Ma, R. S. Adelstein, and A. R. Horwitz, *Non-muscle myosin II takes centre stage in cell adhesion and migration*, Nat. Rev. Mol. Cell Biol. **10**, 778 (2009).

BIBLIOGRAPHY

- [98] K. M. Trybus, *Myosin V from head to tail*, Cell. Mol. Life Sci. **65**, 1378 (2008).
- [99] A. D. Mehta et al., *Myosin-V is a processive actin-based motor*, Nature **400**, 590 (1999).
- [100] T. Sakamoto, A. Yildiz, P. R. Selvin, and J. R. Sellers, *Step-Size Is Determined by Neck Length in Myosin V*, Biochem. **44**, 16203 (2005).
- [101] S. J. Kron and J. A. Spudich, *Fluorescent actin filaments move on myosin fixed to a glass surface*, Proc. Natl. Acad. Sci. U.S.A. **83**, 6272 (1986).
- [102] A. Baskaran and M. Marchetti, *Hydrodynamics of self-propelled hard rods*, Phys. Rev. E **77**, 011920 (2008).
- [103] H. Chate, F. Ginelli, and R. Montagne, *Simple Model for Active Nematics: Quasi-Long-Range Order and Giant Fluctuations*, Phys. Rev. Lett. **96**, 180602 (2006).
- [104] P. C. Hiemenz, *Principles of colloid and surface chemistry*, CRC Press.
- [105] https://en.wikipedia.org/wiki/Lipid_bilayer.
- [106] <https://www.mechanobio.info/what-is-the-plasma-membrane/what-is-membrane-curvature>.
- [107] T. Tadros, Critical Micelle Concentration, in *Encyclopedia of Colloid and Interface Science*, pages 209–210, Springer Berlin Heidelberg, 2013.
- [108] R. Bartosz and L. Reinhard, *Spontaneous curvature of bilayer membranes from molecular simulations: Asymmetric lipid densities and asymmetric adsorption*, J. Chem. Phys. **142**, 054101 (2015).
- [109] H. T. McMahon and E. Boucrot, *Membrane curvature at a glance*, J. Cell Sci. **128**, 1065 (2015).
- [110] R. Lipowsky and E. Sackmann, *Structure and Dynamics of Membranes*, North Holland.
- [111] G. Cooper and R. Hausman, *The cell, a molecular approach*, Macmillan Education.
- [112] J. S. O'Brien, *Cell membranes Composition: Structure: Function*, J. Theor. Biol. **15**, 307 (1967).
- [113] https://en.wikipedia.org/wiki/Cell_membrane.
- [114] S. J. Marrink and D. Peter Tieleman, *Perspective on the Martini model*, Chem. Soc. Rev. **42**, 6801 (2013).
- [115] A. Saric and A. Cacciuto, *Self-assembly of nanoparticles adsorbed on fluid and elastic membranes*, Soft Matter **9**, 6677 (2013).

- [116] W. Helfrich, *Elastic properties of lipid bilayers: Theoy and possible experiments*, Z. Naturforsch. C Bio. Sci **28**, 693 (1973).
- [117] L. Blanchoin, R. Boujemaa-Paterski, C. Sykes, and J. Plastino, *Actin Dynamics, Architecture, and Mechanics in Cell Motility*, Physiol. Rev. **94**, 235 (2014).
- [118] P. Hotulainen and P. Lappalainen, *Stress fibers are generated by two distinct actin assembly mechanisms in motile cells*, J. Cell Biol. **173**, 383 (2006).
- [119] H. Yamaguchi, J. Wyckoff, and J. Condeelis, *Cell migration in tumors*, Curr. Opin. Cell Biol. **17**, 559 (2005).
- [120] P. Sens and J. Plastino, *Membrane tension and cytoskeleton organization in cell motility*, J. Phys. Condens. Matter **27**, 273103 (2015).
- [121] S. Tojkander et al., *A Molecular Pathway for Myosin II Recruitment to Stress Fibers*, Curr. Biol. **21**, 539 (2011).
- [122] J. V. Small, K. Rottner, I. Kaverina, and K. I. Anderson, *Assembling an actin cytoskeleton for cell attachment and movement*, Biochim. Biophys. Acta - Molecular Cell Research **1404**, 271 (1998).
- [123] X.-F. Zhang, A. W. Schaefer, D. T. Burnette, V. T. Schoonderwoert, and P. Forscher, *Rho-Dependent Contractile Responses in the Neuronal Growth Cone Are Independent of Classical Peripheral Retrograde Actin Flow*, Neuron **40**, 931 (2003).
- [124] J. A. West-Mays and D. J. Dwivedi, *The keratocyte: Corneal stromal cell with variable repair phenotypes*, nt. J. Biochem. Cell Biol. **38**, 1625 (2006).
- [125] K. Anderson, Y. Wang, and J. Small, *Coordination of protrusion and translocation of the keratocyte involves rolling of the cell body.*, J. Cell Biol. **134**, 1209 (1996).
- [126] T. M. Svitkina, A. B. Verkhovsky, K. M. McQuade, and G. G. Borisy, *Analysis of the Actin–Myosin II System in Fish Epidermal Keratocytes: Mechanism of Cell Body Translocation*, J. Cell Biol. **139**, 397 (1997).
- [127] R. MacKie, *Skin Cancer : An Illustrated Guide to the Aetiology, Clinical Features, Pathology and Management of Benign and Malignant Cutaneous Tumours*, Taylor Francis.
- [128] P.-y. Lam, E. A. Harvie, and A. Huttenlocher, *Heat Shock Modulates Neutrophil Motility in Zebrafish*, PLoS ONE **8**, e84436 (2013).
- [129] B. Rubinstein, M. Fournier, K. Jacobson, A. Verkhovsky, and A. Mogilner, *Actin-Myosin Viscoelastic Flow in the Keratocyte Lamellipod*, Biophys. J. **97**, 1853 (2009).

BIBLIOGRAPHY

- [130] T. M. Svitkina and G. G. Borisy, *Arp2/3 Complex and Actin Depolymerizing Factor/Cofilin in Dendritic Organization and Treadmilling of Actin Filament Array in Lamellipodia*, J. Cell Biol. **145**, 1009 (1999).
- [131] <http://www.sciencephoto.com/media/11993/view>.
- [132] C. L. M. H. Navier, *Memoire sur les lois du mouvement des fluides*, Mem. Acad. Sci. Inst. France **6**, 389 (1822).
- [133] J. Dhont, *An Introduction to Dynamics of Colloids*, Elsevier.
- [134] S. Chattopadhyay, R. Moldovan, C. Yeung, and X. L. Wu, *Swimming efficiency of bacterium Escherichiacoli*, Proc. Natl. Acad. Sci. U.S.A. **103**, 13712 (2006).
- [135] E. Purcell, *Life at low Reynolds number*, Am. J. Phys. **45**, 3 (1977).
- [136] E. Lauga, *Life around the scallop theorem*, Soft Matter **7**, 3060 (2011).
- [137] R. Kubo, *The fluctuation-dissipation theorem*, Rep. Prog. Phys. **29**, 255 (1966).
- [138] M. Doi and S. Edwards, *The theory of polymer dynamics*, Oxford university press.
- [139] C. Bechinger et al., *Active Brownian particles in complex and crowded environments*, Rev. Mod. Phys. **88**, 045006 (2016).
- [140] M. Abkenar, K. Marx, T. Auth, and G. Gompper, *Collective behavior of penetrable self-propelled rods in two dimensions*, Phys. Rev. E **88**, 062314 (2013).
- [141] C. Abaurrea Velasco, S. Ghahnaviyeh, H. Pishkenari, T. Auth, and G. Gompper, *Complex self-propelled rings: a minimal model for cell motility*, Soft Matter **13**, 5865 (2017).
- [142] M. Fisher and D. Ruelle, *The Stability of Many-Particle Systems*, J. Math. Phys. **7**, 260 (1966).
- [143] H. Wensink and H. Löwen, *Aggregation of self-propelled colloidal rods near confining walls*, Phys. Rev. E **78**, 031409 (2008).
- [144] A. Kaiser, H. Wensink, and H. Loewen, *How to Capture Active Particles*, Phys. Rev. Lett. **108**, 268307 (2012).
- [145] Y. Fily, A. Baskaran, and M. F. Hagan, *Dynamics of self-propelled particles under strong confinement*, Soft Matter **10**, 5609 (2014).
- [146] M. Nickaen et al., *A free-boundary model of a motile cell explains turning behavior*, PLoS Comput. Biol. **13**, 1 (2017).
- [147] R. Shlomovitz and N. S. Gov, *Membrane Waves Driven by Actin and Myosin*, Phys. Rev. Lett. **98**, 168103 (2007).

-
- [148] D. Foss and J. Brady, *Brownian Dynamics simulation of hard-sphere colloidal dispersions*, J. Rheol. **44**, 629 (2000).
- [149] S. Khrushchev et al., *Brownian-dynamics simulations of protein-protein interactions in the photosynthetic electron transport chain*, Biophys. **60**, 212 (2015).
- [150] U. Agarwal, R. Bhargava, and R. Mashelkar, *Brownian dynamics simulation of a polymer molecule in solution under elongational flow*, J. Chem. Phys. **108**, 1610 (1998).
- [151] A. Gelblum et al., *Ant groups optimally amplify the effect of transiently informed individuals*, Nat. Commun. **6**, 7729 (2015).
- [152] A. Vicsek and A. Zafeiris, *Collective motion*, Phys. Rep. **517**, 71 (2012).
- [153] J. Elgeti, R. Winkler, and G. Gompper, *Physics of microswimmers single particle motion and collective behavior: a review*, Rep. Prog. Phys. **78**, 056601 (2015).
- [154] J. Hu, M. Yang, G. Gompper, and R. Winkler, *Modelling the mechanics and hydrodynamics of swimming E. coli*, Soft Matter **11**, 7867 (2015).
- [155] F. Peruani, A. Deutsch, and M. B. *Nonequilibrium clustering of self-propelled rods*, Phys. Rev. E **74**, 030904 (2006).
- [156] A. Wysocki, R. Winkler, and G. Gompper, *Cooperative motion of active Brownian spheres in three-dimensional dense suspensions*, EPL **105**, 48004 (2014).
- [157] J. Stenhammar, D. Marenduzzo, R. Allen, and M. Cates, *Phase behaviour of active Brownian particles: the role of dimensionality*, Soft Matter **10**, 1489 (2014).
- [158] D. Pearce, A. Miller, G. Rowlands, and M. Turner, *Role of projection in the control of bird flocks*, Proc. Natl. Acad. Sci. U.S.A. **111**, 10422 (2014).
- [159] L. Barberis and F. Peruani, *Large-Scale Patterns in a Minimal Cognitive Flocking Model: Incidental Leaders, Nematic Patterns, and Aggregates*, Phys. Rev. Lett. **117**, 248001 (2016).
- [160] J. Deseigne, S. Leonard, O. Dauchot, and H. Chate, *Vibrated polar disks: spontaneous motion, binary collisions, and collective dynamics*, Soft Matter **8**, 5629 (2012).
- [161] G. Volpe, I. Buttinoni, D. Vogt, H. Kümmerer, and C. Bechinger, *Microswimmers in patterned environments*, Soft Matter **7**, 8810 (2011).
- [162] R. Isele-Holder, J. Elgeti, and G. Gompper, *Self-propelled worm-like filaments: spontaneous spiral formation, structure, and dynamics*, Soft Matter **11**, 7181 (2015).
- [163] A. Costanzo, J. Elgeti, T. Auth, G. Gompper, and M. Ripoll, *Motility-sorting of self-propelled particles in microchannels*, EPL **107**, 36003 (2014).

BIBLIOGRAPHY

- [164] Y. Yang, V. Marceau, and G. Gompper, *Swarm behavior of self-propelled rods and swimming flagella*, Phys. Rev. E **82**, 031904 (2010).
- [165] M. Paoluzzi, R. DiLeonardo, M. Marchetti, and L. Angelani, *Shape and Displacement Fluctuations in Soft Vesicles Filled by Active Particles*, Sci. Rep. **6**, 34146 (2016).
- [166] X. Fu et al., *Stripe Formation in Bacterial Systems with Density-Suppressed Motility*, Phys. Rev. Lett. **108**, 198102 (2012).
- [167] C. Liu et al., *Sequential Establishment of Stripe Patterns in an Expanding Cell Population*, Science **334**, 238 (2011).
- [168] M. Cates, D. Marenduzzo, I. Pagonabarraga, and J. Tailleur, *Arrested phase separation in reproducing bacteria creates a generic route to pattern formation*, Proc. Natl. Acad. Sci. U.S.A. **107**, 11715 (2010).
- [169] J. Anderson, *Colloid Transport by Interfacial Forces*, Annu. Rev. Fluid Mech. **21**, 61 (1989).
- [170] M. Yang and M. Ripoll, *Simulations of thermophoretic nanoswimmers*, Phys. Rev. E **84**, 061401 (2011).
- [171] M. Yang and M. Ripoll, *Thermophoretically induced flow field around a colloidal particle*, Soft Matter **9**, 4661 (2013).
- [172] J. Moran and J. Posner, *Phoretic Self-Propulsion*, Annu. Rev. Fluid Mech. **49**, 511 (2017).
- [173] I. Theurkauff, C. Cottin-Bizonne, J. Palacci, C. Ybert, and L. Bocquet, *Dynamic Clustering in Active Colloidal Suspensions with Chemical Signaling*, Phys. Rev. Lett. **108**, 268 (2012).
- [174] T. Chiang and D. Velegol, *Multi-ion diffusiophoresis*, J. Colloid Interface Sci. **424**, 120 (2014).
- [175] A. Sokolov, I. Aranson, J. Kessler, and R. Goldstein, *Concentration dependence of the collective dynamics of swimming bacteria*, Phys. Rev. Lett. **98**, 158102 (2007).
- [176] T. Ohta and S. Yamanaka, *Traveling bands in self-propelled soft particles*, Eur. Phys. J. Spec. Top. **223**, 1279 (2014).
- [177] S. Mishra, A. Baskaran, and M. Marchetti, *Fluctuations and pattern formation in self-propelled particles*, Phys. Rev. E **81**, 061916 (2010).
- [178] F. Farrell, M. Marchetti, D. Marenduzzo, and J. Tailleur, *Pattern Formation in Self-Propelled Particles with Density-Dependent Motility*, Phys. Rev. Lett. **108**, 248101 (2012).

- [179] C. Abaurrea Velasco, M. Abkenar, G. Gompper, and T. Auth, *Collective behavior of self-propelled rods with quorum sensing*, Phys. Rev. E **98**, 022605 (2018).
- [180] F. Peruani, L. Schimansky-Geier, and M. B. *Cluster dynamics and cluster size distributions in systems of self-propelled particles*, Eur. Phys. J. Spec. Top. **191**, 173 (2010).
- [181] S. van Teeffelen and H. Löwen, *Dynamics of a Brownian circle swimmer*, Phys. Rev. E **78**, 020101 (2008).
- [182] F. Peruani and L. Morelli, *Self-Propelled Particles with Fluctuating Speed and Direction of Motion in Two Dimensions*, Phys. Rev. Lett. **99**, 010602 (2007).
- [183] A. E. Patterson, A. Gopinath, M. Goulian, and P. E. Arratia, *Running and tumbling with E. coli in polymeric solutions*, Sci. Rep. **5**, 15761 (2015).
- [184] J. Lee, M. Leonard, T. Oliver, A. Ishihara, and K. Jacobson, *Traction forces generated by locomoting keratocytes.*, J. Cell Bio. **127**, 1957 (1994).
- [185] D. E. Frank and W. G. Carter, *Laminin 5 deposition regulates keratinocyte polarization and persistent migration*, J. Cell. Sci. **117**, 1351 (2004).
- [186] R. Jannat, M. Dembo, and D. Hammer, *Traction Forces of Neutrophils Migrating on Compliant Substrates*, Biophys. J. **101**, 575 (2011).
- [187] J. Elgeti and G. Gompper, *Run-and-tumble dynamics of self-propelled particles in confinement*, EPL **109**, 58003 (2015).
- [188] H. Miyoshi et al., *Characteristics of motility-based filtering of adherent cells on microgrooved surfaces*, Biomater. **33**, 395 (2012).
- [189] H. Miyoshi et al., *Control of highly migratory cells by microstructured surface based on transient change in cell behavior*, Biomater. **31**, 8539 (2010).
- [190] https://www.youtube.com/watch?v=I_xh-bkiv_c.
- [191] H. Döbereiner, E. Evans, M. Kraus, U. Seifert, and M. Wortis, *Mapping vesicle shapes into the phase diagram: A comparison of experiment and theory*, Phys. Rev. E **55**, 4458 (1997).
- [192] E. Barnhart, J. Allard, S. Lou, J. Theriot, and A. Mogilner, *Adhesion-Dependent Wave Generation in Crawling Cells*, Curr. Biol. **27**, 27 (2017).
- [193] S. VandeVondele, J. Voros, and J. A. Hubbell, *RGD-grafted poly-l-lysine-graft-(polyethylene glycol) copolymers block non-specific protein adsorption while promoting cell adhesion*, Biotechnol. Bioeng **82**, 784 (2003).
- [194] H. Basu, A. Dharmadhikari, J. Dharmadhikari, S. Sharma, and D. Mathur, *Tank Treading of Optically Trapped Red Blood Cells in Shear Flow*, Biophys. J. **101**, 1604 (2011).

BIBLIOGRAPHY

- [195] H. Noguchi and G. Gompper, *Dynamics of fluid vesicles in shear flow: Effect of membrane viscosity and thermal fluctuations*, Phys. Rev. E **72**, 011901 (2005).
- [196] S. Weitz, A. Deutsch, and F. Peruani, *Self-propelled rods exhibit a phase-separated state characterized by the presence of active stresses and the ejection of polar clusters*, Phys. Rev. E **92**, 012322 (2015).
- [197] N. Darnton, L. Turner, S. Rojevsky, and H. Berg, *On Torque and Tumbling in Swimming Escherichia coli*, J. Bacteriol. **189**, 1756 (2007).
- [198] Y. Sun et al., *Keratocyte fragments and cells utilize competing pathways to move in opposite directions in an electric field*, Curr. Biol. **23**, 569 (2013).
- [199] R. Poincloux et al., *Contractility of the cell rear drives invasion of breast tumor cells in 3D Matrigel*, Proc. Natl. Acad. Sci. U.S.A. **108**, 1943 (2011).
- [200] Q. Chi et al., *Rear actomyosin contractility driven directional cell migration in three-dimensional matrices: a mechano chemical coupling mechanism*, J. Royal Soc. Interface **11**, 20131072 (2014).
- [201] A. Sokolov, I. S. Aranson, J. O. Kessler, and R. E. Goldstein, *Concentration dependence of the collective dynamics of swimming bacteria*, Phys. Rev. Lett. **98**, 158102 (2007).
- [202] D. Nanba et al., *Cell motion predicts human epidermal stemness*, J. Cell Biol. **209**, 305 (2015).
- [203] S. Tate et al., *Rotation is the primary motion of paired human epidermal keratinocytes*, J. Dermatol. Sci. **79**, 194 (2015).
- [204] H. Turlier et al., *Equilibrium physics breakdown reveals the active nature of red blood cell flickering*, Nat. Phys. **12**, 513 (2016).
- [205] V. G. Almendro-Vedia et al., *Nonequilibrium fluctuations of lipid membranes by the rotating motor protein F1F0-ATP synthase*, Proc. Natl. Acad. Sci. U.S.A. **114**, 11291 (2017).
- [206] C. Monzel and K. Sengupta, *Measuring shape fluctuations in biological membranes*, J. Phys. D **49**, 243002 (2016).
- [207] A. Biswas, A. Alex, and B. Sinha, *Mapping Cell Membrane Fluctuations Reveals Their Active Regulation and Transient Heterogeneities*, Biophys. J. **113**, 1768 (2017).
- [208] T. Banerjee and A. Basu, *Active processes make mixed lipid membranes either flat or crumpled*, New J. Phys. **20**, 013028 (2018).

Acknowledgements

I would like to first thank my thesis committee for accepting to read this thesis and for their patience: Prof. Dr. Gerhard Gompper, Prof. Dr. Matthias Sperl, and Prof. Dr. Berenike Maier.

This thesis would not have been possible without my Doktorvater, Prof. Dr. Gerhard Gompper, or my supervisor, Dr. Thorsten Auth. Gerhard, I am very thankful that you gave me the opportunity to work on this project. You always try to find time for scientific discussions in spite of your endless commitments. I would like to especially thank you for your scientific insight and on-point observations and comments. Discussing with you always helps me see and understand problems more clearly.

Thorsten, thank you for your infinite patience, availability and readiness. Your office door is always open, late during the evening or during weekends, independently of how busy you might be. Your attention to detail and your readiness are crucial in helping me when I am stuck with a code or result.

Most of the simulations and results shown here would not have been possible without Jureca and the Jülich Computing Centre (JSC). I would also like to thank the entire group of ICS-2. I would be remiss not to highlight some of my past and present colleagues: Ewan, Jin Suk, and Ahmet thank you all for being wonderful officemates. In particular Ahmet, for starting the tea and chocolate stash in our office, and the eclectic conversations about yoga, Turkey and gaming. Thanks to Özer for his infinite knowledge of Python and Cpp and his patience when helping me with my codes. Thanks to Arvind for all the wonderful conversations these last three years, and for introducing me to electroswing and the amazing sketches of Rowan Atkinson. Muchas gracias también a Marisol, por sus esclarecedores consejos. No puedo terminar este párrafo sobre el ICS-2 sin dar las gracias a Sergi y a Judit por la multitud de risas y las muy necesarias conversaciones de besugos de los últimos meses. Sois muy “TOP↑” chicos.

I think that my PhD would have been very different had I not been part of Biosoft. It is impossible for me to talk about Biosoft without mentioning Sabrina, Tamar, and Dusan. Thank you all for all the fun and all the ridiculous and hilarious conversations both during coffee breaks and during lunch.

Gracias al grupo italiano de Aachen, natal y adoptado: Annita, Pao, Clau, Andrea, Menica, Matic y Thomas. Gracias por haberme incluido en la pequeña comunidad mediterranea de Aachen. Cuando se vive en el extranjero es lujo poder encontrar amigos que entienden y comparten tu cultura, tu lengua, tus problemas y tus ilusiones. Mil gracias por haber hecho estos años entre “crucchi” mucho más llevaderos e interesantes. En particular muchísimas gracias a Annita por ser una fantástica compañera de piso, y a Clau por sus consejos y ayuda en mis ratos más neurás.

Mil gracias a mi familia, tíos y primos, mayores y pequeños, de sangre y políticos, por vuestro apoyo y cariño. Gracias, en especial, a mi tía Maite, también conocida como Tante, por sus llamadas, por preocuparse siempre a pesar de la distancia y por los deliciosos hatillos. Muchísimas gracias a mi prima Laribus por las muy necesarias y siempre hilarantes conversaciones de Whatsapp. Esta tesis hubiera sido mucho más aburrida sin tus comentarios y motes con los que bautizaste mis resultados, véase por

BIBLIOGRAPHY

ejemplo “the climbing bean” y “los espermatozoides de colores”. Gracias, también, a mi prima Teresa María por aguantar y compartir mis peroratas sobre política española.

En último lugar y por encima de todo, me gustaría dar las gracias a mis padres, Jesús y Curra, a los que dedico esta tesis. Gracias por vuestro apoyo incondicional, vuestra guía y por habérmelo dado todo en esta vida.

Ich versichere, daß ich die von mir vorgelegte Dissertation selbständig angefertigt, die benutzten Quellen und Hilfsmittel vollständig angegeben und die Stellen der Arbeit — einschließlich Tabellen, Karten und Abbildungen —, die anderen Werken im Wortlaut oder dem Sinn nach entnommen sind, in jedem Einzelfall als Entlehnung kenntlich gemacht habe; daß diese Dissertation noch keiner anderen Fakultät oder Universität zur Prüfung vorgelegen hat; daß sie — abgesehen unten angegebenen Teilpublikationen — noch nicht veröffentlicht worden ist sowie, daß ich eine solche Veröffentlichung vor Abschluß des Promotionsverfahrens nicht vornehmen werde. Die Bestimmungen der Promotionsordnung sind mir bekannt. Die von mir vorgelegte Dissertation ist von Professor Gompper betreut worden.

(A) C. Abaurrea Velasco, S.D. Ghahnaviyeh, H.N. Pishkenari, T. Auth, G. Gompper
Complex self-propelled rings: a minimal model for cell motility
Soft Matter **13**, 5865-5876 (2017)

(B) C. Abaurrea Velasco, M. Abkenar, G. Gompper, T. Auth
Collective behavior of self-propelled rods with quorum sensing
Phys. Rev. E **98**, 022605 (2018)

Jülich, den 14. August 2018

| | |
|--------------------------|--|
| | Clara Abaurrea Velasco |
| Adresse | Elisabethstrasse 6 Aachen 52062, Deutschland |
| Geburtsdatum | 04.09.1991 |
| Geburtsort | Zaragoza |
| Familienstand | Ledig |
| Staatsangehörigkeit | Spanisch |
| 1997 – 2003 | Grundschule C.E.I.P. Basilio Paraíso Zaragoza |
| 2003 – 2009 | Gymnasium I.E.S. Miguel Servet Zaragoza |
| 2009 – 2014 | Licenciatura en Física Universidad de Zaragoza Zaragoza |
| 2014 | Diplomarbeit mit dem Thema „Effective interactions in DNA-stars“ |
| seit Oktober 2014 | Doktorarbeit Forschungszentrum Jülich Universität zu Köln |
| | Jülich, den 11. März 2018 |

